5-2009

Developing Reactive Molecular Dynamics for Understanding Polymer Chemical Kinetics

Kenneth D. Smith
University of Massachusetts Amherst, kensmithnj@gmail.com

DEVELOPING REACTIVE MOLECULAR DYNAMICS FOR UNDERSTANDING POLYMER CHEMICAL KINETICS

A Dissertation Presented

by

KENNETH D SMITH

Submitted to the Graduate School of the
University of Massachusetts Amherst in partial fulfillment
of the requirements for the degree of

DOCTOR OF PHILOSOPHY

May 2009

Chemical Engineering

DEVELOPING REACTIVE MOLECULAR DYNAMICS FOR UNDERSTANDING POLYMER CHEMICAL KINETICS

A Dissertation Presented

by

KENNETH D SMITH

Approved as to style and content by:

Phillip R. Westmoreland, Chair

Dimitrios Maroudas, Member

Murugappan Muthukumar, Member

T. J. Mountziaris, Department Head
Chemical Engineering

ACKNOWLEDGMENTS

While at UMASS there have been many challenges, but after all that is what a dissertation is all about. While the challenges of fire safe polymers, reactive molecular dynamics, and everything else are not yet resolved, the challenge of finishing the dissertation is completed. I would first like to thank my advisor, Phil Westmoreland. Phil provided a lot of valuable insight and knowledge, and his guidance and support were absolutely necessary for completing this dissertation. He took time to help guide me through many different aspects of life as a graduate student, and I am grateful for all that he has provided. I would also like to thank Prof. Maroudas and Prof. Muthukumar for their participating in my dissertation committee and guidance.

Marc Nyden and Stas Stoliarov were also instrumental in the work of this dissertation. They took time to help argue and work through many issues that arose through the course of this dissertation. It was also an enjoyable time spent working together on the code at the FAA, where many great discussions help to form the course of this work.

This work was also possible only through the funding of the Center for UMASS-Industry Research on Polymers (CUMIRP) Cluster F for Fire-Safe Polymers, who sponsored my work for five years. Currently, the cluster is made up of Boeing, Federal Aviation Administration, Multina, NIST, Sekisui Chemical, Solvay, and US Army; although, there have been other supporters as well in the past that I cannot remember at the moment. I would also like to acknowledge the time granted by the National Center for Supercomputing Applications for use of the supercomputers for some of the computational work completed in this dissertation.

The environment and support of the university and specifically the Chemical Engineering Department has made the time quite enjoyable. I would like to thank all the staff and faculty for their time and support in many activities from classes to what seem to be minor details. It was always a great group of individuals who made everything go as smoothly as possible.

Additionally, there have been many friends throughout the area who have helped me through my times in school. Several at school who provided help, and much needed breaks when everything seemed overwhelming. Also friends from church who have been immensely supportive through everything and kept me sane and on the right path. And also friends from work who consistently encouraged me to finish up.

My family has been very supportive and loving through all the endeavors of graduate school. Although they may not understand chemical engineering, there love and support has made this possible. I would like to thank my parents, sister, and grandparents for all the encouragement they have provided during the course of my studies.

I also must thank my wife, Amy, for all her loving support through many long and tough times during my dissertation. Her support through it has meant a lot to me and has helped me to be able to finish this dissertation. I love you.

Finally, I must thank God for granting me the abilities and patience accomplish this task. It was truly not something I could have ever done myself.

ABSTRACT

DEVELOPING REACTIVE MOLECULAR DYNAMICS FOR UNDERSTANDING POLYMER CHEMICAL KINETICS

MAY 2009

KENNETH D SMITH

B.S., ROWAN UNIVERSITY

M.ChE., UNIVERSITY OF DELAWARE

Ph.D., UNIVERSITY OF MASSACHUSETTS AMHERST

Directed by: Professor Phillip R. Westmoreland

One of the challenges in understanding polymer flammability is the lack of information about microscopic events that lead to macroscopically observed species, and Reactive Molecular Dynamics is a promising approach to obtain this crucially needed information. The development of a predictive method for condensed-phase reaction kinetics can provide significant insight into polymer flammability, thus helping guide future synthesis of fire-resistant polymers. Through this dissertation, a new reactive forcefield, RMDff, and Reactive Molecular Dynamics program, RxnMD, have been developed and used to simulate such material chemistry.

It is necessary to have accurate description of chemical kinetics to describe quantitative chemical kinetics. Typical equilibrium forcefields are inadequate for describing chemical reactions due to the inability to represent bonding transformations. This

issue was resolved by developing a new method, RMDff, that allows standard equilibrium forcefields to describe reactive transitions. The chemical reactions are described by employing switching functions that permit smooth transitions between the reactant and product descriptions available from traditional forcefields. Because all of the chemical motions are described, a complete potential energy surface is obtained for the course of the reaction. Descriptions of scission, addition/beta-scission, and abstraction reactions were developed for hydrocarbon species. Reactive potentials were developed using a representative reaction involving small molecules. It is shown that the overall geometric and energetic changes are transferable to larger and substituted molecules. The main source of error found in RMDff resulted from errors within the equilibrium forcefield descriptions.

In order to simulate the chemical kinetics, it was necessary to create a molecular dynamics program that could implement the reactions from RMDff. RxnMD was developed as a new C++-based Reactive Molecular Dynamics code to simulate the dynamics using RMDff. Polymer kinetics were predicted for high-density polyethylene and used to test the method and code. Conformational changes and polymer length in the initial polyethylene molecules did not significantly alter the backbone decomposition kinetics. The results also revealed that the backbone carbon-carbon bonds could break with an activation energy approximately 100 kJ/mol below the carbon-carbon bond dissociation energy. This decrease was believed to occur from intramolecular polymer stress, which is relieved via backbone scission. Such stress was also observed to increase the beta-scission reaction rate at high temperatures, apparently because the scission reaction alone is not always sufficient to remove the energy associated with the polymer stress concentrated near the scission location. Finally, the RMD method was also shown to be transferable and applicable in describing the decomposition of novel fire-resistant polymers.

TABLE OF CONTENTS

APPENDICES

LIST OF TABLES

Table **Page**

LIST OF FIGURES

Figure **Page**

CHAPTER 1

INTRODUCTION AND BACKGROUND

1.1 Introduction

"Reactive Molecular Dynamics" or RMD [3] is a technique that models reactions atomistically and dynamically by coupling standard molecular dynamics simulations with an algorithm permitting access to chemically reactive trajectories. Through natural evolution of the temporal dynamics, the structures can pass through reactive transitions into chemically different structures. By a smooth, seamless description of the chemical transformations, reactions can occur by sampling all the available reactive phase space.

RMD provides an ability to investigate the mechanistic view of individual reactions based on a dynamical evolution of the system without *a priori* kinetics information. RMD probes the atomistic-level interactions during the course of simulation. Interactions such as collisional energy transfer are inherently captured due to the atomistic interactions being simulated.

The time scales probed by RMD are relatively short due to computational demands of molecular dynamics. This constraint presents a challenge for RMD because chemical reactions are rare events compared to the simulated time. Even one of the slower rovibrational motions of a dihedral flip will occur 10^{10} times faster than a reactive event.

However, dealing with this challenge promises technological as well as fundamental advances. Development of fire-safe polymers is one such area that should benefit from RMD. Many common products such as furniture and bedding are required to pass

flammability tests. The aircraft industry has very stringent regulations on flammability. Yet the development of polymers with the desired properties is a difficult task, even without the additional requirements of flame resistance. For example, when an aircraft fire occurs, there are typically only a few minutes to escape prior to flashover. Flashover is a phenomena where all combustible products ignite spontaneously, engulfing the entire plane. These gases come from the combustion-driven pyrolysis from the approximately two tons of flammable materials within the plane, including materials in walls, seat cushions, pillows, and sealants [4]. After flashover, there is very little chance of survival [5]. For aircraft, the flashover time can be highly variable, but it can be only five minutes or less, which results in much of the death related to aircraft crashes [6]. RMD can be used as tool to investigate polymer flammability and help guide and direct novel polymer synthesis or flammability-reducing additives prior to laboratory experimentation.

The objective of this dissertation was to develop RMD as a technique that can be used to investigate chemical reactions without specifying particular reactions or reaction sites. A new RMD code and reactive forcefield method have been developed for the present simulations. These tools were used to investigate the decomposition of hydrocarbon polymers and the effects of different structural components. These phenomena are related to the elementary reactions obtained from RMD and macroscopically observed decomposition kinetics. To carry out this research, extensive quantum thermochemistry calculations have also been required.

1.2 Polymer Flammability

Several different components making up polymer flammability are depicted in Fig. 1.1. Heat induces pyrolysis of the condensed phase, yielding pyrolysis gases. These gases are released through any solid or molten surface layer into the gas phase above the polymer, where combustion occurs. The combustion generates heat, which

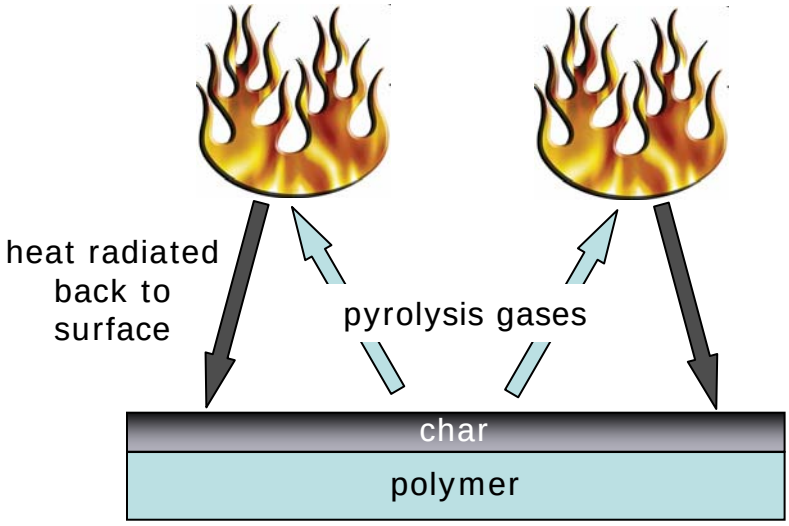

Figure 1.1. Depiction of polymer decomposition during flammability.

is radiated back to the surface and promotes further polymer pyrolysis. Thus, a feedback cycle sustains the fire. Various methods are used to defeat this cycle, such as halogens included to act as gas-phase inhibitors by radical scavenging [7–10] and porous char layers that reduce the amount of conducted into the surface [11, 12].

Characterizing the flammability of polymers is difficult because of the many variables to be considered. Some of the standard characterization parameters are heat release rate (HRR), ignitability, flame spread, smoke density, and toxicity. HRR is thought to be the most significant parameter for describing flammability [13]. In order to determine flammability, various tests are used. Limiting Oxygen Index (LOI) [14] and the UL-94 procedure [15] are two tests used for determining ignitability. Calorimetric techniques used to measure heat release include the OSU calorimeter [16], cone calorimeter [17], and microscale combustion calorimetry [18]. Techniques such as Pyrolysis-GC/MS [19] and FTIR [20] are used to identify the gaseous products that result from decomposition and aid degradation mechanism development. Additionally, other tests can be implemented for flame resistance and modeling.

There are a variety of methods to make flame-resistant polymers, from synthesizing novel polymers to using flammability-reducing additives. Because there are many commodity plastics that already contain desirable properties, one method of reducing flammability is through fillers. Inert fillers can take up volume of the flammable material and also potentially act as rheology modifiers. Some of the fillers are flame retardants, which help to stop the spread of the flame. Intumescence, a swelling of a material when exposed to heat, can be used to reduce the flammability by creating a heat-shield effect. The addition of chemical species such as halogens or phosphorous are commonly used to reduce or alter the chemical reactivity in either the gas or condensed phase. Sometimes only a small amount of a species is needed to affect flammability significantly.

Experimentally, polymer degradation is measured at the macroscopic level using methods such as Thermogravimetric Analysis (TGA) or Pyrolysis-GC/MS. While these techniques can give overall ideas of the decomposition, they do not provide the mechanistic molecular perspective needed to guide polymer synthesis. There has also been a variety of different proposed mechanisms for hydrocarbon polymer pyrolysis, including random scission [21–23]; random scission and β-scission [24–29]; random scission and hydrogen transfer [30]; and mixtures of random scission, β-scission, and hydrogen transfer [31–34]. Each of these different mechanisms has been able to model overall decomposition data reasonably well with various sets of rate equations. However, none of these techniques provide any of the necessary molecular insight.

1.3 Simulation Methods

1.3.1 Reactive Simulation Techniques

There are a variety of different techniques available for simulating chemical kinetics. Each technique investigates different time and spatial domains, creating a wide

range of available system conditions that can be investigated. There are situations in which these different techniques potentially have the ability to excel in terms of modeling polymer flammability, which are discussed below.

One of the more useful coarse-grained techniques for simulating chemical kinetics is a stochastic method called Kinetic Monte Carlo (KMC). This method was developed by Gillespie [35, 36] to simulate a series of elementary kinetic reactions within a global reaction mechanism, and it is described very lucidly in Ref. [37]. In this technique, one reaction is selected randomly, weighted by its probability of occurrence. The amount of time between each of these discrete events is then determined stochastically. From the reactions that occur, a total history of reactive events as a function of time is created. This method permits the solution of large coupled mechanisms without solving the series of coupled differential equations. KMC has been used to simulated a variety of situations including soot mechanisms [38], photon-induced dissociation [39], catalysis [40, 41], chemical activation [42], and energy transfer mechanisms [43, 44]. However, KMC requires prior knowledge of potential reactive steps and their kinetics. Failure to incorporate a critical step will yield a completely incorrect picture. While KMC is able to handle long time scales with large mechanisms, it does not permit a view of the detailed interactions of dynamics with structural effects that can affect chemical reaction kinetics.

A recent advance is to couple KMC with molecular dynamics [45–47]. This method allows for the simulation of dynamics of larger structural features over long time scales by assuming that the reactions will occur on a relaxed structure. The method starts by selecting and implementing a reaction event using the KMC method. Afterwards, molecular dynamics is used to relax the structure prior to the next reactive event. The reaction mechanism must still be developed outside of the simulation, typically from quantum chemical calculations. The dynamics are only used for structure relaxation

and do not lead to or identify any potential reaction. This method has been used to simulate soot particle formation [45–47] in order to understand particle evolution.

Including dynamical, spatial, and structure effects into the simulation of chemical kinetics requires the full inclusion of molecular dynamics. "*Ab initio* MD" methods like Car-Parrinello MD [48, 49] are techniques that couple *ab initio* calculations with molecular dynamics. Essentially, quantum chemical forces are used to integrate the equations of motion during each time step. There are also no explicit assumptions of any reactions because the dynamics dictate the motions and bonding is determined from *ab initio* calculation of the molecular orbitals at the current trajectory state. Therefore, no prior information is required as to potential reactive pathways. As one example, this technique has been applied to the adsorption of 1,3-butadiene on a Si surface [50], where these RMD simulations demonstrated the role of thermal decomposition that would not have been identified using either experiments or static *ab initio* calculations. The major drawback to this technique is the lengthy time required for calculation of the *ab initio* forces, even when using a very modest basis set and level of theory.

RMD can still be employed, if instead of using *ab initio* calculations, valence-bond forcefields are used to describe the interatomic interactions. These descriptions then provide the representation of the larger-scale structural interactions in a more course-grained manner than *ab initio* calculations. However, the implicit assumption is that the valence-bond forcefield is an essentially harmonic representation of the current structure. This treatment requires reactive pathways to be specified in order to describe the transition between harmonic PES's that otherwise do not naturally accomodate chemical transitions. With transitions from one structural description to another in hand, RMD using valence-bond forcefields can be implemented to describe the interatomic interactions. Therefore, the use of valence-bond forcefields with RMD makes it a useful technique for modeling the elementary kinetics of large,

condensed-phase systems. Valence-bond forcefields have been employed previously using modified conventional forcefields [3, 51–54]. Bond-order potentials have also been used in ReaxFF [55, 56] and REBO/AIREBO [57–60]. While these techniques cannot capture fine quantum-chemical details that are calculated in *ab initio* MD, the effects of structure and dynamics are still simulated simultaneously while avoiding infeasible *ab initio* calculations.

1.3.2 Molecular Representation

A representation of the electronic and nuclear interactions is required for computer simulations of molecules. The two common theories for representing these interactions in molecules are molecular orbital (MO) theory and valence-bond (VB) theory. The MO representation uses hybridized representations of the basic atomic shells to represent interactions between electrons within the system. However, a MO representation of reacting molecules requires optimization of energy and MD structure with respect to nuclear positions. Because RMD allows the reaction pathway to be developed by the dynamics, it can become very difficult to follow changes in MO structure along reaction pathways for many-atom systems [61, 62].

By contrast, bonds and interactions are directly specified in a VB representation. Electronic interactions are incorporated into the various modes that describe the bonded structure. The explicit representation of bonding structure and its changes, started from a molecular structure, makes VB forcefield descriptions natural and common choice for modeling intramolecular interactions.

The forcefield modes can be developed from a variety of means, including quantum chemistry calculations and experimental data. Model compounds are used that include the mode of interest, capping the adjacent bonds with hydrogen atoms where possible [63]. In other cases, experimental data may be used to determine parameters.

The process of forcefield development has been described more as an art than an science [64]. Benefitting from this art can be especially difficult when harmonic forcefields can typically have errors exceeding 5 kJ/mol [65], and transferability errors between larger and smaller molecule properties arise [66].

- Harmonic and Morse potentials are typically used to represent the bond stretches [63, 67]. Harmonic potentials are typically only valid for very small deviations, while Morse potentials reflect the dissociation behavior more accurately.

- Three-atom angular motions are typically fitted to harmonic potentials [68]. However, harmonic potentials can results in errors for significant deviations from the equilibrium bond angle and for nearly linear species and non-linear species approaching 180^o [69].

- Torsional potentials are typically determined by freezing the target torsional motion and allowing all other modes to relax [68]. The entire 360^o motion must be checked to obtain an accurate potential [63], and the potentials may not be symmetrical.

Forcefield methods can still easily lead to problems with transferability [70, 71], especially when considering a 5 kJ/mol error in a torsional barrier may be of the same magnitude as the barrier [72]. Cyclic systems can provide additional difficulties due to the interdependence of bond stretches and angles [67] and a need to estimate the ring strain properly [63].

One of the major difficulties in molecular simulation can be the representation of the non-bonded interactions. Accurate results are required at small separation distances. The non-bonded forces can make a significant difference in the reliability of a forcefield [64]. Lennard-Jones potentials can be too repulsive [69, 73–75], while the exp-6 potential can fail to have a repulsive wall under certain conditions [69, 74, 75]. In many cases, a Morse-style van der Waals potential is best suited to represent

he entire interaction range [64, 74, 76–78]. The parameters for van der Waals interactions also raise questions, especially parameter transferability [75, 76, 79, 80]. However, parameter estimation provides challenges including the effects of interaction parameters [81], unlikely reliability of using inert probes like Ne or Ar in conjunction with combination rules [77], and screened pair interactions [75]. Understanding and overcoming potential pitfalls of various non-bonded interactions is key to representing the interatomic potentials accurately between molecules, especially for energy transfer [82–85]. Additionally, a requirement for polar species is the inclusion of partial charges. Accurate representation of the partial charges can be difficult. Partial charges are determined frequently from quantum chemical calculations using techniques such as Mulliken population analysis [86]. However, these techniques can be error-prone as the charges are typically structure-dependent [68, 70]. Lone-pair representations can also provide an additional error [86].

There are two main types of forcefields. The first type is an all-element forcefield, which seeks to have a single description for each element within the periodic table. The Universal Forcefield (UFF) [69, 87–89] is an example. While these forcefields attempt to become the most general, the inability to represent complex structures, hybridization, and charges are common problems [65, 69, 90]. The second type of forcefield is atom-type based, where each element is described in a variety of different situations including hybridization and neighbors for example. Examples of atom-type forcefields include AMBER [91–93], GROMOS [94–96], Consistent Forcefield (CFF91 and CFF93) [97, 98], COSMIC [64, 99], Consistent Valence Forcefield (CVFF) [100], CHARMM [101, 102], MM2 [103], MM3 [104–106], MM4 [107], and COMPASS [108]. These forcefields can also fail for hybridization problems due to insufficient atom-type parameterization.

The different forcefields are typically parameterized for certain systems. The AMBER forcefield can have reasonably good agreement [65], especially for biologi-

cal systems like DNA [109, 110]. CFF and CVFF were also developed for biological applications yet had difficulty with conserving helical structure [110]. However, even the representation of simple hydrocarbon species with forcefields is not a simple task. AMBER was observed to overstabilize long alkane torsions [71]. MM2 does not represent crowded alkanes well [64]. CHARMM92 does not represent small alkanes properly [66, 81, 111]. Unsatisfactory van der Waals interaction resulted in COSMIC not representing saturated hydrocarbons well [64]. Ultimately, each forcefield tends to excel for certain conditions, yet struggle at other conditions. Therefore, it is necessary that the proper forcefield be used to represent the interactions properly.

1.3.3 Reactive Molecular Dynamics Simulations

RMD simulations take certain factors into consideration in order to obtain reliable chemical kinetics. First, the forcefield must be able to represent the reactive PES. Second, because reactions are rare events, the full simulation can be dominated by near-equilibrium processes like rovibrational motions. In the present work, a modified equilibrium forcefield is used.

Simulation of polymer decomposition is one potential application for RMD because of length and time scales that cannot be probed directly using experimental techniques. For polymer degradation, not only thermal effects but also the structural interactions of the entangled chains must be included in the decomposition model. Previous simulations of RMD have already been conducted on polyethylene [51–53, 112, 113], polypropylene [112, 114], polyisobutylene [112, 115], polystyrene [54], poly(methyl methacrylate) [3], and poly(dimethyl siloxane) [116]. These simulations were able to detect the structural affects of coiling on the polymer degradation mechanisms and Arrhenius parameters. These various physical interactions are keys to understanding the elementary events of polymer decomposition and thus to reliable elementary-reaction mechanisms.

While the previous program, MD_React, was able to simulate chemical kinetics, there were several issues that warranted the development of a new RMD code to alleviate these issues. For one, the energy was not conserved in MD_React, making NVE calculations impossible. Additionally, there were discrete changes in the energy upon bond breaking resulting from altering partial charges and sudden inclusions van der Waals interactions. Another issue was the inability to represent hybridization changes, which will greatly impact recombination kinetics for example. However, these were issues that mainly pertained to MD_React itself. There are more general issues with respect to forcefield and time issues that will be considered now.

Forcefields. Two types of forcefields based on bond orders have been used for reactive simulations. The first is the the Reactive Empirical Bond-Order (REBO) [57, 58] and its modified version AIREBO [59, 60]. These reactive forcefields are based on a modified Tersoff potential [117–120] and have been used in numerous applications [121–135]. The second forcefield is ReaxFF [55, 56], which uses a central-force approach to determine empirical bond orders. Parameterization has been carried out and used for a wide variety of systems [116, 136–145].

Each of these forcefields has significant drawbacks. REBO and AIREBO are insufficient for modeling gas-phase kinetics due to its lack of non-bonded forces. Additionally, it does not yet describe transition states. In general, it was assumed that the central-force representation would account for atoms not directly involved in a covalent bond such as angular and torsional motions. However, this approach was found inadequate and these motions had to be explicitly included [56–58]. ReaxFF has difficulty in describing potentials accurately, particularly bond energies [55, 56, 116, 137, 146], a result of the empirical bond-order approach opposed to specified atom types.

Reactive simulations have also been completed using modified, conventional forcefields in MD_React [3, 53, 54, 112, 115] and also the CRACK forcefield [147]. Such

methods take advantage of previously developed equilibrium forcefields to describe the chemical reactions. In these methods, the bonding is evaluated at each molecular dynamics step, and the lowest-energy bonding structure is selected. The bonding to a particular atom may not exceed its valence plus one, and the sum of bond orders to a particular atom must not exceed its valence. The bond angles and torsions are allowed to relaxed as the bonds stretch by gradually truncating these motions off using switching functions that depend on the bond order.

Another problem with valence-bond forcefields is the inability to capture any electronic quantum effects such as concerted reactions [148, 149]. These effects could only be observed for physical and not electronic reasons. An additional challenge to valence-bond forcefields is the representation of conjugated structures. These structures are key to the formation of porous char structures during polymer degradation; however, they can not be represented adequately using atom-typing alone and may require more refined descriptions such as bond-typing as well.

Time issues. RMD simulations presently require significant computational time because a large number of different simulations must be completed to amass the proper statistics for determining reliable chemical kinetics [115, 150, 151]. Furthermore, in the time scales of RMD, reactions are rare-event processes, exacerbating the time issue that also must be considered.

Computational strategies can make RMD a viable option for investigating chemical kinetics. Typical equilibrium molecular-dynamics simulations use spatial decomposition to accelerate the parallel calculations on many processors. However, the accumulation of statistics necessary for quantitative kinetics from RMD allows temporal decomposition [150, 151]. Because each of the simulations is independent in how the dynamics evolve, "embarrassingly parallel" calculations can be employed. The temporal decomposition has been demonstrated to yield the appropriate statistics [150, 151].

Acceleration can also be accomplished through methods that directly make reactive events more likely. These methods can work well especially when there are many reactive pathways with no prior knowledge of which pathway will react [150]. Techniques such as bond-boosting introduce additional energy into the high-frequency motion of the bonds to make the energy well effectively shallow, permitting quicker transitions between states [152–155]. The hyperdynamics maintains the relative kinetic rates because the same ratio of rates is preserved through Transition State Theory [152]. Raising the temperature to increase the rate of infrequent events has limitations [156], but such temperature-accelerated dynamics [157–160] can be used for accelerating infrequent processes while screening out the incorrect processes. Additionally, coarse time-stepping techniques such as coarse molecular dynamics [161–164] allows the simulation of short bursts of the system between coarse-grained integration of the system dynamics.

1.4 Outline of Dissertation

The overall objective of this dissertation is to develop RMD as a computational tool for simulating and understanding chemical kinetics at the atomistic level. This tool is used to understand polymer flammability and the effects of various fundamental polymer units.

Chapter 2 provides the details of the techniques involved in RMD and how each is implemented for the reactive forcefield development, determination of elementary rate equations, effects of polymer architecture, and overall polymer decomposition mechanisms. In order to develop and use RMD for understanding polymer flammability, existing methods for development and analysis must be understood in context. These methods include quantum chemical calculations, frequency calculations, RMD annealing and simulation processes, and Kinetic Monte Carlo. Description of a new

RMD algorithm and code, RxnMD, is also provided. With this information in hand, a complete understanding of polymer flammability modeling can be sought.

In Chapter 3, development of the new reactive forcefield, RMDff, is described. The reactive descriptions for hydrocarbon scission, abstraction, and addition/β-scission reactions are developed, where the energy models are developed from small molecules. Structures near the minimum energy pathway are used to test model validity for these structures. Model transferability is completed by comparison to similar molecules containing heteroatoms. Vibrational frequencies are also determined for the scission reactions to verify that RMDff smoothly transitions the frequencies along the reactive pathway.

The necessary statistical analyses to obtain reliable kinetics are discussed in Chapter 4. The goal of using RxnMD and RMDff is to obtain quantitative kinetics. It is thus necessary to acquire statistically sufficient samples, quantifying effects of backbone decomposition, structure, conformation, side-groups, and chain interactions. The kinetic rate constants obtained from scission reactions in polyethylene are compared to determine the effects of number of simulations conducted, polymer conformation, chain length, annealing, and chain interactions.

Chapter 5 describes the study of the overall decomposition mechanism of polyethylene and the effects of side groups on hydrocarbon polymer decomposition, including PTFE. This analysis provides the basis for understanding polymer pyrolysis from a set of fundamental, elementary reactions. The polyethylene reaction kinetics are then assembled, and predictions using Kinetic Monte Carlo are compared to the observed macroscopic decomposition. The combination of length and time scales through the different techniques elucidates various molecular details of the pyrolysis mechanism that can not be observed through experimental methods.

An extension of RMD to BHDB, a novel, flame-resistant polymer, is made in Chapter 6. The extension of the reactive forcefield demonstrates that the RMD

method can capture effects of backbone stress on polymer decomposition. The effect of different backbone bond types is observed in the decomposition. This chapter demonstrates the RMD methodology with respect to understanding the complete decomposition through various polymer effects and simulation techniques.

Finally, Chapter 7 provides a summary of the main conclusions from the development and use of RMD for polymer flammability. Some suggestions for future investigations are also given.

CHAPTER 2

REACTIVE SIMULATION METHODS

2.1 Introduction

The objective of this chapter is to detail the methods used and developed in this dissertation, particularly the Reactive Molecular Dynamics (RMD) and Kinetic Monte Carlo (KMC) methods. Quantum chemistry was used to develop and validate the forcefield as well as to parameterize the models. Validation of frequencies along the forcefield development was checked using the vibrational analysis method described.

2.2 Quantum Chemical Calculations

In principle, one could solve the complete, time-dependent Schrödinger equation in order to determine reaction kinetics. While this approach is not possible practically, increasingly accurate thermochemistry has been obtained from the time-independent form of the Schrödinger equation in conjunction with Transition-State Theory. However, high-level quantum chemical calculations are presently computationally prohibitive for all but small molecules, generally containing no more than about 20 atoms.

The time-independent form of the Schrödinger equation is:

$$\mathcal{H}\Psi = E\Psi \tag{2.1}$$

where $\mathcal{H}$ is the Hamiltonian operator, Ψ is the wavefunction, and E is the energy. If Ψ can be determined, then all the properties of the system are specified. However, analytical solutions to Eq. 2.1 are only possible for the one-electron system.

A numerical solution technique must be applied in order to determine the wavefunction for an atom or molecule of an arbitrary number of electrons. The Born-Oppenheimer approximation is usually invoked initially. It states that because the nuclear motion of the atoms is so much slower, nuclear positions can be considered effectively frozen compared to the electronic motion. This choice results in only having to solve the Schrödinger equation for the electronic structure to obtain the energy of a given set of nuclei positions. In order to solve Eq. 2.1, one specifies a type and level of theory (Hartree-Fock [165, 166], Møller-Plesset [167], etc.) used to approximate the electronic Hamiltonian. An electronic basis set must be supplied (STO-3G [168, 169], 6-31G [170], etc), which includes a set of partially parameterized functional representations that make up an approximation of the possible electron orbitals of the molecule. Using the Hamiltonian and the basis set, Eq. 2.1 is solved iteratively to self-consistency to determine the minimum energy. These types of calculations are generally referred to as *ab initio* calculations.

A second solution approach to the Schrödinger Equation is called density functional theory (DFT) [171, 172]. It is based upon the fact that if the spatial electronic charge distribution is specified along with the nuclear positions, the system is completely specified. The objective is to then solve for the charge distribution, Ψ^2. In this approach, the Hamiltonian must be approximated to account for electron correlation. Similarly to the *ab initio* calculations, DFT specifies the Hamiltonian through methods such as B3LYP, and again a basis set is selected. Then Eq. 2.1 is solved to self-consistency for the charge distribution. One of the major allures of DFT over *ab initio* calculations is the need to solve Eq. 2.1 only for each of the three coordinates as coupled differential equations, whereas *ab initio* calculations require the solution to $3N$ coupled differential equations.

Quantum chemical calculations were completed using the Gaussian 98 [173] and 03 [174] programs (Gaussian, Inc., Wallingford, CT). Gaussian is a commercially

available program that calculates a variety of different types of quantum chemical properties using a wide-variety of basis sets and levels of theory. The program numerically solves Eq. 2.1 at 0 K.

In principle, single-point energies can be calculated from any level of theory with any size of basis set. While the simplest Hartree-Fock theory can typically account for more than 99% of the total atomization energy, larger basis sets with more accurate theory are required for sufficiently accurate thermochemistry. The remaining error in the energy can contribute significantly to quantitative errors, in kinetics for example. Compound theories have also been developed to extrapolate to an infinite basis set and to exact theory, such as the complete basis-set methods (e.g. CBS-Q and CBS-QB3) [175–180] and the Gaussian theories (e.g., G-2 and G-3) [181, 182]. The compound methods are found to be accurate within 8 kJ/mol for heats of formation [183–186] compared to results obtained from DFT methods having at least 12 kJ/mol errors [187]. However, high-level coupled-cluster calculations were demonstrated to have less than 1 kJ/mol mean absolute error in total atomization energies [188].

Molecular structures (nuclei positions) are then optimized in order to identify the minimum-energy point on the potential energy surface. The minimum-energy point corresponds to minimum in all directions of the surface; i.e., for all degrees of freedom. By comparison, transition states can be identified by optimizing for the saddle point, where all energy variations are minima except one which is a maximum. Gaussian uses a modified method called the Berny algorithm [189] as its default for optimization calculations. The use of a frequency calculation helps to confirm the appropriate transition state is found by observing the appropriate imaginary eigenvalue. Frequency calculations must be performed at a minimum-energy structure, at a transition state, or along a reaction coordinate. Therefore, these calculations are only valid when completed at the same level of theory and basis set as the optimization.

Once a transition state has been located, it can be assigned to reactant and product structures using reaction-path-following methods. The Intrinsic Reaction Coordinate method (IRC) [190, 191] follows the minimum-energy path from the transition state toward the reactant and product minima by optimizing the geometry along the path.

2.3 Vibrational Analysis

2.3.1 Vibrational Analysis on Equilibrium Molecules

The classical analysis of molecular vibrations considers the dynamics involved in molecular motions. The vibrations are analyzed around the equilibrium geometry under the conditions that the rotational motion is completely separable from the vibrational motion.

Cartesian coordinates provide a method to describe the molecular geometry. However, it is convenient to transform the coordinates x_1, y_1, z_1, x_2, ..., z_N to a new set of coordinates q_1, q_2, ..., q_{3N}, where $q_1 = \sqrt{m_1}\Delta x_1$, etc.

The kinetic energy, K, can then be defined in terms of q_i as given in Eq. 2.2.

$$2K = \sum_{i=1}^{3N} \dot{q}_i^2 \tag{2.2}$$

Similarly, the potential energy, V, can be defined in terms of the q_i displacements expanded in a Taylor series as given in Eq. 2.3.

$$2V = 2V_0 + 2\sum_{i=1}^{3N}\left(\frac{\partial V}{\partial q_i}\right)_0 q_i + \sum_{i=1}^{3N}\sum_{j=1}^{3N}\left(\frac{\partial^2 V}{\partial q_i \partial q_j}\right)_0 q_i q_j + \ldots \tag{2.3}$$

$$= 2V_0 + 2\sum_{i=1}^{3N} f_i q_i + \sum_{i=1}^{3N}\sum_{j=1}^{3N} f_{ij} q_i q_j + \ldots \tag{2.4}$$

However, the requirement that the geometry be a minimum requires that

$$\left(\frac{\partial V}{\partial q_i}\right)_0 = f_i = 0,\ i = 1, 2, \ldots, 3N$$

which means the first derivatives are zero in Eq. 2.3. Additionally, V_0 can be eliminated by setting the minimum structure to zero energy. For small-vibration amplitudes, the cubic and higher-order terms can be neglected so that the potential energy reduces to Eq. 2.5.

$$2V = \sum_{i=1}^{3N} \sum_{j=1}^{3N} f_{ij} q_i q_j \tag{2.5}$$

Newton's equations of motion may be expressed as:

$$\frac{d}{dt}\frac{\partial K}{\partial \dot{q}_j} + \frac{\partial V}{\partial q_j} = 0,\ j = 1, 2, \ldots, 3N \tag{2.6}$$

Because the kinetic energy is a function of the velocities only, while the potential energy is a function of the positions only, Eq. 2.5 can be substituted for the potential energy and Eq. 2.2 substituted for the kinetic energy, yielding:

$$\ddot{q}_j + \sum_{i=1}^{3N} f_{ij} q_i = 0,\ j = 1, 2, \ldots, 3N \tag{2.7}$$

This set of $3N$ simultaneous second-order linear differential equations has a known possible solution of:

$$q_i = A_i \cos(\sqrt{\lambda} t + \epsilon) \tag{2.8}$$

where A_i, λ, and ϵ are constants. By substituting this result into Eq. 2.7, a set of algebraic equations results:

$$\sum_{i=1}^{3N}(f_{ij} - \delta_{ij}\lambda)A_i = 0,\ j = 1, 2, \ldots, 3N \tag{2.9}$$

where δ_{ij} is the Kronecker delta. Eq. 2.9 is a series of equations with amplitudes A_i, which only has a non-zero solution for special values of the eigenvalues, λ. These values of λ are the values that satisfy the relation:

$$\begin{vmatrix} f_{11} - \lambda & f_{12} & f_{13} & \ldots & f_{1,3N} \\ f_{21} & f_{22} - \lambda & f_{23} & \ldots & f_{2,3N} \\ \vdots & \vdots & \vdots & \ddots & \vdots \\ f_{3N,1} & f_{3N,2} & f_{3N,3} & \ldots & f_{3N,3N} - \lambda \end{vmatrix} = 0 \tag{2.10}$$

Eq. 2.10 is an eigenvalue problem; i.e., particular λ values may be selected at which the determinant becomes zero and each of the amplitudes becomes proportionally fixed. Therefore, each of the $3N$ λ values obtained from the solution of Eq. 2.10 results in a unique set of motions associated with that value of λ.

The λ values in units of s^{-2}, can be converted into frequencies in units of cm^{-1} by

$$\nu_i = 0.01 \left(\frac{\lambda_i}{4\pi^2 c^2} \right)^{\frac{1}{2}} \tag{2.11}$$

where the factor of 0.01 is used to convert m^{-1} to cm^{-1}. The eigenvectors correspond to the amplitudes of each motion within the molecule for each value of λ. The center-of-mass translational and rotational motions have not been separated out of the determinant, so the zero-frequency motions corresponding to these motions must also be returned as eigenvalues.

2.3.2 Calculating Hessian components using forcefield descriptions

Calculation of the force constants requires a Hessian matrix of second derivatives of the potential energy function ($V(\mathbf{r_1}, \mathbf{r_2}, \ldots, \mathbf{r_N})$) as a function of the coordinates of all N particles in the molecule, where the individual element is:

$$H_{ij} = \frac{\partial^2 V}{\partial x_i \partial x_j} \tag{2.12}$$

Each of the Hessian components is then calculated from the derivative of the gradient of $V(\mathbf{r})$ with respect to each of coordinates of $V(\mathbf{r})$.

$$H_{ij} = \frac{\partial}{\partial x_j}\left(\frac{\partial V}{\partial x_i}\right) = \frac{\partial}{\partial x_j}\left(\frac{\partial V}{\partial r(\mathbf{x})}\frac{\partial r(\mathbf{x})}{\partial x_j}\right) \tag{2.13}$$

Applying the chain rule differentiation to Eq. 2.13 results in two separate terms to be calculated for the force constant.

$$H_{ij} = \left(\frac{\partial r(\mathbf{x})}{\partial x_i}\right)\left[\frac{\partial}{\partial x_j}\left(\frac{\partial V}{\partial r(\mathbf{x})}\right)\right] + \left(\frac{\partial V}{\partial r(\mathbf{x})}\right)\left[\frac{\partial}{\partial x_j}\left(\frac{\partial r(\mathbf{x})}{\partial x_i}\right)\right] \tag{2.14}$$

Finally, Eq. 2.14 can be simplified and applied as shown below and stored in the Hessian matrix, where $r(\mathbf{x})$ is a function that relates separation distances, angles, or torsional angles to the respective $\mathbf{x}$ coordinates of the atoms associated with that motion.

$$H_{ij} = \frac{\partial r(\mathbf{x})}{\partial x_i}\frac{\partial^2 V}{\partial r(\mathbf{x})^2}\frac{\partial r(\mathbf{x})}{\partial x_j} + \frac{\partial V}{\partial r(\mathbf{x})}\frac{\partial^2 r(\mathbf{x})}{\partial x_j \partial x_i} \tag{2.15}$$

2.3.3 Projecting out frequencies

The projected frequencies were calculated using the method of Baboul and Schlegel [192]. Along a reaction pathway, the tangent is calculated at a point via

$$\nu_0 = \frac{d\mathbf{x}(s)}{ds} = -\frac{\mathbf{g}}{|\mathbf{g}|} \tag{2.16}$$

where $\mathbf{x}(s)$ is the reaction pathway in mass-weighted coordinates, and $\mathbf{g}$ is the gradient at that point. Projecting these forces results in the projected Hessian given in Eq. 2.17.

$$\mathbf{H}_{projected} = (\mathbf{I} - \nu_0\nu_0^T)\mathbf{H}(\mathbf{I} - \nu_0\nu_0^T) \tag{2.17}$$

Once the projected Hessian has been set up, the frequency analysis on the projected Hessian proceeds as described above for equilibrium structures.

For each molecule, the Hessian for each forcefield mode is calculated and combined into the entire molecular Hessian. Once all the modes have been evaluated, the eigenvalues and eigenvectors are calculated by solving Eq. 2.10.

2.4 RxnMD: A Program for Reactive Molecular Dynamics

2.4.1 RMD Methodology

The RMD method computes the atomic trajectory via numerical integration of the classical equations of motion. Although reactive events are relatively rare on the time scale of MD integration, RMD allows the trajectory to access the reactive portions of the phase space where chemical reactions arise. This access is accomplished using a valence-bond forcefield that accurately describes both equilibrium and reactive molecular conformations. This forcefield is comprised of the standard mechanical descriptions of molecular interactions, including modifications to account for chemical reactivity.

$$V = \sum_{N_{bonds}} V_{bond} + \sum_{N_{angles}} V_{angle} + \sum_{N_{torsions}} V_{torsion} + \sum_{ij} V_{nonbond} \tag{2.18}$$

RMDff [193, 194], the reactive forcefield developed here, gives a full description of the reactive phase space for scission, addition/β-scission, and abstraction reactions. (Complete description and development is deferred to Chapter 3.) RMDff uses a standard, equilibrium forcefield to describe the near-equilibrium conformations. In this work, the MM3 forcefield is chosen as the basis [104–106]. MM3 has been demonstrated to be reasonably accurate at describing near-equilibrium conformations, with

Table 2.1. Parameters for HH, CH, and CC Morse-type van der Waals potential.

Parameter	HH	CC	CH
D (J/mol)	230.1	623.4	380.8
b	5.193	4.754	4.970
r_e (nm)	0.3076	0.3724	0.3406
r_s (nm)	0.175	0.205	0.190

an average error of 1.5 kJ/mol for hydrocarbons and 2.6 kJ/mol total error [65]. RMDff then further applies switching functions to the modes which transform during a reaction. These switching functions permit smooth transitions between reactant and product descriptions, making the simulations accurate for constant-energy simulations, as well as for thermostat and barostat conditions.

During the course of simulations, it was found that the MM3 van der Waals potential had an unsuitable form at close ranges. The MM3 van der Waals potential is an exp-6 form, which has a barrier at short interatomic distances and then turns over and approaches negative infinity, as seen in Fig. 2.1. It was found that two atoms could be continuously pushed together until they passed over the maximum, where the simulation became unstable. This problem was corrected by grafting a Morse-type van der Waals potential onto the MM3 van der Waals potential near the barrier. The Morse-type van der Waals potential has an inner repulsive barrier, which prevents the atoms from approaching too closely. Its functional form is:

$$E_{\text{Morse-type vdW}} = D\left[e^{b\left(1-\frac{r}{r_e}\right)^2} - 2e^{b\left(1-\frac{r}{r_e}\right)}\right] \tag{2.19}$$

where D is the well depth, b is the dimensionless steepness parameter, and r_e is the equilibrium separation distance, and it is used at a distance less than r_s. Parameters D, b, and r_e are determined by matching the energy and first and second derivatives at the specified point r_s. These parameters are shown in Table 2.1. The standard MM3 values were used for $r > r_s$.

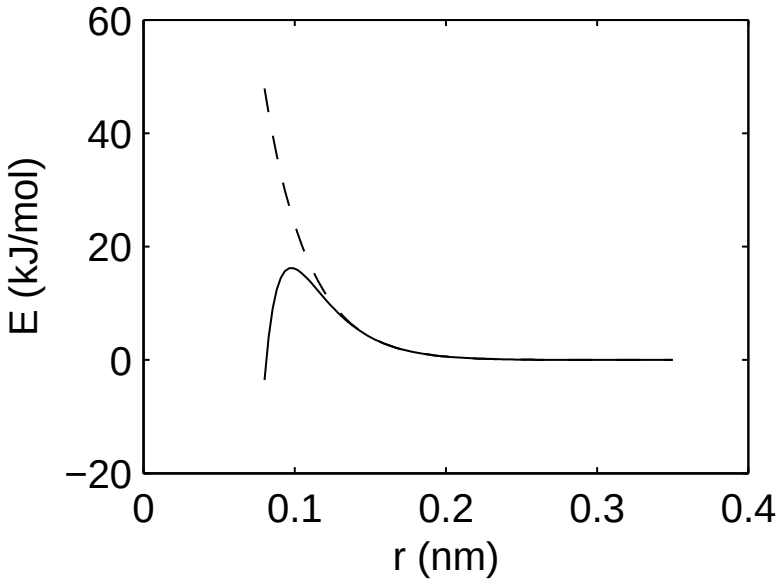

Figure 2.1. Comparison of MM3 van der Waals potential (solid line) and hybrid Morse-MM3 van der Waals potential (dashed line) for H-H interaction.

The switching functions are dependent on the reaction coordinate (RC), which describes the progress along a reactive pathway, as described in the prior section. A suitable switching function is:

$$S(RC) = 0.5\left[1 - \tanh\left(a(RC - RC_0)\right)\right] \tag{2.20}$$

where a is the steepness parameter and RC_0 is a parameter such that $S(RC_0) = 0.5$. The reaction description identifies atom-type modes that change during the course of a reaction. Once the conformation has distorted enough, the RC becomes active (defined as between 0 and 1). Once the RC is active, the switching functions are applied to the forcefield terms to describe the changes that occur during the reaction. Because the reactions describe the entire path, the descriptions are reversible. Therefore, a reaction can start at RC=0 and proceed to completion at RC=1 or the reverse. A reaction may also begin along the path but complete it, instead returning to its initial state.

For each bond pair in which at least one of the two atoms has a change in atom type, the bonded forcefield description is switched or turned off completely if the bond breaks. The bending and torsional modes are treated in a similar scheme. However, it is possible to specify which type of bending and torsion modes are switched during the course of a reaction. Let "1" represent an atom that is actively participating in a reaction and "x" any atom not participating. It is possible to specify separately whether the x1x and xx1 bending modes are to be transitioned or not during a reaction. This approach provides flexibility in the choice of terms to be included and the description of changes of modes as necessary. Likewise, the torsional x1xx and 1xxx modes can be specified. Any angular or torsional mode that includes two or more reactive atoms is automatically included. It is important that exclusion of these bending or torsional modes within a reaction description must not affect the mechanical description and flexibility of the molecule.

The non-bonded forcefield description is altered to the new atom types when atoms change their bonded interactions. For the van der Waals interactions, the parameters for the radical atom were the same as those for the standard atom description.

An additional energy function may also be included to correct the energetics of the reaction pathway. Currently, only a polynomial functional form is available. This function is dependent on the RC and is switched on/off during the reaction using the switching functions. The functional form is used to correct items such as energy barriers which may not be correctly represented by just the modes available.

2.4.2 The RxnMD Method

The RMD method is implemented using a C++ code developed in this research and named RxnMD. The program computes and implements the reactive forcefield as well as integration of the equations of motion. The trajectories are visualized via Hyperchem dynamics files. The program creates a script file which plays the

trajectories for each system bonding, allowing for the updated bonding to be observed. The program can also create a variety of other trajectory files and static structure files.

The basic program modules and interactions are shown in Fig. 2.2. The first action taken by the program is for the instruction reader module to interpret the commands found in the job specification text file. The commands are sent to the appropriate modules including the structure reader for setting up the initial atomic coordinates and bonding, setting the initial velocities, integrator specification, and output reporting commands. These units together define the current point on the trajectory, which uses the forcefield, integrator, and connectivity information at each step to advance the current trajectory point to the next time step. This information is also output for storage during the course of the simulation. Together, these modules create the entire program execution routine.

Within the execution of the forcefield and atomic connectivity is a routine to implement particular reactions at each time step. The application of the reactive forcefield is shown in the flow diagram in Fig. 2.3. Once the appropriate equilibration has been completed, the reactive algorithm is employed for each integration step. The molecular dynamics step begins by identifying all potentially active reactions. If any active reactions have completed, the bonding structure is updated to reflect the new atomic connectivity and the set of potentially active reactions is developed based on this new atomic structure. Once there are no reactions left to be completed, the next objective is to determine if any of the reactive modes between different reactions overlap. This routine is required because there is no direct method for having two potential competing reactions active in the same time step. (The reaction selection routine will be described in detail below.) Once the reaction selection routine has identified the set of non-competing reactions, the integration is completed for this molecular dynamics step.

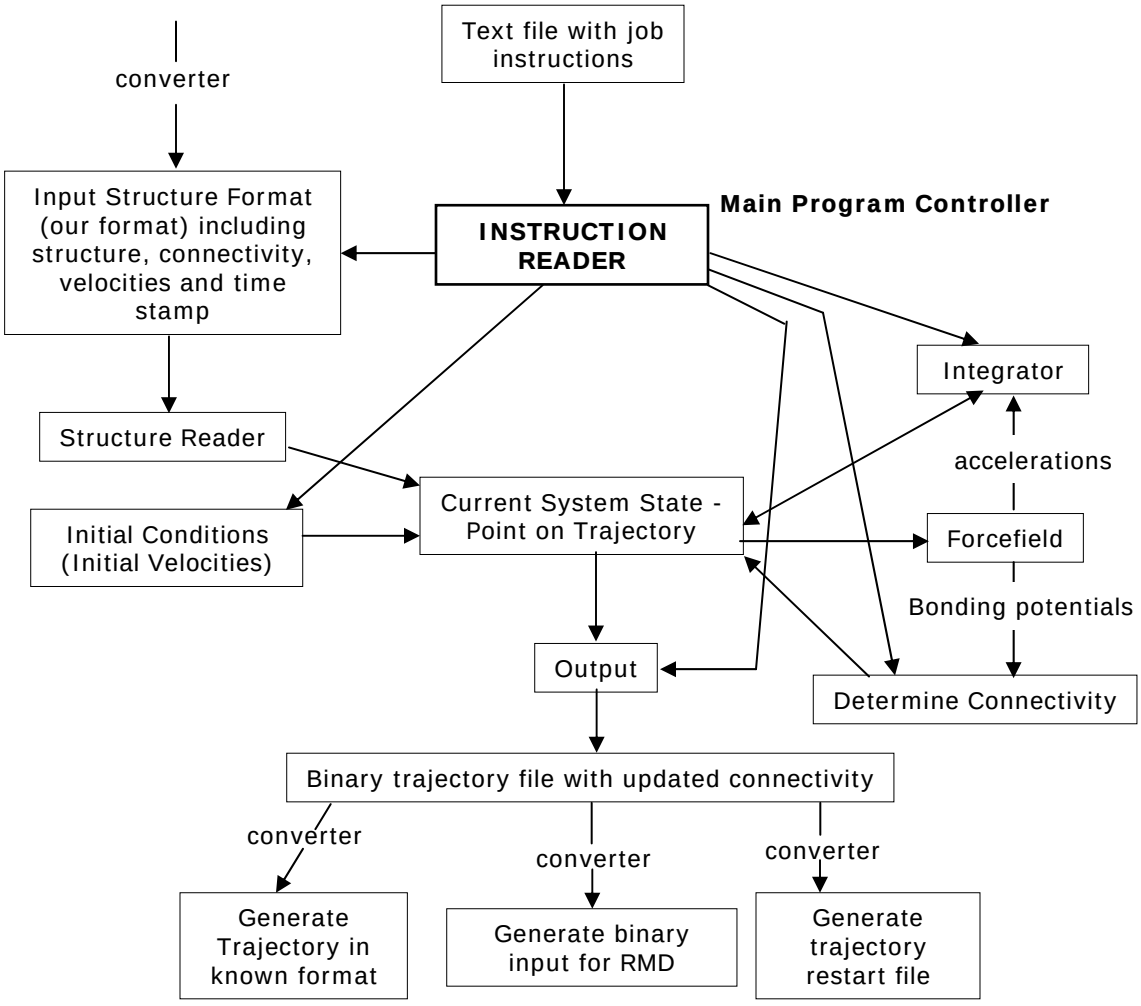

Figure 2.2. Diagram of the modules used in RxnMD and the interactions.

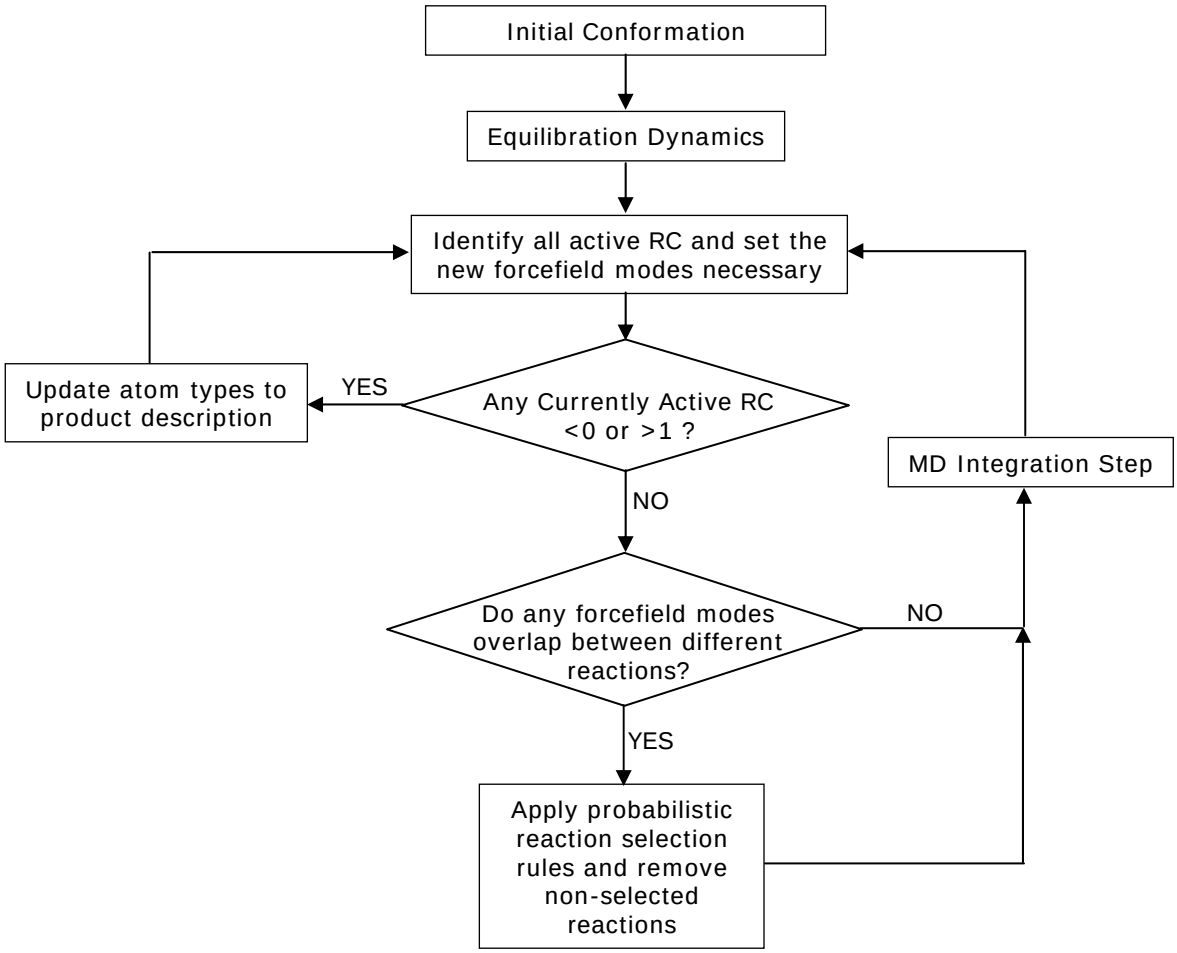

Figure 2.3. Flow diagram of the reactive methodology applied in RxnMD.

Reaction descriptions are written using the assumption of localized effects. The assumption is that a reaction in a molecule is essentially a localized phenomena, described mainly by the atoms directly involved in the reaction. The reaction also contains descriptions of changes in modes that immediately surround that reactive mode. The bonded atoms far away, down the chain, have no direct interaction with the reaction description. This assumption allows the changes that describe a C-C bond scission in ethane, for example, to also be applied to propane, butane, decane, and even polymers. The approximation is valid to the extent that the reactions are truly localized in their effects.

This treatment also allows for transferability beyond extending the C-C scission in ethane to other hydrocarbons. For example, this same approach could easily be extended to non-hydrocarbon molecules when the heteroatoms are removed from the bond undergoing the reaction. However, care and examination should be considered prior to assuming transferability because either the descriptions may really not be sufficient or the equilibrium forcefield may not accurately describe the necessary components.

The reactions involve not only the atoms directly changing their atom types, but also any bonded, non-bonded, angular, or torsion mode that includes any of the atoms that will change atom type during the reaction. Consider the simplified molecule shown in Fig. 2.4. If the 3-4 bond labeled R3 is undergoing a scission reaction, atoms 3 and 4 would be directly participating with their atom types changing upon completion. In this case, the 2-3 and 4-5 bond would also change due to the changes in the 3 and 4 atoms during the reaction. Additionally, the 1-2-3, 2-3-4, 3-4-5, and 4-5-6 angular modes would change as well as the 1-2-3-4, 2-3-4-5, and 3-4-5-6 torsion modes and 2-4 and 3- 5 non-bonded interactions. Under these circumstances, no other reaction could be active when R3 is active because the reactive modes from any other

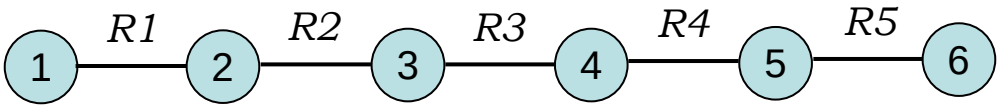

Figure 2.4. Example of overlapping reactions for reaction selection process.

reaction would overlap with R3. In fact, due to the small number of atoms involved in this molecule, only one reaction could be active at a time.

The reaction selection method is implemented to help resolve the cases where there are competing reactions. For the molecule shown in Fig. 2.4 each bond could be potentially undergoing a scission reaction; however, the problem is to select which reaction to implement. This selection is performed for each integration time step, allowing each potential reaction to be active. Once the reaction to implement for this time step is selected, the remaining potential competing reactions are discarded as treated using their equilibrium descriptions.

Now consider another situation, still using the molecule shown in Fig. 2.4. Angular and torsion modes that include the breaking bond(s) are normally included, but for this example, only consider the directly bound neighbors as overlapping modes (bonds only). Under these circumstances, there is the possibility of multiple reactions being active within the same molecule. The possibility of multiple non-competing reactions within the same molecule is possible because their reactive modes do not overlap. There are four different reaction chains that can be constructed: (i) R1, R3, and R5, (ii) R1 and R4, (iii) R2 and R4, and (iv) R2 and R5. The combination of only R3 and R5 is not a reaction chain because if these two reactions occur, then R1 should also occur as there is no overlap between these three reactions. These four reaction chains represent all the complete combinations that can be constructed from this simplified picture, with one of the reaction chains being implemented this integration time step.

In each case, the reaction chain is a unique combination of non-overlapping reactions. Now a criterion must be used to determine which particular reaction chain to implement during each integration time step. The method implemented assumes that the lowest energy reaction chain for each integration step will always be implemented. For each reaction, an assumption is made that if the reactive pathways were not available the atoms would remain on a harmonic potential energy surface. This assumption is employed even when dissociative bond models such as a Morse potential are used. Therefore, as bonds stretch significantly beyond the equilibrium bond distance, a very large amount of energy would be required to describe the mode as equilibrium as opposed to reactive. Therefore, once a reaction becomes sufficiently active, it becomes the lowest energy pathway because a large amount of energy would be required to make another reaction active. This particular reaction will stay active until it either completes or returns to or near the non-reactive state. Near the non-reactive state (roughly RC *leq* 0.05), there is not sufficient amounts of harmonic potential included to make one reaction dominate over another. For reaction chains, if R2 is significantly stretched in Fig. 2.4, this reaction would always be active; however, either R4 or R5 could be also active. In fact, its possible to switch between R4 and R5 depending on which pathway provides the lowest energy at each time step.

The energy of each reaction chain is determined from the summation of energy differences of each reaction within the reaction chain. For each reaction, the energy difference is calculated from two contributions. The first contribution is the amount of energy reduction that results from the breaking or removing of the particular atom-type description of that mode. This reduction is calculated as the amount of energy reduction from the harmonic potential of each mode to the reactive mode energy. For bonds that use a dissociative model, a harmonic potential is used to determine the energy reduction only. The second contribution is the amount of energy required to form the new atom-type description of that mode. Because that particular mode

description was not previously present, it is assumed that the amount of energy must be added from zero and is the reactive energy of that mode. The addition of these two numbers is the energy required for that potential reaction to be in the equilibrium state as opposed to the reactive state. Therefore, the reaction chain with the highest energy is implemented, as this is the set of reactions that would require the most energy not to be described in the reactive state, making it the lowest-energy structure.

This process is repeated for each integration step, allowing for a sampling of the different states available. Therefore, as the time step becomes very small, the actual distribution of possible states is approached. This process removes any bias that may occur from inappropriately selecting a reaction too early. As the dynamics dictate the evolution, a reaction that is initially less likely may become more likely. The change in reaction likelihood may lead to a different reaction being implemented. Therefore, this process allows for the evolution of possible interactions to be observed. Because the selection is based on the Boltzmann weighting, it also approximates the real probability of an unlikely reaction still being selected to occur. The implicit assumption is that the electronic rearrangement of the system is extremely fast, so that at any one time step, any reaction chain can occur. Also, any reaction that does not overlap with any other reaction is automatically implemented.

2.4.3 Annealing Procedure

The hydrogen-terminated polymer structures are generated using Materials Studio from Accelrys. Each structure is identified using its abbreviation followed by the number of repeat units (e.g. PE50 is a 50-repeat unit polyethylene chain). The condensed phase was simulated using periodic boundary conditions (PBC).

The structures were annealed using Discover in Materials Studio. The annealing was completed using the non-reactive CVFF [100] forcefield. Each structure was

initially annealed using increasing pressure to accelerate the convergence towards the condensed phase density. Then 100-ps dynamics simulations were completed at atmospheric pressure, sampling 100 trajectories from each simulation. The six lowest energy points were then minimized allowing both the atoms and PBC box vectors to relax. The lowest energy structure obtained was used as input into the next dynamics simulation. This procedure was repeated until five consecutive repetitions of dynamics and minimization did not result in a lower energy structure. The annealing was completed at 1000 K and 101 kPa.

2.4.4 Simulation Procedure

The RMD simulations were performed at high temperatures in order to observe kinetics within computationally feasible times. The lowest temperature values were dictated by the need to see reactions within a reasonable computational window, typically within 60 hours (using an Operton 240 64-bit processor).

The reactive simulations began with a non-reactive velocity annealing phase.Velocities were sampled from a Maxwell-Boltzmann distribution at the desired temperature. An equilibrium simulation (i.e., without the reactive forcefield) used Verlet-velocity algorithm [195] for 10000 steps with 0.5-fs time steps. An NVT-ensemble was employed using velocity scaling to maintain the temperature.

The reactive simulations were then completed using the Verlet-velocity algorithm [195] with 0.5-fs time steps and an NVT ensemble. The temperature was controlled using velocity scaling. The velocities from the end of the equilibration routine were used as the initial velocities for the reactive dynamics. The simulations used the RMDff reactive forcefield method [193, 194] using MM3 [104] as the basis forcefield. Generally, 40 simulations were conducted per temperature, requiring at least five temperatures to obtain reliable Arrhenius plots.

2.4.5 First-order Kinetic Process Analysis Method

Because the rate of initial bond scission is proportional to the number of bonds in the chain, the probability of a reaction in the time interval between t and $t + dt$ is given by:

$$p_s(t)dt = k_s \exp(-k_s t)\, dt \tag{2.21}$$

where k_s is the rate constant for initial bond scission at a specified temperature. The average time for initial scission is given by:

$$\langle t \rangle = \frac{1}{k_s} \tag{2.22}$$

Therefore, the rate constant at a specified temperature can be calculated by averaging reaction times obtained from independent simulations. In this study, rate constants for initial scission reactions were calculated from the following formula [115], which is amenable to parallel computation [150]:

$$k_s = \frac{n_s}{N_{bb} \sum^{N_{trj}} t_s} \tag{2.23}$$

In this equation, t_s is the time of the first backbone scission observed in a given RMD simulation, n_s is the number of simulations where at least one backbone scission was observed, and N_{trj} is the total number of simulations (trajectories). In order to compare the kinetics of the first scission of PE chains having different lengths (i.e., number of repeat units), the rate constants were normalized by the initial number of backbone bonds, N_{bb}, in the models. After evaluating the rate constants over a range of temperatures, the activation energy and pre-exponential factor were obtained from the slope and intercept of a plot of $\ln k_s(T)$ versus $1/T$, commonly referred to as an Arrhenius plot.

2.5 Kinetic Monte Carlo

Classically, systems of N spatially uniform species that can undergo M independent reactions can be modeled though a series of coupled-differential equations. Assuming that the species concentration as a function of time $X_i(t)$ is a continuous, single-valued function and that each of the M reactions can be represented by a continuous process, then a series of differential equations similar to Eq. 2.24 can be constructed.

$$\frac{\partial X_i}{\partial t} = f_i\left(X_1, \ldots, X_N\right) \tag{2.24}$$

However, the solution to Eq. 2.24 is not always trivial, frequently requiring numerical integration. Gillespie [35, 36] developed a discrete, stochastic method for simulating reaction networks, which is called Kinetic Monte Carlo (KMC).

The KMC method begins by taking a system in a particular state. The method determines the answer to two important questions: (i) when does the next event occur and (ii) what reaction will it be. These questions lead to a reaction probability density function that provides the possibility of transferring from the current state to each of the next possible states. This probability density $P(\tau, \mu)$ is the probability that at time t the next reactive event will be an R_μ event, occurring in an infinitesimally small interval $d\tau$. Therefore, a_μ is defined as the probability of an R_μ event occurring based on the current state.

The probability $P(\tau, \mu)$ can now be calculated as the product of two distinct possibilities: first, the probability that no reactive event occurs at time t, given by $P_0(\tau)$; second, the probability that an R_μ event will occur given by the probability a_μ, yielding Eq. 2.25.

$$P(\tau, \mu)\, d\tau = P_0(\tau) \dot{a}_\mu\, d\tau \tag{2.25}$$

Using $[1-\sum_{\nu} a_{\nu}\, d\tau]$ as the probability that no reactive event occurs, an expression for $P_0(\tau)$ is derived, where a_{ν} accounts for the total number of R_{μ} events possible from the current state. This yields a probability distribution of:

$$P(\tau,\mu) = \begin{cases} a_{\mu} \exp\left(-a_0 \tau\right) & \text{if } 0 \leq \tau < \infty \text{ for } \mu = 1, \ldots, M \\ 0 & \text{otherwise} \end{cases} \tag{2.26}$$

A stochastic method is employed using a uniform random-number generator. The first random deviate, r_1, is taken to account for the time between random events using Eq. 2.27.

$$\tau = \frac{1}{a_0} \ln\left(\frac{1}{r_1}\right) \tag{2.27}$$

The second random deviate, r_2, accounts for which reactive event is selected using Eq. 2.28.

$$\sum_{\nu=1}^{\mu-1} a_{\nu} < r_2 a_0 \leq \sum_{\nu=1}^{\mu} a_{\nu} \tag{2.28}$$

KMC is a method that coarse-grains systems when large numbers of possible reactions occurr that exist in uniform distribution. The method also allows for infrequent events to be observed. Because of the nature of the time evolution of the kinetic events, significant computational time is not spent in integration time periods where no events occur. Therefore, KMC provides the ability to link atomistic events to macroscopically observed events. The main deficiency of KMC is the possibility of erroronously leaving out feasible pathways from the list of allowable events. Such events seriously compromise the results obtained from a KMC simulation.

CHAPTER 3

RMDff: A SMOOTHLY TRANSITIONING FORCEFIELD FOR SIMULATING CHEMICAL REACTIONS

3.1 Introduction

A valence-bond reactive forcefield was developed for our previous RMD code, MD_React using a modified version of the Consistent Valence Forcefield (CVFF) [3]. Reactions occur between explicitly bonded and non-bonded atoms. The present method uses localized descriptions of reactive events to describe the chemical transitions that occur during a reaction. This approach is derived partially from previous efforts to model transition-state structures from forcefield methods [61, 62, 73, 196]. In those studies, several groups have devised methods to determine the minimum energy path between a reactant and product using forcefield representations of the potential energy. Also of note is the work of Truong and coworkers [197, 198], who have developed the Reaction Class transition-state theory. This analysis relates the kinetics of reactions for larger molecules to gas-phase reactions of simple molecules. A combination of these two ideas suggests that accurate chemical representations of forcefield-based reactions can be developed and implemented for use in RMD from simple localized valence-bond representations.

The objective of this chapter is to develop RMDff, a chemically accurate, forcefield-based model for representing reactions within a dynamic simulation. RMDff employs a standard equilibrium forcefield representation of the atomic interactions in the vicinity of the equilibrium products, where these forcefields are known to provide adequate chemical accuracy. Switching functions are employed to facilitate smooth transitions

between the reactant, transition state, and product structures within the context of a complete and generic reactive potential energy surface (PES).

3.2 Computational Details

3.2.1 Quantum Chemical Calculations

The *ab initio* calculations for parameterization and comparison were performed using the Gaussian 98 [173] and 03 [174] programs. All geometry optimizations and frequency calculations were completed using the UB3LYP/6-311++G(2d,p) level of theory. The energies of the optimized structures were determined from UCCSD(T)/cc-pVTZ calculations using an initial guess of a mixture of HOMO and LUMO orbitals. The unrestricted coupled-cluster energy calculations as opposed to restricted calculations due to the inability of the restricted model to correctly model the energetics at large separation distances.

For scission reactions, the geometry was optimized by holding the dissociating bond length fixed and allowing all other modes to relax to equilibrium. For abstraction and addition/β-scission reactions, the transition state structure was identified and verified that it contained only one imaginary frequency. Intrinsic Reaction Coordinate (IRC) calculations were used to obtain structures along the MEP from the TS towards the reactant and product structures. The IRC calculations terminated prior to reaching the equilibrium reactant and product structures, so optimization scans were conducted to obtain the remainder of the necessary structures along the MEP.

The Counterpoise Basis-Set Superposition error was corrected by the method of Boys [199]. Changes in zero-point energy were taken into account by a multiplicative factor, scaling the product energy to the value with the zero-point energy correction applied. For carbon-carbon dissociation in ethane, a comparison is shown in Fig. 3.1 between the scaled and exact zero-point energy from a UB3LYP/6-311++G(2d,p)

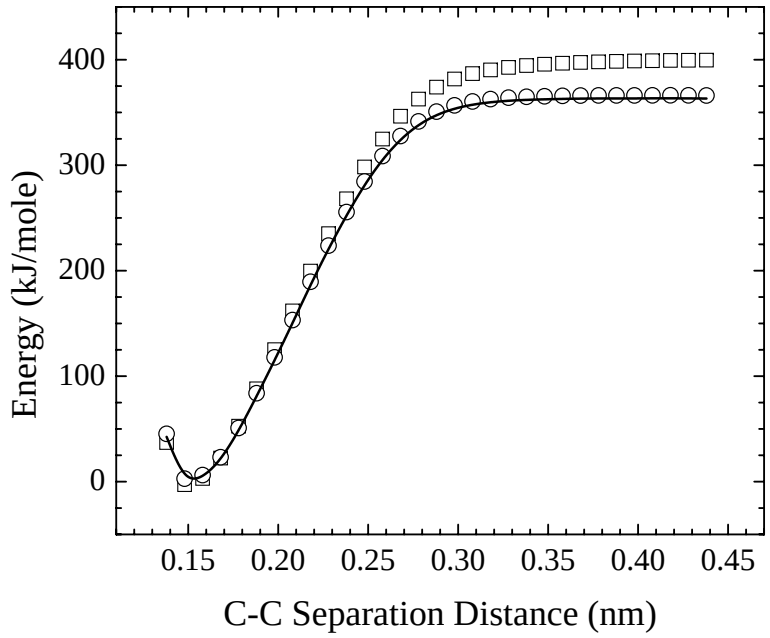

Figure 3.1. Correcting the energy of C-C dissociation in ethane (□) for the change in zero point energy explicitly by the zero point energy at each geometry (○) and by scaling the dissociation energy (line).

calculation. The change in zero-point energies during homolytic bond dissociations appears to be represented accurately by this approximation.

3.2.2 MM3 Forcefield

The MM3 forcefield [104–106] was used to represent the atomic interactions in this study. This forcefield has been demonstrated to provide reasonably accurate results near equilibrium of molecular conformations with an average conformational energy error of 1.5 kJ/mole for hydrocarbons and a total error of 2.6 kJ/mole [65]. Other comparisons of the MM3 forcefield have demonstrated that it is capable of representing a wide range of chemical complexity [66, 81, 200, 201].

Parameters for the hydrogen-hydrogen model were not available in the MM3 forcefield, so they were taken from UB3LYP/6-311++G(2d,p) optimization calculations.

On the basis of these calculations, the force constant was determined to be 6.59×10^2 N/m and the equilibrium bond distance 0.0744 nm.

3.3 Development of Scission Reactions

3.3.1 Dissociation of Bonds using MM3 Quartic Potential

The MM3 forcefield uses a quartic bond-stretching potential, which is inadequate for the description of chemical bond dissociation. Consequently, a correction was applied to represent any bond stretches by a hybrid between the MM3 quartic and Morse potentials. At a bond distance greater than r_s, the MM3 quartic bond potential is switched to a Morse-type potential.

In order to ensure continuity and smoothness of the forces, the values of the energy and first and second derivatives of the MM3 quartic and Morse potentials are required to be equal at r_s. Because the parameters of the MM3 quartic potential are used in the vicinity of the equilibrium conformation, there are four parameters to be determined from three equations. The single degree of freedom was chosen to be the dissociation energy, D_E, of the Morse potential. These values were calculated from CBS-QB3 *ab initio* calculation [3], and were corrected for zero-point energy by setting it equal to $\Delta H^o(T = 0K)$. The parameters of the modified-Morse-potential portion of the composite bond potential are shown in Table 3.1.

3.3.2 The Homolytic Scission Model

The reaction coordinate (RC) is a measure of the location of the transient structures on the PES relative to the positions of reactant(s) and product(s). For each reaction, a mathematical function for the RC was developed. The forward reaction begins at RC = 0 and ends at RC = 1. Because the reactions are descriptions of the complete PES, the reverse reaction was described by starting at RC = 1 and proceeding to RC = 0.

Table 3.1. Parameters for Transition from MM3 Quartic to Morse Bonding Potential[a].

Bonded Pair	D_E (kJ/mole)	α (nm^{-1})	r_e (nm)	r_s (nm)
h-h	436.8	18.91	0.0740	0.0871
cg-h	406.3	17.44	0.1108	0.1251
c1-h	394.6	17.77	0.1108	0.1249
c2-h	406.3	17.44	0.1108	0.1251
c3-h	418.0	17.13	0.1108	0.1254
c4-h	433.8	16.73	0.1107	0.1257
cf-h	443.9	17.53	0.1097	0.1240
c-c1	348.5	18.59	0.1522	0.1655
c-c2	353.6	18.42	0.1522	0.1657
c-c3	356.1	18.34	0.1521	0.1657
c-cf	411.7	18.35	0.1496	0.1632
c1-c1	353.6	18.42	0.1522	0.1657
c1-c2	358.6	18.25	0.1521	0.1658
c1-c3	361.1	18.17	0.1521	0.1659
c1-cf	411.7	18.35	0.1496	0.1632
c2-c2	363.6	18.09	0.1521	0.1659
c2-c3	366.1	18.01	0.1521	0.1660
c2-cf	411.7	18.35	0.1496	0.1632
c3-c3	370.3	17.88	0.1521	0.1661
c3-cf	411.7	18.35	0.1496	0.1632

[a] Atom types are defined in Table A1 of Ref. [3].

Table 3.2. Parameters for HH, CH, and CC scission profiles.

Parameter	HH	CC	CH
RC Region (nm)	0.085-0.375	0.169-0.393	0.124-0.370
m (nm^{-1})	3.448	4.45	4.07
b	-0.293	-0.752	-0.504
a_1	5.164	14.05	5.50
$RC_{0,1}$	0.491	0.610	0.502
a_2	-	33.60	19.87
$RC_{0,2}$	-	0.100	0.299
E_{base} (kJ/mole)	436.8	364.0	401.7

Reaction potentials were developed initially for simple homolytic scissions. For these reactions, the RC of interest is the bond distance between the dissociating atoms. The RC is represented by a simple linear function,

$$RC = mr + b \tag{3.1}$$

where m and b are parameters. The RC parameters are given in Table 3.2 for H-H, C-H, and C-C scission reactions. Bounds on the active RC range (RC = 0 and 1) are set to 5% and 99% of the dissociation energy, respectively.

Switching functions were used to transition smoothly between the atom types that describe the reactant(s) and product(s), capturing transitions such as sp^3 to sp^2 hybridization changes in carbon as a bond breaks. In each case, the switching function creates a transition for any forcefield term where a change in atom type is encountered. The switching functions are unity at RC = 0 and transition to zero at RC = 1. A suitable switching function is:

$$S(RC) = 0.5\left[1 - \tanh\left(a(RC - RC_0)\right)\right] \tag{3.2}$$

where $S(RC)$ is the value of the switching function as a function of RC, a is the steepness parameter, and RC_0 is a parameter such that $S(RC_0) = 0.5$.

For the simplest case, dissociation of a hydrogen molecule, the energy is given by:

$$E_{H_2\,Dissociation} = S(RC)E_{bond} + [1 - S(RC)]\,(E_{vdw} + E_{base}) \tag{3.3}$$

where E_{bond} is the H_2 bonding potential, E_{vdw} is the van der Waals potential, and E_{base} is the baseline energy value from Table 3.2. A single switching function was used to represent all the atomic changes that occur during dissociation of hydrogen.

The situation is more complicated for dissociation of the C-C and C-H bonds in ethane. In the case of the C-C bond, the carbon atoms change hybridization from sp^3 to sp^2. This transition creates more complexity in the representation of energetics. Thus, as the C-C bond breaks, related H-sp^3C-H bond angles also transform to H-sp^2C-H bond angles. The H-sp^3C-sp^3C bond angles and H-sp^3C-sp^3C-H torsions may be smoothly turned off because these constraints are not longer active in the resulting methyl radicals. At the same time, necessary non-bonded interactions are turned on. A similar set of changes occurs when the C-H bond dissociates, except only one of the carbon atoms changes hybridization. In larger molecules, any atom with connectivity to another atom that alters its bonding would also be included. For example, if the central C-C bond underwent a scission reaction in n-decane, a C-C-C-C torsional motion (plus H-C-C-C and H-C-C-H torsions, two C-C-C and multiple H-C-H, H-C-C bond angles) would also be turned off, as well as the non-bonded interactions turned on.

Two switching functions, denoted as S_1 and S_2, were needed to yield an accurate description of the changes in the PES accompanying the C-C and C-H bond scissions in ethane. S_1 was used to model all bonded and non-bonded interactions. It was also used for the transformation of any angular or torsional terms that do not contain both of the dissociating atoms. S_2 was used to model the transition of any angular or torsional term that contains both dissociating atoms. Although both switching functions depend on the same reaction coordinate, they have different values of a and

RC_0. S_1 is a more gradual transition, while S_2 is a much quicker transition occurring very early in the dissociation process. The distinction between the modes associated with S_1 and S_2 is supported by changes observed in the geometries obtained from quantum chemical calculations.

The energetics of the fits obtained for H-H dissociation in hydrogen and C-C and C-H dissociation in ethane are shown in Fig. 3.2, and the switching functions are shown in Fig. 3.3. Good agreement between the *ab initio* calculations and the reactive forcefield is obtained, although there is a slight non-monotonic deviation for C-C scission (Fig. 3.2b). The use of the complete and smooth PES allows this method to conserve energy. Because the value of E_{base} is tracked throughout the simulations, energy is conserved even once a reaction is completed. Therefore, the method is accurate for use in NVE as well as thermostatted and barostatted calculations.

3.3.3 Vibrational analysis along the reaction path

Reaction path following methods such as Variational Transition State Theory [202], reaction path Hamiltonian [203], and reactive molecular dynamics [3, 53, 54] require accurate and smooth frequency transitions along the reactive path. Ensuring a smooth transition of the frequencies satisfies the continuity of the pathway through second derivative, and makes transition state analysis valid. For RMDff, the frequency profile is calculated for ethane decomposition to methyl radicals in order to verify this property of the forcefield.

The calculation of the Hessian for the reactive modes in RMDff require the consideration of several terms. Using a similar procedure to that presented in Sec. 2.3.2, the component of the Hessian for a reactive mode is

$$H_{ij} = S\frac{\partial^2 E}{\partial \mathbf{x_j}\partial \mathbf{x_i}} + \frac{\partial E}{\partial \mathbf{x_i}}\frac{\partial S}{\partial \mathbf{x_j}} + \frac{\partial E}{\partial \mathbf{x_j}}\frac{\partial S}{\partial \mathbf{x_i}} + V\frac{\partial^2 S}{\partial \mathbf{x_j}\partial \mathbf{x_i}} \tag{3.4}$$

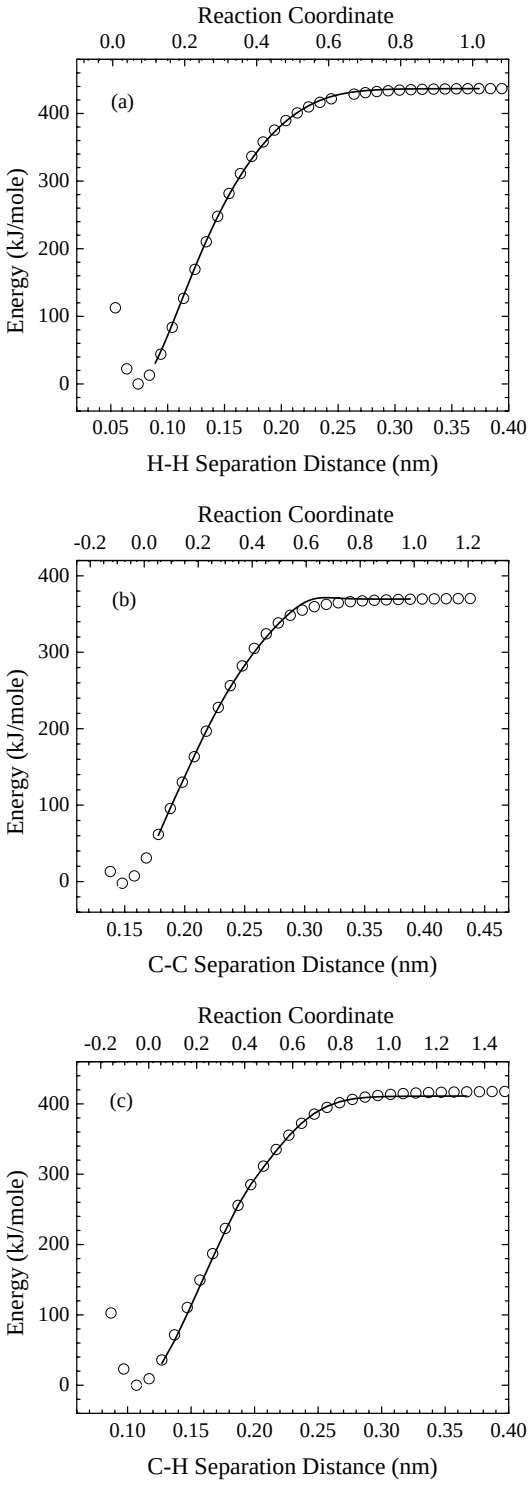

Figure 3.2. Fits of (a) H-H, (b) C-C, and (c) C-H dissociation energy models, shown as lines, to *ab initio* data, shown as circles.

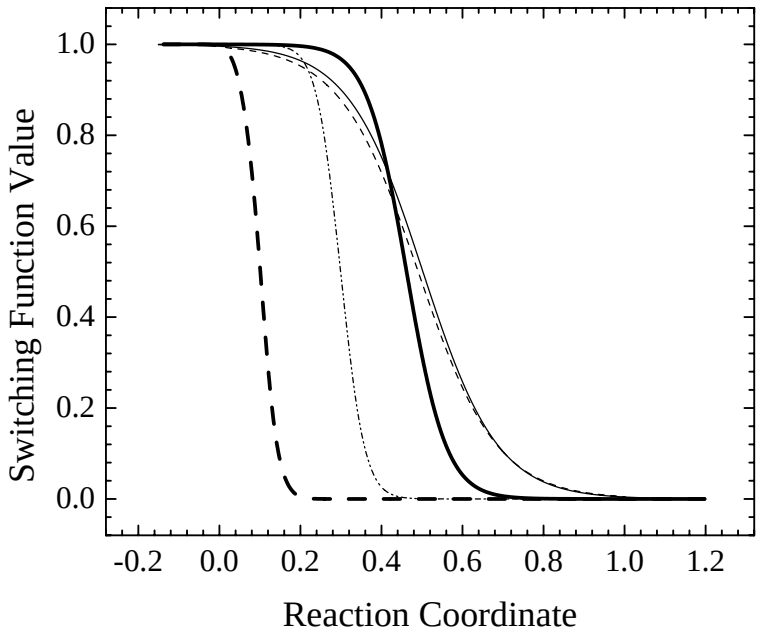

Figure 3.3. Switching function versus RC for H-H dissociation (dashed line), C-C S_1 switching function (thick line) and C-C S_2 switching function (thick dashed line), and C-H S_1 switching function (thin line) and C-H S_2 switching function (dash-dot line).

where S is the switching function with the derivative taken with respect to r via chain rule differentiation.

Constrained, minimized structures were obtained along the minimum energy path using RMDff for C-C separation distances of 0.178 to 0.378 nm in increments of 0.02 nm. The frequency analysis was then performed on these minimized structures with the forcefield component along the reaction path projected out as described in Sec. 2.3.3.

The real component of the frequencies are shown graphically in Fig. 3.4(a). In general, the transitions in the frequencies occur mostly when one of the switching functions are most active. A comparison of the reactive frequencies from UB3LYP/6-31G(d) *ab initio* calculations and RMDff is shown in Fig. 3.4(b). While, the RMDff frequencies do not transition as slowly as the *ab initio* calculated frequencies, reasonable agreement is observed between the two methods.

While the equilibrium methyl radical appears to lose a frequency, this is a result of the MM3 forcefield because there is no out-of-plane motion included in this analysis. Similar results are seen for RMDff at 0.378 nm C-C separation distance, where 10 frequencies are observed as opposed to the 12 expected frequencies.

The frequencies obtained along the reactive path indicate a smooth transition from reactant to product, also expected because no anomalies are observed in the forces. The frequencies show good comparison with literature values near the reactant and product structures. It appears that RMDff correctly captures the trends of the frequency transitions along the reaction pathway.

3.3.4 Comparison of Near Minimum Energy Path Structures

Random geometric distortions were introduced at random points along the minimum energy path to test the robustness of the forcefield. Deviations were kept small to prevent additional RC's from becoming active. The average variation in the bond

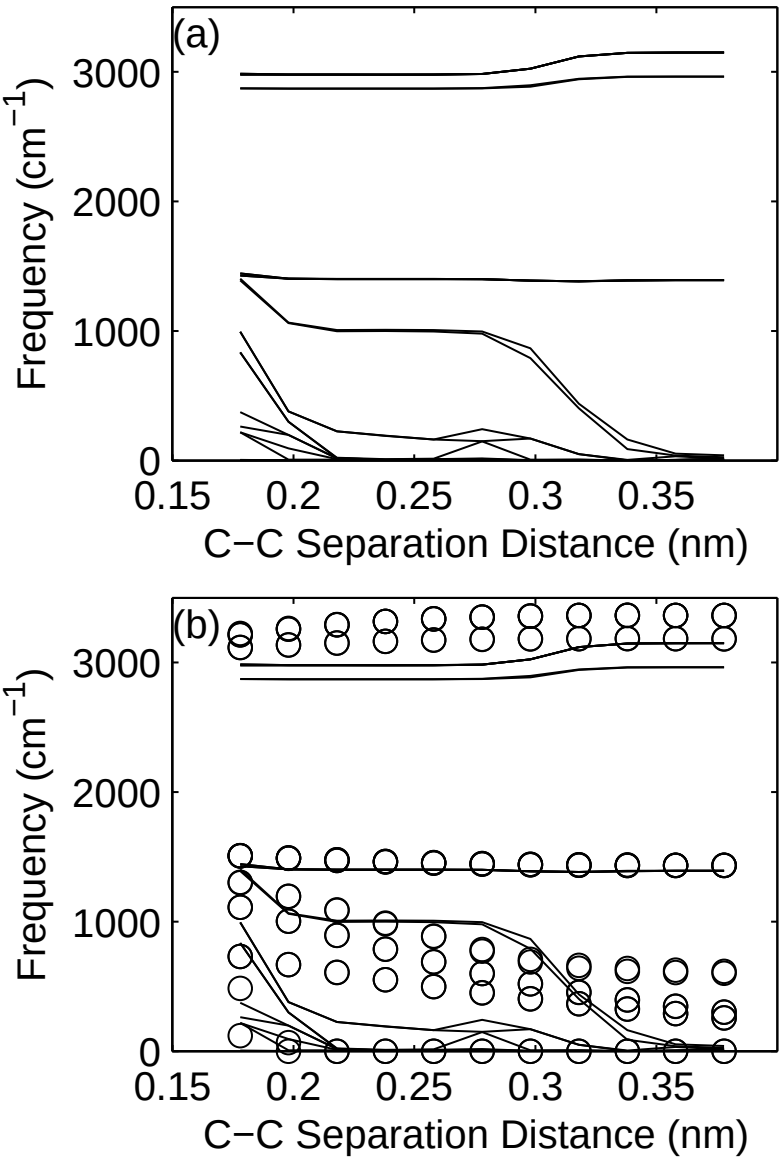

Figure 3.4. (a) Real component of the frequencies calculated for dissociating C-C bond in ethane using RMDff as a function of separation distance. (b) Comparison of the frequencies calculated for dissociating C-C bond in ethane using RMDff (lines) and UB3LYP/6-31G(d) *ab initio* calculations (circles) as a function of separation distance.

lengths was approximately ±0.005 nm, while average deviations of the bond angles and torsions were about ±5°. Energies from the forcefield are compared to values obtained from the quantum calculations in Fig. 3.5. The forcefield tends to over-predict the *ab initio* energy by about 40 kJ/mole for C-H bond scission and 45 kJ/mole C-C for bond scission. This over-prediction in energy appears to be independent of the reaction coordinate. In Fig. 3.5(a), a notable distribution of forcefield energy is observed at a quantum chemical energy of 0 kJ/mole. These deviations reflect those of the MM3 forcefield alone, as the C-C bond is not yet stretched sufficiently to cause the reactive potential to be active. Therefore, the deviations observed are the result of the MM3 forcefield description.

3.3.5 Testing Transferability of the Scission Model

Dissociations of C-C and C-H bonds were tested in other molecules to examine the transferability of the reactive forcefield parameters. In each case, the RC and switching-function parameters listed in Table 3.2 were used to model the scission reactions. It is important to note that the value of E_{base} represents the forcefield-based dissociation energy for the molecular structure of interest. To correct the value of E_{base} for other molecules, a direct additive scaling was applied between the CBS-QB3 value of $\Delta H^o(T = 0K)$ and the value of E_{base} of the basis molecule. Although the MM3 potential contains a radical-carbon atom type, it is parameterized for hydrocarbon species as opposed to the compounds we tested, which contain hetero-atoms. Because the radical carbon and alkene sp^2 carbon types for hydrocarbons are similar with respect to bond angles and torsions, we assumed that they would provide a reasonable approximation to the radical carbon types for CHX species.

The switching functions, parameterized by our calculations of the dissociation of the C-C bond in ethane, were compared for propane, fluoroethane, and ethyl amine (Figs. 3.6a-c), while the switching functions obtained from the calculations of the C-H

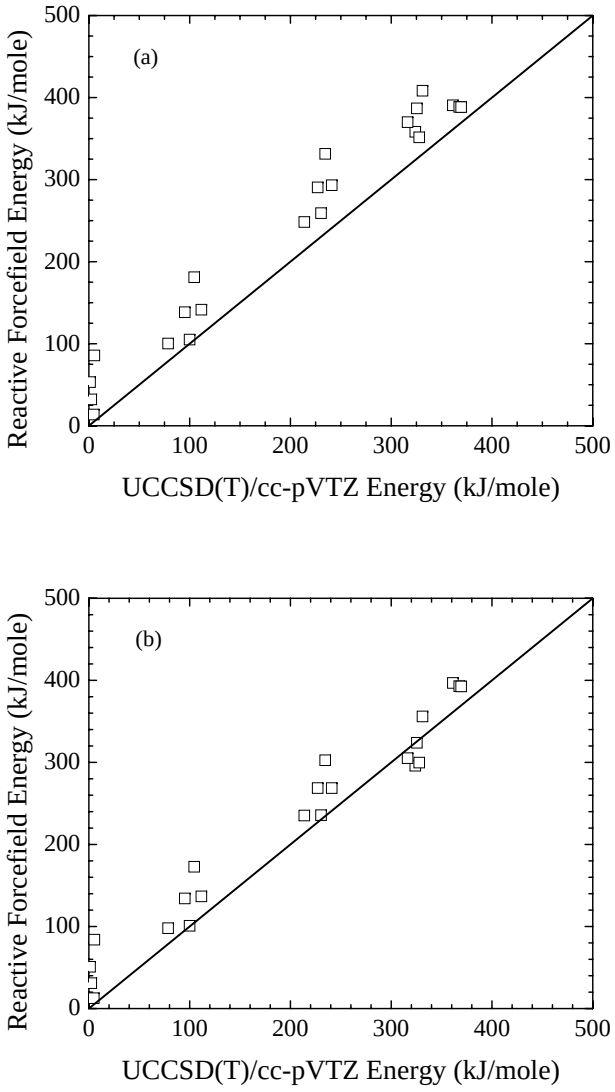

Figure 3.5. Calculated energy as compared to *ab initio* energy for randomly distorted structures near the bond scission minimum energy path for (a) C-C scission and (b) C-H scission.

bond dissociation in ethane were compared for methane, methanol, and acetaldehyde (Figs. 3.6d-f). In general, the model appears transferable to a variety of species.

The main source of error appears to be description of the radicals (i.e., the simplified treatment of the radical carbon type), as opposed to the switching function parameters. The errors were small when minor substitutions were made to the base chemical structure, but larger deviations were observed for non-alkanes. For example, the forcefield energy over-predicted the energy of acetaldehyde (H-CH_2CHO). This is not surprising because CH_2CHO is resonance-stabilized and is not well described by a simple sp^2 radical carbon atom. For ethyl-amine, the use of the switching function causes the potential energy to overshoot the MM3 energy of the dissociated radical by about 7 kJ/mole. While it is possible that use of larger a in the switching function would force the PES curve down, it may also be that the evolving radical is resonance-stabilized by the lone pair on the nitrogen atom [204, 205]. In any case, it appears likely that a more accurate model representation could be obtained by adjusting the forcefield parameters to provide a better description of the radical species.

3.4 Development of Abstraction Reactions

3.4.1 The Abstraction Model

The next reaction model developed was for the abstraction reaction. As opposed to the homolytic scission reactions, the abstraction reaction involves a classical TS with an energy maximum. Additionally, the RC is more complex because there are now two bond stretches that must be considered simultaneously. These effects necessitate a different approach compared to the description of homolytic scission reactions.

For abstraction reactions, two separate RCs were used to describe the entire surface of the reactions. The first RC description starts at the reactant and proceeds to the TS. The RC begins at the reactant structure with RC = 0 and proceeds to the TS where RC = 1. The second RC description starts at the product with RC = 0

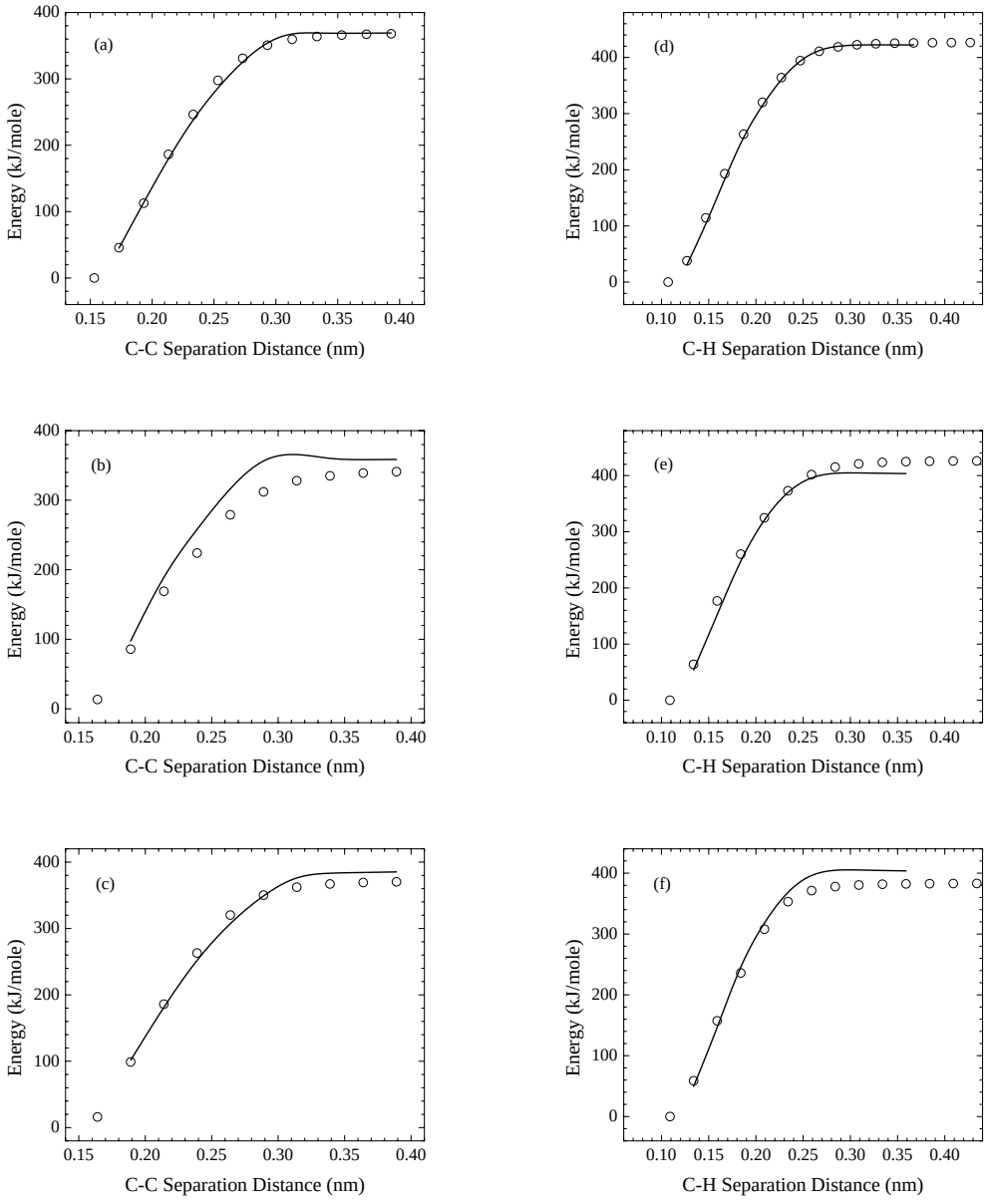

Figure 3.6. Comparison of the C-C scission reactive potential, shown as lines, in (a) propane, (b) ethyl amine, and (c) ethyl fluorine and of the C-H scission reactive potential in (d) methane, (e) methanol, and (f) acetaldehyde. *Ab initio* points are shown as circles.

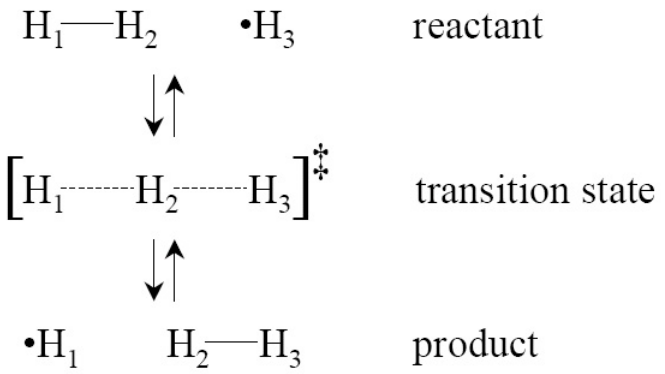

Figure 3.7. Reaction Description of H_3 abstraction reaction.

and proceeds toward the TS where RC = 1. For symmetric abstraction reactions, the same reaction description is applied to both sides of the TS because of the symmetry.

The basic abstraction reaction model was first developed for $H_2 + H \rightleftarrows H + H_2$ or the H_3 reaction. The structures involved in the H_3 abstraction reaction are depicted in Fig. 3.7. The dependence of the 1-2 and 2-3 bond distances along the minimum energy path (MEP) during the reaction are shown in Fig. 3.8. It is seen that the non-bonded distance r_{23} initially decreases while the bonded distance r_{12} remains relatively constant. This region must be included because the energy is changing from non-bonded interactions. Once r_{23} reaches approximately 0.15 nm, the r_{12} bond begins to stretch towards the TS separation distance.

For the abstraction reaction, the RC cannot be described sufficiently by any single separation distance due to the interdependence of r_{12} and r_{23}. Because the RC must be represented accurately along the reactive pathway, a series of related r_{12} and r_{23} points along the MEP is needed as a measure of the current position along the reactive path. Because there is no mathematical function available to represent the relationship between r_{12} and r_{23} for small values of r_{12}, the relationship between r_{12} and r_{23} must be through a separate variable, t. This t-relationship is required because structures off the MEP must be related accurately to the location on the MEP. Therefore, a relationship can be developed between r_{12} and t through a function

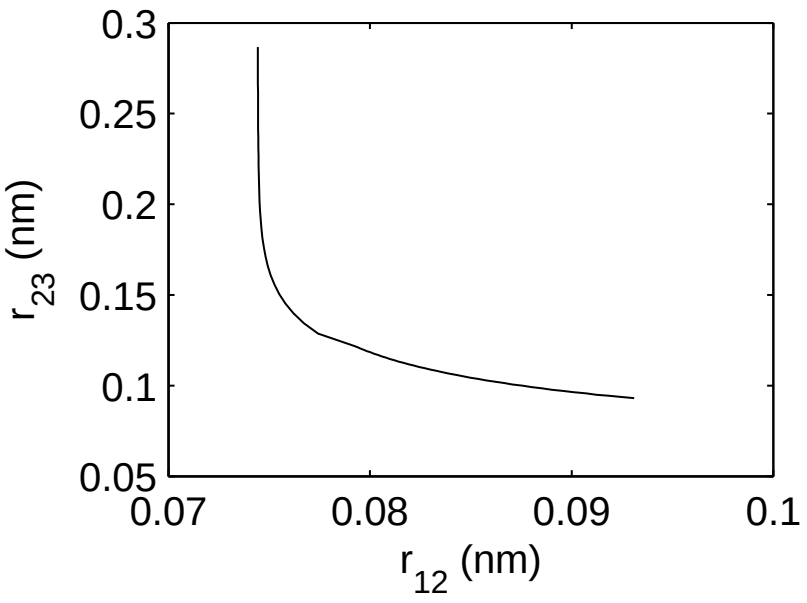

Figure 3.8. Dependence of the bond distances r_{12} and r_{23} during the reaction.

$\psi(t)$. A separate relationship can also be developed between r_{23} and t through $\phi(t)$. These two functions together interrelate any set of r_{12} and r_{23} separation distances. Finally, using the location along the MEP, the RC can be determined as the fractional distance along the curvilinear reaction path.

The first step in determining the RC required assignment of the t-values from the structures along the MEP. The structures along the MEP were obtained first using IRC calculations in both directions from the TS. Because the IRC calculations terminated prior to reaching the minimum-energy structures, optimization calculations were used to continue the surface scan to the minimum-energy structures. The reactant/product structures at the start of the reactive description were assigned $t = 1$. The t-values were assigned in integer order based on the points obtained along the MEP, regardless of separation between two different points. However, there are no specific requirements on the assignment of t-values except that they can resolve the r_{12}/r_{23} separation distances.

Table 3.3. Parameters for abstraction reactions.

	H_2 + H	C_2H_6 + H	C_2H_5 + H_2	CH_4 + CH_3
A_ϕ (nm)	0.0756	0.05269	0.09436	0.1096
B_ϕ (nm)	0.2338	0.2729	0.2282	0.2928
C_ϕ	-0.0385	-0.05779	-0.06467	-0.06445
A_ψ (nm)	0.0756	0.09287	0.05156	0.1135
B_ψ (nm)	0.00784	0.007943	0.01188	0.001281
C_ψ	0.0385	0.05984	0.05705	0.7447
t_{start}	1	1	1	1
t_{TS}	74	29	26	45
l (nm)	0.2135	0.2129	0.1789	0.2703

The entire MEP pathway was fitted from reactant to product structure, even though the actual energetic models have the surface divided into two separate pieces. The entire pathway was to assist in obtaining a good fit for the t-values. The dependence of the t-values on the separation distances observed here most closely resembled a exponential decay/growth function, as given in Eq. 3.5. An exponential decay function was used to fit the $\phi(t)$ (where a negative C value results in exponential decay). An exponential growth function was used for the $\psi(t)$ function that relates the 1-2 bonded interaction.

$$\phi(t) = \psi(t) = A + B\exp(Ct) \tag{3.5}$$

The fits for $\phi(t)$ and $\psi(t)$ for the H_3 abstraction reaction are shown in Fig. 3.9. The change in slope of the curves with respect to t is the result of the change from IRC to geometry optimization calculations, because each method uses a different step size between the optimized structures. In general, the exponential growth/decay functions capture the essential features of the separation distance transitions over the course of the reaction. The parameters for $\phi(t)$ and $\psi(t)$ are given in Table 3.3.

The length l of the curvilinear path can be computed using two functions of t, $\phi(t) = r_{12}$ and $\psi(t) = r_{23}$ as

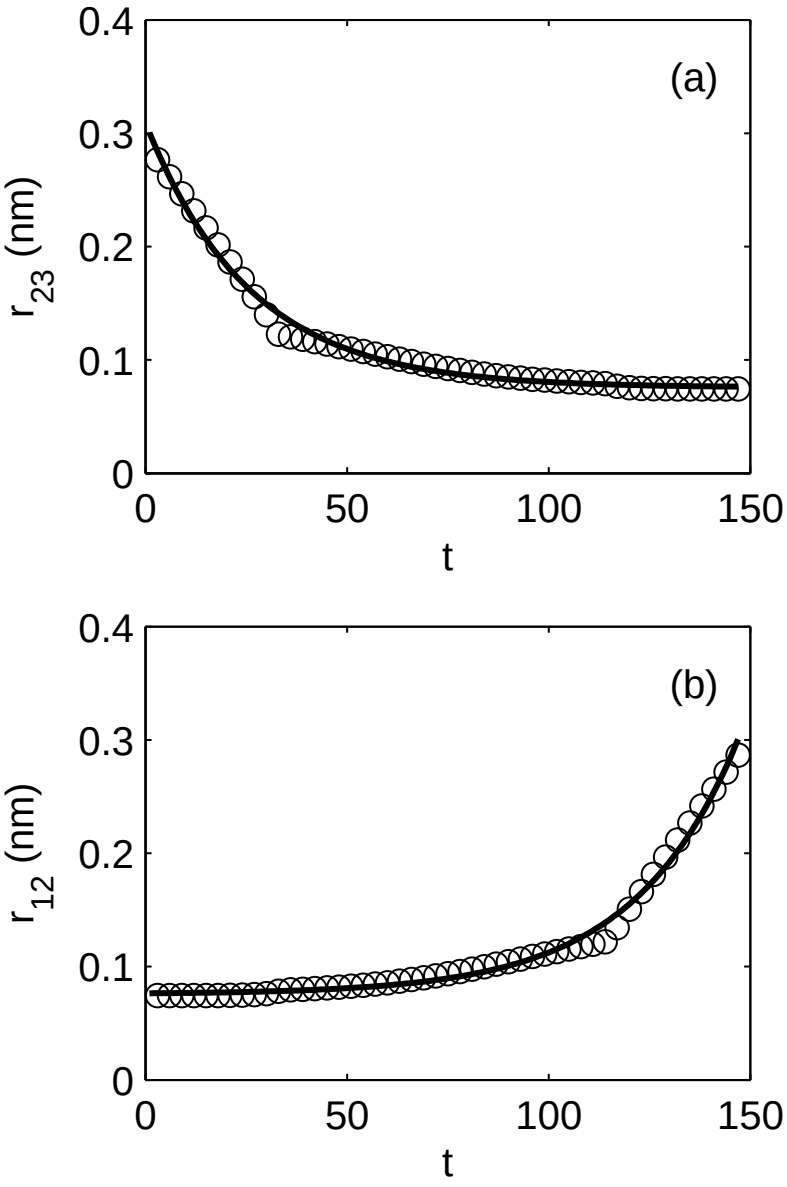

Figure 3.9. Fits obtained for (a) $\phi(t)$ and (b) $\psi(t)$ for the description of the H_3 abstraction reaction.

$$l = \int_{t_R}^{t_{TS}} \sqrt{\left(\frac{d\phi}{dt}\right)^2 + \left(\frac{d\psi}{dt}\right)^2}\, dt \tag{3.6}$$

where t_R is the value of t for the reactant (RC = 0) and t_{TS} is the value of t at the TS (RC=1). Once l is known for the MEP, the RC is simply the ratio of the current value of the integral in Eq. 3.6 to l as shown in Eq. 3.7.

$$RC = \frac{\int_{t_R}^{t} \sqrt{\left(\frac{d\phi}{dt}\right)^2 + \left(\frac{d\psi}{dt}\right)^2}\, dt}{l} \tag{3.7}$$

In order to describe the changes in atomic interaction during a chemical reaction, switching functions were used again to transition smoothly between the reactant/product atom types and TS. For abstraction reactions, these functions capture the transition between the reactant/product structure and the weakly-bonded TS structure. The switching function used was

$$S(RC) = 0.5\,[1 - \tanh(a(RC - RC_0))] \tag{3.8}$$

where $S(RC)$ is the value of the switching function as a function of RC, a is the steepness parameter, and RC_0 is a parameter such that $S(RC_0) = 0.5$.

For the abstraction reaction, two separate switching functions were used. The first switching function (S_1) was used to describe the changes in the bonded and angular terms. The second switching function (S_2) describes the attenuation of the van der Waals forces, as these forces are too strong and must be attenuated prior to the transition of the bonded modes. The H_3 model along the MEP is given in Eq. 3.9.

$$E_{H_3} = S_1 E_{bond}^{1-2} + S_2(E_{vdw}^{2-3} + E_{vdw}^{1-3}) + (1 - S_1)(E_{morse}^{1-2} + E_{morse}^{2-3} + E_{ang}^{1-2-3}) \tag{3.9}$$

E_{bond}^{ij} is the meshed MM3-Morse bond potential used for near-equilibrium structures for the ij bond, which is switched off at the TS. E_{vdw}^{ij} is the van der Waals interaction

for the ij pair. E^{ij}_{morse} is a Morse potential to describe the weakly bound TS structure. The parameters for E^{ij}_{morse} are determined for atom pairs in the fitting of the MEP and are given in Table 3.5. E^{ijk}_{ang} is the angular interaction of the ijk angle that is present for the weakly-bound three-atom TS structure. The 1-2-3 angle was determined by making distortions to the 1-2-3 angle at the TS structure. The parameters are given in Table 3.6.

The fitted H_3 abstraction reaction profile is shown in Fig. 3.10(a). The fitted model is compared to UCCSD(T)/cc-pVTZ quantum-chemical calculations. The quantum-chemical calculations were corrected for zero-point energy (ZPE) changes by multiplicative scaling of the change in the energy between the reactant and TS without the ZPE and with the ZPE included. The switching function values as a function of RC are shown in Fig. 3.10(b). A good representation of the MEP is obtained by switching the bonded structure to a three-atom interaction via Morse potentials at the TS. The sharp corner in the H_3 PES is a result change in step size from IRC calculations to geometry optimization in the definition of the t-value definition. There is no discontinuity in the derivatives at that point because the reactive PES is derived from continuous and smooth functions. The switching function parameters for the reactive potential are given in Table 3.4. Because of the symmetry of the H_3 surface, only one side of the reaction is shown. For the H_3 reaction, $E_{base} = 0$ because no additional energy correction is required. ΔH is the enthalpy of along the MEP, which accounts for the ΔH_{rxn} values upon completion of an abstraction reaction.

For structures not on the MEP, a relationship must be developed between the current geometry and the RC, which is based on the MEP. This was accomplished by assuming that each point along the MEP is associated with a RC contour. For structures near the MEP, it was assumed that the RC contour is not significantly curved. Therefore, using the minimum distance between the current state and the MEP allowed approximation of the RC contour corresponding to the current state

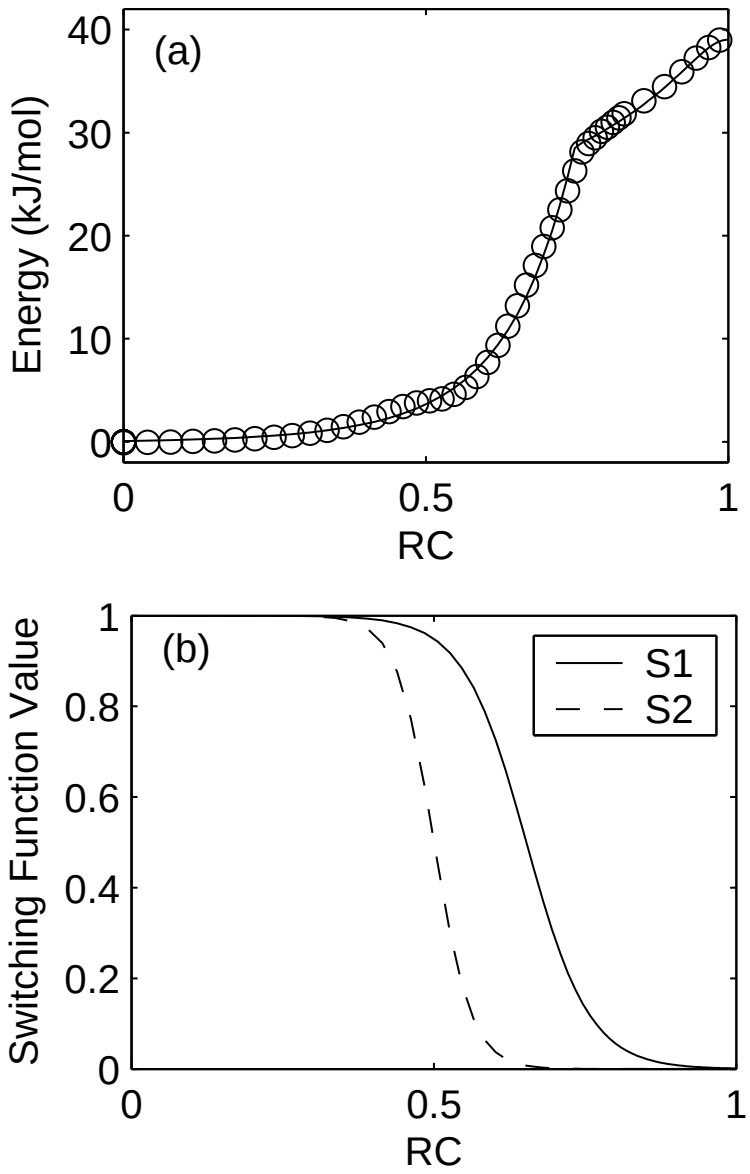

Figure 3.10. (a) Fitted energy model for the H_2 + H abstraction reaction, shown as the line, compared to the UCCSD(T)/cc-pVTZ *ab initio* energy calculations, shown as circles. (b) Switching functions used for the H_3 abstraction reaction with S_1 shown as a solid line and S_2 shown as a dashed line.

Table 3.4. Switching function parameters for abstraction reactions.

	H_2 + H	C_2H_6 + H	C_2H_5 + H_2	CH_4 + CH_3
a_1	9.554	9.000	12.00	12.968
$RC_{0,1}$	0.653	0.765	0.840	0.800
a_2	16.001	10.793	12.87	6.623
$RC_{0,2}$	0.500	0.522	0.748	0.623
E_{base} (kJ/mol)	0	0	16.318	0
ΔH (kJ/mol)	38.99	43.57	55.38	73.01

Table 3.5. TS Morse bond parameters for abstraction reactions.

	H-H	C-H (CHH)	C-H (CHC)
D (kJ/mol)	23.86	15.71	38.03
α (nm^{-1})	110.06	115.34	181.83
r_E (nm)	0.0716	0.1111	0.1103

Table 3.6. TS Abstraction Angular Potentials with k_θ in kJ mol^{-1} deg^{-2} and θ_e in degrees.

Angle	k_θ	θ_e
H^{TS}-H^{TS}-H^{TS}	0.1078	180.0
H-C^{TS}-H^{TS}	6.4071	106.6
C^{TS}-H^{TS}-H^{TS}	0.5130	177.3
C^{TS}-H^{TS}-C^{TS}	0.8621	172.4

and the value of the RC. Once the RC is determined, the energy is calculated using the previously developed model.

The validity of the approximation was tested by investigating linear structures of the H_3 PES. The r_{12} bond was varied between 0.074-0.093 nm, while the r_{23} non-bonded distance was varied between 0.096-0.286 nm. Fig. 3.11(a) shows the PES from the reactive model and Fig. 3.11(b) shows the *ab initio* PES for comparison. Most of the PES appears to model the *ab initio* surface well. The most significant deviations occur when r_{12} is close to the equilibrium bond distance while the non-bonded distance r_{23} closely approaches the bound molecule. The *ab initio* PES indicates a high energy barrier in this region if r_{12} is close to the equilibrium bond distance and the non-bonded distance r_{23} closely approaches the bound molecule. However, the reactive model incorrectly allows the abstraction reaction to proceed in this region, not having the correct energy barrier observed in the *ab initio* calculations. Fig. 3.12 shows the calculated RC as an atom approaches a molecule at the equilibrium bond distance. Because the RC approaches one regardless of the bonded separation distance, the reaction is able to proceed without overcoming the correct energetic barrier.

In order to correct for this error, the energy function of abstraction reactions was modified to include an additional term that responds as a repulsive penalty term for when $r_{23} < \phi(t)$, where the deviations occur. Because the additional energy penalty is included in S_1 the penalty is small for near-reactant/product structures (RC = 0). The additional energy is represented as:

$$E_{correction} = E_p \left(\phi(t) - r_{23}\right) \tag{3.10}$$

where E_p is a constant with a value of 10000 kJ mol^{-1} nm^{-1}.

The PES, reflecting total energy with the energy penalty given in Eq. 3.10, is shown in Fig. 3.11(c). In this situation, a properly high energy barrier is realized

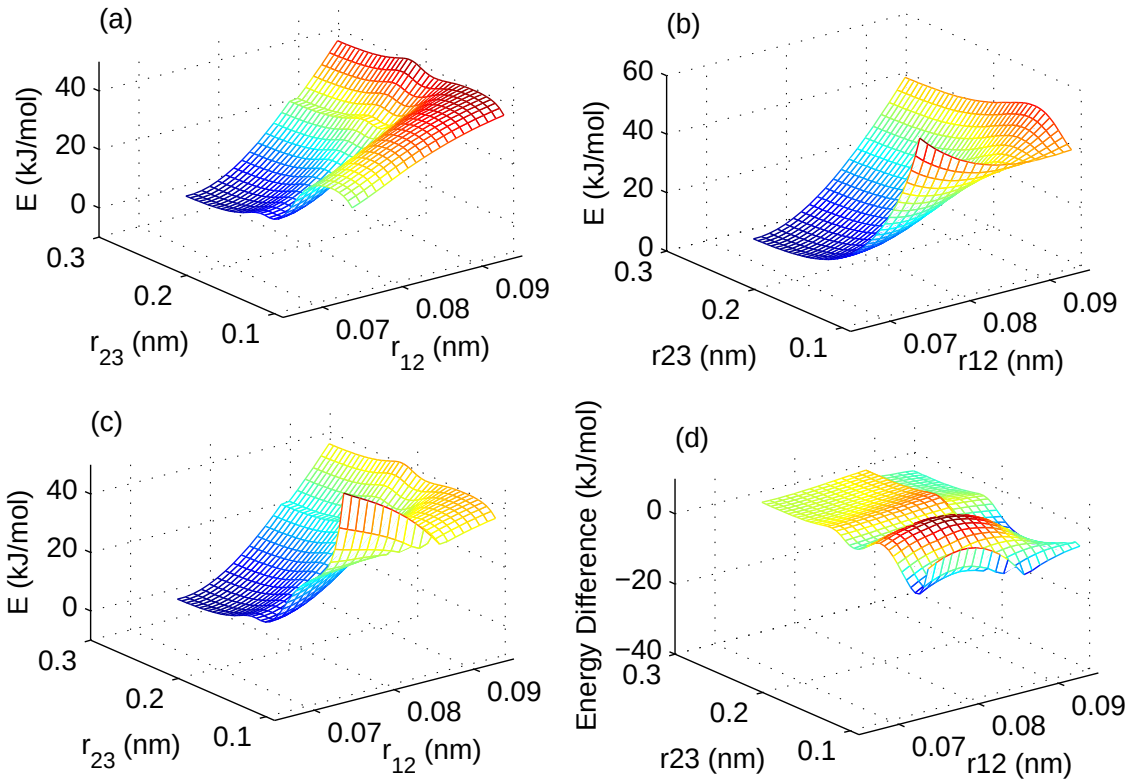

Figure 3.11. H_3 reaction model compared to structures near the minimum energy path for (a) the reactive model using only the MEP representation, (b) UCCSD(T)/cc-pVTZ representation, (c) reactive model using the corrected energy function, and (d) difference between figures b and c.

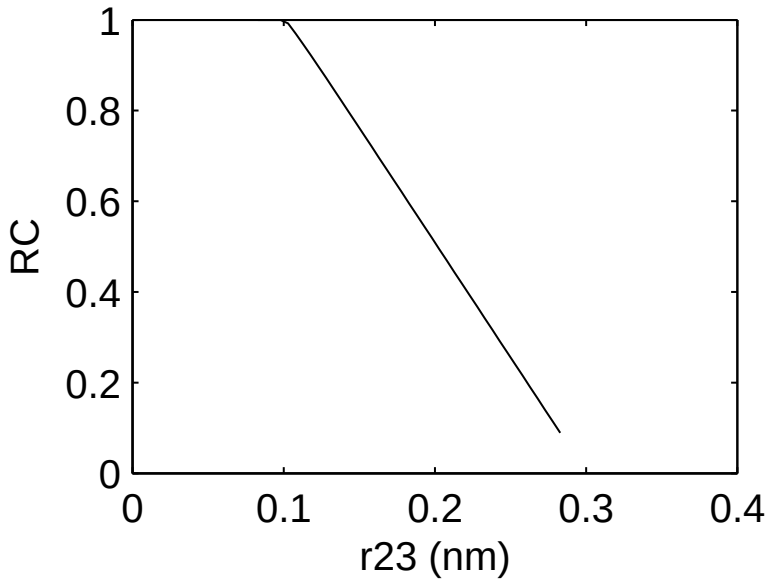

Figure 3.12. RC calculated as a function of non-bonded distance r_{23} at a fixed bonded atom distance, $r_{12} = 0.074$ nm.

when the bonded r_{12} distance is close to equilibrium and the non-bonded r_{23} distance is near the TS structure distance.

The energetic penalty function in Eq. 3.10 is assumed to be transferrable to all abstraction reactions without being parameterized again. Because it is a simple scaling function for the distance off the MEP, there is nothing inherent that restricts the parameters to only the H_3 case. The energy penalty term is included to handle unreasonably low barriers that would be present in all abstraction systems.

3.4.2 Abstraction Reaction Model for Hydrocarbon Systems

Abstraction reaction models also were developed for hydrogen abstraction in hydrocarbons. First, a model was developed for abstraction of H in a hydrocarbon by a hydrogen atom. This is termed a CHH abstraction reaction because of the active atoms in the reaction. The second abstraction reaction modeled was the abstraction of H from hydrocarbons by hydrocarbon radical, a CHC abstraction reaction.

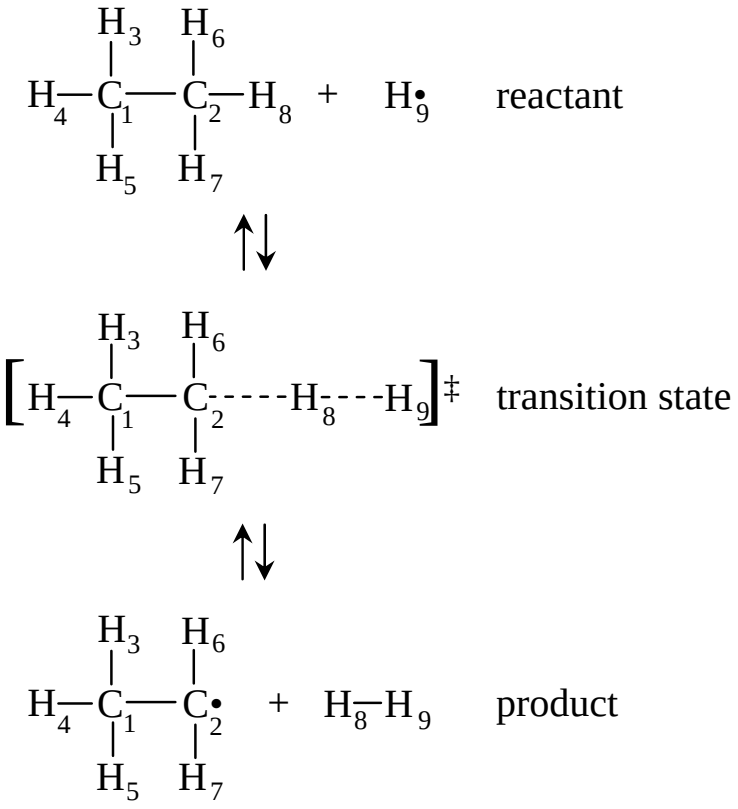

Figure 3.13. Diagram of hydrogen abstraction from ethane reaction.

The first model was developed using the C_2H_6 + H abstraction reaction. A diagram of the reaction is shown in Fig. 3.13. This CHH reaction uses the same type of RC description as the H_3 reaction. The same trends in separation distance are observed. However unlike H_3, this reaction is not a symmetric reaction. The reaction asymmetry leads to two separate descriptions, one for each side of the TS. One RC and set of switching function parameters describes C_2H_6 + H proceeding to the TS. The other RC and set of switching function parameters describes C_2H_5 + H_2 proceeding toward the TS. Because of the asymmetry, each side of the TS has a separate set of RC parameters. The RC parameters for both sides are given in Table 3.3.

The reaction energetics were again described by two separate switching functions, using the same methodology as with H_3. S_1 controls all bonded modes within the molecule along with the additional energy term, E_{base}, and the energy penalty term, $E_{correction}$. S_2 controls attenuation of the van der Waals interactions that occurs as the TS is approached. This is necessitated in order to turn off the van der Waals interactions at the weakly-bound TS complex. The weakly-bound bonded interactions at the TS (between atoms 2, 8, and 9 in Fig. 3.13) are described by weak Morse potentials given in Table 3.5.

For the CHH reaction, there are additional angles and torsions to be considered beyond the simple H_3 case. Any mode that includes two or three of the atoms directly involved in the reaction has angular parameters determined from fitting the quantum chemical PES using a representative molecule at the TS. These parameters are given in Table 3.6. Torsional motions containing two or three of the reactive atoms are set to zero at the TS, as the motion is relatively weak. For any angular or torsional modes that include only one of the transitioning atoms, the mean of the individual reactant and product parameters is used for the TS representation of that mode.

An additional energy contribution was also needed that was not present in the H_3 description. For the C_2H_5 + H_2 reaction, an additional constant E_{base} term was

Table 3.7. Switching functions for angular and torsional modes in CHH reaction.

S_i	Types	Modes
S_1	angles	2-1-3, 2-1-4, 2-1-5, 1-2-6, 1-2-7, 6-2-7
	torsions	3-1-2-6, 3-1-2-7, 4-1-2-6, 4-1-2-7, 5-1-2-6, 5-1-2-7
S_2	angles	1-2-8, 6-2-8, 7-2-8, 2-8-9
	torsions	3-1-2-8, 4-1-2-8, 5-1-2-8, 1-2-8-9, 6-2-8-9, 7-2-8-9

needed in order to properly represent the energetics of the reaction. This term is switched on using S_1. There is no E_{base} term for C_2H_6 + H.

Because of the reaction asymmetry, there is also a change in the enthalpy of reaction, ΔH_{rxn}, over the course of the entire reaction. This is reflected by using different ΔH values for each side of the TS. These values together represent the overall ΔH_{rxn} change during the reaction and also account for energetic changes during the course of the reaction.

The comparison of the fitted model and UCCSD(T)/cc-pVTZ quantum chemical calculations are shown for C_2H_6 + H in Fig. 3.14(a) and for C_2H_5 + H_2 in Fig. 3.14(c). The switching function values for both S_1 and S_2 are shown in Figs. 3.14(b) and (d), respectively. The switching function parameters for the model are given in Table 3.4. This description models the design reaction well. The model energy is reduced to reflect the forcefield energy present at the UB3LYP/6-311++G(2d,p) equilibrium structures. The quantum chemical calculations were corrected for ZPE changes by multiplicative scaling of the change in the energy between the reactant and TS structures without the ZPE and with the ZPE included on each side of the TS.

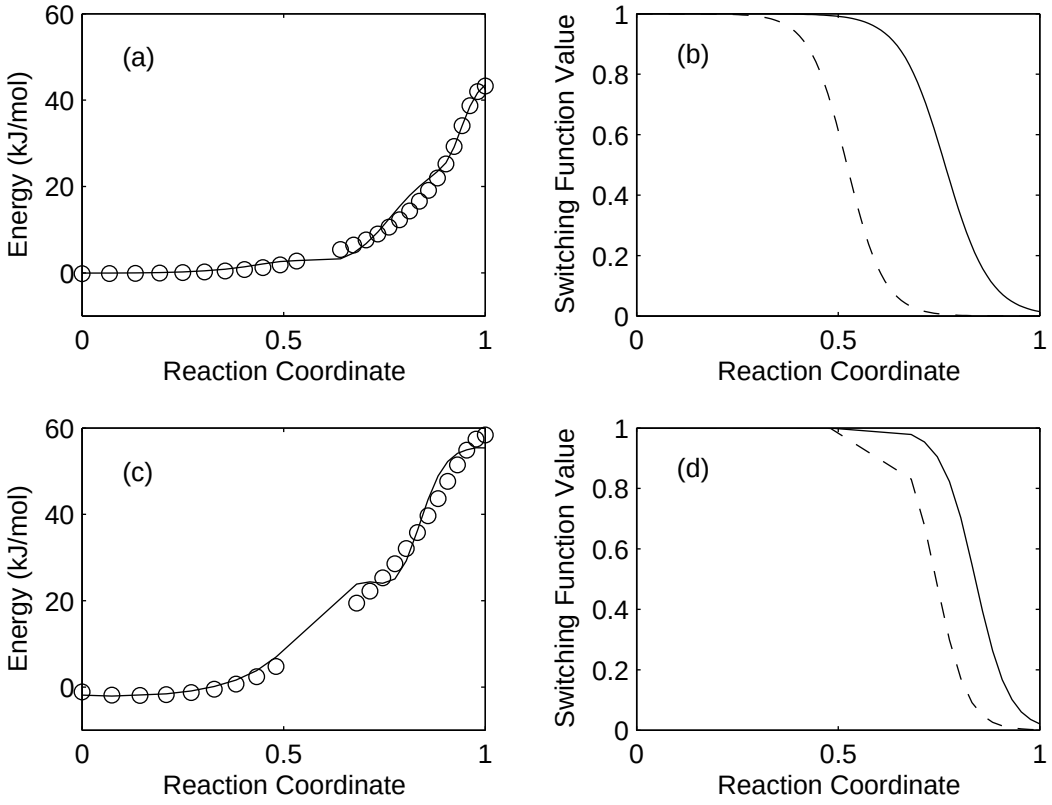

Figure 3.14. Fitted energy model for (a) C_2H_6 + H and (b) C_2H_5 + H_2 to the TS. Model is shown as the line and the UCCSD(T)/cc-pVTZ *ab initio* energy data are shown as circles. The switching functions used for (c) C_2H_6 + H and (d) C_2H_5 + H_2 are shown as solid lines for S_1 and dashed lines for S_2.

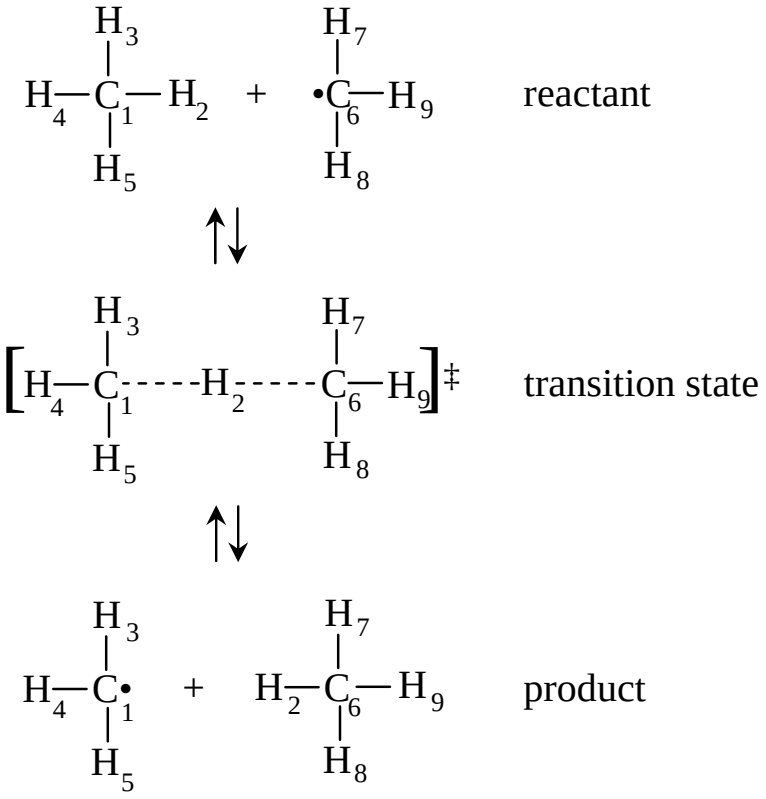

Figure 3.15. Diagram of hydrogen abstraction from methane by methyl reaction.

The final abstraction reaction model developed was for methyl abstraction of a hydrogen atom from methane, a CHC abstraction reaction. This reaction is depicted in Fig. 3.15.

While this particular reaction is symmetric, in general this class of reaction is not. However, the presence of similar structures on both sides of the TS indicates developing these reactions based on a symmetric model should be sufficient, compared to the dissimilarity between alkane + H versus alkyl radical + H_2. For this reaction, there is no additional E_{base} value necessary on either side of the TS. Also, $\Delta H_{rxn} = 0$ for this particular reaction because of the symmetry, so that the same ΔH value is used in the descriptions on both sides of the TS. For other CHC reactions this will result in an error of the thermochemistry; however, this effect should be small

in RMD simulations as the rate constants are calculated directly from the dynamics. Otherwise, the same procedure as for the CHH abstraction reaction is applied here. The RC parameters are given in Table 3.3.

Comparison of the fitted model to UCCSD(T)/cc-pVTZ *ab initio* calculations is shown in Fig. 3.16(a). The switching function values are shown in Fig. 3.16(b). The parameters for the model are given in Table 3.4. Again, multiplicative scaling is applied between both reactants and the TS to account for ZPE corrections. The reaction description models the quantum chemical calculations well. Again, the energy is reduced by the forcefield energy present at equilibrium.

3.4.3 Testing Transferability of the Abstraction Model

The CHH and CHC abstractions reaction models developed were compared to similar species with the same type of abstraction reaction. In Fig. 3.17, the CHH abstraction model is compared to hydrogen abstraction from methane (forward-a, reverse-e), methanol (forward-b, reverse-f), methyl fluoride (forward-c , reverse-g), and propane (forward-d, reverse-h). Fig. 3.18 shows the comparison of the CHC abstraction model of methyl abstracting from ethane (forward-a, reverse, d), methanol (forward-b, reverse-e), and ethyl-fluoride (forward-c, reverse-f).

One of the main sources of errors continues to be the MM3 description of radicals. In many cases, radicals were not defined for heteroatom cases. The assumption employed was that a radical carbon could be approximated by an sp^2C atom. Additionally, approximations were made to represent the modes at the TS; however, these approximations do not seem to be out of line with respect to the geometries and force constants observed at the TS. The fact that TS energy and ΔH_{rxn} are not exactly the same is an additional source of error in the transferability.

The more complex RC definition creates another approximation within the abstraction reaction description. The fact that the RC has to be approximated to the

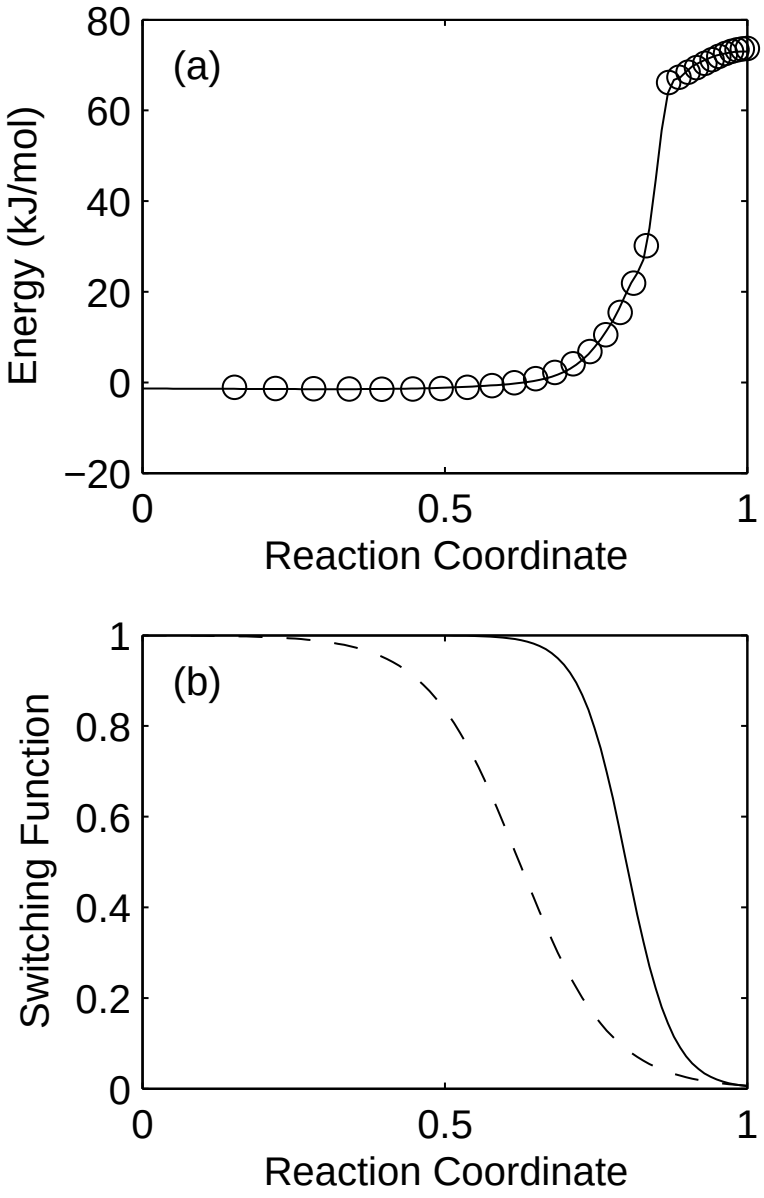

Figure 3.16. (a) Fitted energy model for CH_3 + CH_4 to the TS. Model is shown as the line and the UCCSD(T)/cc-pVTZ *ab initio* energy data are shown as circles. (b) Switching functions used for CH_3 + CH_4 are shown as solid lines for S_1 and dashed lines for S_2.

MEP curve results in the different *ab initio* MEP not precisely lining up with the model MEP developed for a specific reaction. However, this error does not appear to be significant for most cases. The shoulder observed in some of the reverse reactions for CHH abstraction reactions in Fig. 3.17 demonstrate some examples. These problems have the potential to become exacerbated by r_{12} to r_{23} relationships that vary more than the design reaction's relationship, such as the inclusion of heteroatoms.

Overall, reasonable transferability is observed between the sets of parameters. While the barrier heights and thermochemistry are certain sources of error, these should not be as significant in terms of RMD simulations. The main source of error appears to result from the inability of the abstraction reactions developed from purely hydrocarbon analogues to model abstraction reactions involving heteroatoms. While only more exact forcefield parameters will resolve the incomplete set of radical mode descriptions, modeling of abstraction reactions involving the heteroatoms directly will likely help improve the accuracy. However, except for the CH_4 + H reaction, which has been observed not to follow the same trends as other alkane + H reactions [197], reasonable comparisons between hydrocarbon abstraction reactions are found.

3.5 Development of β-scission reactions

3.5.1 The β-scission Model

A reaction model was also developed for addition/β-scission reactions. The models were developed using hydrocarbon additon/β-scission reactions from n-propyl forming (i) C_2H_4 + CH_3 and (ii) C_3H_6 + H.

The first reaction modeled was the addition/β-scission of n-propyl undergoing a β-scission reaction to form ethylene and methyl. A diagram of the reaction is shown in Fig. 3.19. For β-scission reactions, the RC description depends only on the breaking bond (r_{15} in Fig. 3.19). The RC is represented by a linear relationship with the

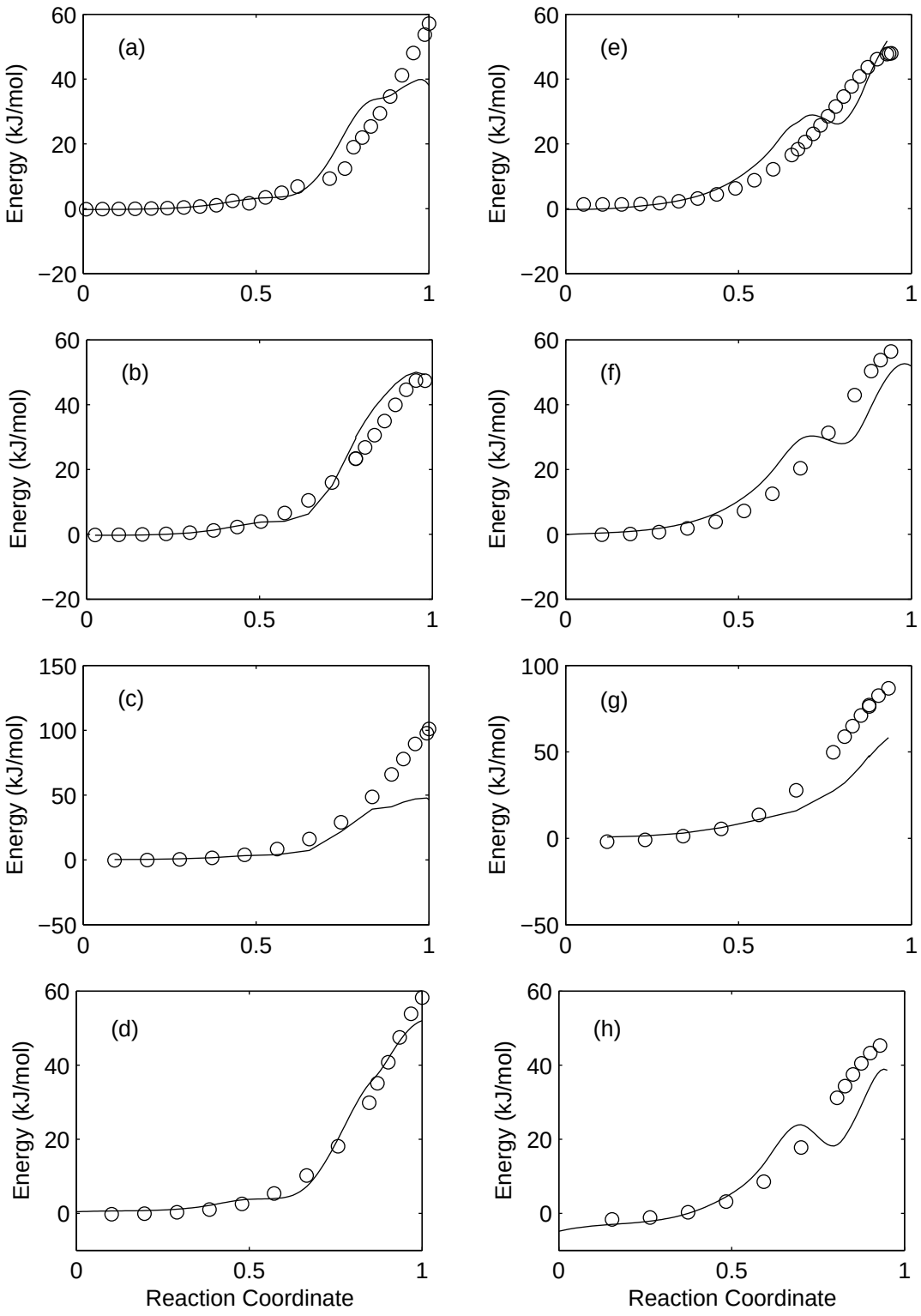

Figure 3.17. Comparison of the CHH model (lines) to UCCSD(T)/cc-pVTZ energy (circles) for (a) CH_4 + H, (b) CH_3OH + H, (c) CH_3F + H, and (d) C_3H_8 + H. Comparison of C_2H_5 + H_2 model to UCCSD(T)/cc-pVTZ energy for (e) CH_3 + H_2 (f) CH_2OH + H_2 (g) CH_2F + H_2, and (h) C_3H_7 + H_2.

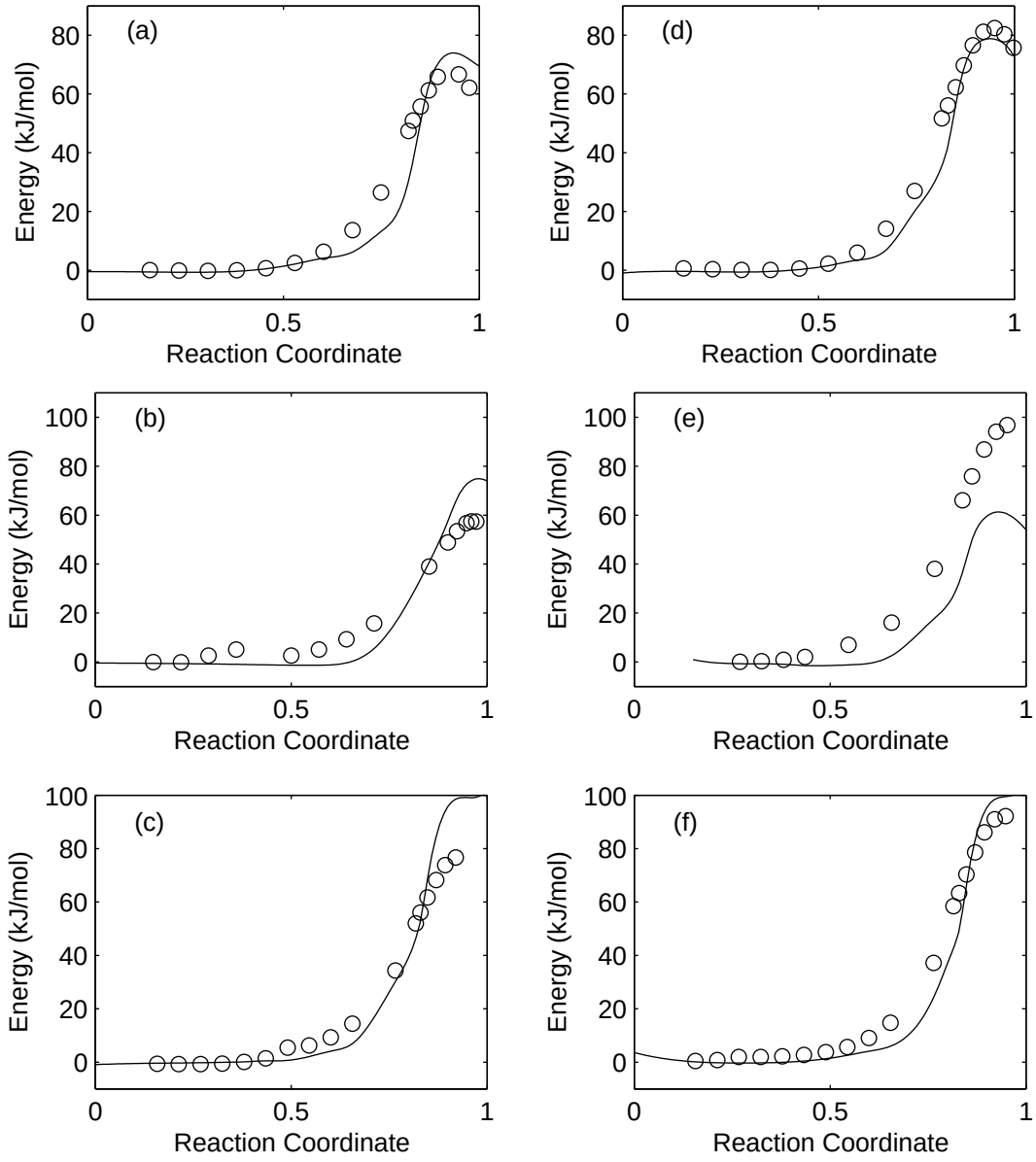

Figure 3.18. Comparison of CHC model (lines) to UCCSD(T)/cc-pVTZ energy (circles) for (a) $C_2H_6 + CH_3$, (b) $CH_3OH + CH_3$, and (c) $CH_3F + CH_3$. Comparison of $CH_3 + CH_4$ model to UCCSD(T)/cc-pVTZ energy for (d) $C_2H_5 + CH_4$ (e) $CH_2OH + CH_4$ and (f) $CH_2F + CH_4$.

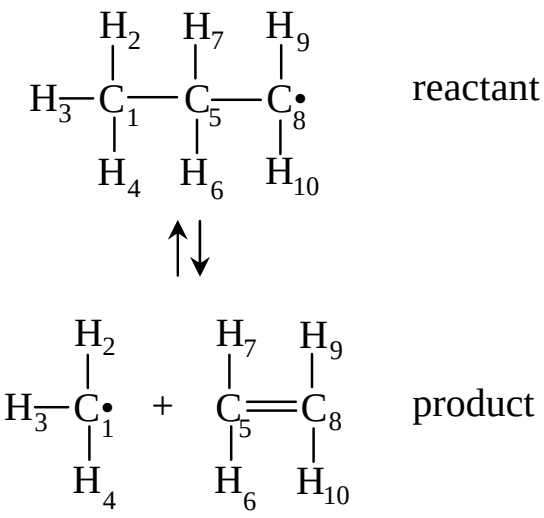

Figure 3.19. Diagram of CC addition/β-scission reaction in n-propyl.

length of the bond, r_{15}, that is breaking/forming during the reaction (hence referred to simply as the breaking bond). The RC definition is given in Eq. 3.11.

$$RC = mr_{break} + b \tag{3.11}$$

Using solely the breaking-bond distance is permissible because there are not significantly large changes occurring in the bond that transitions to a double bond (r_{58}). The change in the two bond lengths along the MEP is shown in Fig. 3.20. Such small changes in r_{58} will be completely undetectable due to standard vibrational motions during the dynamics simulations.

During an addition/β-scission reaction, the p-orbitals must align properly for the formation of the double bond. This alignment can be obtained by using substantially large angular and torsional terms for the double bond. With large angular and torsional barriers for the double bond, any attempt for an addition/β-scission reaction to proceed with perpendicular p-orbitals will be rejected based on the considerable

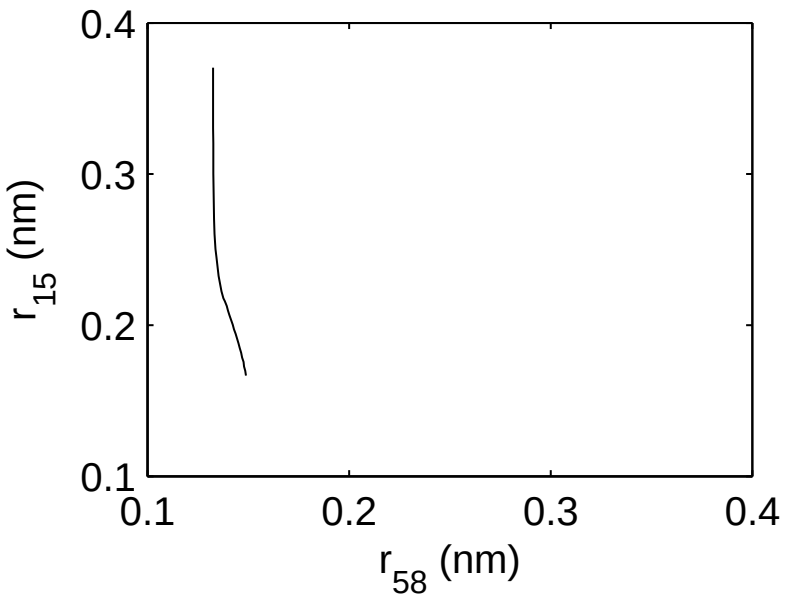

Figure 3.20. Dependence of the r_{15} and r_{58} bond distances during the CC addition/β-scission reaction.

amount of energy required. The barrier to incorrect p-orbital alignment needs to be large enough to quickly reject any inappropriate alignment.

The first addition/β-scission reaction modeled was the C-C β-scission in n-propyl, yielding C_2H_4 and CH_3. The RC parameters for this reaction are given in Table 3.8. Two separate switching functions (S_1 and S_2) are required to describe the transitions that occur during the reaction. All the angles and torsional motions that are broken during the β-scission reaction are transitioned using S_2. The π-bond energy correction, E_π is also turned on using S_2. All angles and torsions that are not broken along with all the bonded and van der Waals interactions are transitioned using S_1. The inclusion of E_{base} is completed using S_1.

For the propyl reaction depicted in Fig. 3.19, a tabulation of each mode and the associated switching function is given in Table 3.9. The total reactive energy for propyl β-scission-scission is a summation of each mode listed in Table 3.9, weighted by the appropriate switching function.

Table 3.8. Reaction coordinate and switching function parameters for β-scission reactions.

	C-C β-scission	C-H β-scission
RC range (nm)	0.16 - 0.37	0.12-0.32
m (nm^{-1})	4.762	5.00
b	-0.762	-0.60
a_1	11.56	17.49
$RC_{0,1}$	0.280	0.367
a_2	11.00	14.18
$RC_{0,2}$	0.270	0.342
E_π (kJ/mol)	-1642.1	-890.2
E_{base} (kJ/mol)	1781.4	1080.0
ΔH_{rxn} (kJ/mol)	130.8	183.8

Table 3.9. Switching functions used for each mode in CC β-scission-scission modes in propyl.

S_i	Types	Modes
S_1	bonds	1-2, 1-3, 1-4, 1-5, 5-6, 5-7, 5-8, 8-9, 8-10
	angles	2-1-3, 2-1-4, 3-1-4, 6-5-7, 9-8-10, 7-5-8, 6-5-8, 5-8-9, 5-8-10
	torsions	6-5-8-9, 6-5-8-10, 7-5-8-9, 7-5-8-10
	vdW	all interactions
	Additional	E_{base}
S_2	angles	2-1-5, 3-1-5, 4-1-5, 1-5-6, 1-5-7, 1-5-8
	torsions	2-1-5-6, 2-1-5-7, 2-1-5-8, 3-1-5-6, 3-1-5-7, 3-1-5-8, 4-1-5-6, 4-1-5-7, 4-1-5-8, 1-5-8-9, 1-5-8-10
	Additional	E_π

Because of the changes that occur during the reaction, two different switching functions are required. S_2 is required to allow angular and torsional modes that are breaking to transition off earlier and to be less constrained, as well as to correct for the π-bond energy.

As the β-scission reaction proceeds, the energy of the breaking bond needs to be softened because of the formation of the π-bond. The softening is required because the bond dissociation occurs with a larger force constant when there is no π-bond being formed. The softening of the breaking bond was accomplished using a constant additional energy term that is turned on as the reaction proceeds using S_2. Additionally, in order to preserve the appropriate system energetics of the two fragments at the completion of the reaction, a constant term E_{base} was also included. It is turned on using S_1 as the reaction proceeds.

The comparison of the reactive model energy with UCCSD(T)/cc-pVTZ *ab initio* calculations is shown in Fig. 3.21(a). The switching functions used during the reaction are shown in Fig. 3.21(b). The parameters for the switching functions are given in Table 3.8. The quantum chemical calculations were corrected for ZPE changes by multiplicative scaling of the change in the energy between the reactant and product structures with and without ZPE included. To obtain a baseline for comparison, the model energy was reduced by the forcefield energy calculated of the optimized n-C_3H_7 structure determined from UB3LYP/6-311++G(2d,p) calculations. A reasonable energetic model of the C-C β-scission reaction was obtained.

A model was also developed for C-H addition/β-scission reactions in n-C_3H_7, forming C_3H_6 and H. The same reactive description developed for C-C β-scission was used. A diagram of the reaction is given in Fig. 3.22. The RC uses the same linear relationship given in Eq. 3.11. The application of switching functions to particular modes used for C-C addition/β-scission was also used for C-H addition/β-scission reactions.

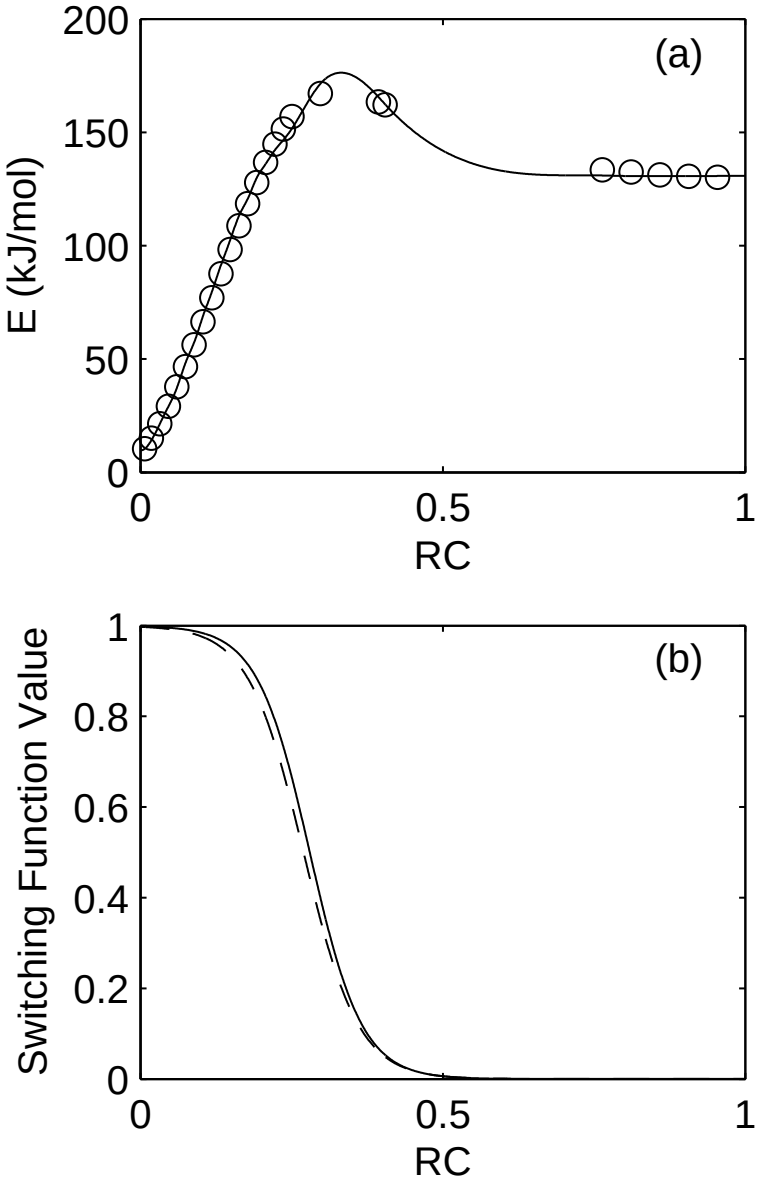

Figure 3.21. (a) Fitted energy model for the C_3H_7 C-C β-scission reaction shown as the line compared to the UCCSD(T)/cc-pVTZ *ab initio* energy calculations shown as circles. (b) Switching functions used for the C_3H_7 C-C β-scission reaction with S_1 shown as a solid line and S_2 shown as a dashed line.

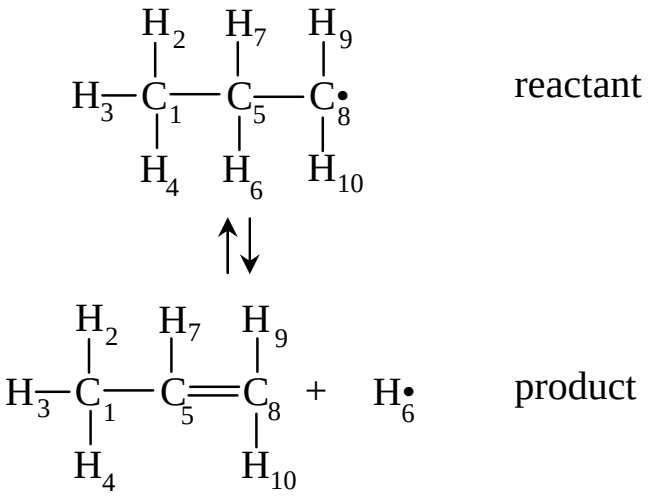

Figure 3.22. Diagram of C-H addition/β-scission reaction in n-propyl.

The reactive model parameters were fitted for the C-H n-propyl β-scission. The parameters are given in Table 3.8. The fitted model was developed from UCCSD(T)/cc-pVTZ calculations is shown in Fig. 3.23(a). The switching function values are shown in Fig. 3.23(b). The same zero-point-energy correction and baseline energy corrections were applied here as to the CC addition/β-scission model. Again, a good representation of the energetic model is obtained along the MEP.

3.5.2 Comparison to Near-Minimum-Energy-Path Structures

In order to validate the model near but not on the MEP, small random deviations were applied to a variety of structures along the MEP. Five different structures had all atoms perturbed slightly, resulting in changes at most of ± 0.01 nm in bond lengths and $\pm 10^{o}$ in bond angles. Structures were sampled from geometries near equilibrium (RC $\approx$ 0), midway between the equilibrium and TS structure (RC $\approx$ 0.16), at the TS (RC $\approx$ 0.30), midway between the TS and the product structure (RC $\approx$ 0.57), and near the final structure (RC $\approx$ 0.95). The comparison of the model energy to the UCCSD(T)/cc-pVTZ calculated energy is shown in Fig. 3.24. There is some

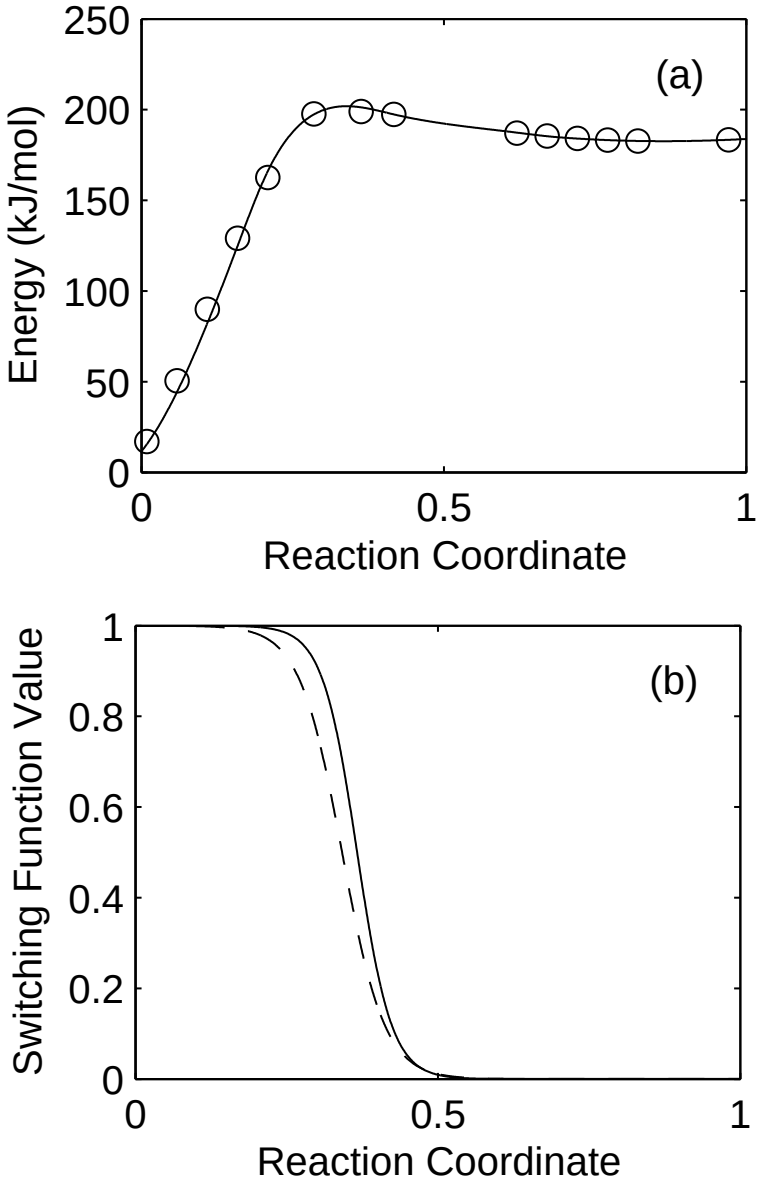

Figure 3.23. (a) Fitted energy model for the C_3H_7 C-H β-scission reaction, shown as the line, compared to the UCCSD(T)/cc-pVTZ *ab initio* energy calculations, shown as circles. (b) Switching functions used for the C_3H_7 C-H β-scission reaction with S_1 shown as a solid line and S_2 shown as a dashed line.

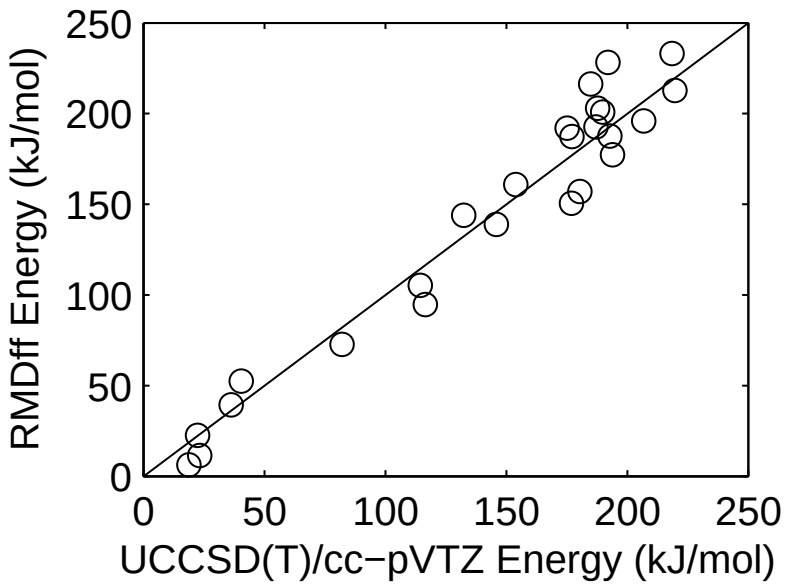

Figure 3.24. Comparison of UCCSD(T)/cc-pVTZ *ab initio* energy to RMDff energy for C_3H_7 C-C β-scission structures near the minimum energy path.

distribution of the reactive model energy compared to the quantum chemical energy; however, the deviations are small, random, and independent of the RC.

3.5.3 Testing transferability of the β-scission model

Extension of the C-C and C-H addition/β-scission models were completed by comparison to other similar species undergoing the same reaction. Fig. 3.25 compares the C-C β-scission model developed in C_3H_7 to (a) C_4H_9 and (b) C_3H_6OH. The C-H β-scission model is compared in Fig. 3.26 to (a) C_4H_9 and (b) $C_2H_4NH_2$. For the C-C addition/β-scission models, thre is a reasonable capture of the forward reaction barrier; however, the reverse reaction barrier is underestimated, especially for C_3H_6OH. The C-H addition/β-scission comparison demonstrates a significant overshoot in terms of the reaction barrier, of approximately 70 kJ/mol. This may result from the parameterization, where the quantum chemical calculations predicted a slightly higher barrier. In addition, internal rearrangements that may occur as a

result of the double bond formation may not be well represented in the forcefield descriptions.

The inability of the forcefield to represent radical heteroatom interactions is a significant source of error. Again, the assumption was that a radical carbon atom could be approximated by an sp^2-C atom. Additionally, some of the heteroatom modes involving the double bond were not parameterized in the MM3 forcefield, so sp^3-O atoms were approximated by sp^3-C atoms. In general, the approximate barrier heights and energy of the separated products are within reason. Additionally, adjusting the E_{base} and E_π parameters helps to model the quantum chemical energy more closely.

3.6 Conclusions

A valence-bond representation of chemical reactions for hydrocarbon systems called RMDff has been developed. Accurate and smooth PES's for scission, abstraction, and addition/β-scission reactions were obtained through the use of switching functions that allow the atom types in the reactant and product to change with the chemical bonding. Good agreement between the forcefield and *ab initio* PES was demonstrated for carbon and hydrogen systems. A comparison to other molecules reveals that the parameters are transferable, with some deviations due to the use of non-optimal parameters for the description of radicals.

The new method provides an accurate description of bond dissociations without the need for molecular-orbital bond-order calculations. RMDff provides a flexible methodology for creating a smooth PES for a reactive potential. The use of equilibrium forcefields allows for the base of the reactive system to be developed from tested equilibrium forcefield models. The use of atom types allows for high specification in each reaction. The application of the switching functions then permits reactions to be developed in a straightforward manner, connecting reactant and product de-

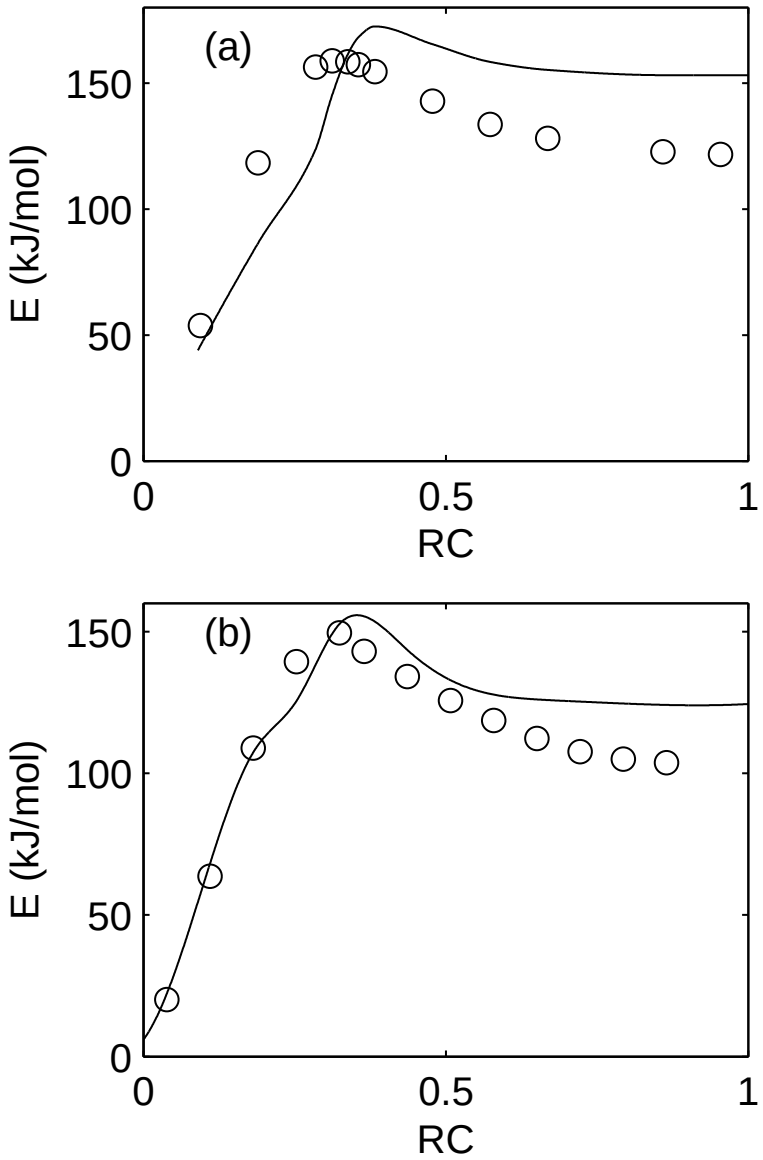

Figure 3.25. Comparison of C_3H_7 C-C β-scission-scission model to UCCSD(T)/cc-pVTZ energy for (a) C_4H_9 forming C_2H_5 and (b) C_3H_6OH.

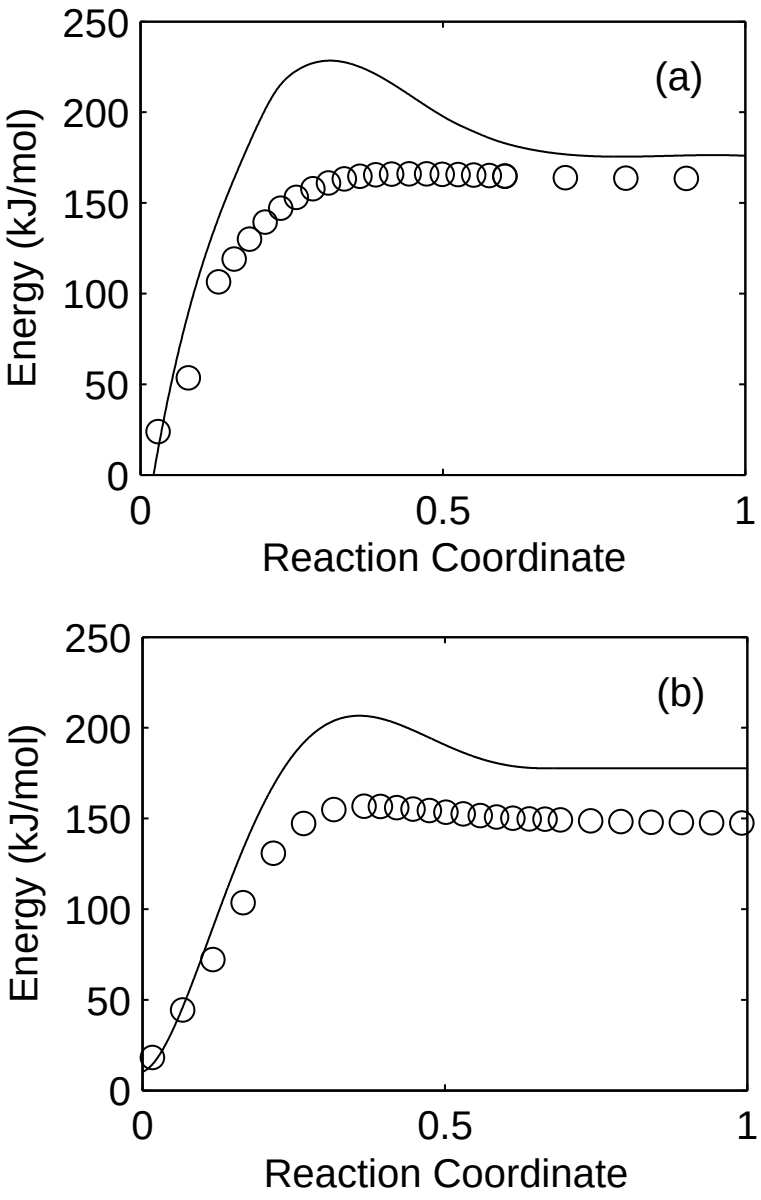

Figure 3.26. Comparison of C_3H_7 C-H β-scission-scission model to CBS-QB3 energy for (a) C_4H_9 forming CC=CC and (b) CH_3CHCH_2OH forming C=CCO.

scriptions together in accurate, smooth potential energy surfaces. Because reactions are relatively rare, the use of equilibrium forcefields as a base to RMDff allows for accurate results in the simulations in the non-reactive cases. Overall, RMDff provides a flexible method that can be easily used to design a representation of reactions using forcefields that have been previously developed and validated.

CHAPTER 4

STATISTICAL ANALYSIS OF POLYMER KINETICS DETERMINED FROM REACTIVE MOLECULAR DYNAMICS SIMULATIONS

4.1 Introduction

In this chapter, RxnMD is used to investigate how kinetic parameters corresponding to backbone scission reactions in polyethylene (PE) depend on the number of repeat units and conformational structures of the polymer chains. Although there have been many experimental studies of the thermal decomposition of PE [23, 26–29, 31, 206–208], there is still disagreement about the relative importance of various elementary reactions and considerable uncertainty about the best values to use for the kinetic parameters needed to describe the temperature dependence of the corresponding rate constants [209].

Rate constants are an inherently statistical quantity even at the atomistic level because reaction times depend on the instantaneous energy distribution. For this reason, sufficient statistics must be accumulated for each kinetic event under investigation. Thus, the first task was to investigate the convergence of the kinetic parameters obtained from our RMD simulations of initial chain scission reactions. The dependence of the rate constants on structure is important when comparing the values calculated from atomistic calculations to the macroscopic values obtained from TGA measurements, and it is abstracted from consideration by performing simulations on the same PE chain. An examination of the effects of variations in conformational structure by analysis of the kinetic parameters obtained from five independently, annealed PE structures was completed. Finally, the effects of chain length on the kinetic

parameters are assessed by comparing results obtained from 50- and 100-repeat unit chains.

4.2 Methods

Polyethylene chains consisting of 50 (PE50) and 100 (PE100) repeat units (-CH_2-CH_2-) were considered in this investigation. The chains were terminated by hydrogen atoms (i.e., methyl groups at the ends of the chains). Periodic boundary conditions (PBC) were employed in all condensed-phase simulations.

The RMD simulations were conducted at a constant volume and temperature (NVT) using the RMDff reactive forcefield method [193] described in Chapter 3. The temperature was controlled by velocity scaling. Simulations were performed between 2350 K and 2000 K, depending on the structure. The lower temperature was dictated by the need for reactions to occur within a reasonable amount of computer time, about 60 hours (on an Opteron 240 64-bit processor). Only C-C scission reactions were active during the simulations, which were performed until the first scission reaction occurred; however, the hydrogen atoms were included in the simulations. Further details about the annealing process and simulation conditions are provided in Sec. 2.4.2.

4.3 Results

4.3.1 Statistics of scission reactions

The thermal decomposition of polyethylene is generally considered to be initiated by random scissions of the bonds that comprise the polymer backbone [22, 33, 34, 210]. This hypothesis was examined by performing 1000 simulations at 2350 K on a single PE50 chain. A different distribution of initial velocities was used in each simulation to ensure their independence. The location of initial polymer backbone scissions was

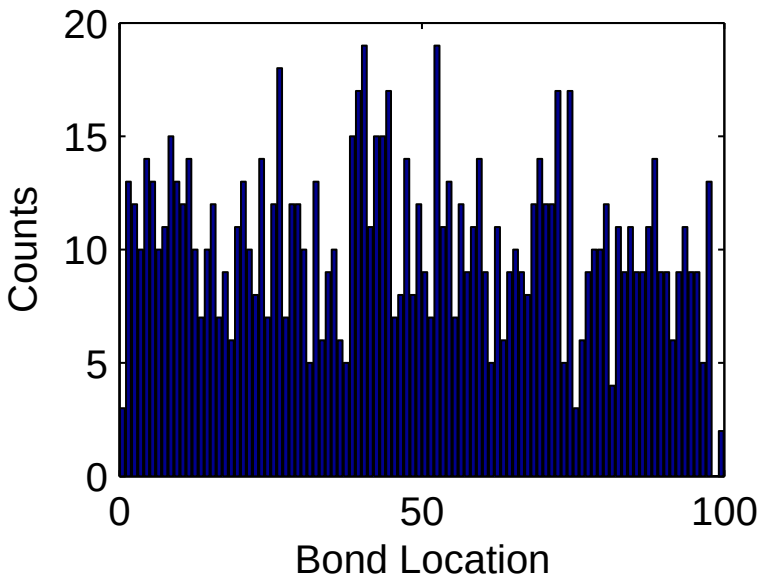

Figure 4.1. Histogram of initial C-C bond scission locations for PE50 using 1000 simulations at 2350 K.

confirmed to be random as shown in Fig. 4.1. The results over the chain are consistent with the presumption that initial backbone scission occurs at random locations.

In order to investigate the effects of the number of simulations on the kinetics, 200 simulations per temperature were conducted on the same PE50 structure at 2100 - 2350 K in increments of 50 K. The statistics of the kinetic data obtained from these 1200 simulations was analyzed by organizing it into three groups in which the activation energies and pre-exponential factors were obtained from Arrhenius plots (Fig. 4.2) constructed from reaction times averaged over N = 10, 20, and 40 simulations at each temperature. Each group consists of five sets of temperature-dependent rate constants obtained by averaging the reaction times over the same number of independent simulations. The kinetic parameters for each set of simulations are listed in Table 4.1. From the Arrhenius plots shown in Figs. 4.2, it is clear that the increased number of simulations results in a more reliable set of Arrhenius parameters.

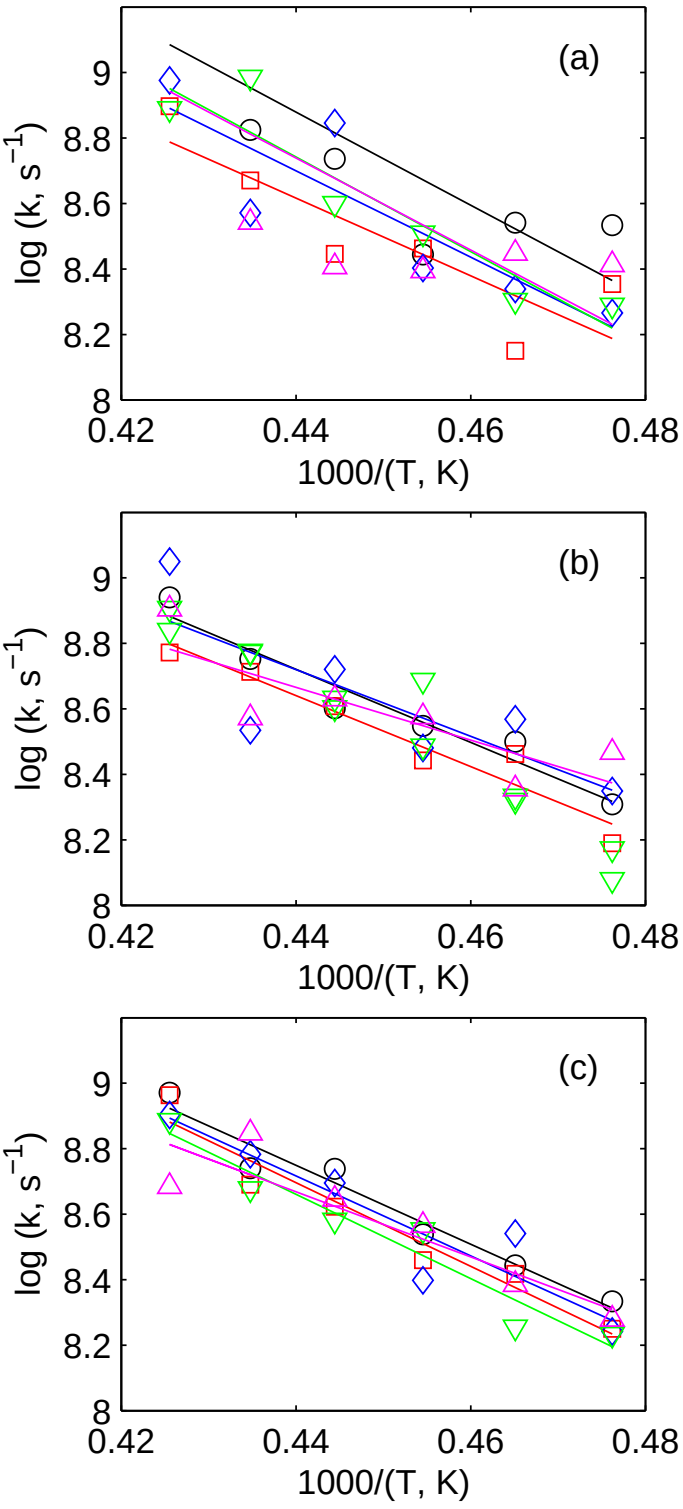

Figure 4.2. Arrhenius plots for the different sets of simulations using (a) 10, (b) 20, and (c) 40 simulations per temperature.

Table 4.1. Arrhenius parameters for each set with A measured in s^{-1} and E_A in kJ/mol with errors resulting from the linear fit.

Set #	$\log A$	$\pm \log A$	E_A	$\pm E_A$
1-10	15.1	1.8	272.1	75.0
2-10	13.8	1.2	227.0	52.9
3-10	14.5	1.4	252.6	58.8
4-10	15.1	1.0	276.6	40.9
5-10	14.9	2.7	268.8	115.5
1-20	13.6	0.5	213.6	20.7
2-20	13.4	0.5	207.6	22.6
3-20	13.2	1.4	194.9	61.6
4-20	15.1	1.0	277.3	43.1
5-20	12.2	1.0	154.4	43.0
1-40	14.0	0.5	230.3	19.2
2-40	14.3	0.6	244.5	24.0
3-40	14.1	0.9	233.7	36.6
4-40	14.3	0.6	246.0	25.5
5-40	13.0	0.8	190.4	35.3
200	14.1	0.3	233.3	12.3

The corresponding means and standard deviations are listed in Table 4.2. The variability of activation energies and pre-exponential factors within a group is significant, especially when N is small. However, the standard deviations associated with the both the activation energies and pre-exponential factors appear to become smaller with a very large number of simulations, suggesting convergence. From Table 4.1, the sets of 20 are observed to have a wider variation of pre-exponential factor and activation energy than any of the other sets, which also significantly affects the standard deviation with the sets of 20.

The activation energy (233 ± 12 kJ/mol) and pre-exponential factor ($\log A = 14.1 \pm 0.3$ s^{-1}) obtained from the full set of simulations indicates that there are additional effects allowing the polymer backbone to break with activation energies significantly lower than that of a C-C bond in PE ($\sim$340 kJ/mol) and the fundamental frequencies associated with vibrations of the C-C bonds ($\sim 10^{13}$ s^{-1}). However,

Table 4.2. Averages and standard deviations between the different data set sizes with A measured in s^{-1} and E_A in kJ/mol.

Sets	$\log A$	$\pm \log A$	E_A	$\pm E_A$
10	14.7	0.5	259.4	20.2
20	13.5	1.0	209.6	44.4
40	14.0	0.5	229.0	22.6
200	14.1	0.3	233.3	12.3

Table 4.3. Reported decomposition kinetics for HDPE.

Reference	E_A (kJ/mol)	k_0 (s^{-1})	n
[211]	268	1.0×10^{16}	0.8 - 1.4
[26]	202	7.8×10^{11}	1
[206]	253	3.8×10^{15}	0.582
[30]	347	2.5×10^{24}	1
[23]	271	2.7×10^{15}	1
[212]	370		
[1]	202 - 269	$3.6 \times 10^{11} - 4.1 \times 10^{20}$	~ 1
[31]	365	7.9×10^{14}	1
[34]	237		0.75
[213]	112 - 130	2.0×10^{13}	1
[214]	200	4.0×10^{13}	1
[28]	220	1.9×10^{13}	1
[215]	343	5×10^{16}	1

the activation energy is similar to the results obtained from some TGA as seen in Table 4.3.

It is of some interest to note, that the rate constants appear to converge somewhat faster than the kinetic parameters (Table 4.4) because of a strong correlation between activation energy and pre-exponential factor (Fig. 4.3).

4.3.2 Effects of conformational structure on the rate constants

Next, the effect of initial chain conformation on the decomposition kinetics was examined. Simulations were conducted using five independently annealed PE50 structures. The structures are identified as S-1 through S-5 (Fig 4.4). The Arrhenius plots

Table 4.4. Kinetic rate constants for initial scission rate in s^{-1} from the different sets at selected temperatures .

Set #	k_{2300K}	k_{2200K}	k_{2100K}
1-10	6.7×10^8	2.8×10^8	3.4×10^8
2-10	4.7×10^8	2.9×10^8	2.3×10^8
3-10	3.7×10^8	2.5×10^8	1.8×10^8
4-10	9.7×10^8	3.2×10^8	1.9×10^8
5-10	3.5×10^8	2.5×10^8	2.6×10^8
1-20	5.7×10^8	3.5×10^8	2.0×10^8
2-20	5.2×10^8	2.8×10^8	1.5×10^8
3-20	3.4×10^8	3.0×10^8	2.2×10^8
4-20	6.0×10^8	4.9×10^8	1.2×10^8
5-20	3.7×10^8	3.8×10^8	2.9×10^8
1-40	5.5×10^8	3.5×10^8	2.2×10^8
2-40	4.9×10^8	2.9×10^8	1.8×10^8
3-40	6.1×10^8	2.5×10^8	1.7×10^8
4-40	4.8×10^8	3.6×10^8	1.7×10^8
5-40	4.8×10^8	3.7×10^8	1.9×10^8
200	5.2×10^8	3.1×10^8	1.8×10^8

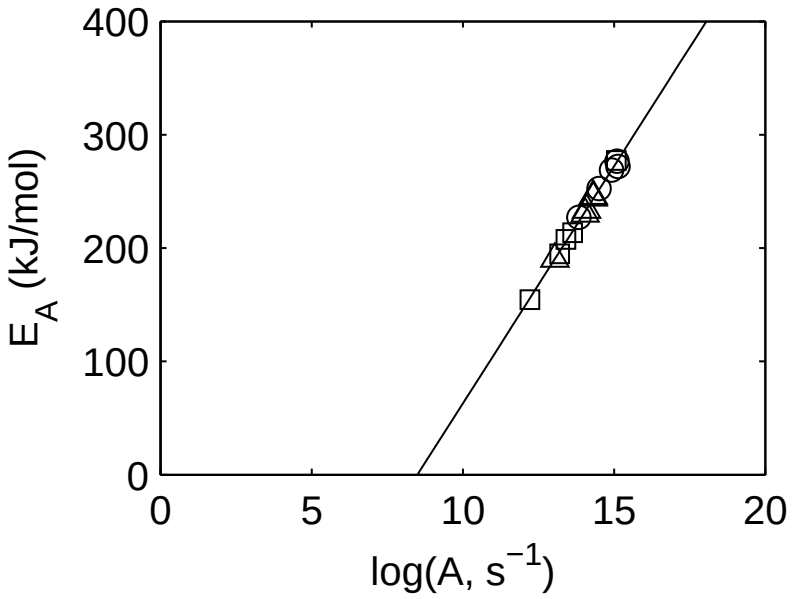

Figure 4.3. Correlation of the activation energy and pre-exponential factor for the decomposition of PE50 structures with N = 10 (○), 20 (□), and 40 (△).

Table 4.5. Effect of different structures on the scission kinetic parameters for PE50.

Structure	ρ (g/cm^3)	E_{anneal} (kJ/mol)	$\log(A, s^{-1})$	E_A (kJ/mol)
S-1	77.2	0.812	12.0	148.8
S-2	41.8	0.807	13.1	195.4
S-3	84.8	0.837	13.2	201.0
S-4	57.3	0.810	13.8	215.7
S-5	25.1	0.827	14.8	267.7
Average			13.4 $\pm$ 1.0	205.7 $\pm$ 42.7

for the initial scission reactions obtained from data collected from 20 simulations at each temperature are shown in Fig. 4.5. The kinetic parameters are listed together with the densities and the potential energies of the initial structure at the onset of the simulations in Table 4.5. The potential energy of the starting structure was obtained using the CVFF forcefield from the final minimized structure during the annealing procedure completed with Materials Studio.

The activation energies and pre-exponential factors for all of the structures fall within the expected range of the statistics compiled for the 20 simulation averages in Table 4.2. Furthermore, the mean values and standard deviations obtained from sets of simulations on chains with and without the structural variations are comparable. Thus, there does not appear to be any significant difference in the Arrhenius parameters that result from random conformational differences introduced during the annealing process.

The differences in the conformational structures of fully annealed structures are relatively minor (Fig. 4.4). In an effort to introduce more dramatic differences, we also performed RMD simulations using intermediate structures generated in the annealing process. These structures are referred to using notation, such as S-2.2, which identifies it as a not-fully annealed substructure along annealing process for S-2. The Arrhenius plots obtain from 20 simulations are shown in Fig. 4.7 and the corresponding kinetic parameters are listed along with the densities and potential energies for the initial

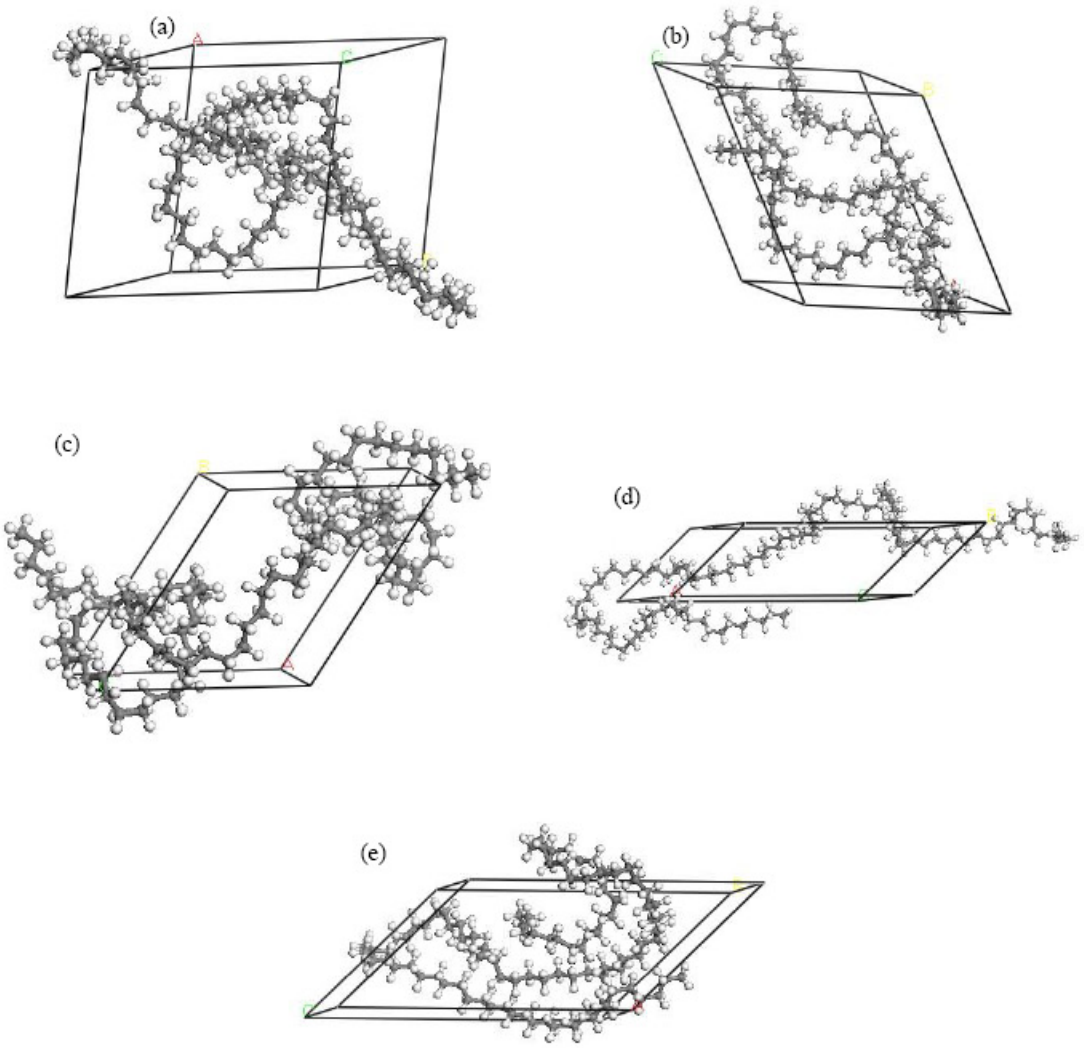

Figure 4.4. Separately annealed structures (a) S-1, (b) S-2, (c) S-3, (d) S-4, and (d) S-5.

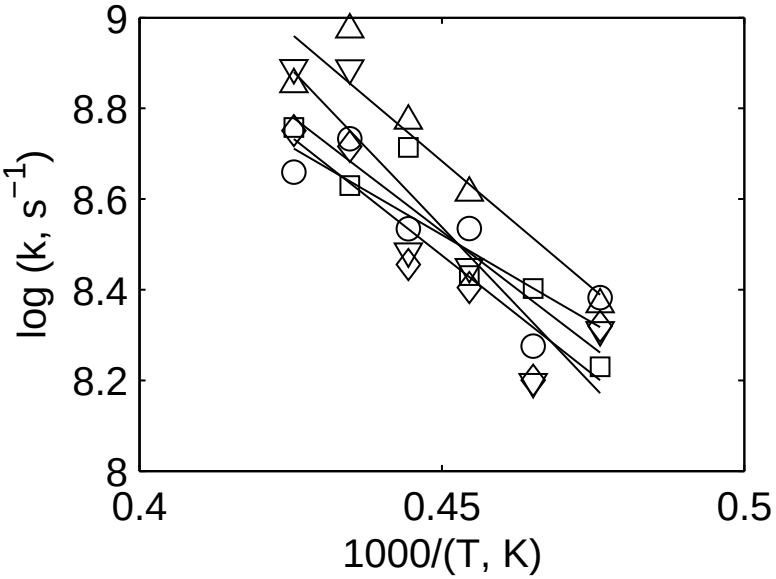

Figure 4.5. Arrhenius plots each of the different structures. Symbols are S-1 (○), S-2 (□), S-3 (◇), S-4 (△), and S-5 (▽).

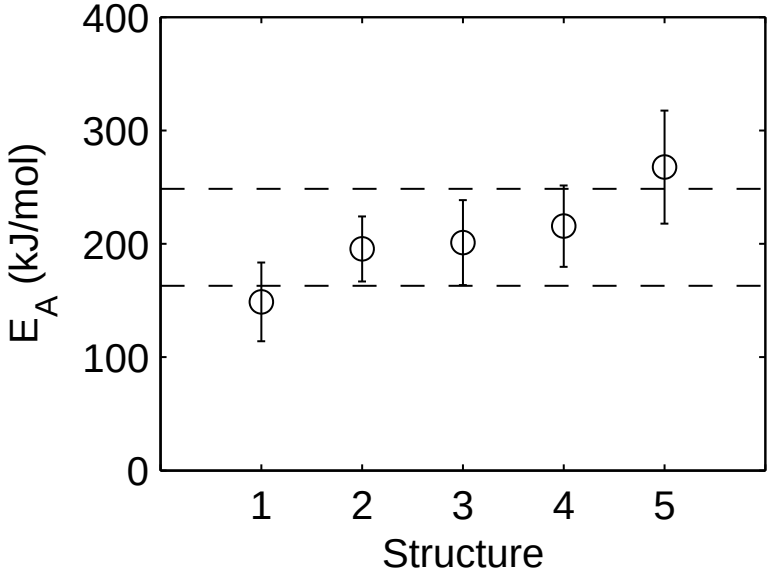

Figure 4.6. Dependence of the activation energy on the different structures.

structures in Table 4.6. Based on this admittedly limited sample, it appears that the kinetic parameters are unaffected by conformational changes unless they affect the density. In that case, the less dense polymer has an increased rate constant by a factor of two.

Table 4.6. Effect of annealing on the kinetics.

Structure	ρ (g/cm^3)	E_{anneal} (kJ/mol)	$\log A$	E_A
S-2	0.807	41.8	13.1	195.4
S-2.2	0.809	127.7	13.4	202.6
S-3	0.837	84.8	13.2	201.0
S-3.3	0.705	126.2	13.6	204.1

4.3.3 Effects of inter-chain energy transfer on the rate constants

It is also necessary to resolve whether a single chain in a periodic box represents the same conditions as multiple polymer chains entangled within a periodic box. These simulations will help resolve if the single-periodic chain can accurately represent the interchain interactions and energy transfer necessary for the description of the decomposition kinetics of the amorphous polymer melt. The simulations were conducted with three PE50 chains contained with in a single periodic simulation box. The simulations were conducted at 2200 - 2000 K, using 20 simulations per temperature. The Arrhenius plots are shown in Fig. 4.8. The kinetic parameters are $\log A$ = 13.9 $\pm$ 0.9 s^{-1} and E_A = 230.9 $\pm$ 36.7 kJ/mol. Also shown in Fig. 4.8 are the Arrhenius fit and random deviation obtained from 200 simulations per temperature on a single chain.

The fact that the decomposition kinetics of the single chain and multiple chain simulations indicates that there is no bias or additional effects in the decomposition kinetics when using a single periodic chain to represent the amorphous polymer decomposition.

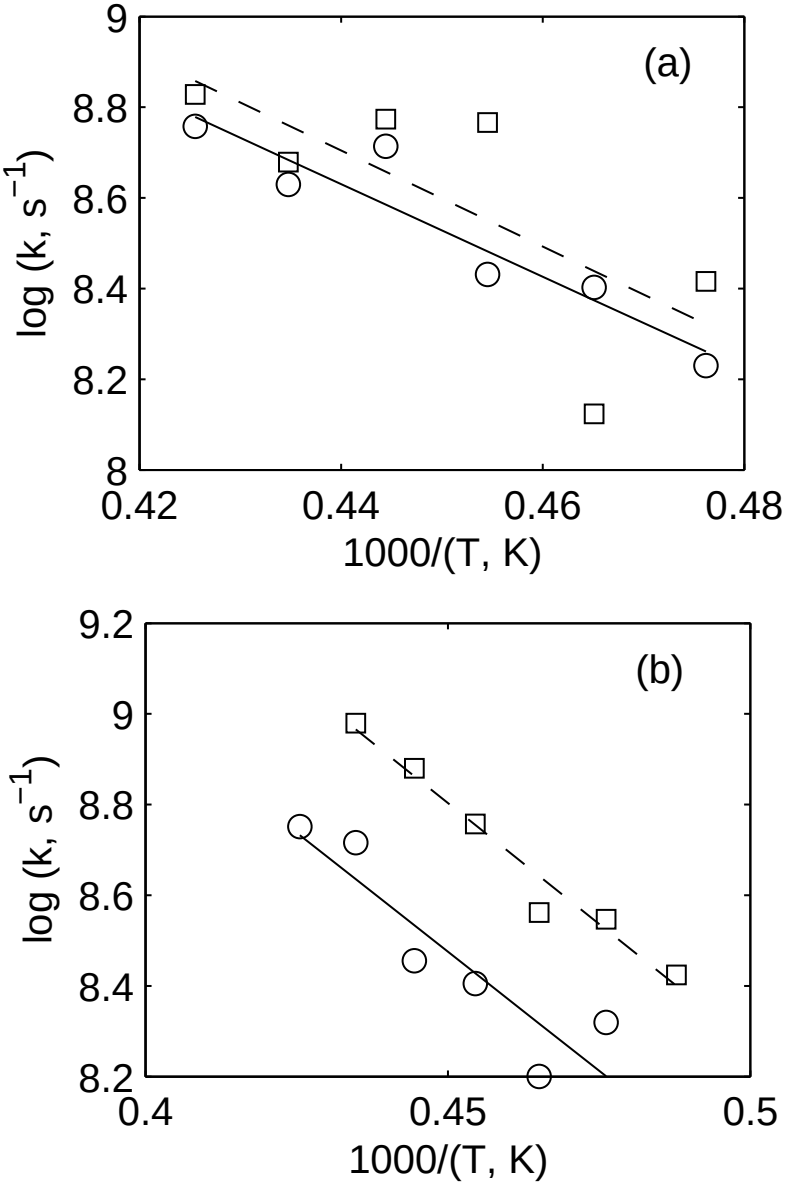

Figure 4.7. Arrhenius plots showing the effect of annealing on the decomposition kinetics using 20 simulations per temperature using (a) S-2 and (b) S-3. Circles are the fully annealed structures and the squares are the not fully annealed structures.

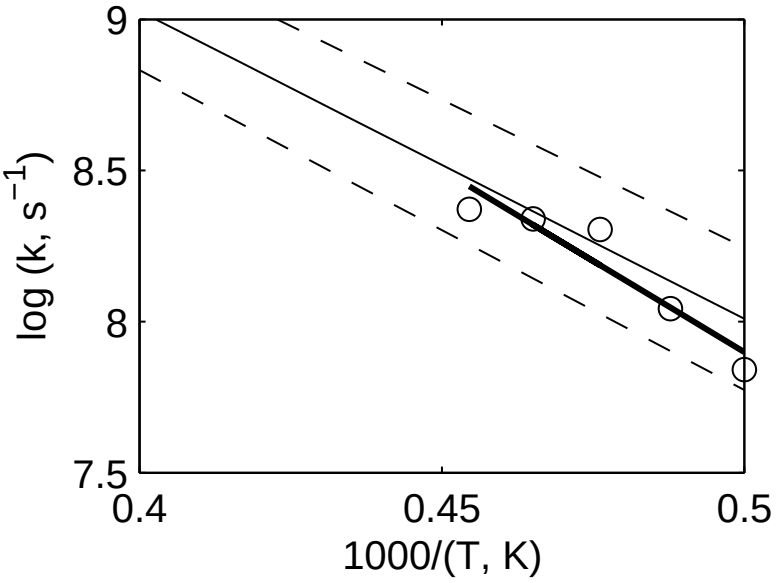

Figure 4.8. Arrhenius plot for decomposition of three entangled PE50 chains with the individual rate constants shown as circles and the fitted Arrhenius equation as the thick, solid line. The thin, solid line is the Arrhenius fit of a single polymer chain using 200 simulations per temperature, and the thin, dashed lines represent a propagation of the random error within the regression of the Arrhenius parameters.

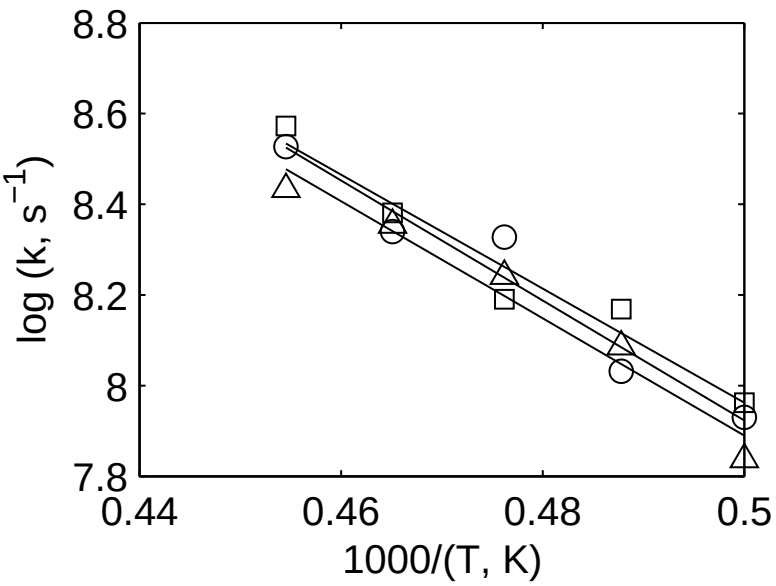

Figure 4.9. Arrhenius plot for decomposition of different PE100 structures for L-1 (○), L-2 (□), and L-3 (△).

4.3.4 Effects of chain length on the rate constants

To understand the effect of polymer chain length on bond scission kinetics, simulations were also conducted on PE chains consisting of 100 monomers. First, rate constants for initial scission reactions from three different PE100 chains (identified as L-1 through L-3) were evaluated by conducting 20 simulations at each of five temperatures (in increments of 50 K) over the range from 2200 K - 2000 K. The Arrhenius plots from these simulations are shown in Fig. 4.9, and the corresponding kinetic parameters are listed in Table 4.7.

Table 4.7. Effect of different structures on the scission kinetic parameters for PE100. A is given in s^{-1} and E_A in kJ/mol.

Structure	$\log A$	E_A
L-1	14.5	253.5
L-2	14.2	240.7
L-3	14.4	247.5
Average	14.4 ± 0.1	247.2 ± 6.4

As was noted in the case of PE50, small changes in the conformational structures of the chains do not appear to have a significant effect on the initial scission kinetics. Agreement of the values in Table 4.7 with those in Table 4.2 implies that there is no significant difference in the Arrhenius parameters between using the different polymer chain lengths. Therefore, shorter chains that capture the same trends as longer chains can also be used to appropriate model the decomposition kinetics.

4.4 Discussion

There is a decrease in the activation energies for initial scission of the polymer chains compared to C-C bond scission in small, gas-phase molecules. A similar decrease of the activation energy for initial bond scission was observed in previous investigations [3, 112, 115]. However, this investigation did not reveal a dependence of the activation energy on the polymer chain length as has been previously reported [115]. The dependence of the activation energy on the polymer chain length in the earlier MD_React simulations may be the result of small integration errors in the method used for the reactive dynamics. The increase of the number of integration errors with polymer chain length may allow the longer chains to decompose with apparently lower activation energies.

However, the decrease of activation energy with polymer chain length effect was not observed by Popov and Knyazev who performed independent RMD simulations on PE [216]. The major difference between the calculations reported in this paper and those of Popov *et al.* is that they did not employ switching functions to attenuate the angular and torsional forces on the atoms involved in the dissociating bonds. It is believed that the attenuation of angles and torsions being removed during a bond scission is crucial for a realistic description of bond scission reactions. The indirectly bonded terms can can a significant accumulation of angular and torsional strain. When bonds begin to stretch, the dissociating fragments can uncoil, alleviating part

of this strain by adapting more favorable conformations. In the absence of angular and torsional switching functions, the motion of the atoms at the ends of the dissociating polymer fragments is impeded, thereby increasing the energy barrier. Thus, inclusion of the angular and torsional switching functions allows for a stabilization of the transition state and a concomitant decrease in the activation energy for bond scission.

It should be noted further that these switching functions effectively couple the angular, torsional, and stretching modes. This can cause hot spots to develop in the vicinity of stretched bonds as the angular and torsional stress is released, resulting in premature scissions with anomalously low activation energies. However, simulations on small, gas-phase hydrocarbon chains had the appropriate activation energy, indicating that the lower activation energy is a real result of the restricted chain mobility.

Comparison of all the decomposition kinetics found from the five different PE50 structures (S-1 through S-5), the three different PE100 structures (L-1 through L-3) and the three entangled PE50 chains within a single box are shown together in Fig. 4.10. All of these different structures fall with the propagation of random error of the Arrhenius fit obtained from 200 simulations per temperature. This indicates that as the polymer chain becomes long enough, the effects become independent of chain length.

The decrease of activation energy and pre-exponential factors compared to experimental gas-phase C-C bond scission rates suggests a plausible explanation of why the values obtained from our simulations are similar to experimental TGA measurements. The lack of chain mobility within the polymer melt may be affecting the decomposition kinetics in both the simulations and the TGA experiments. Some experiments have shown a decrease in activation energy for longer chain polymers [214, 217]. Additionally, an increase in activation energy with conversion has been seen in the

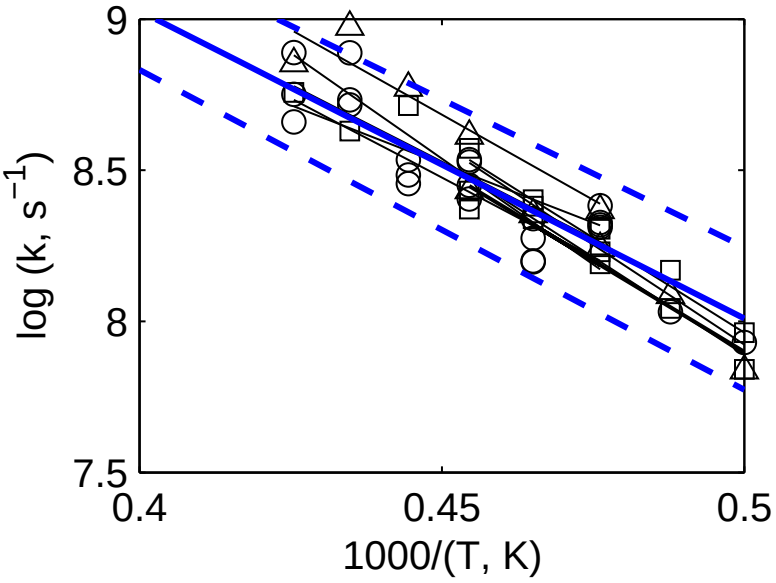

Figure 4.10. Rate constants and fitted Arrhenius parameters obtained from the five different PE50 structures S-1 through S-5, three different PE100 structures L-1 through L-3 and the three entangled PE50 chains shown as thin lines and symbols. The Arrhenius fit from 200 simulations per temperature is shown as the thick, solid, blue line with the thick, dashed blue lines the propagation of the random error associated in the regression of the Arrhenius parameters.

analysis of TGA experiments [26], although other results have shown activation energy to be independent of conversion [30]. However, it is difficult to draw conclusions of the overall decomposition based solely on the initial bond breakage. Effects such as hot-adduct decomposition pathways, surface effects on decomposition kinetics, and volatile molecule diffusion to the surface are not included in these calculations. Because the average chain length decreases during decomposition, there is the possibility of an increased activation energy as the chains become shorter. This process continues until the resulting fragments are small enough to volatilize, making the last scission potentially rate determining.

4.5 Conclusions

Reactive Molecular Dynamics simulations were conducted to examine the effects of conformational structure and degree of polymerization on the rate of scission reactions thought to initiate the thermal decomposition of polyethylene and other polymers. The calculations were performed using a new program, RxnMD, that incorporates an extension of the MM3 forcefield (RMDff) to enable realistic descriptions of molecular forces accompanying chemical transformations.

The statistics necessary to obtain quantitative chemical kinetics were investigated. It was found that a minimum of 20 simulations at each temperature was needed to obtain reliable kinetic parameters. Minor differences in the chain conformation did not have a detectable effect on the reaction kinetics.

CHAPTER 5

DECOMPOSITION MODEL OF HIGH-DENSITY POLYETHYLENE

5.1 Introduction

There are many different effects to be considered in condensed-phase polymer decomposition. The lack of polymer mobility can inhibit the ability of the polymer to rearrange and relieve stress. The condensed phase significantly changes the energy transfer mechanisms, which likely allows for more efficient and continuous energy transfer throughout the melt. These kinds of effects can easily make gas-phase kinetics an inappropriate model for polymer decomposition. In this chapter, different effects on polymer decomposition are investigated including effects of side groups and β-scission kinetics. In order to determine the energy concentration effects on polymer decomposition, the overall RMD decomposition is simulated. Finally, the microscopic kinetic rates for bond scission and β-scission are compared to overall macroscopic decomposition via Kinetic Monte Carlo.

5.2 Reactive Simulation Methods

5.2.1 RMD Calculations

Polyethylene chains consisting of 50 (PE50) repeat units (-CH_2-CH_2-) were considered. Simulations were also conducted using polyethylene chains consisting of 5 monomers (decane) in the gas phase and as 10 entangled chains (10PE5). Polymers consisting of 50 repeat units with propylene monomer (PP50) and tetrafluoroethylene (PTFE). The chains were terminated by hydrogen atoms (i.e., methyl groups at the

ends of the chains), except for PTFE, which used fluorine atoms. Periodic boundary conditions (PBC) were employed in all condensed-phase simulations.

The RMD simulations were conducted at a constant volume and temperature (NVT) using the RMDff reactive forcefield method [193] described in Chapter 3. The temperature was controlled by velocity scaling. The lowest temperature used for each simulation was dictated by the need for reactions to occur within a reasonable amount of computer time (about 60 hours on an Opteron 240 64-bit processor). The hydrogen/fluorine atoms were explicitly included in the simulations. Further details about the annealing process and simulation conditions are provided in Sec. 2.4.2.

5.2.2 Simulated TGA Calculations

Thermal decomposition was also simulated using Kinetic Monte Carlo. Polymer chains were allowed to decompose using the kinetic rates determined from the RMD simulations. As each reaction occurs, the temperature was incremented according to the temperature ramp in order to approximate TGA experiments. The KMC simulations began with 100 HDPE chains of 140,000 daltons each. Any chain containing 10 or fewer carbon atoms was assumed to be volatile, and this segment was immediately removed from the simulation. For C-C bond scission, the rate equation was $k_{CC} = 1.26 \times 10^{14} \exp(-233.3/RT)$, and for C-C-C β-scission reactions the rate equation was $k_{\beta s} = 7.94 \times 10^{13} \exp(-153.5/RT)$. No other reactions were considered in the KMC simulations.

5.3 Scission Reactions

5.3.1 Effects on Backbone Scissions

Decomposition kinetics were investigated with RMD for gas-phase decane. The simulations consisted of a single decane molecule in a periodic box with non-reactive hydrogen atoms or argon atoms. The Arrhenius plot of the decomposition is shown

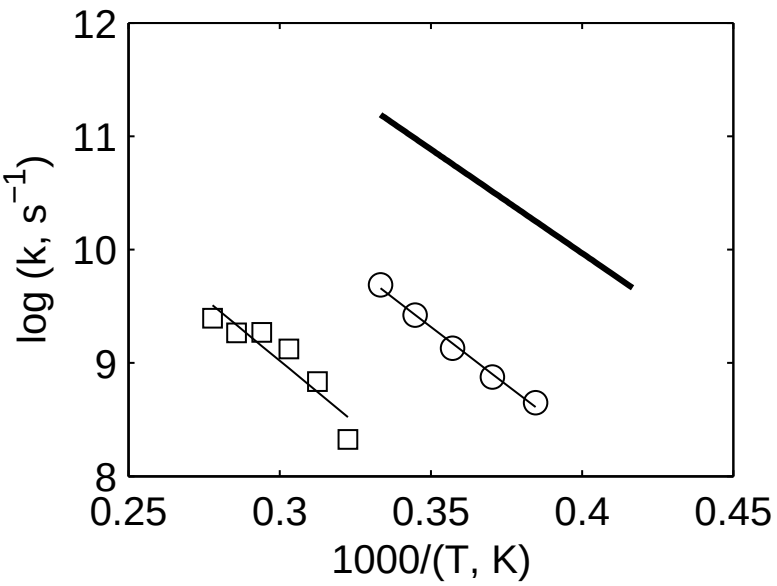

Figure 5.1. Arrhenius plot for the decomposition of decane using a bath gas of non-reactive hydrogen atoms (circles) and argon (squares), compared to the *ab initio* predicted high-pressure-limit decomposition of decane (thick line).

Table 5.1. Arrhenius parameters for gas-phase decane decomposition.

	E_A (kJ/mol)	A (s^{-1})
Ref. [218]	351	2.0×10^{17}
Non-Reactive H atoms	391	2.95×10^{16}
Argon	422	4.24×10^{15}

in Fig. 5.1, and the Arrhenius parameters are given in Table 5.1. While the RMD pre-exponential factors are less than the *ab initio* calculated pre-exponential factor, the activation energies agree. Because the van der Waals forces can significantly affect the energy transfer, the scission reaction rate would be affected if the van der Waals repulsive interaction was incorrect. However, the ability of the RMD simulations to predict the correct activation energy indicates that the entire bond energy must be accumulated prior to reaction, implying that there are no additional energy sources for the bond scission.

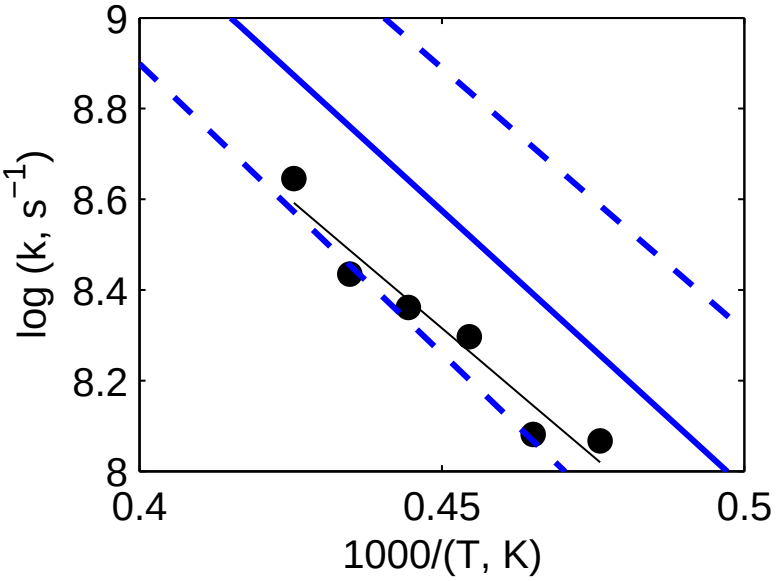

Figure 5.2. Arrhenius plot of 10 entangled PE 5 chains (10PE5) decomposition shown as the circles and thin line compared to the decomposition of PE50 (thick line) and the 1σ random error associated with the rate constants (dashed lines).

Because polymer decomposition kinetics were not observed to depend on chain length, the kinetics were also investigated for 10 entangled PE5 (decane) chains at the condensed-phase density. These chains also have the same decomposition kinetics as the PE50 chains with $E_A = 216$ kJ/mol and $A = 2.51 \times 10^{13}$ s^{-1}. The Arrhenius plot is shown in Fig. 5.2. The similarity of the results between the 10 entangled PE5 chains and PE50 chain indicates that the significant change in decomposition kinetics is likely a condensed-phase effect affecting the kinetics.

In HDPE, the polymer can be effectively represented as a tube, without any significant effects of the hydrogen atoms on the polymer mobility. In order to determine the side-group effect on the backbone decomposition kinetics, a comparison is made between PE50 and PP50. Although the methyl group is a relatively small side group compared to other bulky side groups, a slight increase in the backbone decomposition rate is observed in Fig. 5.3. However, compared to the estimated random errors in the

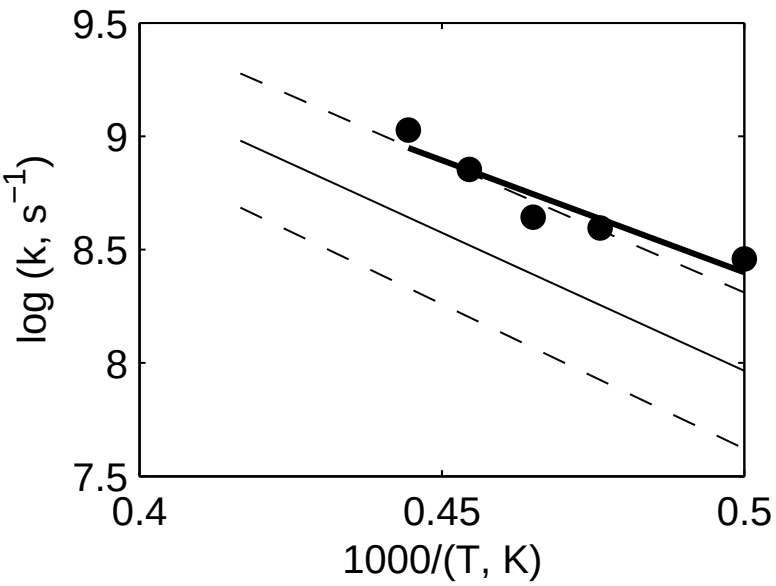

Figure 5.3. Arrhenius plot of backbone decomposition of PP50 (cirlces, thick line) compared to the backbone decomposition of PE50 (thin line).

PE50 Arrhenius parameters, the PP50 decomposition is on the boundary of the 1σ random error, making it difficult to determine if the results are significantly different. The effect may become more pronounced with larger, bulkier side groups.

Polyethylene and poly(tetrafluoroethylene) (PTFE) are isoelectronic structures as far as bonding, where all the hydrogen atoms in PE are replaced by fluorine atoms in PTFE. This change in chemical structure results in remarkably increased fire resistance for PTFE compared to PE. The objective is to understand how these seemingly simple exchanges are manifested in the dramatically different fire resistance of the two polymers.

Additional parameters were required for the reactive modeling of fluorinated species. The meshed MM3-quartic-Morse potential parameters are given in Table 5.2. The meshed MM3-Morse van der Waals potential parameters are given in Table 5.3. The MM3 angular parameters for fluorine-radical carbon-fluorine angle required reparam-

Table 5.2. Parameters for Transition from MM3 Quartic to Morse Bonding Potential for fluorinated species.

Bonded Pair	D_E (kJ/mole)	α (nm^{-1})	r_e (nm)	r_s (nm)
c - c	421.2	16.46	0.152	0.167
c - f	534.0	16.84	0.139	0.153
cr - f	600.3	14.94	0.135	0.151

Table 5.3. Parameters for Morse-type van der Waals meshed potential for BHDB-PA.

Atom Pair	D (J/mol)	b	r_e (nm)	r_s (nm)
c - c	623.4	4.754	0.372	0.205
c - f	34020	2.499	0.302	0.150
f - f	36360	2.788	0.275	0.140

eterization because the MM3 parameters incorrectly formed a planar FCF radical. The revised parameters are $k_\theta = 1.375\ mdyne\ \AA/rad^2$ and $\theta_0 = 111.36\ ^\circ$.

Although, the backbone scission in PTFE is only a C-C scission, the switching functions obtained from ethane under predicted the energy at intermediate separation distances. Therefore, new parameters were determined for the C-C scission in PTFE using C_2F_6. The RC parameters are $m = 3.846\ nm^{-1}$ and $b = -0.6538$. The switching function parameters are $a_1 = 7.463$, $RC_{0,1} = 0.3704$, $a_2 = 6.498$, $RC_{0,2} = 0.3703$, and $E_{base} = 395.4$ kJ/mol.

Because PTFE in a simple sense just has a bulkier side atom compared to PE, simulations were conducted to capture these effects. Therefore, the PTFE decomposition is modeled using four different cases to build from PE to PTFE. Each case is identified by its name and a description is given below.

1. PE - This is a standard 50 repeat-unit chain of PE.

Table 5.4. Arrhenius parameters for changes from PE to PTFE with A measured in s^{-1} and E_A in kJ/mol with 1σ errors resulting from the linear fit.

Set #	$\log A$	$\pm \log A$	E_A	$\pm E_A$
PE	14.1	0.3	233.3	20.2
Strong PE	13.2	0.7	244.5	37.6
Heavy PE	13.6	1.1	225.1	46.8
PTFE	14.4	1.5	307.5	75.8

2. Strong PE - This is a PE chain that has C-C bond strength increased from 370 kJ/mol to 421 kJ/mol to reflect the change in C-C bond strength in fluorinated species.

3. Heavy PE - This is a PE chain that has the mass of the hydrogen atoms changed from 1 g to 18 g to reflect the change from H to F.

4. PTFE - This is a fully annealed 50 repeat unit structure of PTFE.

The kinetics for the initial backbone scission of each case is shown in Fig. 5.4. The Arrhenius parameters from each case are given in Table 5.4. The change from PE to Heavy PE more slightly decreases the rate of backbone scission. The heavier "hydrogen" atoms can absorb more energy from collisional processes that require additional energy to be transferred for a reactive event to occur. The change from PE to Strong PE is observed to decrease the kinetic rate of initial backbone scission dramatically. This results from the additional force exerted by the stronger C-C backbone exerts on the structure, making it more stable. Finally, combining these effects into the overall PTFE structure results in a similar initial backbone scission rate to the Strong PE, indicating that the increased bond strength played a significant role in the decomposition kinetics.

Dramatic changes in the decomposition kinetics were observed from the isoelectronic change from hydrogen to fluorine in PE to PTFE. The kinetic rate constants decreased dramatically, causing the decomposition to occur at much higher tem-

peratures. Extrapolating the initial backbone scission rate from PE and PTFE at simulation conditions to typical decomposition conditions results in a large difference in the relative rates as seen in Fig. 5.5. The effect on the kinetics does not include any quantum chemical effects. The gas-phase scavenging activity of halogen atoms [7–10] is also not captured from these simulations. These provide additional means which could further increase flame resistance, which are not included in the model. Even without explicit inclusion of these effects, a portion of the flame resistance in PTFE is revealed through the changes in both C-C bond strength and increased mass of the side-group atom (fluorine).

5.3.2 Side-group scissions

The assumption has been that the side-group scission rate is significantly less than that of the backbone polymer scission rate. Because individual reaction events are not coupled [150], this assumption allows reactions involving the side groups to be excluded from the simulations. The effects of the hydrogen scission in PE and methyl group and hydrogen scission in PP are investigated to determine the overall decomposition rates of these side groups.

The C-H scission rate in PE was investigated, without allowing the C-C bonds to break. The Arrhenius plot of the C-H kinetics is shown in Fig. 5.6 compared to the C-C scission kinetics. The Arrhenius fit results in $E_A = 468.6$ kJ/mol and $\log A = 16.9$ s^{-1}. These Arrhenius parameters compare very closely to gas-phase C-H bond scission rates in ethane, where $E_A = 410$ kJ/mol and $\log A = 16.1$ s^{-1} [219]. The similarity of the C-H scission kinetics between the gas-phase ethane and condensed-phase polymer indicates that the polymer stress or condensed-phase effects do not affect the C-H bond, which allows it to respond in a manner similar to gas-phase kinetics. This effect would indicate that the PE polymer can be treated as a tube, where hydrogen atoms do not hinder the motion of the chain, and the overall

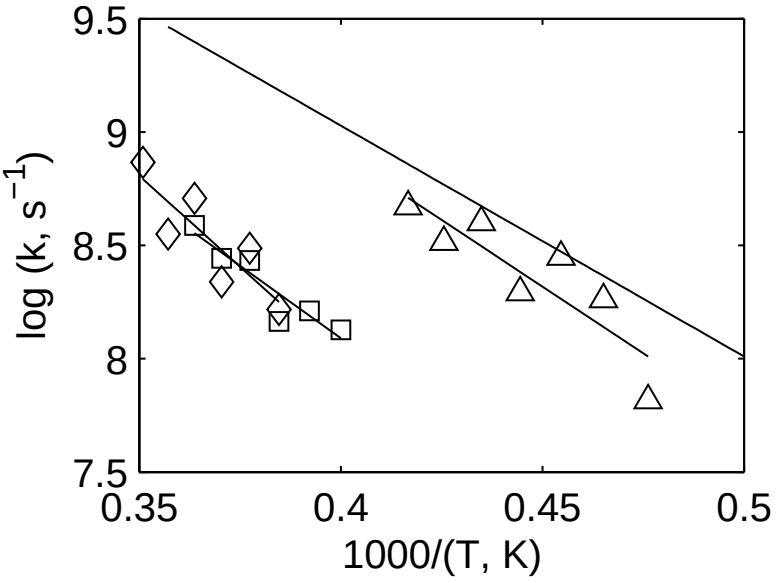

Figure 5.4. Arrhenius plot of initial backbone scission for 50-repeat unit polyethylene (line), heavy polyethylene (△), strong polyethylene (□), and PTFE (◊).

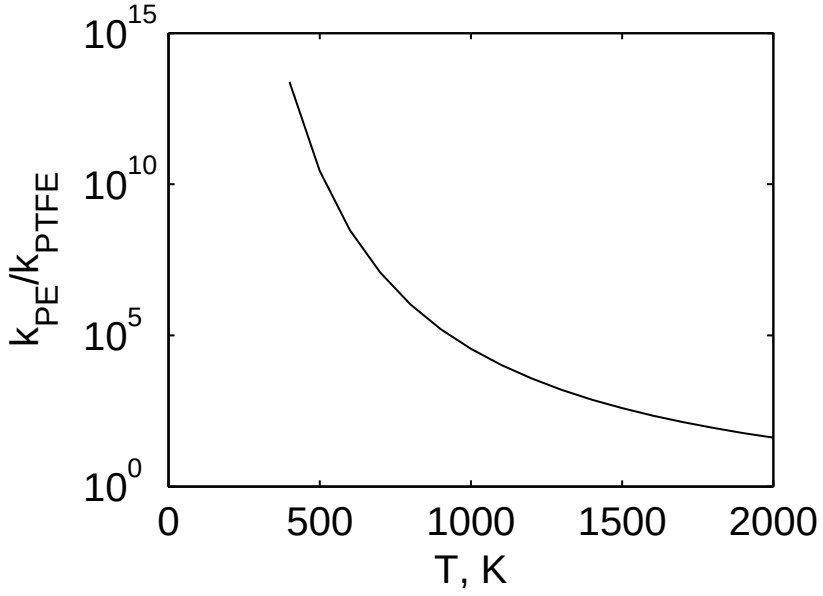

Figure 5.5. Ratio of initial backbone scission rates between HDPE and PTFE.

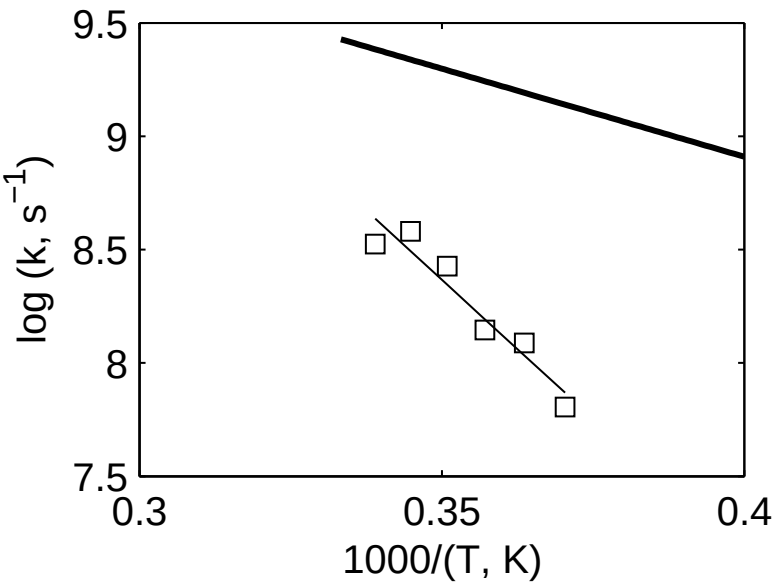

Figure 5.6. Arrhenius plot for C-H scission in PE50 shown as squares and fitted Arrhenius parameters as the thin line. The thick line is the PE50 C-C scission decomposition rate.

chain motion is the main effect resulting in the increased decomposition rates. This also allows the C-H bond scission to be neglected within the simulations, especially at normal decomposition temperatures as shown in Fig. 5.7. However, using unified CH_2 atoms may still be unacceptable because explicitly inclusion of the C-H bonds provides a means for energy accumulation via bonds, angles, and torsions. This accumulation likely contributes in some manner to the backbone scission reaction. Therefore, using united atoms could significantly change the backbone scission kinetics along with other associated reaction rates.

For polypropylene, there is a methyl side group that can hinder polymer mobility. Simulations were also conducted allowing just the side group to scission in order to determine the stress associated with the methyl side group. The Arrhenius plot is shown in Fig. 5.8, which reveals the methyl side group to have the same scission kinetics as the C-C backbone in polypropylene. Therefore, the methyl side group

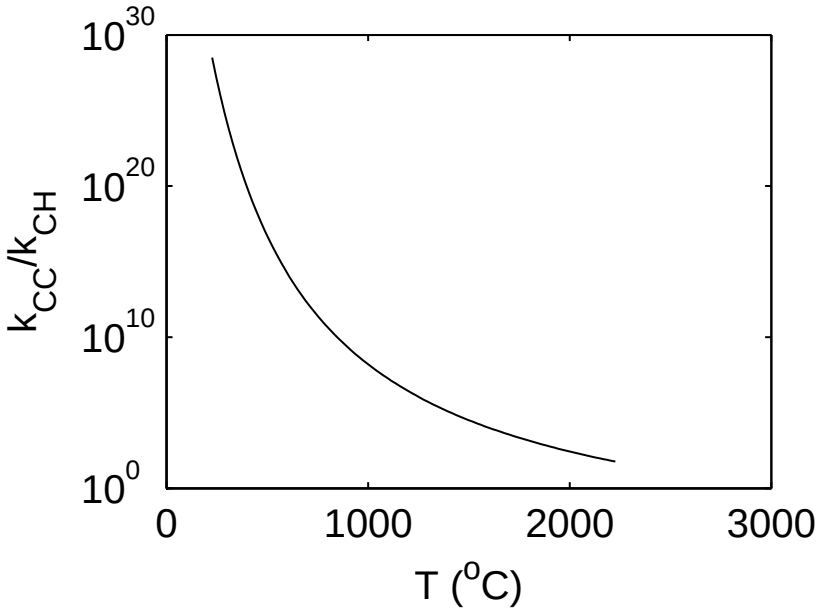

Figure 5.7. Comparison of the rate constants for C-C and C-H scission reactions as a function of temperature.

in polypropylene experiences the backbone stress. These results indicate that the polypropylene stress and kinetics may be different that polyethylene.

5.3.3 Allylic/Weakened-Bond Decomposition

It has been hypothesized that weaker allylic bonds formed during the polymer decomposition could result in the reduced activation energies observed in the experimental decomposition of PE. The allyl bond occurs when a double bond is formed within a hydrocarbon polymer. The allyl bond is located as the β-bond to the double bond. These weaker bonds have a bond dissociation energy around 290 kJ/mol, compared to the typical value of 350 kJ/mol for C-C bonds. A depiction of the molecules are shown in Fig. 5.9.

Comparison of allylic bond decomposition was first investigated using small molecules. The decomposition kinetics for decene in argon and 10 entangled, condensed-phase PE5 (decene) chains is shown in Fig. 5.10(a). In these models, the double bond and

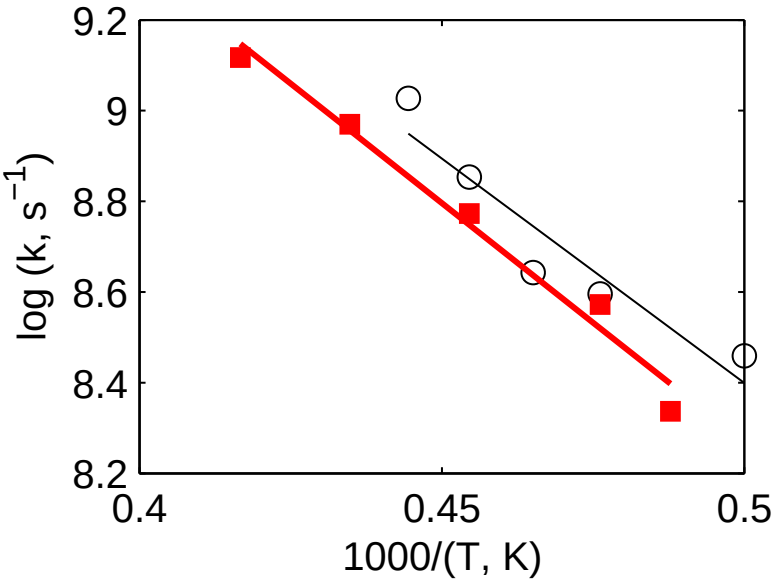

Figure 5.8. Comparison of PP50 decomposition for the backbone (circles, thin line) to the side group C-C scission (squares, thick line).

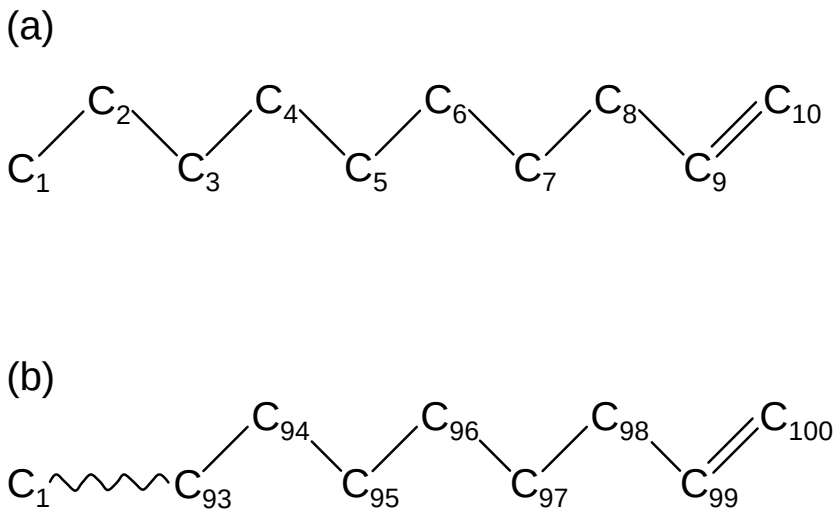

Figure 5.9. Bonding with the allylic molecules for (a) PE5 with the allylic bond between carbons 7 and 8 and (b) PE50 with the allylic carbon between carbons 97 and 98.

vinylic bonds were not permitted to break due to their higher strengths compared to the other bonds in the molecule. The decomposition of decene in argon does not demonstrate a significant deviation from the decomposition of decane in argon. However, the 10 entangled decene chains demonstrate a significant increase in the decomposition rate. This increase in kinetic rates could be due to the condensed-phase effect being magnified by the weakened bond. In these simulations, the lack of mobility to relieve molecular stress and the constant contact allowing for continuous energy transfer may result in further increases in the bond decomposition. A comparison was also made of allylic bond decomposition in condensed-phase PE50. Again, the double bond and vinylic bonds were not allowed to break. The decomposition kinetics of PE50 with an allyl bond is shown in Fig. 5.10(b). In this case, there does not seem to be any significant change in the decomposition kinetics. The lack of change in decomposition kinetics for the PE50 compared to the condensed-phase decene simulations may result from the significant number of other backbone bonds that can break within the polymer. Therefore, even a series of several entangled longer polymer chains may not demonstrate a significant difference in the decomposition rate because the overall concentration of allyl bonds would still be relatively low.

In fact, the allyl bond is observed to break quite frequently in the decene molecules compared to the PE50 compared to all the other single bonds present (excluding the vinyl bond) as shown in Fig. 5.11 for 50 simulations per temperature. Additionally, the number of allyl bonds breaks found for all simulations are tabulated in Table 5.5. The rates of allyl bond breakage compared to all other bonds is consistent between simulations using 20 and 50 simulations per temperature. Therefore, it appears that allyl bond decomposition likely does not contribute significantly to the polymer decomposition until possibly very late, when only very small molecules remain.

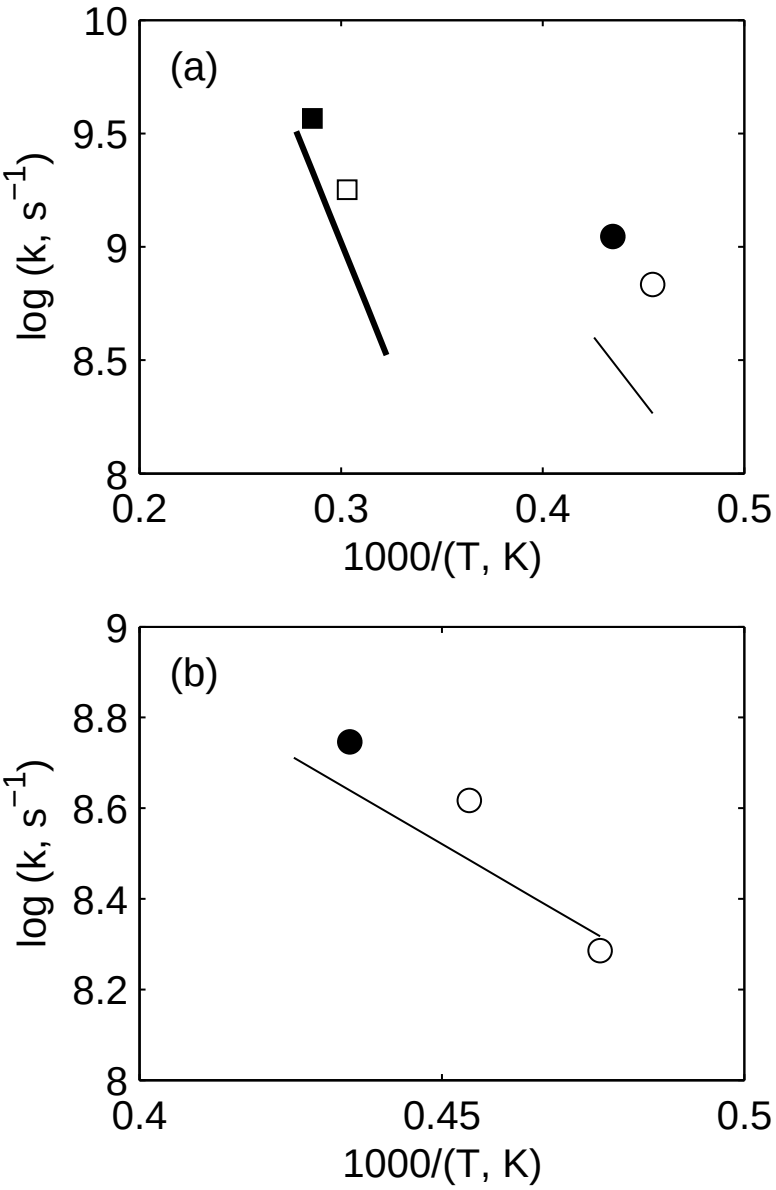

Figure 5.10. Decomposition kinetics of allylic molecules, where the filled symbols represent 50 simulations per temperature and open symbols represent 20 simulations per temperature. The lines represent the Arrhenius kinetics determined from the non-allylic version of the same chain. (a) PE5 with Ar (thick line and squares) and 10 PE5 chains (thin line and circles) (b) PE50

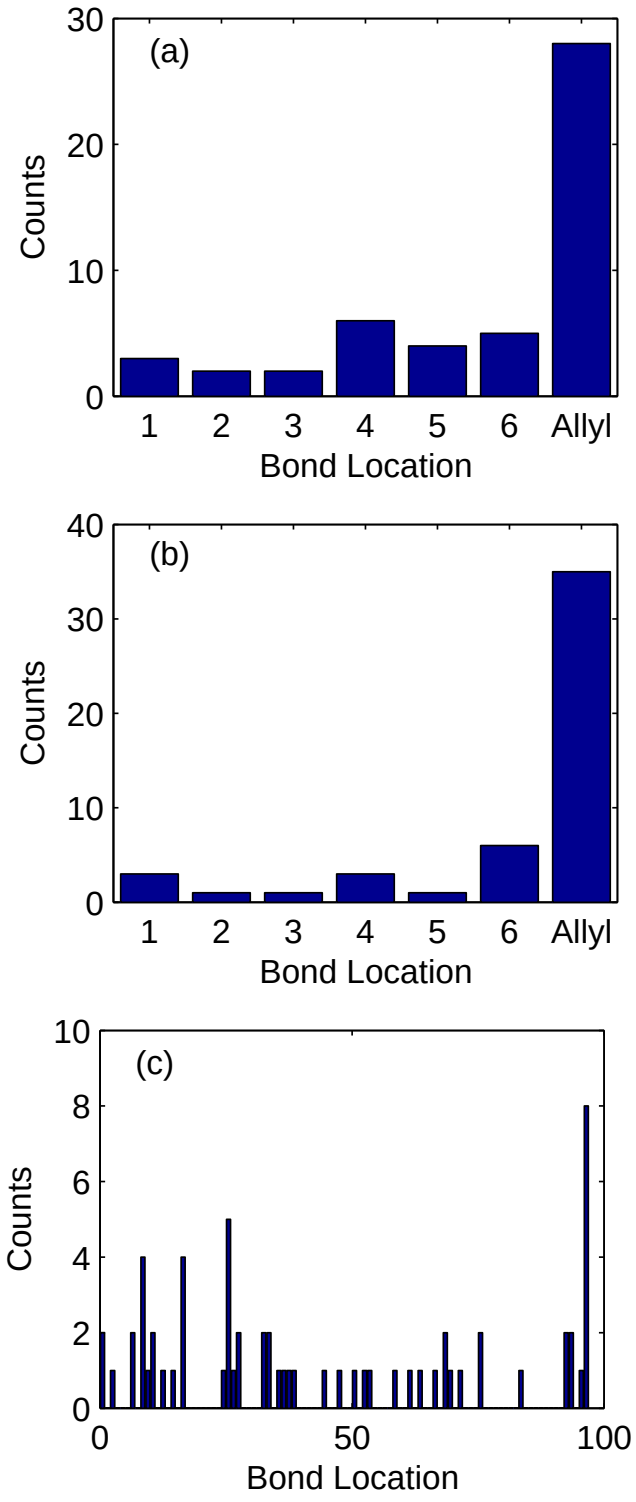

Figure 5.11. Location of bond scission reactions occurring from 50 simulations on (a) PE5 in Ar at 2900 K, (b) 10 PE5 chains at 2000 K, and (c) PE50 chain at 2000K.

Table 5.5. Numbers of Allylic bond breakages in different simulation cases.

System	Temperature	Number of Allylic Breaks
PE5 in Ar	3500	28/50
	3300	12/20
10 PE5 chains	2300	35/50
	2200	13/20
Single PE50 chain	2300	8/50
	2200	2/20
	2100	1/20

5.4 β-scission Kinetics

The β-scission reaction has been inferred to be a dominant route in many polymer decompositions. In this scenario, once the backbone scission reaction occurs, the polymer unzips to form monomer units, making a π-bond from the bond α (next to) the original radical site and breaking the β-bond (second bond from the radical site, moving the radical to the chain end).

The β-scission reaction rate was investigated in PE50 using by forming a structure containing a radical at the end of the chain and another structure with a radical in the middle of the chain. Each simulation was allowed a velocity thermal-equilibration period prior to reactive dynamics. The C-C-C and C-C-H kinetic rates are shown in Fig. 5.12. The Arrhenius parameters are given in Table 5.6. The appropriate ratio of C-C-C to C-C-H β-scission reactions were observed when the two reactions were allowed to compete. It was also observed that except for the C-C-C β-scission reaction occurring in the middle of the polymer, the reaction rates are similar to gas-phase β-scission rates. The C-C-C β-scission reaction in the middle of the polymer is again affected by the polymer strain. The C-C-H β-scission reaction occurring in the middle of the polymer chain does not reveal as significant a difference. Releasing a hydrogen atom during the β-scission reaction does not significantly relieve the stress within the polymer.

It should also be noted that at equilibrium, the relative rate of the β-scission scission reaction to the backbone scission reaction is similar due to the number of potential C-C scission sites. Therefore, as the equilibrated polymers are considered as increasingly longer, the β-scission reaction rate in terms of reactive sites per second would become much smaller than the C-C scission rate in terms of reactive sites per seconds at high temperatures. However, such a comparison will likely not hold at normal decomposition temperatures.

Even though the C-C-C β-scission reaction rates for the sites in the middle of the polymer are faster than for the radicals at the end of the polymer, radicals may not be likely to develop in the center of the polymer. Radicals forming in the middle of the polymer without a backbone scission from scission reactions would involve the very slow C-H scission reaction. The other way of producing radicals in the middle of the polymer chain without backbone scission would be from hydrogen abstraction reactions, which have not been investigated here. Therefore, β-scission reactions would not provide a dominate path for HDPE decomposition.

Table 5.6. Effect of different structures and radical locations on the β-scission kinetic parameters. A is given in s^{-1} and E_A in kJ/mol.

Structure	$\log A$	E_A
PE50 C-C-C End Radical	13.9	153.5
PE50 C-C-C Mid Radical	13.5	116.1
PE50 C-C-H End Radical	13.7	188.3
PE50 C-C-H Mid Radical	14.2	201.3

5.5 Volatilization Kinetics from RMD Simulations

In order to investigate the overall decomposition of HDPE from RMD simulations, a single PE50 chain in a periodic box was simulated for 100 ps at 2150, 2200, 2250, and 2350 K. The decomposition products containing 10 carbon atoms and fewer were

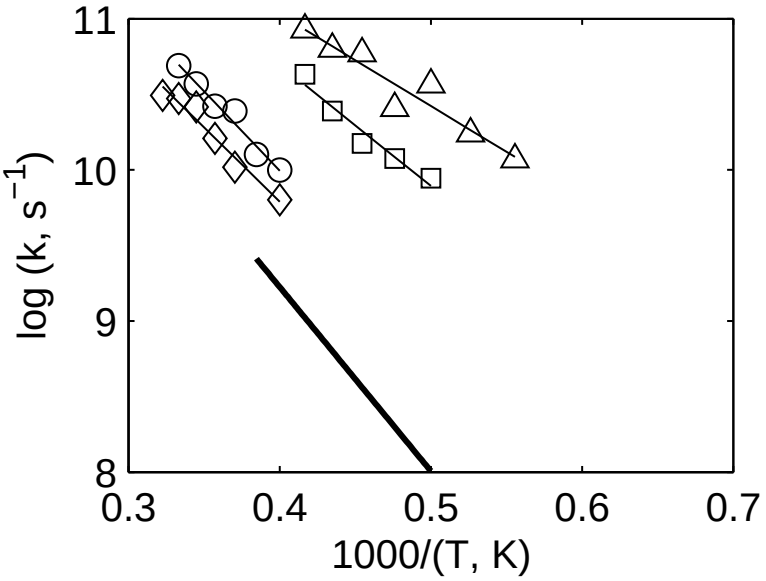

Figure 5.12. Arrhenius kinetics for C-C-C β-scission occurring at the end of a PE50 chain ($\square$) and at a random location in the middle of the chain ($\triangle$) and for C-C-H β-scission occurring at the end of a PE50 chain ($\circ$) and at a random location in the middle of the chain ($\Diamond$).

assumed volatile. The value of 10 carbon atoms was based on the fact that the majority of components have been reported as 10 carbon atoms or smaller [22, 33, 34, 210], although larger distributions are possible [33, 220]. Simulations were tracked for either the full 100 ps or until 20% of the polymer was volatile in order to maintain low conversion. Scission, recombination, and β-scission reactions were allowed to occur during the simulation. The decomposition rate constants were calculated as:

$$k_v = \frac{\sum_{N_{traj}} m_v}{m_i \sum_{N_{traj}} t} \tag{5.1}$$

where m_v is the mass of volatile products, m_i is the initial mass of the polymer, and t is the total simulated time until either greater than 20% conversion was obtained or the simulation had reached 100 ps of reactive simulation time.

The calculated volatilization rate constants are shown in Fig. 5.13. The Arrhenius parameters for volatilization kinetics are $E_A = 388$ kJ/mol and $A = 1.29 \times 10^{18}$ s^{-1}. These decomposition kinetics are similar to the results typically seen for C-C bond scission in gas-phase chemistry, despite the very low activation energies observed for polymer decomposition kinetics. For comparison, the decomposition of gas-phase decane is also shown in Fig. 5.13. The high activation energy may be a function of the slow rate at which volatile products are produced. Even though the polymer can scission at an increased rate, several scission and β-scission reactions are necessary for significant volatile products to be realized. Therefore, while an individual reaction may have a much lower decomposition rate, the overall rate may be significantly slower. These effects may be more accurately captured in Kinetic Monte Carlo simulations of overall polymer decomposition kinetics.

A still frame shot from the starting structure and the decomposition from one simulation at 2200 K is shown in Fig. 5.14. The decomposition products realized at the end of the simulation were are shown in Fig. 5.15. There is a wide distribution of volatile products determined in a relatively short time. It is also noted that a sig-

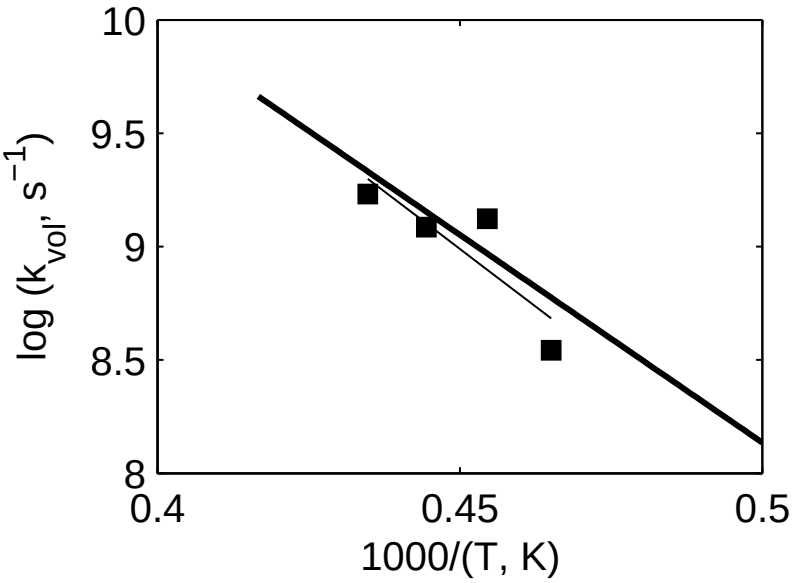

Figure 5.13. Volatilization kinetics of PE50 and fitted Arrhenius equation (black squares; thin line) compared to the gas-phase *ab initio* calculated decomposition kinetics of decane.

nificant portion of the products are relatively long radical chains that require further decomposition to become volatile products. Cyclic species were also observed. A few very large cyclic molecules were observed; however, some small C_4-C_6 cyclic species are also formed during the simulations. Additionally, the strong temperature dependence on overall decomposition is also observed in the product distribution. As the simulation temperature is decreased to 2150 K, significantly fewer overall molecules are observed from the simulations.

The simulations did reveal the ability for recombination reactions to occur. The distribution of recombination times is shown in Fig. 5.16. In Fig. 5.16(a), only the time required for the scissioned bond to reformed was tracked. In Fig. 5.16(b), the time required for any recombination reaction to occur was tracked, where the time was determined from the point where both of the recombining atoms were radicals

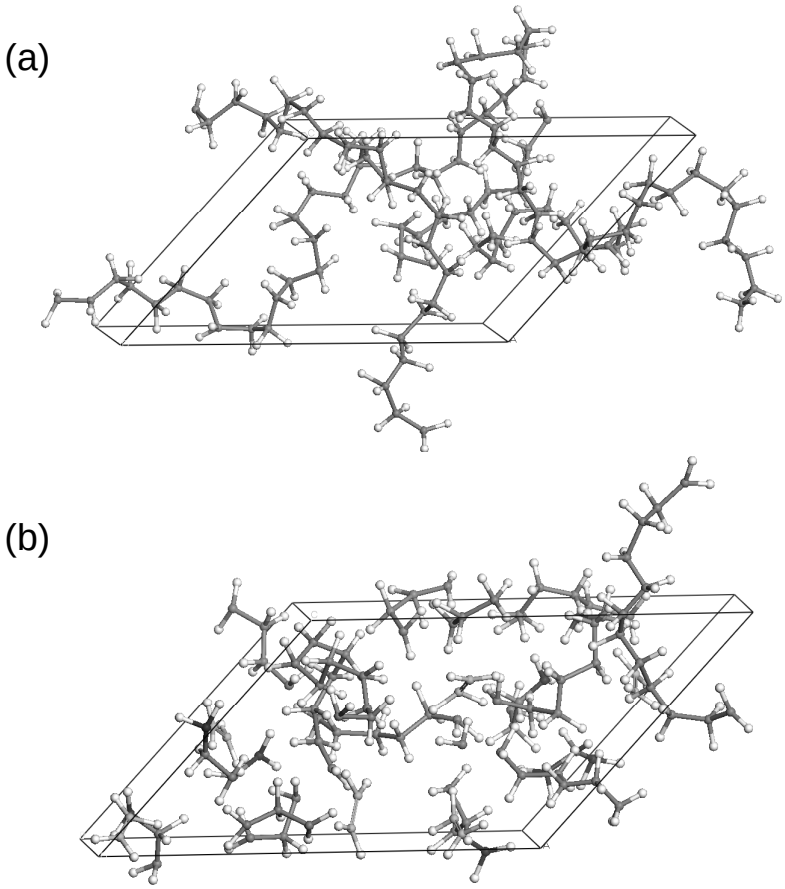

Figure 5.14. Polymer at (a) the start of the reactive dynamics and (b) after 100 ps of reactive dynamics for a simulation at 2200 K.

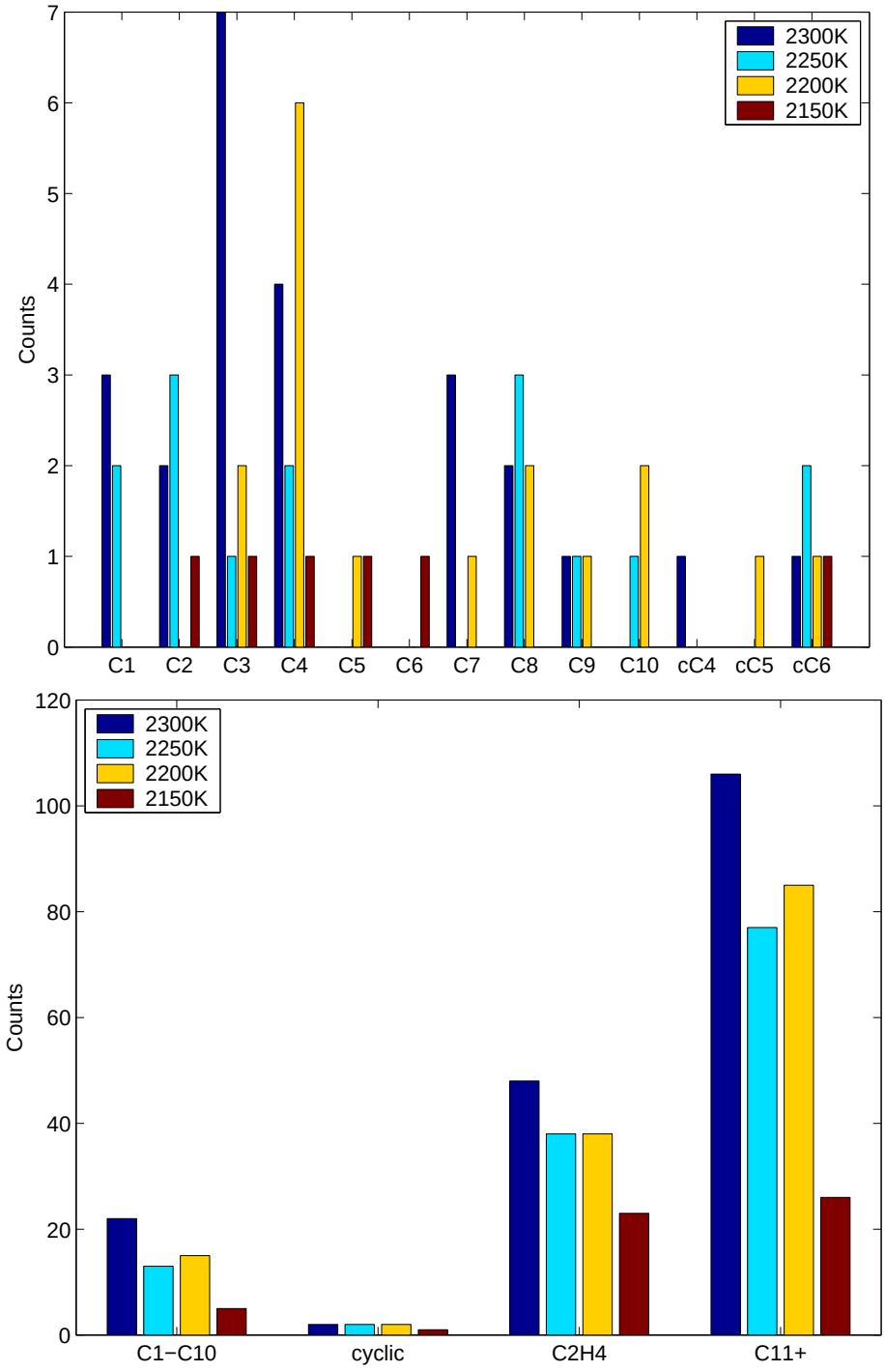

Figure 5.15. (top) Counts of volatile molecules evolved for each temperature. cC4 denotes cyclic C4. (bottom) Total molecules evolved at the end of the simulation. For simulations where there are no breaks occurred, no molecules are recorded as C11+ due to no polymer breaks detected.

that could recombine. Including the time for all possible recombination pairs resulted in an increase in time for recombination reactions.

The recombination reactions were observed to occur in a variety of ways. Some recombination reactions would occur very quickly after the scission reaction occurred, before the polymer ends had a chance to move significantly apart. However, if there was significant energy concentration within the neighborhood of that recombination reaction, either that bond or a neighboring bond was observed to dissociate quickly. Other recombination reactions would occur after a longer period of time when the two fragments had time to separate from one another sufficiently prior to the recombination reaction. Additionally, recombination reactions were observed between the two fragments sometimes after a quick ethylene molecule had been released. Finally, recombination reactions were observed between two fragments from very different parts of the polymer. The variations in recombination reactions indicate that there is no explicit prescribed manner to handle recombination reactions.

The polyethylene simulations did not reveal β-scission scission kinetics as a dominating role for polymer decomposition. Both C-C scission-recombination reactions and C-C-C β-scission reactions occurred during the decomposition. Polymer decomposition rates were observed to vary greatly among the different simulations. In some cases, backbone scission reactions occurred followed by periods where there were no immediate β-scission reactions. In these cases, β-scission reactions must independently accumulate sufficient energy for the β-scission reaction to occur. However, in other cases, the β-scission reactions were observed to occur very quickly and in rapid succession following the initial scission reaction. The probability density of observed β-scission times is shown in Fig. 5.17. Using the observed β-scission rates, the Arrhenius plot is constructed in Fig. 5.18, resulting in $E_A = 62$ kJ/mol and $A = 2.03 \times 10^{12}$. These Arrhenius parameters are significantly faster relative to the β-scission kinetics determined previously starting from a thermal energy distribution.

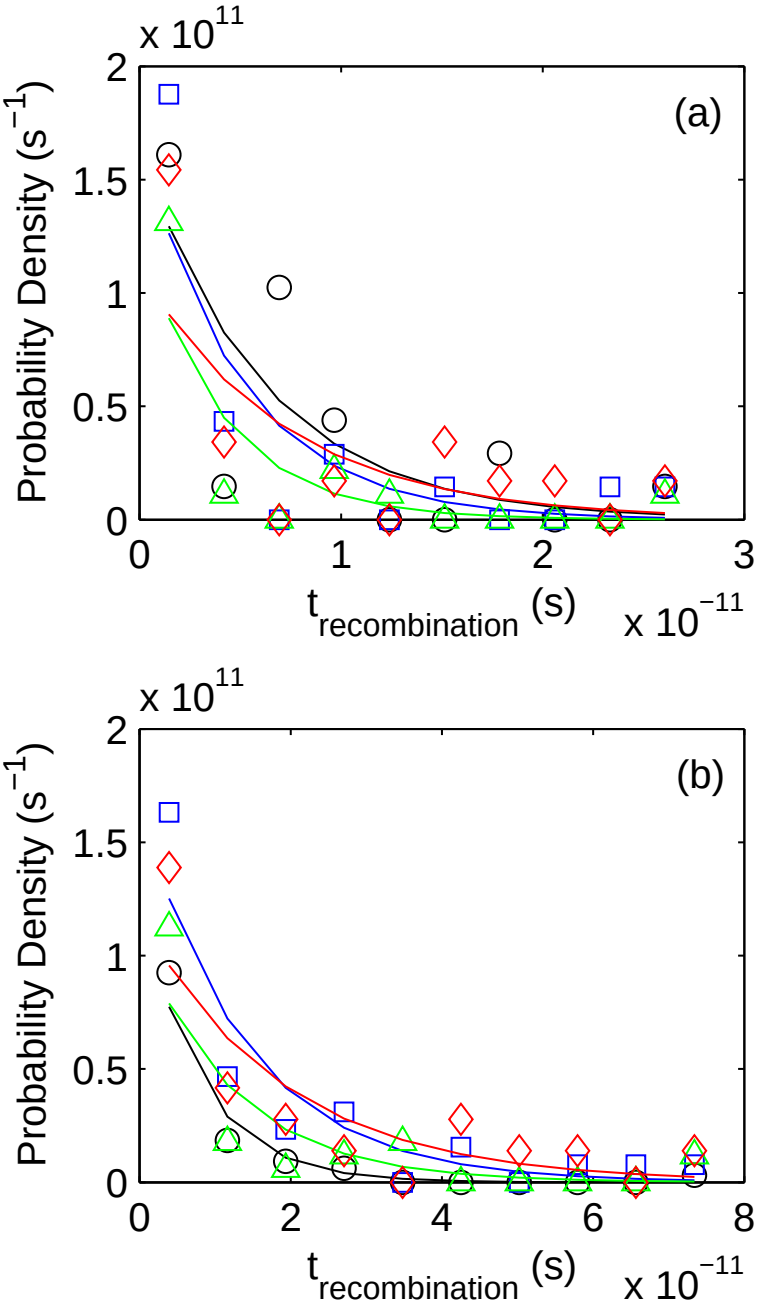

Figure 5.16. (a) Distribution of recombination times when the bond that broke is recombined. (b) Distribution of recombination times for any recombination reaction. For both plots, the points and lines correspond to black circles for 2300 K, blue squares for 2250 K, green triangles for 2200 K and red diamonds for 2150 K.

This rapid succession of β-scission reactions likely results from a high concentration of energy in the vicinity of the scission reaction. This energy accumulation can result from standard energy transfer or polymer stress. The backbone stress may not be fully relieved by the backbone scission alone, and the remaining high energy concentration is released through the rapid succession of β-scission scission reactions. The β-scission route is not the only way observed to relieve the stress, as scission reactions forming propyl radicals and occasionally butyl radicals were also observed. This competition between β-scission and scission reactions indicates that the accumulation of energy can still cause the scission reaction to occur instead of the β-scission reaction. Even for the relatively short PE50 simulations, one backbone scission reaction is observed to be insufficient to relieve the polymer stress. These results agree with the results of ten entangled PE5 chains, which demonstrated the same backbone scission rate as the longer polymers. However, it should be noted that the increased temperature provides a means for the rapid relieving of stress, which would not be available at typical decomposition temperatures.

5.6 Comparison to Macroscopic Decomposition

In order to compare the microscopic kinetics determined from RMD simulations to macroscopic experimental results, Kinetic Monte Carlo (KMC) simulations were conducted to determine the long-time effects of these microscopic rate constants. The KMC simulations were conducted with only scission and scission/β-scission reactions. Recombination reactions were not included in either case. The decomposition was analyzed in terms of mass loss as shown in Fig. 5.19. For either scission only or scission/β-scission decompositions, the decomposition zone is in the general area of experimental decomposition kinetics [1, 2]. The KMC simulations in Fig. 5.20 demonstrate increasing decomposition temperature with higher temperature ramps, which are also seen in TGA experiments.

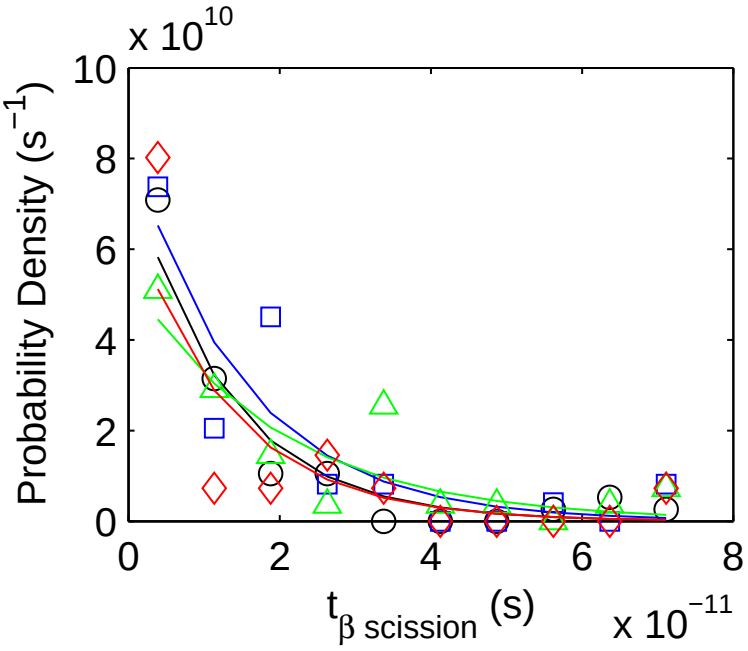

Figure 5.17. Distribution of the first β-scission reaction for the radical formed from a bond-scission reaction. The points and lines correspond to black circles for 2300 K, blue squares for 2250 K, green triangles for 2200 K and red diamonds for 2150 K.

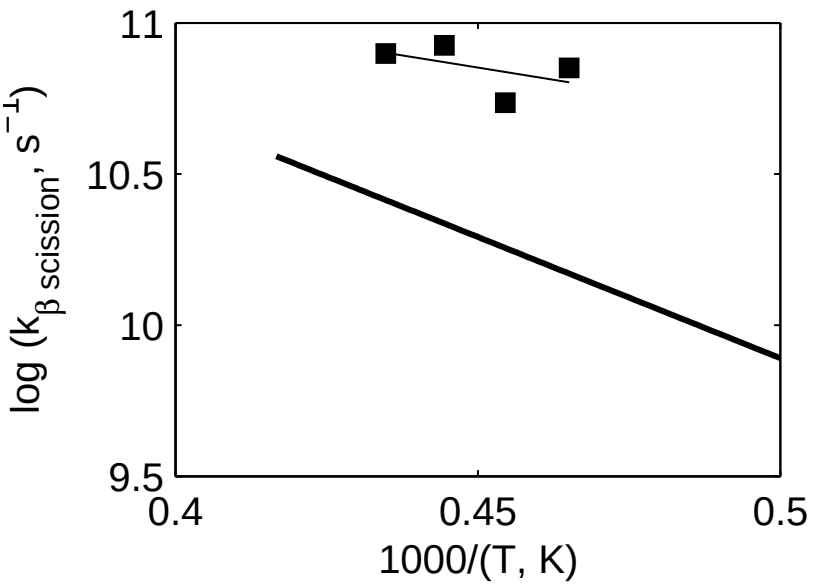

Figure 5.18. Kinetics of β-scission reaction kinetics under volatilization kinetics (black squares and thin line) compared to the β-scission kinetics obtained from equilibrated PE50 structures (thick line).

The KMC simulations completed with both scission and β-scission reactions revealed decomposition almost entirely through unzipping to ethylene monomer. However, Pyrolysis GC/MS analysis indicate a large variety of alkanes and alkenes resulting from HDPE decomposition [22, 34, 210]. Therefore, while the decomposition via the β-scission pathway is qualitatively in the correct decomposition temperature region, it is likely not correct. Additionally, the scission decomposition is highly sensitive to the activation energy. A decrease in the activation energy from 233 kJ/mol to 221 kJ/mol changed the decomposition temperature by 40 °C. The scission kinetics were not sensitive the pre-exponential factor. Therefore, slight changes in the backbone scission activation energy could significantly alter the mass loss kinetics, which indicates that scission reactions alone may be sufficient to describe the decomposition. Therefore, thermal β-scission rates may underpredict the extent of reaction, while neglecting the recombination reactions contributes by overpredicting the β-scission rate.

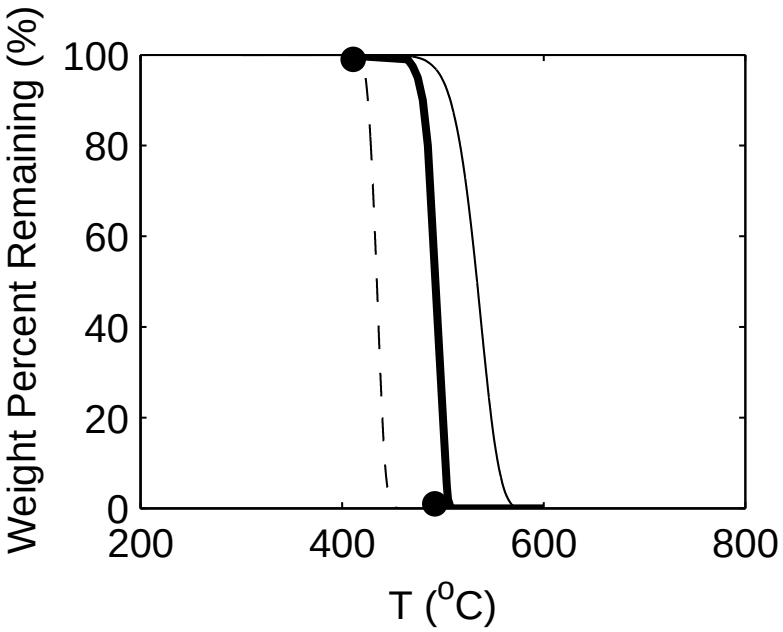

Figure 5.19. Simulated TGA via Kinetic Monte Carlo results for decomposition considering bond scission only at 10 K/s (thin solid line), bond scission and β-scission reactions at 10 K/s (thin dashed lines), HDPE data from Reference [1] at 10 K/s (thick solid line) and from Reference [2] (solid circles).

More complete mechanisms are required in order to sort out these effects as well as any effect the high-temperature may have on decomposition kinetics.

5.7 Conclusions

In this chapter, it was shown that RMD simulations can help identify polymer decomposition mechanisms. The simulations revealed the significantly higher reaction rate of C-C bond scission to C-H bond scission. Additionally, the allyl bond decomposition was not observed to have a significant effect compared to the overall polymer decomposition rate. The simulations also revealed a significant difference between the β-scission rate when starting from a non-energetically excited state and the energetically excited state. While the RMD simulations indicate that energetically excited simulations may reveal the decomposition pathways, the comparison to

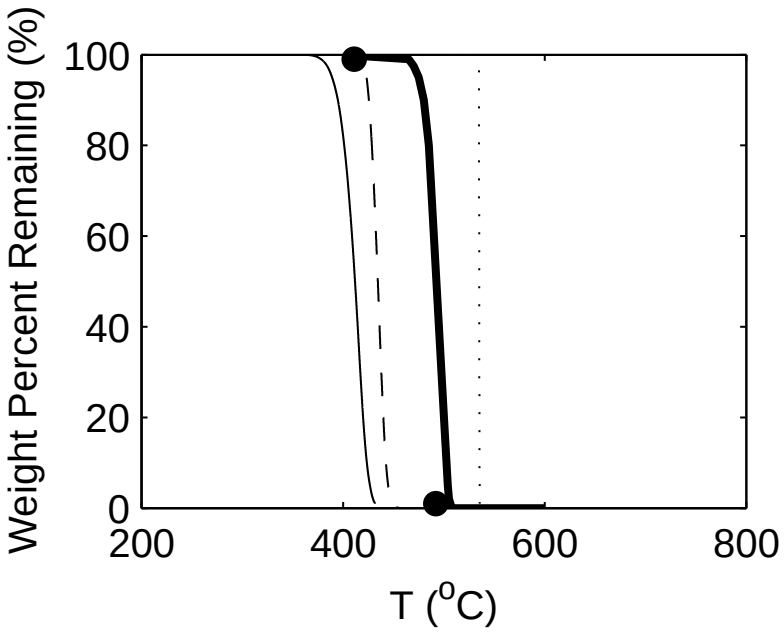

Figure 5.20. Simulated TGA results via Kinetic Monte Carlo for decomposition considering bond scission and β-scission reactions for 5 K/s (thin solid line), 10 K/s (thin dashed lines), and 20 K/s (thin dotted line), HDPE data from Reference [1] at 10 K/s (thick solid line) and from Reference [2] (solid circles).

the macroscopic TGA decomposition using the non-energetically excited β-scission rates reveals that the lower experimental decomposition temperatures may not be well described by the highly energetically excited reactions.

These results make it difficult to determine the best method for simulating the polymer decomposition. While the high temperatures employed in these simulations can overpredict decomposition rates that would not be observed at lower temperatures, other methods may present additional problems. Methods such as bond excitation would still obscure any hot adducts that would only be realized with the appropriate thermal distributions. Therefore, while the RMD simulations can provide valuable insight into potential decomposition pathways, questions still remain as to the best method to represent the energetics in both an appropriate manner and an efficient manner that permits for feasible computational times. Additionally, these findings indicate that RMD captures the combined chemistry and physics for the high-temperature kinetics, while the extension of these rates through random scission and β-scission to typical decomposition temperatures via KMC do not capture the appropriate molecular distribution spectrum.

CHAPTER 6

APPLICATION OF RxnMD TO NOVEL POLYMERS: POLY(BISHYDROXYDEOXYBENZOIN-ARYLATE)

6.1 Introduction

Development of inexpensive, fire-resistant polymers is important in many applications. Bisphenol-A (BPA) is a typical polymer available for commodity production; however, it does not meet some of the more stringent flame-resistance standards. An alternative is bisphenol-C (BPC). Yet, this polymer architecture is undesirable due to the chlorine atoms contained within the BPC monomer. Bishydroxydeoxybenzoin (BHDB) is a novel, halogen-free polymer which can produce flame resistance similar to BPC [221, 222]. BHDB has been synthesized with polyarylates (PA), resulting in the BHDB-PA repeat-unit structure shown in Fig. 6.1. This polymer has demonstrated low heat-release capacity and high char formation similar to BPC-polyarylates. These two key characteristics are very important for flame-resistant polymers.

One objective of the RMD method is to be extendable to novel polymers such as BHDB-PA. Because of the wide range of chemistry possible with each structural change, the development of individualized switching-function parameterizations for each possible novel polymer would not be practical. However, a reasonably accurate model would provide very useful information, especially when the objective is to determine the effects of various molecular structural units in the condensed phase. Therefore, if the deviations are on the order of those seen in in Chapter 3, a reasonable estimate would be adequate to approximate the decomposition kinetics using analogous structural units. When the objective is to investigate a potential new fire-safe

polymer, for example, this level of model accuracy would be more than sufficient to help guide polymer synthesis towards viable structures.

The purpose of this chapter is to model the decomposition kinetics and paths of BHDB-PA and thus to demonstrate the extension of RxnMD to simulate the decomposition of novel polymers. First, quantum-chemical calculations were used to determine bond energies within the polymer. These calculated bond energies were used in the previously developed C-C and C-H scission reaction descriptions, which here are applied to BHDB-PA. Comparisons were made to demonstrate the validity of this approximation. RxnMD simulations were then conducted to identify the ratio of backbone scission locations observed and the effect of the condensed-phase on the decomposition kinetics. Finally, quantum-chemical calculations relevant to the char formation within the polymer were carried out in order to help elucidate the decomposition mechanism.

6.2 Model Decomposition Development

In order to model the decomposition of novel polymers, it is necessary to determine the bond energies. The quantum-chemical bond energies for BHDB-PA were determined from UB3LYP/6-31G(d) *ab initio* calculations between the representative polymer molecule and the individual fragments. The bond energies were calculated from molecular representations of the structures shown boxed in Figs. 6.2(a) and (b), capping the external bonds with hydrogens.

The quantum bond energies are shown in Fig. 6.2. The overall structural interactions decrease the bond energy significantly for some bonds in the BHDB-PA repeat unit compared to bonds in analogous small molecules. The carbonyl-methylene bond decreases from 372 kJ/mol in acetaldehyde to 279 kJ/mol in BHDB-PA, where it is a carbonyl-benzyl bond. (All comparisons here are between the UB3LYP/6-31G(d) calculated bond energies.) The carbon-hydrogen bond also decreases from 472 kJ/mol in

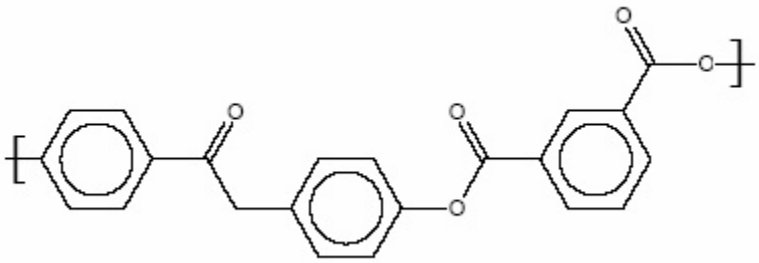

Figure 6.1. Repeat-unit structure of BHDB-PA.

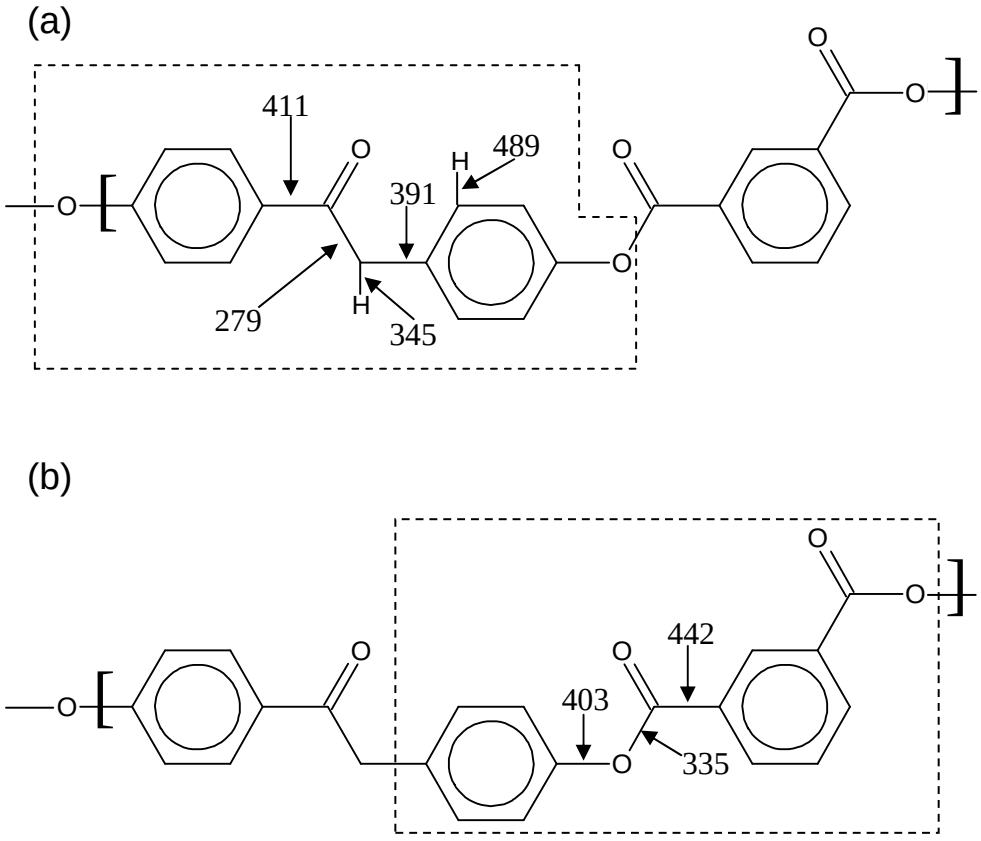

Figure 6.2. UB3LYP/6-31G(d) bond dissociation energies in representative structures of BHDB-PA.

methane to 345 kJ/mol in BHDB-PA. The oxygen-carbonyl bond in the acrylic group decreases from 477 kJ/mol in formic acid to 335 kJ/mol in BHDB-PA. Some of these decreased bond energies probably result from the resonance stabilization around the aromatic groups within the polymer backbone. However, such effects will greatly alter the decomposition chemistry and affect the flame resistance observed experimentally.

In order to include the backbone scission reactions in RxnMD decomposition of BHDB-PA, an assumption was made that the reaction coordinates and switching functions developed in Chapter 3 could be applied to BHDB-PA as well. Transferability was observed between the C-C homolytic scission in ethane and C-C scission in similar species. However, in BHDB-PA the scission reactions are not between sp^3-sp^3 carbon atoms. In fact, except for the C-H scission in BHDB-PA, all the other scission reactions involve either sp^2 or aromatic carbon atoms or oxygen atoms. This is an extension beyond the tested transferability of the switching function parameters.

The one parameter that was adjusted was E_{base}, which is the constant value that is turned on as the bond breaks in order to represent the appropriate dissociation energy as the bonded description is turned off during the scission reaction. The value of E_{base} in RMDff was shifted additively to reflect the change in the bond dissociation energy. For the C-C bond scission in ethane, there is a 6 kJ/mol decrease in E_{base} from the CBS-QB3 bond dissociation energy. The value of E_{base} for BHDB-PA was reduced by the same amount as the scission profiles for the C-C scission in ethane. While this approach appears to be a reasonable approximation to correct the value of E_{base} in sp^3C-sp^3C scission reactions, it may not be appropriate here. The reduction of E_{base} from the actual dissociated species energy reflects the inherent energy present in the quantum-chemically calculated geometry of molecule from the forcefield. This is valid for sp^3C-sp^3C bond scission because the majority of the mode changes with respect to the reaction were previously included in the model. However, the modes for bond scission reactions in BHDB-PA may result in even larger errors due to

Table 6.1. Parameters for transition from MM3 quartic to Morse bonding potential.

Bonded Pair	D_E (kJ/mole)	α (nm^{-1})	r_e (nm)	r_s (nm)
c´ - cp	411.0	16.4	0.147	0.162
c´ - o´	815.1	18.1	0.121	0.134
c´ - c2	279.0	22.3	0.151	0.160
c´ - o	335.0	22.9	0.135	0.144
c2 - h	345.0	19.4	0.111	0.124
c2 - cp	391.0	21.5	0.150	0.160
cp - cp	1000.0	12.1	0.138	0.156
cp - o	403.0	19.6	0.137	0.149
cp - h	489.0	16.3	0.110	0.125
o - h	435.6	22.6	0.095	0.104
c´ - h	406.3	16.6	0.111	0.126
cp - c´r	600.0	23.5	0.131	0.139
o´ - c´r	815.1	18.1	0.121	0.134
c2r - cp	611.7	18.0	0.138	0.147
c2r - h	443.9	17.5	0.110	0.124
c2r - c´	431.0	24.2	0.135	0.142
cp - cpr	1000.0	12.1	0.138	0.156
c´ - or	815.1	18.1	0.121	0.134
or - h	435.6	22.6	0.095	0.104
cp - or	403.0	19.6	0.137	0.149
c´r - o	815.1	18.1	0.121	0.134
c´r - c2	279.0	22.3	0.151	0.160
c´r - h	406.3	16.6	0.111	0.126

lack of transferability and the fact that approximations were made for bond, angle, and torsion mode descriptions when the desired mode was not present in the MM3 forcefield.

The new atom types present in BHDB-PA required additional parameterization of the MM3 forcefield for the meshed bond and van der Waals potentials. Parameters were determined for the meshed MM3-Morse bond potential, which are given in Table 6.1. Parameters were also determined for the meshed Morse-type-MM3 van der Waals potential, which are given in Table 6.2. The atom types are described in Table 6.3

Table 6.2. Parameters for Morse-type van der Waals meshed potential for BHDB-PA.

Atom Pair	D (J/mol)	b	r_e (nm)	r_s (nm)
c´ - c´	34.4	1.751	0.342	0.147
c´ - c	41.3	1.468	0.389	0.148
c´ - cp	39.6	1.675	0.351	0.147
c´ - o	58.5	1.488	0.364	0.140
c´ - o´	58.5	1.488	0.364	0.140
c´ - h	20.1	1.765	0.313	0.135
c´ - ho	50.0	1.269	0.394	0.130
c - c	27.0	1.497	0.393	0.152
c - cp	31.8	1.598	0.370	0.150
c - o	48.0	1.409	0.389	0.143
c - o´	48.0	1.409	0.389	0.143
c - h	32.7	1.34	0.386	0.135
c - ho	24.1	1.427	0.363	0.135
cp - cp	45.8	1.598	0.362	0.147
cp - o	55.2	1.516	0.361	0.141
cp - o´	55.2	1.516	0.361	0.141
cp - h	23.4	1.682	0.322	0.135
cp - ho	27.4	1.54	0.337	0.133
o - o	68.4	1.427	0.363	0.135
o - o´	68.4	1.427	0.363	0.135
o - h	22.6	1.714	0.306	0.130
o - ho	26.6	1.568	0.320	0.128
o´ - o´	53.9	1.542	0.344	0.136
o´ - h	22.6	1.714	0.306	0.130
o´ - ho	26.6	1.568	0.320	0.128
h - h	24.3	1.405	0.328	0.120
h - ho	32.6	1.235	0.369	0.118
ho - ho	22.7	1.335	0.338	0.118

Table 6.3. Atom Type descriptions used for BHDB-PA.

Atom Type	Description
c´	carbonyl carbon
c2	sp^3 carbon bonded to 2 heavy atoms
c	sp^3 carbon bonded to 2 heavy atoms
cp	aromatic carbon
o	sp^3 oxygen
o´	carbonyl sp^2 oxygen
h	hydrogen (non-alcohol)
ho	alcoholic hydrogen

Overall, these calculations demonstrate that the RMD calculations will have limitations on the quantitative data that can be extracted reliably. The bond scission profiles in BHDB-PA were represented using the C-C scission model from ethane, except the C-H scission in BHDB-PA, which used the C-H scission model from ethane. A comparison of the UB3LYP/6-31G(d) bond dissociation surfaces and the RMDff bond potential for some of the more likely bonds to break is shown in Fig. 6.3. Both the quantum-chemical and RMDff energy calculations overpredict bond energies during the separation. There are likely no significant contributions to errors in the quantum-chemical bond energies from electron correlation effects, because the UMP2/6-31G(d) energy calculations for the UB3LYP/6-31G(d) structures during the c2-h bond stretch demonstrate the same trend (Fig. 6.3(b)). The failures of the energy calculations for the c´-o bonds in Fig. 6.3(d) could be the result of the oxygen atom. The quantum chemical calculations may have difficulty with the lone pairs during the dissociation, and the RMDff may be demonstrating significant limitations for using sp^3C-sp^3C parameters for significantly different cases.

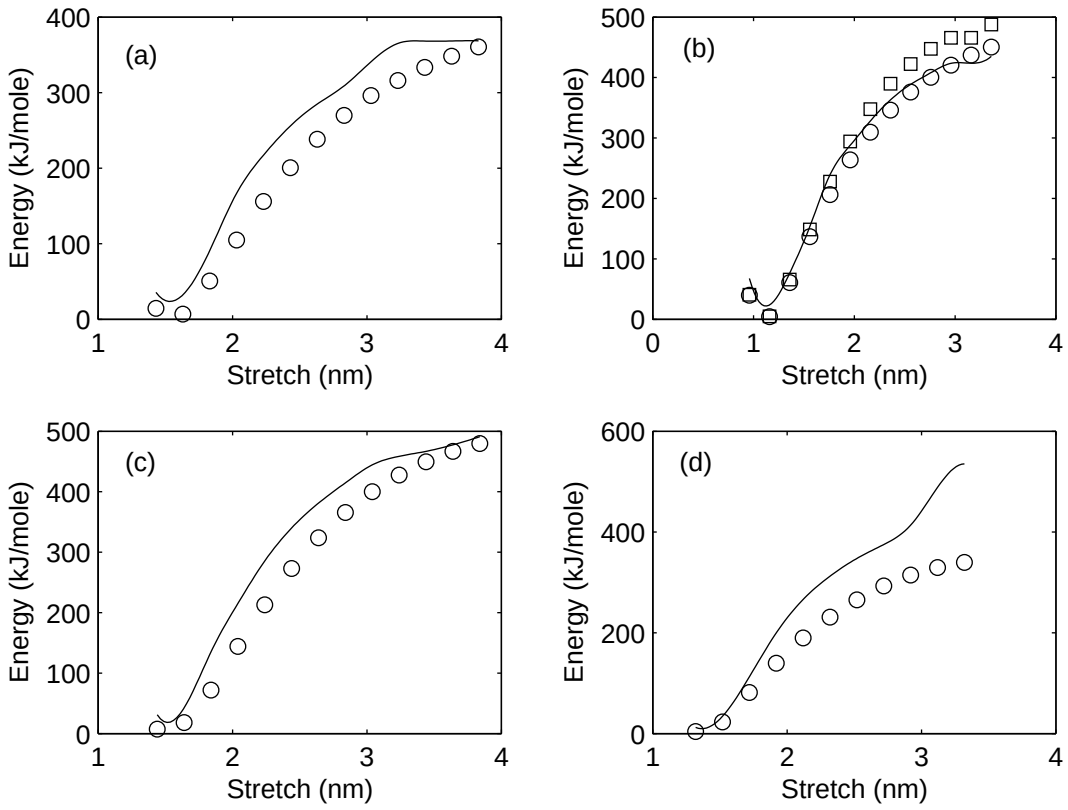

Figure 6.3. Comparison of the UB3LYP/6-31G(d) BHDB-PA (circles) and UMP2/6-31G(d) (squares) bond scission profiles using the reaction coordinate and switching functions parameterizations for scission reactions of C-C and C-H in ethane for (a) c´-c2, (b) c2-h, (c) cp-c2, and (d) c´-o bonds.

6.3 Initial Backbone Scission Kinetics

6.3.1 Simulation Details

The BHDB-PA structures were generated using Materials Studio from Accelrys. The structures are 20 repeat units in length with hydrogen terminations. This configuration yields a single-structure molecular weight of 7642 g/mol. Periodic boundary conditions were invoked to represent the condensed-phase interactions.

The BHDB-PA structure was annealed using Materials Studio with the COMPASS forcefield [108]. The COMPASS forcefield was used because of a programming error in Materials Studio that results in the inability to handle oxygen-containing species using CVFF [223]. Initially, increasing pressure during annealing was used to help accelerate convergence towards the condensed-phase structure. Afterwards, 100 ps simulations were conducted at atmospheric pressure to obtain the minimum energy structure. After each 100-ps simulation, the lowest-energy points along the trajectory were minimized. If a lower-energy structure was obtained, it was used as the input to the next dynamics step. This final procedure was repeated until five successive steps did not yield a reduction in energy. This structure was declared the minimum energy structure. All annealing was conducted at 1000 ^{o}C. The final structure had a density of 1.263 g/cm^3.

The RMD simulations were performed at temperatures of 2400-2800 K. The reactive simulations first need a non-reactive velocity annealing phase. Velocities were sampled from a Maxwell-Boltzmann distribution at the desired temperature. An equilibrium simulation (i.e., without the reactive forcefield) used Verlet-velocity algorithm [195] for 10000 steps with 0.5-fs time steps for velocity annealing. An NVT ensemble was employed using velocity scaling to maintain the temperature.

Reactive simulations were then completed using the Verlet-velocity algorithm [195] with 0.5-fs time steps and NVT ensemble. The temperature was controlled using

velocity scaling. Velocities from the end of the equilibration routine were used as the initial velocities for the reactive dynamics.

6.3.2 Results

Twenty different simulations were conducted at 2400 K for 30 ps of reactive dynamics each. The numbers of bond breakages during the total simulation time are shown by bond in Fig. 6.4. The figure also shows the quantum-chemical bond dissociation energy. The carbonyl-benzyl bond is observed to break most frequently, 74 times of 98 breakages in these simulations.

The relative number of scission reactions between the carbonyl-benzyl bond and the oxygen-carbonyl bond gives the approximate ratio of occurrence. The oxygen-carbonyl bond scission occurs 13 times, which was 13% of the total reactions. This result may be compared with the ratio of the exponential factors (energetic term) in the Arrhenius equation for each reaction, applying the quantum chemical bond dissociation energy at 2400 K. The ratio of exponential factors (including pathway degeneracy) results in the oxygen-carbonyl bond breaking 12% of the reactions. It should be noted that this analysis assumes pre-exponential factors are identical; however, the analysis verifies that RxnMD consistently showed reasonable bond-scission locations for the different bond dissociation energies.

Fig. 6.4 also shows that three methylene-phenyl bonds broke during the reactive simulations. While the methylene-phenyl bond has a quantum-chemical bond dissociation energy of 391 kJ/mol, there are a similar number of scissions observed for the adjacent benzyl-hydrogen bond, which has a lower bond dissociation energy of 345 kJ/mol. In this case, the reactive simulations are capturing the steric and dynamic effects of the decomposition. Bonds along the polymer backbone can be stressed and stretched by motions of the entire polymer chain. In contrast, the benzyl-hydrogen

bond should break thermally by vibrational bond stretching, thus having a higher activation energy and breaking rate.

Quantitative kinetics of carbonyl-benzyl bond breaking were also measured between 2000-2400 K. Simulations were conducted until a carbonyl-benzyl bond broke, regardless of any previous scission reactions not involving a carbonyl-benzyl bond. The Arrhenius plot for the carbonyl-benzyl bond scission is shown in Fig. 6.5. Its activation energy is 202 kJ/mol with a pre-exponential factor of $10^{14.2}$ s^{-1}. The decrease in activation energy is observed for the carbonyl-sp^3C bond compared to the UB3LYP/6-31G(d) bond dissociation energy.

6.3.3 Char-forming pathways

Quantum-chemical calculations can also be used to identify polymer decomposition steps. Using calculations on small, representative structures, the energetics of creating char-forming products can be determined. While these energetics do not account for the steric effects of the chains, they can help provide insight into the potential decomposition pathways.

The decomposition of the BHDB monomer unit was investigated using UB3LYP/6-31G(d) calculations. The objective was to identify routes that lead to the formation of char. One mechanism to char formation is through diphenylacetylene, which has been observed to create polycyclic aromatic hydrocarbons through acid catalysis [224] and photocatalysis [225].

Two routes to the formation of diphenylacetylene are shown in Fig 6.6. The top route shows the energy profile when the hydrogen atom dissociates from the methylene carbon atom. The bottom route shows the energy profile when a hydrogen atom abstracts the hydrogen from the methylene carbon atom. Afterwards, the two routes follow the same pathway to diphenylacetylene. Besides the high energy barrier, the lack of stress on the hydrogen atom seen through the RxnMD simulations would make

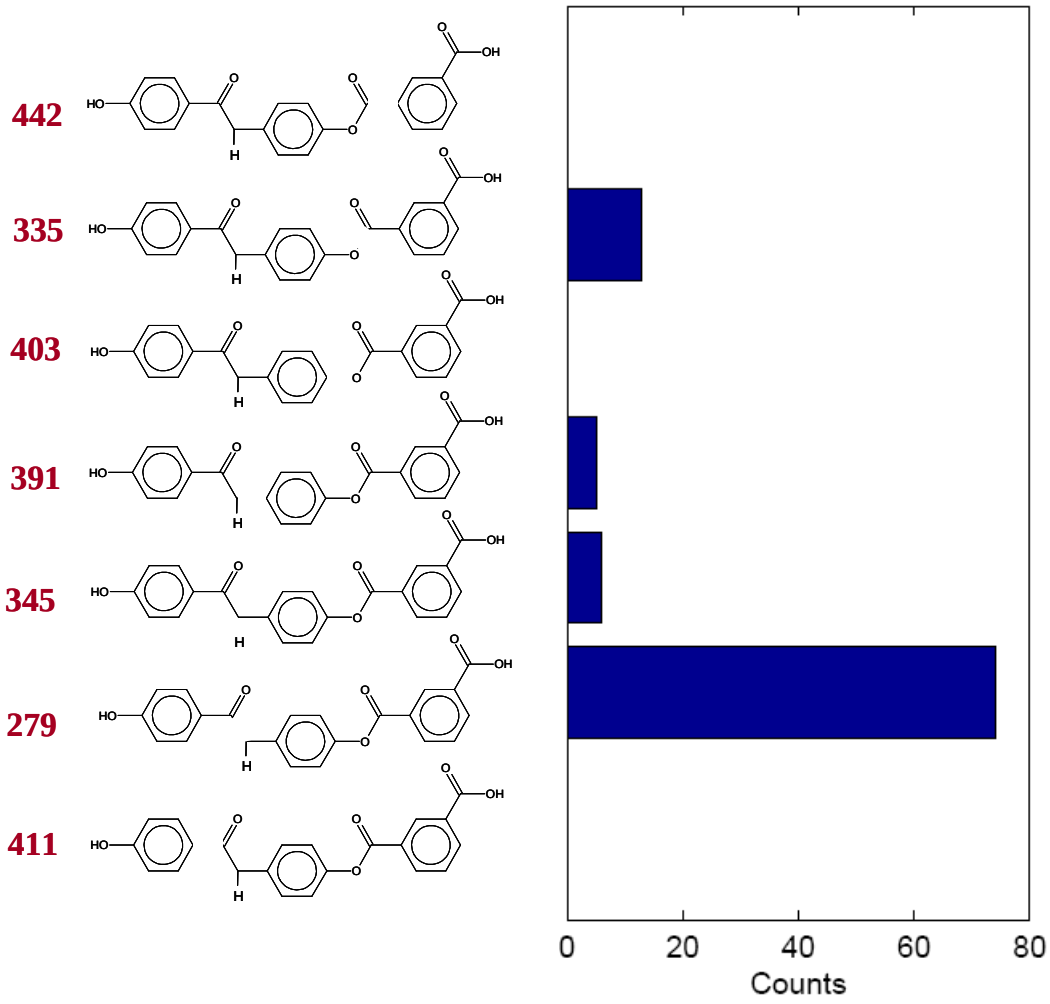

Figure 6.4. Distribution of bond breaking locations from 20 simulations of 30 ps duration at 2400 K. The UB3LYP/6-31G(d) bond energy is shown to the left of each structure.

homolytic scission a very unlikely route to char formation. However, the abstraction route could be quite active.

Additionally, char formation can occur from combination of phenyl radicals. The RxnMD calculations did demonstrate that the carbonyl-benzyl bond broke readily. There were also some scission reactions observed for the carbonyl-oxygen bond in the arylate group. The carbonyl-phenyl bond can be cleaved with activation energies of approximately 120 kJ/mol [226], resulting in carbon monoxide and a phenyl radical. This reaction creates another potential pathway for char formation, because phenyl-phenyl combination forms a strong bond.

6.4 Conclusions

One of the challenges in fire-safe polymer development is to understand decomposition behavior and the nature of the flame resistance. For the BHDB-PA polymers, the high level of char formation increases its flame resistance. Routes for formation of char could proceed through both phenyl-phenyl combination and formation of diphenylacetylene. The combination of these two methods could greatly enhance the char formation within BHDB-PA.

The coupling of the quantum chemical calculations with the RxnMD simulations demonstrate potential pathways that lead to char formation. While some of these barriers are large, heat produced through the burning process causes temperature rise that permits these barriers to be overcome and results in the char-forming ability of the polymer. By using the various techniques together, a more complete picture of the polymer decomposition is obtained.

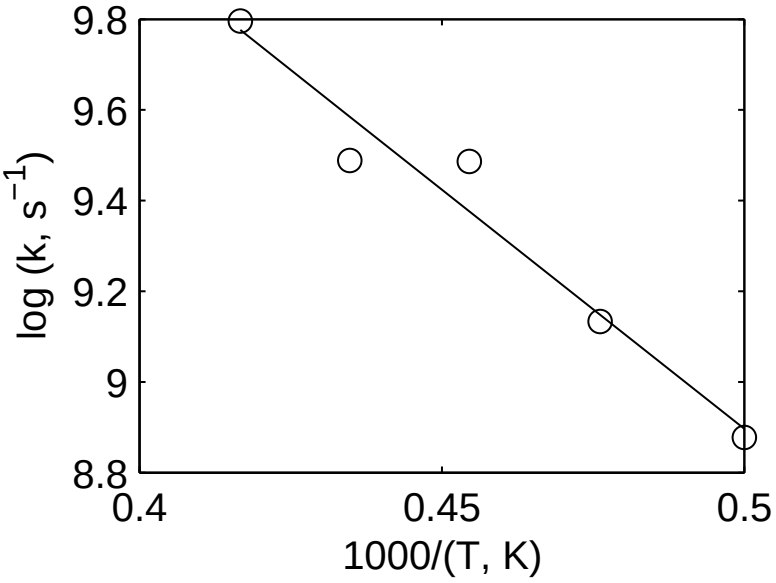

Figure 6.5. Kinetics of the first carbonyl-benzyl backbone bond scission in BHDB-PA.

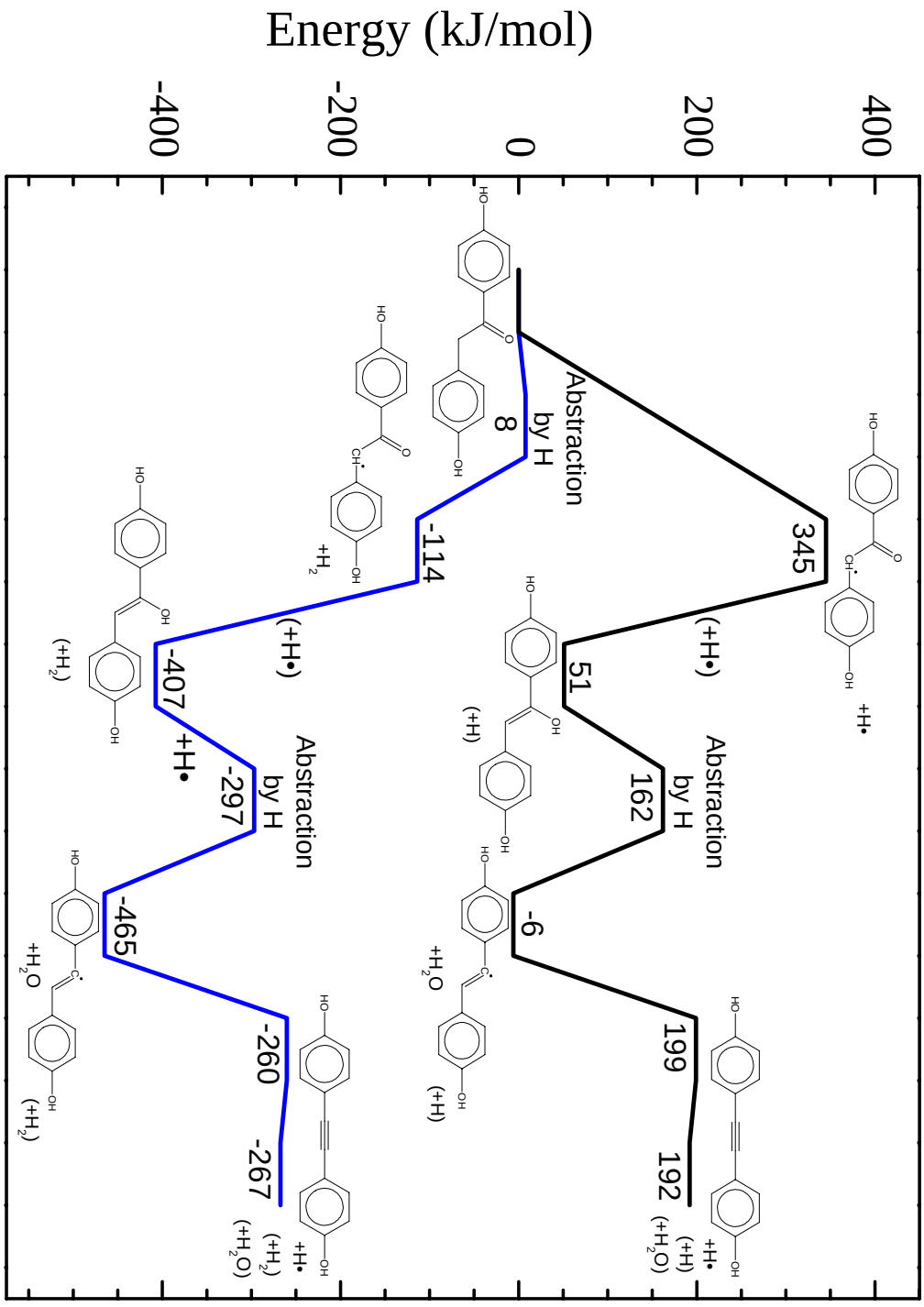

Figure 6.6. UB3LYP/6-31G(d) calculated decomposition pathways of BHDB.

CHAPTER 7

CONCLUSIONS AND RECOMMENDATIONS

The goal of this dissertation was to develop and implement a forcefield-based method of Reactive Molecular Dynamics for modeling polymer decomposition. The results of the study are summarized in this chapter along with suggestions for future work. Conclusions can be summarized as follows:

- A reactive forcefield, RMDff, was developed employing equilibrium forcefields coupled with switching functions that permit the reactive transitions to occur smoothly between reactant and product atom types.
- While RMDff potentials were developed based on small molecules, comparisons have demonstrated reasonable accuracy for larger and substituted molecules.
- Statistical analysis of polymer decomposition has demonstrated the decomposition kinetics to be independent of random polymer conformations.
- The individual rate constants are known from significantly fewer simulations than the Arrhenius parameters.
- By investigating individual effects, the simulations are able to identify the magnitude of different structural effects on decomposition.
- Using elevated temperature, RMD simulations may provide reliable rate constants for individual reactions; however, subsequent reactions may result from hot adducts not normally available at experimental decomposition kinetics.

- The rate constants obtained from polymer decomposition at high temperatures approximate the mass loss experiments as simulated through Kinetic Monte Carlo; however, additional effects such as recombination reactions and stress-related β-scission rates are required in order to compensate correctly for the kinetic rates.

- Qualitative bond scission kinetics can be obtained by approximate corrections to the bond strengths of previously developed reactive potentials of novel polymers such as BHDB, which do not yet have reactive-potential functions developed.

7.1 Conclusions

The combined used of RMDff and RxnMD were developed as an alternative to using quantum chemistry or density functional theory to simulate chemical kinetics. While the latter methods solve the first-principles problem and contain all the necessary information for reactions to occur, both of these methods are computationally expensive and not presently feasible for exploring the decomposition mechanisms of complex, condensed-phase systems. Therefore, RMDff and RxnMD more efficiently simulate both the dynamical and structural interactions that are key to reaction kinetics without explicitly requiring the electronic structure to be solved.

In order to decrease computational expense, forcefields were used to represent the near-equilibrium structures. Because reactions are relatively rare on the time scale of RMD simulations, a large amount of the computation involves the standard equilibrium modes. However, standard forcefields do not permit chemical changes, so RMDff is necessary to allow equilibrium forcefield descriptions to change during the course of a reaction. These changes occur through switching functions that allow the atomic descriptions to uniformly and smoothly transition from the reactant to product atom types during the course of the reaction.

Although the reaction descriptions in RMDff are developed for small gas-phase molecules, it is assumed that the reactive changes are extremely localized, and therefore the models are transferable to similar species. The reactive descriptions were shown to be transferable to both larger molecules and molecules with substituted non-reactive atoms. This transferability and localized description allows for a small set of reactive potentials to be used in a variety of cases. So far, reactive potentials have been developed for hydrocarbon species involved in scission, addition/β-scission, and abstraction reactions. Tests of these reactions have given the correct energy barriers, which are critical in determining the appropriate reaction probabilities and overall kinetic decomposition pathways. The main source of the error was the inability of the equilibrium forcefield to accurately describe radical-containing species, because except for a few hydrocarbon species there was no parameterization of the radical containing modes within the MM3 forcefield. An assumption was made that the sp^2 atom types were similar to the radical atom types; however, this approximation may result in errors as the two are not identical. Further radical-atom-type parameterization will help remove the description of these species.

One of the necessary aspects of RMD is to understand how the statistics of reactions and kinetics depend on individual structures and numbers of simulations. Using polyethylene, it was determined that differences in the random structure do not significantly affect the decomposition rate. It was also observed that the rate constants converge significantly faster than the Arrhenius parameters. In order to determine reliable Arrhenius parameters, it is necessary to conduct several simulations at a variety of temperatures. The effects of interchain energy transfer were also shown not to affect the decomposition kinetics. These results provide necessary information for guiding simulation conditions.

RMD simulations have also shown the ability to help identify the structural effects on decomposition. It was shown that the carbon-hydrogen bond in polyethylene is

not affected by the polymer stress, while the methyl side group in polypropylene is significantly stressed and has a C-C scission rate similar to the polypropylene backbone. Additionally, allylic bond decomposition effects were not observed to be significant, in contrast to gas-phase kinetics. Overall, the simulations have the ability to highlight differences between various condensed-phase structures as well as between condensed-phase and gas-phase kinetics.

The simulations have also demonstrated that high-temperature simulations do provide reasonable Arrhenius parameters when compared to normal experimental TGA experiments. Most simulations were conducted with energy equilibration prior to the reactive simulations. These models require the energy to become concentrated in the vicinity of the reaction prior to the reaction proceeding. Therefore, the necessary energy transfer processes and accumulation appears to be similar at both high and low temperatures. There is the possibility of the elevated temperatures exciting low energy barriers, such as torsional motions. However, polymer decomposition typically occurs around 400-700 ^{o}C, so these modes would likely be fully thermalized under normal decomposition conditions. Simulations conducted without the ability of the simulation to randomize the energy prior to the next reactive event demonstrated a significant amount of hot adducts leading to decomposition products. Yet, these kinetics were not consistent with the simulated TGA experiments via KMC, resulting in decomposition occurring too quickly. The equilibrated simulations have demonstrated the ability to model the individual rate equations at high temperatures; however, still do not account for stress-induced β-scission reactions and the effects of recombination reactions have been completed neglected. The inclusion of these effects may help elucidate the overall decomposition mechanism.

The ability to determine qualitative results on novel polymers has also been demonstrated. This ability provides a useful screening tool for providing qualita-

tive trends and understanding new chemistries prior to developing all the necessary reactive potentials.

7.2 Recommendations

There are two areas of RMD where further development is necessary. One area is development of the RMD methodology for both RMDff and RxnMD necessary for further use and application. The second area involves simulations and the areas of development for analysis and understanding of the information contained within the RMD simulations, which contains a significant amount of information. First, recommendations are provided for methodology development, followed by recommendations for analytical development.

Further development of the RMDff reactive potentials is one of the first needs for expanding the capabilities of RxnMD. The inclusion of reactions involving oxygen and nitrogen would provide key steps necessary to have accurate descriptions of a range of chemical structures. The inclusion of these species is paramount in order to model a majority of polymers and other species. While transferability seems very reasonable when substituted atoms are not directly involved in the reaction, transferring descriptions between similar but not identical reactive species can present errors. Additionally, the addition of the lone pairs of oxygen and nitrogen may require new reactive descriptions. The development of more reactive descriptions is necessary to further describe chemical reactions.

It will also be necessary to include partial charge effects into the simulations. For hydrocarbons, these effects are generally small and can be neglected. However, inclusion of oxygen and nitrogen species into the descriptions will require the inclusion of partial charges into the program and reactive description.

The development of pericyclic reaction descriptions also needs development. These reactions can be important in ring formation and low-energy reactive pathways. One

difficulty for pericyclic reactions will be the development of the reaction coordinate. Because there are several, small geometric changes that occur during the progress of the reaction, a detailed method of monitoring these small changes with respect to normal vibrational motions will be required. However, inclusion of pericyclic reactions is necessary as these routes can be key pathways in the formation of reactive intermediates or products.

The current method of selection the lowest-energy reaction provides a reasonable method of selection between scission and β-scission reactions, which are referenced to the same state. However, the lowest-energy method employed in the calculations only permits non-competing reactions to be active at the same time. Additionally, another competing reaction can only become active once the currently active reaction either completes or returns to very near the non-reactive state. This creates issues for competing reactions that may become more energetically competitive once another reaction is already active. These situations can be resolved by taking a Boltzmann weighting of each of possible reaction at every time step. By taking the appropriate Boltzmann weighting of each possible reactive state, the simulation can explicitly include each competing reactive state at every time step. Additionally, such a method may possibly represent the appropriate weighting among all potential competing reactions including scission, β-scission, and abstraction reactions.

In terms of simulations, one of the first aspects to be studied further is the side-group effect. This investigation can even be studied largely using hydrocarbon and halogenated hydrocarbon polymers in order to determine the contributions of individual side groups on polymer decomposition. These effects may be important in understanding the effects on polymer flammability, which can be further used to guide fire-resistant polymer chemistry.

Recombination reaction rates are also important and need to be included in overall decomposition mechanisms. These reactions involve an ability of the molecule to

diffuse apart, decreasing proximity of neighboring radicals. While overall decomposition mechanisms could use radical densities as opposed to explicit chain simulations, it is key to understand the effects of radical density on recombination reactions. Additionally, recombination reactions may lead to other, unconsidered species. For example, recombination in polyethylene could lead to cyclic species. Abstraction reactions may also provide important routes to decomposition, providing a means for investigating the probability and effects of suspected hydrogen backbiting reactions. Understanding the radical density will likely be important in these reactions as well. The uniformity of the radical density must also be determined in order to determine if certain regions are highly reactive compared to other regions.

It is hypothesized that the lower backbone scission activation energy results from polymer stress. This stress contributes the additional energy necessary to obtain the entire bond dissociation energy. Determining a relationship between polymer tension and the decomposition kinetics may provide a valuable tool for guiding flame-resistant polymer synthesis. Additionally, the either polymer entropy or rotational energy may be another measure of the inherent stress within the polymer. By simulating the polymer tension, correlations may be developed that predict the relatively flammability.

At an even more fundamental level, the effects of condensed phase energy transfer are necessary to understand how energy leading to a reactive event is both accumulated and released. In terms of condensed-phase systems, effects such as energy transferring species can become important, providing insight into modes for energy dissipation. There are two main methods for energy transfer: intermolecular and intramolecular. Because the polymer is long, there is the possibility that the molecular length provides a means to more efficiently distribute the energy leading to decreased flammability. The intermolecular energy transfer also provides another mechanism because of the entangled nature of the chains providing an additional route to distribute the energy efficiently. It will also be important to determine how the strength

of the repulsive Lennard-Jones barrier affects the energy transfer between chains. These effects may be combined in a matter that couples the various modes of energy transport through the polymer in order to obtain microscopic rate constants.

APPENDIX A

GETTING STARTED WITH RxnMD CALCULATIONS

This appendix gives the basic components of RxnMD providing the key features in the steps to running a simulation are given. Additional information pertaining to the full specification of the files can be found in the other appendices.

A.1 Input Structure File

In order to start a simulation, a description of the atomic structure is necessary. The description of the atomic structure is contained in a structure file, which describes the position and bonding of all the atoms within the simulation. For RxnMD, the bonding must be provided within the structure file. The files that contain bonding information are *mdf/car* files from Materials Studio and *hin* files from Hyperchem.

Files generated from Materials Studio need to be converted to a binary **.ncf* (new configuration file) file for RxnMD. This conversion is completed prior to being using RxnMD using the conversion program *mdfcar2binary*. To run mdfcar2binary, which is run using the command line. The command for the program is mdfcar2binary followed by the *mdf/car* file name, without the extension. For example, if you have a *mdf/car* files with the names *pe50.mdf* and *pe50.car*, the program would be called as *mdfcar2binary pe50*. (Note: Except for the extension, the pair of *mdf/car* file names must be identical).

The files generated from Hyperchem are **.hin* files. The *hin* files require no special transformation to be read by RxnMD. The text file is interpreted directly by the program.

A.2 instruction file

The instructions for any simulation is contained within the instruction file. This is a file that will direct the program on the conditions such as desired temperature, number of integration steps, etc. The instruction file will describe all the commands for completing a specific job, where a job is one set of simulation instructions. There can be many different jobs within a single instruction file, organized into job blocks, which specify the commands to be executed for each particular job within the program. The job blocks are separated by a blank line.

Within the instruction file, each line contains a keyword which specifies the property being set (e.g., temperature). The keyword is separated from the parameters by

an equals sign (=). Sometimes multiple parameters are specified for a single keyword. The different individual parameters for a single keyword are separated by a comma (,). Some parameters may also take their own options. The options to a particular parameter are separated from the parameter name by a colon (:). For example, in the first line of the text shown below, *BC* is the keyword and *none* is the parameter. In the second line, *FF* is the keyword, and *file* and *method* are both parameters. Each parameter takes an option. Notice, the *mm3* option for the *file* parameter is separated by a colon. The two specifications of the parameters are separated by a comma.

```
BC = none
FF = file :  mm3, method :  mm3
```

Within the instruction file, the spacing and capitalization of a line does not matter. The commands are reduced to characters only for analysis so `time step` is the same as `timeStep` and `t ime st E p`. Also capitalization is not considered each line is converted to lower case prior to analysis. The conversion to lowercase does present an important consideration for case-sensitive operating systems such as Linux. In this case, the file name of any files that RxnMD will need to read must be all lower case, or the program will not be able to find the appropriate file resulting in an error. Only a brief explanation of the basics of the job specification will be given below. Complete information about all keywords is given in Appendix B.

The first two lines of the text file specify the output text file and the input structure file containing information for the program execution. The output text file is specified using the *Output Log File* keyword followed by the file name, which is a text file where information will be written during the simulation. The input structure is the file that contains all the atom positions and bonding information described in Sec. A. It is specified using the *Input Structure File* followed by the file name (the file extension is necessary to know how to process the structure file). After these two lines is a blank line separating the starting information from the job block. An example of this portion of the instruction file is shown below.

```
Output Log File = ethanerecomb.out
Input Structure File = ethanerecomb.hin
```

Next a job block is specified. An example of a reactive job block is shown below. Each of the following points will explain the lines within the job block specification. After the first keyword specifying the job block type (reactive in this example), the remainder are in no particular order. The description will simply go down the list.

- The first item specifies that this is a reactive job by the *Reactive* keyword. An equilibrium job block only differs by being specified by *Equil* as opposed to *Reactive* and will not have the keyword *rxn file* used. The first line of the job block contains the job type specification, *Reactive* in this case.

- The title gives a description of this job block. For titles that contain spaces, enclose the title in single quote marks as shown in order to protect the spaces from being removed in the output file.
- The *reactions* keyword specifies the commands for the reactive dynamics. This is a required keyword for a reactive job. The file option specifies which file contains the reaction descriptions. The selection method specifies which method to use to resolve competing reactions.
- The *ensemble* keyword specifies the type of integration that will be done. NVE integration refers to constant number of atoms, constant volume, and constant energy. This is a required keyword.
- The *time step* keyword provides the integration time step size, which is specified in units of femtoseconds.
- The temperature is specified using the *temp* keyword, which is required for NVT or NPT simulations. It is also required for velocity initialization if it is not specified directly in the structure file.
- The *nstep* keyword specifies the number of integration steps to be completed. It is a required keyword.
- The *BC* keyword specifies type of boundary conditions to be used. It is a required keyword even if no boundary conditions are being used.
- The forcefield components are specified using the *FF* keyword. It takes a *file* parameter, which specifies the file name excluding the required **.fff* extension. The *method* parameter describes the particular forcefield method within the specified file to implement. This is a required keyword.
- The *integrator* keyword specifies the type of integrator to use. This is a required keyword.
- The *initial vel* keyword specifies how the initial velocities are set up. This keyword is required if there is no velocity information contained in the structure file or from a previous job block.
- The *random seed* keyword specifies the integer to be used to seed the random number generator.
- The *Trajectory Output* keyword details how to handle the trajectory information. The trajectory is written to a file ethanerecomb.trj using the *file* parameter and the frequency of writing out the velocity data to the trajectory file is set to every step using the *Vel Freq* parameter.
- The end of the calculations is signalled by the *end* command. If another job block was to be used, the *end* command would not be used, but rather a blank line separating each of the job blocks. The *end* command specifies the end of all jobs blocks within the file.

```
Reactive
Title = 'ethane recomb test'
reactions = file:cc2, selection method:  lowest energy
Ensemble = NVE
time step = 0.5
Temp = 500
Nstep = 6000
BC = none
FF = file:mm3, method:mm3
Integrator = VerletVelocity
InitialVel = file:ethanerecomb.vel
RandomSeed = 676
TrajectoryOutput = file:ethanerecomb.trj, VelFreq:2
END
```

The instruction file is run in RxnMD using the command line. The input is *RxnMD instruction_file_name*, where *RxnMD* is the program execution name and *instruction_file_name* is the name of the instruction file.

A.3 Movie Generation

The movie generation/trajectory analysis routine analyzes a previously completed trajectory file, or a file that contains the information of the structure during a previously completed simulation. The job type is specified using the *Traj Analysis* indicating that this job block will be analyzing a previous trajectory file. As with the file example given above, an input structure and output text file name must be specified first. Even if a file only contains a trajectory analysis routine, an input structure file must be specified; however, the trajectory analysis will be conducted on the file specified within the trajectory analysis job block. Trajectory analysis can be completed within an instruction file that also contains other actual simulations being conducted. The required information is different for trajectory analysis blocks compared to dynamics simulation blocks.

A description of the trajectory analysis block below will now be described. Each line will be described in order. Except for the *title* keyword, all other keywords are required for a trajectory analysis.

- The first line contains the job block type. Here it is a *Traj Analysis* type, but is the same as a *reactive* or *equil* job type.
- The title is specified using the *title* keyword.
- The *movie generator* keyword specifies that the movie generator generator routine is being used to generate a movie file. This keyword would be to turn it off if only an *Analysis* type of method were being used.

- The *Traj Input File* specifies the name of the file containing the trajectory to be analyzed in this job block.
- The *Traj Output File* specifies the name of the output files to be generated.
- The *Traj Type* keyword specifies the type of structure/movie output file(s) to be generated. In this case a Hyperchem dynamics file is to be created.
- The *FF* keyword, which contains the method and file information as described above. It is required because it is necessary for some conversions.
- The *Traj Last Frame* keyword specifies the last integer step number to be analyzed by trajectory analysis. The *end* option was given here in order to use all the steps in the trajectory file. This is a required keyword.
- The *Traj Element Conv File* keyword specifies the file that converts the atom types to the appropriate element/description and atomic number required for generating certain movie/structure file(s).

This terminates the job block for the trajectory analysis, which can be followed by another job description separated by a blank line or the *end* command to signify there are no more jobs to complete.

```
Traj Analysis
Title = 'Movie Generation Routine'
Movie Generator = on
Traj Input File = ethane.trj
Traj Output File = ethane
Traj Type = hyperchem dynamics
FF = file:mm3, method:mm3
Traj Last Frame = end
Traj Element Conv File = ff_type_conv.txt
```

A.4 Visualization

Visualization of trajectories can be accomplished using any viewer that supports a particular file type generated. The two main viewers of molecular dynamics movies we have used are MolecView and Hyperchem. Details are given below for each program.

A.4.1 MolecView

In order to view the movies in MolecView, first a text file must be generated that specifies which files are available. For example, if that file is named *molec.mlv*, then open *molec.mlv* in a text editor and add the following two lines to view the file *ethane_movie.mbv* with MolecView. (MolecView reads a binary trajectory format, which is given an **.mbv* extension within RxnMD.)

```
MOLEC
ethane_movie.mbv
```

Next, start MolecView either at the command line by typing *molecview2 molec.mlv*, where *molec.mlv* is the name of the file containing the list of files MolecView can visualize. From Windows, you can alternatively just start MolecView and a dialogue box will open asking for the input file, in which you will just need to browse through and select the file, *molec.mlv* in this case. Once the program has started, click the right mouse button. This will provide access to loading a particular file for viewing and other options and help for the keyboard commands for using MolecView.

A.4.2 Hyperchem

For Hyperchem dynamics files, a series of different files are generated. These are all automatically generated during the trajectory analysis process. Once Hyperchem is started, simply go to the *Script* menu and select *Open Script*. Then browse to where the trajectory analysis was completed and select the file with the **.scr* extension (you had previously specified the name of the *scr* file). Then click OK and the visualization will start.

APPENDIX B

INSTRUCTION FILE KEYWORDS

Below is the description, defaults, and optional parameters for the various keywords available for use in the job specification file of RxnMD. Any parameter or option that has a default value is optional.

B.1 Analysis

This keyword calls for the analysis package to be used on a trajectory. The analysis package provides a means of analyzing the simulation for statistics and other information. As opposed to most other keywords, the *Analysis* keyword can be used multiple times in the same job block without resetting or losing any of the previous analysis jobs requested in this job block, using *Analysis=...* to start the line each time.

It should be noted that the output file name from each analysis instance can be specified. Default names will be generated if none is provided. However, these names could become quite difficult to distinguish and link together with the appropriate simulations in the future. Therefore, it is advised that names be specified for each output file.

The analysis package can be used either during a simulation (*Equil* or *Reactive* jobs) or during trajectory analysis jobs (*Traj Analysis*).

Calc Entropy

This analysis calculates the configuration entropy of a structure. The entropy is calculated from the covariance matrix using the method of Schlitter [227].

File sets the name of the output file. A default file name is generated in the format *CS_PID.out*, where PID is the system process identification number. This is an optional argument.

Freq specifies the frequency of the calculation of the entropy from the covariance matrix. The default value is 10000 steps.

NSteps specifies the number of dynamics steps to be used in the completion of the entropy calculation. The default value is to use all the dynamics steps.

Read Restart specifies to read the covariance matrix from a file, which was generated in a previous dynamics run, and use it as the starting point for continued analysis. This option requires the file name.

Write Restart writes the covariance matrix to a text file, which can later read and used for restarting from a previous dynamics set of steps. The file name for writing the restart information must be provided with this option.

Distance Distribution

This analysis investigates the distribution of distances between each *i-j* atom pair specified.

There are no required keywords to complete the analysis. By default, the entire job block is analyzed every 20 steps for all atoms using a cut distance of 6 Å with 200 sorting bins.

Several different instances of the distance distribution analysis can be specified in each job block. This provides the ability to create specific and varied analysis of different kinds on the same trajectory. Each instance of a distance distribution must be specified on a separate line, using *Analysis=...* to start the line each time.

AtomTypes specifies the atom types to be considered in completing the analysis. If both atoms in the *i-j* pair are not within the atom types being considered, the pair is not considered within the distribution. The atom types are specified as a list separated by colons, such as *AtomTypes:c2:c1*, where only atom pairs that consist of a mixture of c2 and c1 atoms types would be considered. A single atom type value is also acceptable. No atom type equivalence is applied to the atom types. If no elements or atom types are specified, then all atom pairs are considered by default.

Centered specifies the step number to center the distribution analysis around. Use this keyword to set a specific region of the job block for analysis, without including the entire job block. By default, *centered* is not used, rather the entire distribution is analyzed. *Centered* also requires the specification the the *Nsamples* options.

Cut Dist specifies the maximum distance to consider within the analysis. This is an optional keyword is specified in meters, with a default value of 6 Å.

Elements specifies the elements to be considered in completing the analysis. If both atoms in the *i-j* pair are not within the elements being considered, the pair is not considered within the distribution. The elements are specified as a list separated by colons, such as *Elements:C:H:O*, where only atom pairs that consist of a mixture of carbon, hydrogen, or oxygen atoms would be considered. A single element value is also acceptable. If no elements or atom types are specified, then all atom pairs are considered by default.

Freq specifies the frequency for analysis. Default value is set to every 20 steps.

File sets the name of the output file. A default file name is generated in the format *distrib_PID_RAND.out*, where PID is the system process identification number and RAND is a random integer used to generate different file names for many Distance Distribution analysts. This is an optional argument, but highly recommended.

Nbins sets the number of bins to use in the creation of the distribution. By default, 200 bins are used.

Nsamples sets the number of samples on each side of the *centered* value to use in the analysis. Only a single value is specified, and that value is applied to the number of samples taken prior and after the *centered* step number value of the distribution.

Initial Pos Corr

This analysis determines the correlation of the current position to the initial position at the start of the job block. The analysis evaluates

$$\rho(r) = \langle \cos\left(\frac{\mathbf{r_o} \cdot \mathbf{r_i}}{|\mathbf{r_o}||\mathbf{r_i}|}\right) \rangle \tag{B.1}$$

so that initially $\rho(r) = 1$, because of the correlation of the positions, and will transition towards 0 as the average positions move away from the initial positions.

Freq Specifies the frequency for analysis. Default value is set to every 10 steps.

File Sets the name of the output file. A default file name is generated in the format *ipc_PID.out*, where PID is the system process identification number. This is an optional argument, but highly recommended.

MSD

This analysis calculates the mean squared displacement (MSD) of the atoms during the simulation. The MSD is relative to the start of the job block. The values are reported in seconds for time and square meters for MSD.

Freq Specifies the frequency for analysis. Default value is set to every 10 steps.

File Sets the name of the output file. A default file name is generated in the format *msd_PID.out*, where PID is the system process identification number. This is an optional argument, but highly recommmended.

Torsion Distribution

This analysis investigates the distribution of torsion angles between each *i-j-k-l* bonded atom group specified. There are no required keywords to complete the analysis. By default, the entire job block is analyzed every 20 steps for all torsional interactions with 200 sorting bins.

Several different instances of the torsion distribution analysis can be specified in each job block. This provides the ability to create specific and varied analysis of different kinds on the same data. Each instance of a torsion distribution must be specified on a separate line, using *Analysis=...* to start the line each time.

AtomTypes specifies the atom types to be considered in completing the analysis. If all four atoms in the *i-j-k-l* torsion are not within the atom types being considered, the torsion is not considered within the distribution. The atom types are specified as a list separated by colons, such as *AtomTypes:c2:c1*, where only torsions that consist of a mixture of c2 and c1 atoms types would be considered. A single atom type value is also acceptable. No atom type equivalence is applied to the atom types. If no elements or atom types are specified, then all torsions are considered by default.

Centered specifies the step number to center the distribution analysis around. Use this keyword to set a specific region of the job block for analysis, without including the entire job block. By default, *centered* is not used, rather the entire distribution is analyzed. *Centered* also requires the specification the the *Nsamples* options.

Elements specifies the elements to be considered in completing the analysis. If all four atoms in the *i-j-k-l* pair are not within the elements being considered, the pair is not considered within the distribution. The elements are specified as a list separated by colons, such as *Elements:C:H:O*, where only torsions that consist of a mixture of carbon, hydrogen, or oxygen atoms would be considered. A single element value is also acceptable. If no elements or atom types are specified, then all torsions are considered by default.

Freq specifies the frequency for analysis. Default value is set to every 20 steps.

File sets the name of the output file. A default file name is generated in the format *distrib_PID_RAND.out*, where PID is the system process identification number and RAND is a random integer used to generate different file names for many Distance Distribution analysts. This is an optional argument (but highly recommended).

Nbins sets the number of bins to use in the creation of the distribution. By default, 200 bins are used.

Nsamples sets the number of samples on each side of the *centered* value to use in the analysis. Only a single value is specified, and that value is applied to the number of samples taken prior and after the *centered* step number value of the distribution.

Velocity Distribution

This analysis investigates the distribution of velocities of the atoms. By default, the entire job block is analyzed every 10 steps for all torsional interactions with 200 sorting bins.

File Thissets the name of the output file. A default file name is generated in the format *distrib_PID_RAND.out*, where PID is the system process identification number. This is an optional argument, but highly recommended.

Freq specifies the frequency of analysis. Default value is set to every 10 steps.

Max vel sets the maximum velocity to be considered in the distribution.

Min vel sets the minimum velocity to be considered in the distribution.

Nbins specifies the number of bins to be used in the construction of the distribution.

B.2 BC

This required keyword specifies the type of boundary conditions to be used in the simulation.

None

This specifies that no boundary conditions are to be used in the simulation (vacuum).

PBC

This applies the periodic boundary conditions to the system using the box specified within the structure file.

Softwall

This option specifies that softwall boundary conditions are to be used in the simulation. The box is the same as that specified in the structure file, and must be specified in the structure file.

MM3 van der Waals potential The energetic potential of the wall is the MM3 van der Waals potential,

$$E_{\text{wall}} = \epsilon \left[-2.25 \left(\frac{r_v}{r} \right)^6 + 1.84 \times 10^5 \exp \left(\frac{-12r}{r_v} \right) \right] \tag{B.2}$$

where ϵ and r_v are parameters in units of J/mole and meters. It is specified as *BC = SoftWall:MM3vdw: 83.682: 3.24e-10*, where the *MM3vdw* specifies that the MM3 van der waals potential is to be used, followed by the ϵ in J/mol value and finally the r_v value in meters.

Repulsive Power specifies the use of a repulsive power law for the softwall repulsive potential in the box. It is specified by the parameters A and B. Eq. B.3 specifies the form of the power law. The units are specified in $\mathrm{Jm}^B/\mathrm{mol}$ for A and m for B. The boundary is the box defined in the structure file.

$$E = Ar^{-B} \tag{B.3}$$

Spherical Softwall

The system is set up with a surrounding sphere, where a softwall potential is used to retain particles within the boundaries. The boundary conditions for softwall spheres are set up using the maximum distance from the center of mass to the furthest particle plus a user specified distance, r_{add}. (Setting r_{add} to zero will cause integration errors from the particle being placed on the wall.) After finding the furthest particle from the center of mass, the value of r_{add} is added to that distance to give the radius of the spherical boundary condition.

MM3 van der Waals potential is specified using by *mm3vdw*, with specifying the value of ε, r_v, and r_{add}. The units are specified in J/mol, m, and m, respectively, as *BC = Softwall Sphere: mm3vdw: 83.682: 3.24e-10: 5.0e-10*. The equation is the same as given above for softwall potentials.

Repulsive Power is specified using *repulsive power*, followed by specifying the value of the A and B parameters, and r_{add}. The units are specified in $\mathrm{Jm}^B/\mathrm{mol}$ for A and m for B and r_{add}. The boundary conditions are specified as *BC = Softwall Sphere:Repulsive Power:A:B:*r_{add}. The equation is the same as given above for softwall potentials.

B.3 Const P

This keyword specifies the methods used to maintain the constant pressure in an NPT ensemble. This keyword is required if an NPT ensemble is used.

Berendsen

uses the Berendsen constant pressure method. The positions and box vectors are scaled to the parameter μ. Note that the cell size, but not the shape, will change.

$$\mu = \left[1 + \frac{\Delta t}{\tau}\gamma\left(P - P_0\right)\right]^{\frac{1}{3}} \tag{B.4}$$

The parameters τ and γ are set by the user. P is the instantaneous pressure, while P_0 is the desired pressure, and Δt is the integration time step size.

Gamma specifies the value of γ to use in Eq. B.4, and it is dimensionless.

Tau specifies the value of τ to use in Eq. B.4. The units of τ are in seconds.

B.4 Const T

This keyword specifies the methods used to maintain constant temperature in an *NVT* or *NPT* ensemble. This keyword is required if an *NVT* or *NPT* ensemble is used.

Vel Scale

uses simple velocity scaling as the method of temperature control applied to the system.

Deviation specifies the deviation in temperature required before velocity scaling will be applied. This keyword is optional and uses a default value of 10 K.

Berendsen

This keyword uses the Berendsen constant temperature scaling method maintain constant temperature control. The velocities are scaled by the value λ in Eq. B.5. Note that setting $\tau = \Delta t$ results in velocity scaling, while $\tau \to \infty$ results in standard NVE integration.

$$\lambda = \left[1 + \frac{\Delta t}{\tau}\left(\frac{T_{desired}}{T_{current}} - 1\right)\right]^{0.5} \tag{B.5}$$

$T_{desired}$ is the desired temperature, while $T_{current}$ is the instantaneous temperature. Δt is the integration time step size. τ is a parameter specified by the user.

tau specifies the τ parameter in units of seconds for the Berendsen-temperature control method in Eq. B.5.

B.5 End

This keyword is used immediately following the last instruction block (without a blank line prior to it). It indicates that the end of the instruction file has been found and this is the last job block to execute. Any text following the *end* keyword will not be executed. This keyword does not take any parameters.

B.6 Ensemble

This required keyword indicates the type of ensemble that will be used to perform the molecular dynamics calculations. Options are *NVE*, *NVT*, or *NPT*.

For an *NVT* or *NPT* ensemble, the *Const T* keyword must also be specified, as well as *Const P* keyword for *NPT* ensemble calculations, or the program will terminate with an error (number 15). This keyword takes no parameters.

B.7 Equil

This keyword specifies that the type of job is an equilibrium job (no reactive dynamics). This is the first required keyword of any job block specification for an equilibrium dynamics calculation (see also *Reactive* - see p. 175 or *Traj Analysis* - see p. 177). This keyword does not take any parameters.

B.8 FF

This keyword specifies the type of forcefield to be used in describing the system. The file is the **.fff* file containing the forcefield information (without the extension specified) and the method is the name of the forcefield components to be used.

File

The file command specifies the name of the file containing the forcefield description. It is required for identifying the forcefield parameters.

Method

The method command specifies the components within the forcefield file specified using the *file* command that will be implemented.

FF Type Convert

The method converts the atom types in the structure file (*.hin, *.ncf, etc.) to the specified types found in the file. It takes two parameters: first the file name where conversion is specified and second the conversion type to apply within the file. The parameters are separated by colons.

The file has a *#define* command to specify the start of each conversion type, followed by its user-given name. Each possible block begins with its own *#define*. An *#end* command marks the end of the file for reading.

After the name definition is a line containing each the old atom types and the bonding type, separated by a colon. The bonding types are single bond (s), double bond (d), or triple bond (t). Each of the old is specified on a single line.

Afterwards, the new bonding information is specified. There is one new atom type per line. First is the old atom type, followed, by the new atom type. Then integers are given for the number of each connection to neighboring atoms is given on the rest of the line. The line `c4 c2 2 2` below specifies that the old atom type *c4* is converted

to a *c2* atom type when the atom is singly bonded to 2 hydrogen atoms and singly bonded to 2 c4 atoms. An example file is below.

```
!MM+ FF Description to MM3
#define mmp_mm3
         h:s  c4:s
 c4  c4  4    0
 c4  c3  3    1
 c4  c2  2    2
 c4  c1  1    3
 c4  c   0    4
 h   h   1    0
 h   h   0    1
#end
```

B.9 Initial Vel

This keyword specifies the method to be used in initializing the velocities of the atoms. This keyword is not required, unless there is no velocity information available. The velocities are initialized to the desired temperature set through the *Temp* keyword. Once the velocities have been initialized, they are not reset between job blocks, unless requested.

Exact Temp

causes the velocities to be scaled to the desired temperature. This keyword requires an option. Currently the only available option is *Velocity Scale*, which applies a direct velocity scaling method.

File

This method reads the velocities for each atom from a text file specified in the form of

```
vx1  vx2  vx3  ...
vy1  vy2  vy3  ...
vz1  vz2  vz3  ...
```

where $vx1$ is the x-component of the velocity vector for atom 1, $vx2$ is the x-component of the velocity vector for atom 2, etc. The keyword is called as *InitialVel=File:Name* where *Name* is the name of the text file containing velocity information specified in units of m/s.

Maxwell Boltzmann

This method assigns each of the three cartesian velocities for each atom by sampling from a Maxwell-Boltzmann velocity distribution.

One Value

This method initializes each velocity to the magnitude of the most-probable velocity, randomly assigning a positive or negative direction for each of the three cartesian directions.

Reinitialize

This keyword will force the system to create a new velocity distribution using the method specified at the desired temperature.

Zero Linear Momentum

Use this keyword to remove any net linear momentum from the system. The state is specified using either the *on* or *off* parameter. The default state is set to *on*.

Zero Rot Momentum

This keyword removes any net rotational momentum of the system about the coordinate origin. The state is specified using either the *on* or *off* parameter. The default state is set to *on*.

B.10 Input Structure File

This is a required keyword that is found in the header of the instructions file. It specifies the file containing the input molecular structure (from an **.ncf* or **.rst* configuration file or a Hyperchem **.hin* file).

B.11 Integrator

This keyword specifies the type of molecular dynamics integration scheme to use.

Verlet Velocity

selects the Verlet-Velocity integration scheme to be applied to the system.

B.12 Log Freq

Specifies the frequency at which the data is written to the text log file. This is an optional keyword with a default value of every step.

B.13 Movie Generator

Specifies if a movie file for playback is to be generated during the *Traj Analysis* block is being run. By default, the movie generator is not set to run.

On

This turns the movie generator portion of the *Traj Analysis* routine on to be used.

Off

This turns the movie generator portion of the *Traj Analysis* routine off. This is the default value.

B.14 NStep

This required keyword specifies the number of integration steps to be completed for a specified job block. This keyword must be specified for each job block within the instructions file (or error 15 will result).

[Number]

Sets the number of integration steps to *N*, an integer value. There is no default value. This is the minimal amount of information that must be specified for number of steps and is required.

Rxn Completed

This option sets the simulation to run until either a reaction completes or a specified number of steps is completed, which ever occurs first. It is specified as *NStep = Rxn Completed : N*, where *N* is the number of steps to complete if a reaction does not occur.

B.15 Output Log File

This is a required keyword found in the header of the instruction file. It specifies the name of the output (text) log file for the set of jobs to be completed.

B.16 Pressure

This keyword specifies the desired pressure to be used in the simulation. The pressure is maintained through the *Const P* method specified when using the NPT ensemble. The pressure is specified in Pascals.

B.17 Random Seed

This keyword sets the random seed used for initializing the random number generators. The same seed is used to initialize both the uniformly-spaced random deviate generator and the Gaussian-spaced random deviate generator, but each generator stores it's seed independent of the other random number generator.

This keyword takes an integer value for initialization. This is not a required keyword for any job to run. If there is no random seed set, one is generated using the integer value of the system time. The random seed does not need to be specified at each job block. Each time it is specified will cause the random seed to be reset at that point. The value is maintained and used in memory until the program terminates execution.

B.18 Reactions

This keyword specifies the commands for the reactions to be used in a reactive dynamics calculation. This is a required keyword.

File

specifies the name of file that contains the reactions descriptions, without the *rxn* file specified. The file must have an *rxn* extension. This option is required for reactive dynamics job blocks and must be specified in each block.

Selection Method

specifies how to resolve competing reactions. This is a required option for every reactive dynamics job block. The options are *lowest energy* for always taking the lowest energy structure or *probabilistic* for selecting an energy-weighted set of reactions from a Boltzmann distribution (not currently recommended due to selection issues with this routine).

B.19Reactive

This keyword specifies that the type of job is an reactive dynamics job. This is the required first keyword of any job block specification (or *Equil* - see p. 171 or *Traj Analysis* - see p. 177). This keyword does not take any parameters.

B.20 Temp

This keyword specifies the desired system temperature in Kelvin. This keyword is required in most job blocks to specify the desired temperature, even if it remains the same.

This value is used in the velocity initialization and as the target temperature. In any job block for which the initial velocities (*Initial Vel* keyword) are not specified

or desired to be re-initialized, the *Temp* keyword must be specified. If the initial velocities are already present and an *NVE* ensemble is employed, this keyword is not necessary.

The temperature specified through the *Temp* keyword is also used as the target temperature in the constant temperature methods in *NVT* and *NPT* ensembles and must be specified.

B.21 Time Step

This keyword sets the time step size for integration. It is a required keyword for the job specification of each separate job section within the instructions file (Error 15 if not specified will result).

[Number]

The time step size is specified in femtoseconds, as *timestep = 0.5*. For a constant time step size, just specify the value in femtoseconds.

Variable

This option specifies a variable time step that depends on the proximity of non-bonded atoms within the system. The following options specify the variable time step. The *slow, fast*, and *cut distance* must be specified when using a *variable time step.*

Cut Distance specifies the minimum non-bonded distance between atoms for use of the larger time step size.

Fast specifies the size of the larger time step size, specified in units of femtoseconds.

Include Torsions specifies whether torsional-nonbond pairs (1-4 pairs) are to be considered when calculating the cut distance. By default they are not included. The option to use them is to specify *yes* as an option, as *include torsions: yes*. Alternatively, there is also a *no* option which excludes torsion consideration.

Slow specifies the size of the smaller time step size, specified in units of femtoseconds.

B.22 Time Start

The *TimeStart* keyword specifies the initial time at the start of the dynamics job block. If *TimeStart* is not specified in the first job block, it is assumed to be 0. In in successive job block where it is not specified it is assumed to continue from where the previous job block ended in time. This is an optional keyword.

B.23 Title

Description

This is an optional keyword that contains the user specified title for that set of jobs. For titles that contain spaces, the title must be contained within single quotes (') in order to preserve the spaces within the output text file.

B.24 Traj Analysis

This keyword specifies the type of job to be conducted, a trajectory analysis. This a job block specification keyword and does not take any parameters. (See also *Equil* on p. 171 and *Reactive* on p. 175).

B.25 Traj Element Conv File

This required keyword for movie generation specifies the text file to be used in trajectory analysis for the conversion of the atom types to the appropriate element/atomic number. The file name is specified through this keyword and is required for trajectory analysis. In the file, each line contains the atom type followed by the element type and finally the integer atomic number, one listing per line. An example is shown below.

```
c2  C  6
c3  C  6
h   H  1
hf  H  1
```

B.26 Traj Last Frame

This required keyword for movie generation specifies the last frame to be analyzed during a trajectory analysis routine. It takes either an integer value for the last step number to be used in the analysis or *end* specifying to use up to the last frame. This is a required keyword for the trajectory analysis method.

B.27 Traj Output File

This keyword specifies the output file for the trajectory analysis routine. The appropriate extension is automatically attached to the filename. This keyword is required for trajectory analysis.

B.28 Traj type

This required keyword for movie generation specifies the type of trajectory analysis and output file that is to be generated.

Gro

This option requests a generic gromacs type dynamics file be created.

Hin at change

This optionrequests a Hyperchem *hin* structure file be generated each time the bonding changes within the structure. A script file will also be generated that will show each structure for 5 seconds and then proceed to the next structure when run in Hyperchem.

Hyperchem Dynamics

This option requests that a Hyperchem dynamics file be created for viewing a movie of the simulation. The bonding is specified in a *hin* file with the dynamics in a corresponding snp file. Because the bonding is specified in the *hin* file, a new *hin* and *snp* file pair are created each time the bonding changes. A script file is also generated for playing the movie as one continuous piece in Hyperchem.

Mdfcar

This option generates a single structure file pair of *mdf* and *car* files for Materials studio. The file is created from the structure at the specified step number.

Molecview

This option generates a binary *mbv* file with the dynamics for each of the included steps. (The *mlv* file is created during the conversion process and can be deleted.)

New Config File

This option creates a new configuration file (*ncf*), which specifies the atoms. It does not contain any velocity information. The structure is created from the structure at the specified step number.

pdb

This option creates a *pdf/psf* file for visualizing dynamics as a pdb file using VMD, with no updated bonding.

Restart

This option creates a single structure file at the closest point prior to or including the specified analysis step in the analysis. Because the restart file contains the velocity information for restarting the dynamics, it can only be generated when there is velocity information present at the particular step. Therefore, it will use generated

at the specified step if it contains velocity information, otherwise it will be generated at the step preceeding the specified point which contains velocity information.

Single Hin

This option requests a single *hin* structure file be generated at the specified point.

xyz

This option requests a single structure be generated at the specified point in the *xyz* file format.

B.29 Trajectory Output

This keyword is required and must be specified in each job block. It specifies how the trajectory output information will be written to the binary file.

Current Point

This is an optional keyword that specifies that only the current point on the trajectory be written to the binary trajectory file, over-writing any previous data every time step. When this option is used, the entire position and velocity and bonding and boundary condition data is specified each time the file is written. Therefore trajectory movies can not be created, however restart structures can be created. This option allows for reduced disk space demands for large runs.

File

specifies the name of the file that will be written with the binary trajectory file. As this file is written separately for each job block, it can be over written each block by specifying the same name. By default, the file is named *traj_PID_CLOCK.trj* if no file name is specified, where PID is the process id number from the system and CLOCK is an integer value of the current time.

No Output

specifies that no binary trajectory file is to be be written for this job block.

Restart

writes out the final structure of a job block into a restart file. The restart keyword takes a parameter of the file name to output the restart information to, specified as *Restart:filename*.

Step Freq

specifies the frequency of writing the structure file out when using Current Point.

Vel Freq

specifies the frequency at which the velocities are written to the trajectory output binary file. This is not a required keyword, and has a default value of every 2 steps. A value of *last* can also be specified indicating that the velocities will be only be written at step *N*.

B.30 VDW

This is an optional keyword for specifying how the van der Waals interactions are implemented. By default the nonbond neighbor list is used in all simulations with a 13 Å cutoff that is updated every 10 steps. By default, no cut-off distance is used.

List Off

To turn off the nonbonding list and consider all interactions at each step, use the option *List Off*.

List Nonbond Dist

This optional keyword specifies the cutoff distance used in setting up the non-bonded neighbor list. The default value is 13 Å. The value is specified in meters.

List Update Freq

This optional keyword specifies the update frequency of non-bonded neighbor list. By default, the update frequency is every 10 steps.

rcut

This specifies the cut-off distance in Angstroms for van der Waals integration of atoms. It is not required, with no default cut-off specified.

Simple Search Rcut

sets the minimum cut off distance for van der Waals integration to the the minimum image distance for a simple search of images in PBC. The criteria requires that $r_{cut} < 0.5 \min(a_x, b_y, c_z)$.

APPENDIX C

FORCEFIELD **.fff* FILE SPECIFICATION IN RxnMD

The forcefield parameters are specified through the forcefield file. Each forcefield file must have a **.fff* extension. Below describes the specification for a forcefield (ff) file generation. All the units used within the forcefield specification are SI as kg, m, s, mole, and radians.

C.1 Reading a line

The first part of reading and interpreting the forcefield file is the reading of each line. Blank lines are ignored. The remainder of the line processing is dependent on the first character of the line. Any line that begins with an exclamation point (!) is a *comment line* (CL) and is ignored entirely (The exclamation point must be the first character preceding everything including spaces and tabs). Lines that begin with a pound sign (#) are *block specification lines* (BSL) that start the reading of information for a different type of specification, such as forcefield components or forcefield parameter specification. Again, the pound sign must be the first character.

Other lines are treated as *information containing lines* (ICL), that specify information (e.g. forcefield parameters) for that block. For each set, all items must be specified on the same line, terminated by a carriage return. The space after the necessary parameters is not analyzed and can be used for additional comments. For example, if five parameters are required, any information after the fifth space is not stored.

C.2 Keywords

C.2.1 Version and Reference Numbers

The first two specifications that can be given in the ff file are whether versions and reference numbers are used in each ICL. By default version and reference numbers are off. These values are provided only as a guide in ff file preparation. If they are on, the line is processed the same independent of the reference and version numbers being present.

The reference numbers and version numbers are accessed through the *#reference_numbers* and *#version_numbers*. To turn on the either property use *on*. The properties can be specified as off using *off*. By default, both reference and version

numbers are set to *off*. These properties must be specified at the beginning of the file (prior to the first #define command) and can not be changed afterwards.

C.2.2 Definition Lines - #define

The definition lines specify which forcefield components will be used in the evaluation of the forces for integration. The forces will be calculated for each forcefield component specified within the definition block, using the *method* specified within the *FF* keyword in the instruction file.

Each definition begins on a new line with the *#define* command left-aligned and is treated as a BSL. After the #define command, the name given to the forcefield method is specified. This is the name specified in the *method* component of the *FF* keyword specified in the instructions file. Multiple *#define* commands can be specified within a single forcefield file; however, only the definition block that corresponds to the method specified in the instruction file will be implemented.

The ff components to be included in that particular forcefield definition are listed on per line, continuing until the next BSL is reached. Each ff component is specified using the commands specified in Sec. C, excluding the #-sign of each keyword. After each component, the maximum energy value is specified, which provides a cut-off for energy evaluation of an individual component specified in J/mol. If the calculated energy is greater than the maximum cut-off, the program will terminate with an error. Afterwards the line continues specifying the method(s) of that component that will be implemented. The method(s) of the component specify the forcefield parameters that will be read and used in the force calculations. Several methods can be specified for each forcefield component, so that the forcefield parameters can be broken into smaller blocks and each section taken as desired for a particular calculation. The definition block ends when the next BSL is encountered. Each of the definition blocks must come after the version and reference specification lines, but prior to any other BSL commands for forcefield components. Once the first forcefield component BSL is encountered, no more define blocks can be specified.

Each block must contain a definition of *atom_types* and *equivalence*. These specify the basis of the forcefield parameters and atom type equivalences between the forcefield components. Both of these definitions do not take the maximum energy cut-off parameter, and this value should be skipped going directly to the method(s) of each component for *atom_types* and *equivalence*.

Shown below is an example of a definition block.

```
#define  mm3
!Ver     Ref  component           Blowup Cutoff  methods
!---     ---  ---------           -------------  -------
1.0      1    atom_types                         mm3
1.0      1    equivalence                        mm3
1.0      1    mesh_quartic_morse  450000         mm3 mm3_2
1.0      1    mm3_angle           100000         mm3 mm3_2
1.0      1    mm3_vdw             100000         mm3
1.0      1    mm3_torsion         10000          mm3
```

C.2.3 End of File

The **#end** marker specifies the end-point of the forcefield file. No further data will be read after the **#end** keyword is encountered.

C.3 Forcefield Components

Each of the forcefield components available are listed below. The **atom_types** and **equivalence** must be specified for each forcefield definition.

C.3.1 Atom Types - #atom_types

The atom types specify the various atom types found in the simulation. Failure to specify an atom type used in a simulation will result in an error. For each atom type, the following information is specified (in order): element type, atom type, mass (in kg/mol), valence). (Note: The text description information is not handled because once the last expected value has been read, the remainder of the line is simply discarded.)

```
#atom_types mm3
!Ver  Ref  atom  FF   Mass         Valence  type
!---  ---  ----  ---  -----------  -------  ----
1.0   1    H     h    0.001007970  1        bonded h atom
1.0   1    C     cg   0.012011150  4        generic carbon atoms
```

C.3.2 Corrected MM3 Quartic Bond Potential -

#mm3_corrected_quartic_bond

This potential uses a switching function to transition the bonded description from the MM3 quartic potential to the Morse potential. The MM3 quartic potential is used for near-equilibrium structures, while the Morse potential describes the dissociation. The parameters are specified the same as for the individual Morse and MM3 quartic potential. The switching parameters are in units of meters for r_0 and inverse meters for a.

$$E_{corr\,mm3\,morse} = S(r)\left[k_b(r-l_0)^2\left[1-2.55\times10^{10}(r-l_0)+3.793125\times10^{20}(r-l_0)^2\right]\right] + [1-S(r)]\left[D\left(1-\exp\left(\alpha\left(r-r_e\right)\right)\right)^2\right] \quad \text{(C.1)}$$

where

$$S(r) = 0.5\left[1-\tanh\left(a\left(r-r_0\right)\right)\right] \quad \text{(C.2)}$$

```
#mm3_corrected_quartic_bond mm3
!Ver  Rf  1  2  k         lo         De      alpha     re         a_sw     r_sw
!---  --  -  -  -------  --------  ------  -------  --------  ------  --------
1.0   1   c  c  1.35E26  1.53E-10  363598  1.92E10  1.53E-10  5.0E12  1.66E-10
1.0   1   c  h  1.42E26  1.11E-10  406276  1.71E10  1.10E-10  5.0E12  1.24E-10
1.0   1   h  h  1.98E26  0.75E-10  436820  1.96E10  0.74E-10  5.0E12  0.85E-10
```

C.3.3 Cosine Dihedral Potential - #cosine_dihedral

This potential uses the cosine dihedral interactions between four connected atoms. k_ϕ is given in J/mol, n is dimensionless, ϕ_0 and ϕ are in radians. The * flag is used for torsional interactions indicating that any atom is acceptable in the 1 and/or 4 positions only; however, specification of all four is also acceptable.

$$E_{cosine\,dihedral} = k_\phi\left[1+cos(n\phi)\right] \quad \text{(C.3)}$$

```
#cosine_dihedral mm3
!Ver  Ref  atom1  atom2  atom3  atom4  kphi      n     phi_0
!---  ---  -----  -----  -----  -----  --------  ----  -----
1.0   1    *      c      c      *      5951.883  3.00  0.00
1.0   1    f      c      c      f      7000.000  3.00  0.00
```

C.3.4 Equivalence - #equivalence

Equivalence allows for parameters to be specified as equivalent between various atom types. For example, various carbon atoms may be specified depending on the number of heavy atoms it is bonded too. However, for torsional parameters, equivalence allows the user to specify a generic c-c-c-c interaction instead of enumerating each possible combination and specifying the parameters again.

An equivalence line must be specified for each atom type. First the atom type is given followed by the equivalence for bond, non-bond, angle, and finally torsion descriptions. An example is shown below.

```
#equivalence mm3
!Ver  Ref  FF    Bond  NB    Angle  Dihedral
!---  ---  ----  ----  ----  -----  --------
1.0   1    h     h     h     h      h
1.0   1    cg    c2    c     c2     c
```

C.3.5 Exponential-6 van der Waals Potential - #exp6_vdw

This uses the exponential-6 vdW interaction between two non-bonded atoms. The parameters are A given in J/mol, B in inverse meters, and C in $\mathrm{Jm}^6/\mathrm{mol}$. The parameters are specified for each ij non-bonded pair.

$$E_{exp-6\,vdw} = Ae^{-Br} - Cr^{-6} \tag{C.4}$$

```
#exp6_vdw cvff
!Ver   Ref    atom1  atom2  A           B            C
!----  -----  -----  -----  ----------  -----------  -----
1.0    1      h      h      2736.0      3.74000E+10  32.00
```

C.3.6 Harmonic Angular Potential - #harmonic_angle

This uses a harmonic angle interaction between atoms 1, 2, and 3 via Eq. C.5. The parameters are specified as k_θ in J/mol/radian and then θ_e in radians for each angular description.

$$E_{harmonic\,angle} = k_\theta \left(\theta - \theta_e\right)^2 \tag{C.5}$$

```
#harmonic_angle mm3
!Ver  Ref  atom1  atom2  atom3  k          Theta_Equilibrium
!---  ---  -----  -----  -----  ---------  ------------------
1.0   1    c2     c2     h      185774.06  1.919862177
1.0   1    h      c2     h      165271.97  1.857030324
1.0   1    c      c      c      194979.08  1.928588823
```

C.3.7 Lennard Jones 12-6 van der Waals Potential - #lj-126

This uses the Lennard-Jones 12-6 interaction between a pair of non-bonded atoms. The A and B parameters are specified for each atom, and the geometric mean is used for A_{ij} and B_{ij}, respectively. The parameters are listed in the order A (in units of J m^{12} mol^{-1}), then B (in units of J m^6 mol^{-1}).

$$E_{LJ\,12-6} = \frac{A_{ij}}{r^{12}} - \frac{B_{ij}}{r^6} \tag{C.6}$$

```
#lj-126 cvff
!Ver  Ref  atom  A             B
!---  ---  ----  ------------  -----------
1.0   1    h     2.97425E-113  1.37535E-55
1.0   1    c     7.49097E-111  2.21122E-54
```

C.3.8 Meshed MM3 Quartic and Morse Bond Potential -

#mesh_quartic_morse

This uses a combination of the MM3 quartic potential and the Morse potential for bonded interactions. The parameters α and r_e along with the switch location, r_s for the Morse potential are determined by matching the energy and first and second derivatives of both equations at a single point. The MM3 quartic parameters are used as specified in the forcefield along with the zero-point energy corrected dissociation energy in the Morse potential. For $r > r_s$, the Morse potential is used, while $r \leq r_s$ uses the MM3 quartic potential. This ensures the MM3 forcefield is maintained for near-equilibrium conformations. The parameters are specified as k_b then l_0 then D_E then α then r_e then r_s.

$$E = \begin{cases} k_b(r-l_0)^2\left[1 - 2.55\times10^{10}(r-l_0) + 3.793125\times10^{20}(r-l_0)^2\right] & \text{if } r \leq r_s \\ D\left[1-\exp\left(\alpha(r-r_e)\right)\right]^2 & \text{otherwise} \end{cases} \tag{C.7}$$

```
#mesh_quartic_morse mm3
!Ver  Ref  a1   a2   k         lo        DE      alpha    re        rs
!---  ---  ---  ---  --------  --------  ------  -------  --------  --------
1.0   1    h    h    1.98E+26  0.74E-10  436820  1.89E10  0.70E-10  0.87E-10
1.0   1    c2   h    1.42E+26  1.11E-10  406276  1.74E10  1.11E-10  1.25E-10
```

C.3.9 Meshed MM3 vdW and Lennard Jones 12-6 Potential -

#mesh_mm3vdw_lj

This uses a combination of the MM3 vdW potential and the Lennard-Jones 12-6 vdW potential for non-bonded interactions. The parameters A and B along with the switch location, r_s for the Lennard-Jones potential are determined by matching the energy and first derivative at a point; however, the second derivative is not continuous at that point. The MM3 vdW parameters are used as specified in the forcefield. For $r > r_s$, the MM3 vdw potential is used, while $r \leq r_s$ uses the Lennard-Jones vdW potential. The parameters are specified as ε then r_v then A then B. Because of the meshing, parameters must be specified for each possible non-bonded atom pair.

$$E = \begin{cases} A_{ij}r^{-12} - B_{ij}r^{-6} & \text{if } r < r_s \\ \epsilon\left[-2.25\left(\frac{r_v}{r}\right)^6 + 1.84\times10^5\exp\left(\frac{-12r}{r_v}\right)\right] & \text{otherwise} \end{cases} \tag{C.8}$$

```
#mesh_mm3vdw_lj mm3
!Ver  Ref  a1  a2  eps     rv        A           B           r_switch
!---  ---  --  --  ------  --------  ----------  ----------  ---------
1.0   1    c   c   112.97  4.08E-10  4.816E-113  -2.061E-54  2.25E-10
```

C.3.10 Meshed MM3 and Morse-type vdW Potentials -

#mesh_mm3vdw_morsevdw

This uses a combination of the MM3 vdW potential and the Morse-type vdW potential for non-bonded interactions. The parameters D, r_e and b along with the switch location, r_s for the Lennard-Jones potential are determined by matching the energy and first and second derivatives at a point. The MM3 vdW parameters are used as specified in the forcefield. For $r > r_s$, the MM3 vdw potential is used, while $r \leq r_s$ uses the Morse-type vdW potential. The parameters are specified as ε then r_v then D, then b, then r_e, and finally r_{switch}. Because of the meshing, parameters must be specified for each possible non-bonded atom pair.

$$E = \begin{cases} D\left[z^2 - 2z\right] & \text{if } r < r_s \\ \epsilon\left[-2.25\left(\frac{r_v}{r}\right)^6 + 1.84 \times 10^5 \exp\left(\frac{-12r}{r_v}\right)\right] & \text{otherwise} \end{cases} \tag{C.9}$$

where $z = \exp\left[b\left(1 - \frac{r}{r_e}\right)\right]$.

```
#mesh_mm3vdw_morsevdw mm3
!Ver  Ref  a1  a2  eps       rv        D       b      re          r_switch
!---  ---  --  --  --------  -------   ------  -----  ---------   --------
1.0   1    c   c   112.97    4.08E-10  623.43  4.754  3.724E-10   2.05E-10
1.0   1    c   h   97.230    3.66E-10  380.75  4.970  3.406E-10   1.90E-10
```

C.3.11 MM3 Angular Potential - #mm3_angle

This uses the MM3 sixth-order polynomial representation of angular interactions between three atoms. The numerical constants have been converted to reflect the SI units and radians. Also k_θ contains the 0.02191418 factor specified in MM3. The parameters are specified as k_θ then θ_e for each angular description, where A, B, C, and D are constants.

$$E_{angular} = k_\theta(\theta - \theta_e)^2\left[1 - A(\theta - \theta_e) + B(\theta - \theta_e)^2 - C(\theta - \theta_e)^3 + D(\theta - \theta_e)^4\right] \tag{C.10}$$

```
#mm3_angle mm3
!Ver  Ref   atom1  atom2  atom3  k             Theta_Equilibrium
!---  ----  -----  -----  -----  ------------  ------------------
1.0   1     h      c2     h      165552.31     1.87797
1.0   1     h      c3     h      165552.31     1.881465
```

C.3.12 MM3 Quadratic Bond Potential - #mm3_quadratic_bond

This uses only the quadratic term from the MM3 quartic potential. The k_b contains the 71.94 factor and is converted to SI units. The parameters are specified as k_b

then l_0 for each bond pair. This is just a simplified and shorten version taken directly from the traditional MM3 quartic potential.

$$E_{quadratic\,bond} = k_b(r - l_0)^2 \tag{C.11}$$

```
#mm3_quadratic_bond mm3
!Ver  Ref  a1   a2   k           lo
!---  ---  ---  ---  ----------  ---------
1.0   1    h    h    1.9836E+26  0.744E-10
1.0   1    c2   h    1.4267E+26  1.112E-10
```

C.3.13 MM3 Quartic Bond Potential - #mm3_quartic_bond

This uses the quartic bond description in MM3. The k_b contains the 71.94 factor and is converted to SI units. The other factors are converted to units of meters. Also note that the 3.793125 factor is the correct value, which is incorrectly stated in the original MM3 paper [104]. The parameters are specified as k_b then l_0 for each bond pair.

$$E_{quartic\,bond} = k_b(r - l_0)^2 \left[1 - 2.55 \times 10^{10}(r - l_0) + 3.793125 \times 10^{20}(r - l_0)^2\right] \tag{C.12}$$

```
#mm3_quartic_bond mm3
!Ver  Ref  a1   a2   k           lo
!---  ---  ---  ---  ----------  ---------
1.0   1    h    h    1.9836E+26  0.744E-10
1.0   1    c2   h    1.4267E+26  1.112E-10
```

C.3.14 MM3 Torsional Potential - #mm3_torsion

This uses the MM3 torsional description between four atoms. The factors V_1, V_2, and V_3 contain the 0.5 factor given in the original MM3 description. The parameters are given in units of J/mol, in the order V_1 then V_2 then V_3.

$$E_{torsion} = V_1(1 + \cos\phi) + V_2(1 - \cos 2\phi) + V_3(1 + \cos 3\phi) \tag{C.13}$$

```
#mm3_torsion mm3
!Ver  Ref  atom1  atom2  atom3  atom4  V1      V2      V3
!---  ---  -----  -----  -----  -----  ------  ------  -------
1.0   1    c      c      c      c      387.03  355.65  1087.87
1.0   1    c      c      c      h      0.000   0.000   585.77
```

C.3.15 MM3 van der Waals Potential - #mm3_vdw

This specifies the MM3 van der Waals interaction between non-bonded pairs. The parameters are specified for each atom. For a particular ij pair the ε parameter is the geometric mean of the ε parameters for each atom type. For the ij pair, the r_v parameter is the addition of the two r_v values for each atom. The ε parameters are specified first in J/mol followed by r_v in meters.

$$E_{vdw} = \varepsilon \left[-2.25 \left(\frac{r_v}{r} \right)^6 + 1.84 \times 10^5 \exp \left(\frac{-12r}{r_v} \right) \right] \tag{C.14}$$

```
#mm3_vdw mm3
!Ver  Ref  atom  eps     rv
!---  ---  ----  ------  --------
1.0   1    c     112.97  2.04E-10
1.0   1    h     83.682  1.62E-10
```

C.3.16 Morse Bonds - #morse_bond

This specifies the Morse potential for a bonded interaction between two bonded atoms. The parameters are defined for each bond pair. The units of the dissociation energy D_E is J/mol, steepness parameter α is inverse meters, and equilibrium bond distance r_e is meters. Because this is a Morse potential, there is dissociated limit of the potential of interaction. The k parameter (units of J mol^{-1} m^{-2}) is for comparing the Morse potential to a quadratic potential during reactive dynamics when using the *lowest energy selection method*. The quadratic potential has the same equilibrium separation distance as the Morse potential.

$$E_{Morse\,Bond} = D \left[1 - \exp \left(\alpha (r - r_e) \right) \right]^2 \tag{C.15}$$

```
#morse_bond mm3
!Ver  Ref  a1  a2  De      alpha      re        k
!---  ---  --  --  ------  ---------  --------  -----------
1.0   1    c   c   363598  1.915E+10  1.53E-10  1.6794E+026
1.0   1    c   h   406276  1.712E+10  1.10E-10  1.2793E+026
1.0   1    h   h   436820  1.956E+10  0.74E-10  1.3396E+026
```

APPENDIX D

REACTION *.RXN* SPECIFICATION FILE

Each of the possible reactions that is permissible during a specific reactive job block, must be read from the *rxn* file. As the file is only read at the start of each reactive job block, all possible reactions for that block must be specified in that *rxn* file. However, different *rxn* files can be read for different reactive job blocks.

D.1 Reading Lines

Blank lines in between specifications of keyword information are permissible, and can provide clarity to the file. During the specification of a keyword, which can take multiple lines, blank lines cannot be used. Additionally, lines can be marked as comment lines which will not be processed by placing an exclamation mark (!) in the first position of the line. Again, comment lines cannot be used in the middle of keyword information.

D.2 Keywords

D.2.1 Starting and Ending Markers

#reaction or reaction

This keyword specifies the start of a new reaction description. The start of each new reaction description starts with this keyword. Either version of the keyword is acceptable, the #reaction version is supplied as a visual queue to aid in visual scanning of the *rxn* file.

#end or end

This keyword specifies the end of the reaction description file. All reading of the file will terminate once this command is found. It is a required keyword. Again, either version is acceptable, with the #end version supplied as an aid in finding the keyword when reviewing the *rxn* file.

D.2.2 Reaction Description

Description

This gives a text description of the reaction being described. This is not a required keyword and does not affect the operation if it is not included. The inclusion of this keyword is for giving a text description, which appears in the text output file during the program execution.

ID

The ID specifies the actual name of the reaction. An ID is given for each reaction and must be provided. The ID will be used in the text output file to specify which reaction is occurring. The ID must be unique for each reaction described within the *rxn* file.

Reaction_dependence

The reaction dependence is a required keyword specifying whether reaction is either *primary* or *dependent*. A *primary* reaction does not depend on any other reaction descriptions. A *dependent* reaction depends on a previous reaction coordinate being active before it can potentially be active. Currently, only *primary* reaction dependence is available.

Reaction_type

The reaction type specifies the type of reaction that will be applied. The available options describe the hard-coded methods of reaction implementations, given by their name (e.g., *dissociation1*). Additionally, a *user_defined* reaction type will eventually be employed that will allow for user specification of reactions.

D.2.3 Atom specification - atoms

The atoms description provides the information about the atomic and bonding changes that occur during the reaction. As a minimum, any atom the changes atom-type must be specified. For example, there are two atoms that change atom types during a scission reaction. These two atoms must be specified. Additional specifications can also be provided to define neighboring atoms that may not change atom type but are required neighbors for this particular reaction description.

The first line of the atoms description contains the *atoms* keyword and then the number of atoms in the reaction description. On the next line the first atom being considered is specified. First the atom type of the reactant is given followed by the atom type of the product (the reaction is defined in the forward direction within the file). This description is repeated one line after another for each atom in the reaction description.

After the atoms comes the specification of the reactants. The reactants specifies the type of interactions between the atoms in the reaction. The reactants are identified

using the *reactants* keyword followed by the number of reactant descriptions that are used. The specification of the reactants involves specifying the atomic interactions. The atoms are referenced by the order in the atoms list provided immediately above, starting with 1 for the first atom. The specification for the first line is how atom 1 interacts with atom 2, for example as *1 singlebond 2*. This indicates there is a single bond present between atoms 1 and 2 (as specified in the atoms listing). Additionally, atoms can have either a double bond (using the *doublebond* keyword) or non-bonded interaction (using the *nonbond* keyword). For non-bonded interactions, only those pertinent to the description of the reaction need to be supplied (e.g., a non-bonded atom pair that will form a bond upon completion of the reaction).

Following the specification of the reactants comes the specification of the products. This is how the atomic interactions will be after the reaction has completed. For example, if it is a dissociation reaction, what was a single bond interaction now becomes a non-bonded interaction. The products are specified immediately after the last reactant specification and are identified using the *products* keyword, followed by the number of product pair descriptions given. The specification of the products follows the same format as for the reactants.

There should be no blank lines between any of the above descriptions given for the atoms in the reaction.

D.2.4 Reaction Coordinate and Switching Functions Specification

Reaction Coordinate

The reaction coordinate is a required specification, which is identified with the *reaction_coordinate* keyword. After the keyword is the number of functions to be included. Eventually, the reaction coordinate will be able to handle compound descriptions of functions; however, currently it can only take a single function. Therefore, a specification of 1 is given.

On the next line is the specification of the function to be used. The available functions to be used are: polynomial and abs_rc (for abstraction reaction coordinate). Complete descriptions of the functions are provided in Sec. D.

After the description of the parameters for the particular function is the description of dependent variable for the function. This is first identified with the *dependent_variable* keyword. Afterwards, the type of atomic interaction is specified, with available options of *bond*, *angle*, *torsion*, or *separation*. These specify whether the interaction is a bonded, angular, torsional, or separation distance between atoms. Next the atom number of the interactions are given, where the atom numbers are based on the order specified in the atoms description, with the first atom being 1. For example, for an angular interaction between atoms 1-3-4, the command is *dependent_variable angle 1 3 4*.

Switching Function

The switching function is a required keyword that specifies the switching functions to be used. The *switching_function* keyword can be used multiple times within a reaction description as multiple switching functions can be employed within a single description. Each switching function is specified in its own block, with the switching functions being specified in the order they will be used. On the same line as the *switching_function* keyword is the type of switching function to be used. The available methods are: tanh. Specifications are given below in the function definitions section.

D.2.5 Additional Specifications

Additional Energy

The additional energy considerations are made using the required *additional_energy* and *additional_energy_s2* keywords. The difference is that the former is controlled by the first switching function (S_1) and the latter is controlled by the second switching function (S_2). This keyword must also specify the functional form to be used for calculating the additional energy function of the reaction. After the keyword is the number of functions used to comprise the additional energy function; however, currently compound functions are not available, so only a single function is used, specified by a value of 1. The additional energy functions available are: polynomial. The dependent variable for the additional energy is the reaction coordinate, so there is no dependent variable to be specified.

Angles and Dihedrals to Include

For each bond pair in which at least one of the two atoms has a change in atom type, the bonded forcefield description is switched automatically. The angular and torsional modes are treated in a similar scheme. However, it is possible to specify which type of angle and torsion modes are switched during the course of a reaction. Consider that '1' represents an atom that is actively participating in a reaction and will transition upon completion. Consider 'x' any atom type that will not transition. It is possible to specify if separately whether the x1x and xx1 angular modes are to be transitioned or not during a reaction. This provides flexibility in the terms to be included and the description of changes of modes as necessary. Likewise, the torsional x1xx and 1xxx modes can be specified. Any angular or torsional mode that includes two or more reactive atoms is automatically included. By default, only the x1x angular mode is included. This can help reduce unnecessary overlaps in the construction of reaction chains when modes do not significantly change during a reaction and are desired to not be included in the overlapping modes analysis for the construction of reaction chains.

The angular modes can be specified using the *angles_include* keyword. Afterwards on the same line goes the specification of the modes to be changed. For example *angles_include x1x on xx1 on* sets both the x1x and xx1 angles to be included. The

angle types are specified using *x1x* and *xx1*. The options are either *on* for inclusion or *off* to not include those modes.

Similarly, the torsional modes are handled using the *dihedrals_include* keyword. Again on the same line, the specification of the modes is done using either the *xxx1* or *x1xx* identifiers. Both modes do not need to be specified.

It is important that the value of the forcefield parameters for each description (x1x, etc.) that is not transitioned during the course of the reaction remains the same in the both the reactant and product states. For example, if the xx1 modes are not included, then the angular interaction c1-c1-c1 and c1-c1-c1r (where c1r is the radical atom who changed during the reaction) must have the same parameters. If not, when the atom types are update upon completion of the reaction, there will be a jump in the energy from a sudden change in parameters. This is true for all angular and torsional modes that are not being considered as changing forcefield parameters as the result of a reaction completing.

Enthalpy Change

This required keyword specifies the ΔH_{rxn} that occurs upon completion of a reaction. The enthalpy change is a constant double-precision value given in J/mol. It is a required specification using the *enthalpy_change* keyword followed by the value.

Reverse Reaction

The reverse reaction is included by default. The reverse reaction can be excluded using the *reverse_reaction* keyword. The keyword takes a specification of either *on* for inclusion of reverse reactions or *off* to not include the reverse reaction.

D.2.6 Function Definitions

D.2.6.1 Abstraction Reaction Coordinate

The abstraction reaction coordinate function is a specialized function used for the description of reaction coordinates in abstraction methods, which require the relationship between two different separation distances. This function should only be used by itself as a reaction coordinate definition, never in a compound function.

Because there is not a functional relationship between the two separation distances, these distances must be related through another variable, t. The relationship is completed through function relationships to two different functions of t, $\phi(t)$ and $\psi(t)$, using exponential growth/decay functions:

$$\phi(t) = \psi(t) = A + B\exp(Ct) \tag{D.1}$$

The variables are specified as *a_bond*, *b_bond*, *c_bond*, *a_nonbond*, *b_nonbond*, *c_nonbond*, where the difference is that the *_bond* are the variables describing the bonded pair. The bonded pair is the $\psi(t)$ function that relates the two atoms that are bound at reactant side of the reaction description. The *_nonbond* description is for

the $\phi(t)$ relationship between the two atoms that are non-bonded on the reactant side of the abstraction reaction, but it would become in a bonded state if the entire abstraction reaction series goes to completion. The units of *a_bond*, *b_bond*, *a_nonbond*, and *b_nonbond* are meters, while *c_bond* and *c_nonbond* are dimensionless.

The *dt* variable specifies the increment value to be used as a integration step size for the completion of the integral specified in 3.7. The *tmax* variable is the maximum t, corresponding the the value of t at the transition state (RC=1). The *tmin* variable corresponds to the value of t at the start of the reactant (RC=0).

The *eps* variable specifies the tolerance for converenge used in the solution of the t-values. The value is a dimensionless difference ratio from the previous step t value to the current step t value. Typical values of 0.001 should be sufficient. The *maxiter* variable specifies the maximum number of iterations to complete in order to determine the t value.

The *maxsep* variable specifies the maximum distance between the non-bonded distance for the abstraction reaction to be considered active. If the nonbond distance is greater than the *maxsep* value, the abstraction reaction would not be active. The *maxsep* variable is specified in meters.

D.2.6.2 Polynomial

A polynomial function can be used for various mathematical descriptions. The polynomial function is specified using the *polynomial* keyword followed by the integer value of the polynomial degree. For example, a quadratic function is specified as *polynomial 2*. On the next line, goes the specification of the coefficients for the polynomial. All the coefficients are placed on the same line, with the first coefficient being the zero-other order term or the constant-value. Next is the first-order term, then second-order term, etc. Any coefficient that is zero must have a zero supplied for its coefficient.

The units provided are all SI, so the coefficients must be provided in the appropriate units, because no conversions will occur within the program. The bond and separation distances will be returned in units of meters. The angular and torsional angles will be returned in radians.

D.2.6.3 Tanh-style Switching Function

The *tanh* specification provides the use of the tanh-style switching function

$$S(RC) = 0.5\left[1 - \tanh\left(a\left(RC - RC_0\right)\right)\right] \tag{D.2}$$

The tanh-style switching function takes the specification of the a and RC_0 variables, one variable per line. The variables can be specified in any order. The a parameter is identified using *a*. The RC_0 is specified using the *rc0* (thats zero). Both of these parameters are dimensionless.

D.3 Example Descriptions

D.3.1 dissociation1

Shown below the description is the text of a rxn file for C-C dissociation reactions using the dissociation1 description.

The first line identifies the beginning of the reaction through the *#reaction* keyword. The next line is a comment line identified by the exclamation mark as the first character of the line (spaces count as the first character). The following line gives the text description of the reaction which will be provided to the text output file from the simulation. The following line gives the required reaction dependence. Afterwards, the required reaction type is specified, *dissociation1* in this case. Finally, the required reaction identification is given, providing a name for the reaction.

The next block of text describes the atoms and bonding changes that occur during the reaction. It is called using the *atoms* keyword followed by the number of atoms involved. There are 2 atoms directly involved in this description. The following line contains the description for the first atom. The description gives the reactant atom type followed by the product atom type. The reaction is written in the forward direction, so for this case the first atom type is the bound-state description and the second atom type is the dissociated atom type. In this case the first atoms is an *c3* atom in the bound state and *c3r* in the unbound state. The same description also applies to the second atom given on the line below. For the dissociation1 reaction type, the first two atoms must be the atoms that are actually breaking/forming a bond. Any additional neighboring atoms that are required for description but do not directly participate must come after these first two atoms.

Immediately after the atom type descriptions comes the reactant bonding description specified by the *reactants* keyword followed by the number of descriptions given. In this case, the first atom has a single bond to atom 2. The atom numbers are the order they appear in the atom-type description listing above the reactants. After the reactants is the product descriptions identified by the *products* keyword, which is specified as having only one description. In this case, the bond breaks upon dissociation so the atoms become non-bonded after the reaction.

The next section describes the reaction coordinate. In this case a single function is used so a 1 follows the *reaction_coordinate* keyword. The next line contains the function being used, which is a polynomial of degree 1, or a linear function. The following line contains the specification of the coefficients. The zero order coefficient (y-intercept) is first, followed by the first-order coefficient (slope) second. The following line contains a description of the dependent variable, which is the bond distance between the atoms 1 and 2.

The next two blocks describe the switching functions. The first block describes S_1 because it is the first switching function given. The second block gives the parameters for S_2 because it is the second switching function defined. This order is always the same. Each switching function uses the *tanh* form and the required parameters are given afterwards, one per line. The parameters do not have to be given in any particular order.

After the switching functions comes the specification of the additional energy term. In this case a constant value of the baseline energy is required as the atoms dissociate. Therefore, the additional energy is specified using the *additional_energy* keyword followed by a 1 indicating that only one functional description is being used. (Remember, the reaction coordinate is automatically the dependent variable for the additional energy function.) In this case, a polynomial of degree zero is used for a constant, as specified using the *polynomial 0* line. The following line contains the coefficient, which is the value of E_{base} here given in J/mol.

The final block contains various information. First is the enthalpy change upon completion of the forward reaction direction given in units of J/mol. The next line specifies that the *x1x* angles will be included, but the *xx1* angles will not be included as changing during the reaction. The following line indicates that neither the *xxx1* nor *x1xx* torsional modes will be included. The next line indicates that reverse reactions are not being considered.

Finally the *#end* command signals this is the end of the file. If another reaction was being included, the *#reaction* command would have been used indicating that a new reaction description is being started.

```
#reaction
!reaction for cc dissociation/association
description c-c = c* + c*
reaction_dependence primary
reaction_type dissociation1
id cc_dissoc

atoms 2
c3 c3r
c3 c3r
reactants 1
1 singlebond 2
products 1
1 nonbond 2

reaction_coordinate 1
polynomial 1
-0.75242 4452169453
dependent_variable bond 1 2

switching_function tanh
a 14.05465
rc0 0.610218

switching_function tanh
a 33.601291
rc0 0.100
```

```
additional_energy 1
polynomial 0
364016.7

enthalpy_change 364016.7
angles_include x1x on xx1 off
dihedrals_include xxx1 off x1xx off
reverse_reaction off

#end
```

D.3.2 beta_scission1

Shown below the description is the text of a rxn file for C-C-C β-scission reaction using the beta_scission1 description.

The first line identifies the beginning of the reaction through the *#reaction* keyword. The next line is a comment line identified by the exclamation mark as the first character of the line (spaces count as the first character). The following line gives the text description of the reaction which will be provided to the text output file from the simulation. The following line gives the required reaction dependence, primary in this case. Afterwards, the required reaction type is specified, *beta_scission1* in this case. Finally, the required reaction identification is given, providing a name for the reaction.

The next block of text describes the atoms and bonding changes that occur during the reaction. It is called using the *atoms* keyword followed by the number of atoms involved. There are 3 atoms directly involved in this description. The following line contains the description for the first atom, which is the atom that will start as bonded but will become the radical atom once the β-scission reaction completes. The description gives the reactant atom type followed by the product atom type. The reaction is written in the forward direction, so for this case the first atom type is the bound-state description and the second atom type is the dissociated atom type, in the radical state. In this case the first atoms is an *c3* atom in the bound state and *c3r* in the radical state. The second atom is the middle atom of the β-scission reaction that will remain fully bound, however one of the bonds will be broken a double bond will be formed. In this case the atom type transitions from *c2* to *c=*. The same description also applies to the second atom given on the line below. The third atom starts as a radical type and will be participating in the double bond upon completion of the reaction. It begins as the radical *c3r* type and transitions to a *c=* double-bonded carbon atom at the completion of the reaction. For the beta_scission1 reaction type, the first three atoms must be the atoms that are actually transitioning during the course of the reaction in the order shown. Any additional neighboring atoms that are required for description but do not directly participate must come after these first three atoms.

Immediately after the atom type descriptions comes the reactant bonding description specified by the *reactants* keyword followed by the number of descriptions given, 2 in this case. In this case, the first atom has a single bond to atom 2 and the second atom has a single bond to the third atom. The atom numbers are the order they appear in the atom-type description listing above the reactants. After the reactants is the product descriptions identified by the *products* keyword, which is specified as having two descriptions. In this case, the bond breaks upon β-scission, so the atoms 1 and 2 become non-bonded after the reaction, while atoms 2 and 3 are now joined by a double bond.

The next section describes the reaction coordinate. In this case a single function is used so a 1 follows the *reaction_coordinate* keyword. The next line contains the function being used, which is a polynomial of degree 1, or a linear function. The following line contains the specification of the coefficients. The zero order coefficient (y-intercept) is first, followed by the first-order coefficient (slope) second. The following line contains a description of the dependent variable, which is the bond distance between the atoms 1 and 2.

The next two blocks describe the switching functions. The first block describes S_1 because it is the first switching function given. The second block gives the parameters for S_2 because it is the second switching function defined. This order is always the same. Each switching function uses the *tanh* form and the required parameters are given afterwards, one per line. The parameters do not have to be given in any particular order.

After the switching functions comes the specification of the additional energy term. In this case a constant value of the baseline energy is required as the reaction completes in order to represent the baseline properly. Therefore, the additional energy is specified using the *additional_energy* keyword followed by a 1 indicating that only one functional description is being used. (Remember, the reaction coordinate is automatically the dependent variable for the additional energy function.) In this case, a polynomial of degree zero is used for a constant, as specified using the *polynomial 0* line. The following line contains the coefficient, which is the value of E_{base} here given in J/mol. A second block is also included using the keyword, *additional_energy_s2*, which specifies an additional energy term dependent on the second switching function, S_2. This term correspons to the E_π penalty included in the β-scission description. Again, a constant value is used, so a polynomial of degree zero is requested, with the constant value specified on the next line.

The final block contains various information. First is the enthalpy change upon completion of the forward reaction direction given in units of J/mol. The next line specifies that the *x1x* angles and the *xx1* angles will be included and change forcefield parameters once the reaction completes. The following line indicates that both the *xxx1* nor *x1xx* torsional modes will change upon completion as well.

```
#reaction
!  reaction description for ccc betascission
description c3h7 = c2h4+ ch3
reaction_dependence primary
```

```
reaction_type beta_scission1
id c3h7_bs

atoms 3
c3 c3r
c2 c=
c3r c=
reactants 2
1 singlebond 2
2 singlebond 3
products 2
1 nonbond 2
2 doublebond 3

reaction_coordinate 1
polynomial 1
-0.762 4.762e+09
dependent_variable bond 1 2

!define switching function
switching_function tanh
a 10.418
rc0 0.3075

switching_function tanh
a 11.00
rc0 0.1989

additional_energy 1
polynomial 0
266391.2

additional_energy_s2 1
polynomial 0
-126431.0

enthalpy_change 139960.2
angles_include x1x on xx1 on
dihedrals-include xxx1 on x1xx on
```

D.3.3 abstraction1

Shown below the description is the text of a rxn file for H-H-H abstraction reaction using the abstraction1 description.

The first line identifies the beginning of the reaction through the *#reaction* keyword. The next line is a comment line identified by the exclamation mark as the first character of the line (spaces count as the first character). The following line gives the text description of the reaction which will be provided to the text output file from the simulation. The following line gives the required reaction dependence, primary in this case. Afterwards, the required reaction type is specified, *abstraction1* in this case. Finally, the required reaction identification is given, providing a name for the reaction.

The next block of text describes the atoms and bonding changes that occur during the reaction. It is called using the *atoms* keyword followed by the number of atoms involved. There are 3 atoms directly involved in this description. The following line contains the description for the first atom, which is the atom that will start as bonded. The description gives the reactant atom type followed by the product atom type. The reaction is written in the forward direction, so for this case the first atom type is the bound-state description and the second atom type is weakly bound transition-state description. In this case the first atoms is an h atom in the bound state and *h3ts* in the weakly bound transition-state complex. The second atom is also bound at the start of the abstraction reaction. Again, the atom type transitions from h to *h3ts*. The same description also applies to the second atom given on the line below. The third atom starts as a radical type and will be having a non-bonded interaction with the second atom as part of the abtraction reaction. It begins as the radical *hr* type and transitions to a *h3ts* as it also participates in the weakly bound transition-state complex at the completion of the reaction (located at the TS for abstraction1 reaction descriptions). For the abstraction1 reaction type, the first three atoms must be the atoms that are actually transitioning during the course of the reaction in the order shown. Any additional neighboring atoms that are required for description but do not directly participate must come after these first three atoms.

Immediately after the atom type descriptions comes the reactant bonding description specified by the *reactants* keyword followed by the number of descriptions given, 2 in this case. In this case, the first atom has a single bond to atom 2 and the second atom has a non-bond interaction to the third atom. The atom numbers are the order they appear in the atom-type description listing above the reactants. After the reactants is the product descriptions identified by the *products* keyword, which is specified as having two descriptions. For the abstraction1 reaction description, the products are located at the transition state, so these descriptions are of a weakly-bound transition state complex. In this case, atom 1 is bound to atom 2, and atom 2 is also bound to atom 3.

The next section describes the reaction coordinate. In this case a single function is used so a 1 follows the *reaction_coordinate* keyword. The next line contains the function being used, which is a *abs_rc*, or a specialized function available for abstraction reactions. The next 12 lines identify the paramters for the abs_rc method. The first three lines describe a, b, and c parameters for the nonbonded t-relationship, $\phi(t)$. The next three lines describe the a, b, and c parameters of the bonded t relationship for $\psi(t)$. The units of the a and b parameters are in meters, while c is unitless. The next line contains the dt variable used for specifying the numerical integration step

size of t. The next two lines specify the maximum and then minimum t values that were used in the development of the reaction coordinate relationship. The *eps* parameter is next, which specifies the ratio of previous step t value to the current step t-value used for iteratively solving for t. The following line contains *maxiter* that specifies the maximum number of iterations to attempt to find the t value. The final parameter is the *maxsep* parameter, which specifies the maximum non-bonded distance between atoms 2 and 3 permitted and the abstraction reaction to be considered (i.e. any separation greater than *maxsep* for atoms 2 and 3, would mean that an abstraction reaction would not be considered as active at all. The following the last line containing the specification of variables is the dependent variable descriptions. The variables do not have to be specified in this order.

In this case two separate dependent variables are required. The first dependent variable describes the bond between the first and second atom at the beginning of the reaction, and the second dependent variable describes the separation distance between the second and third atoms, which will become weakly bound at the transition state. The dependent variables must be specified in this order.

The next two blocks describe the switching functions. The first block describes S_1 because it is the first switching function given. The second block gives the parameters for S_2 because it is the second switching function defined. This order is always the same. Each switching function uses the *tanh* form and the required parameters are given afterwards, one per line. The parameters do not have to be given in any particular order.

After the switching functions comes the specification of the additional energy term. In this case a constant value of zero is being used. Therefore, the additional energy is specified using the *additional_energy* keyword followed by a 1 indicating that only one functional description is being used. (Remember, the reaction coordinate is automatically the dependent variable for the additional energy function.) In this case, a polynomial of degree zero is used for a constant, as specified using the *polynomial 0* line. The following line contains the coefficient, which is the value of E_{base} here given in J/mol. Although no specific function was requested, the *additional_energy* must be specified, therefore a value of zero is used.

The final block contains the enthalpy change upon completion of the forward reaction direction given in units of J/mol.

```
#reaction
!  reaction description for h3 abstraction
description h2 + h = h + h2
reaction_dependence primary
reaction_type abstraction1
id h3abs

atoms 3
h h3ts
h h3ts
hr h3ts
```

```
reactants 2
1 singlebond 2
2 nonbond 3
products 2
1 singlebond 2
2 singlebond 3

!Define rc
reaction_coordinate 1
abs_rc
a_nonbond 0.75596e-10
b_nonbond 2.33807e-10
c_nonbond 0.038499342
a_bond 0.75596e-10
b_bond 0.00784e-10
c_bond 0.038499342
dt 0.05
tmax 74.0
tmin 1.0
eps 0.001
maxiter 40
maxsep 2.866e-10
dependent_variable bond 1 2
dependent_variable separation 2 3

!define switching function
switching_function tanh
a 9.5536
rc0 0.6530

!define second switching function
switching_function tanh
a 16.0009
rc0 0.5004

additional_energy 1
polynomial 0
0.0

enthalpy_change 0.0
```

BIBLIOGRAPHY

[1] Sinfrônto, F.S.M., Santos, J.C.O., Pereira, L.G., G, S.A., Conceição, M.M., Fernandes, Jr., V.J., and Fonseca, V.M., *J. Therm. Anal. Cal.*, **79** (2005), 393–399.

[2] Inguilizian, T., *Correlating polymer flammability using measured pyrolysis kinetics*, Master's thesis, University of Massachusetts Amherst (1999).

[3] Stoliarov, S.I., Westmoreland, P.R., Nyden, M.R., and Forney, G.P., *Polymer*, **44** (2003), 883–894.

[4] Lyon, R.E., Speitel, L., Walters, R.N., and Crowley, S., *Fire Mater.*, **27** (2003), 195–208.

[5] Sarkos, C.P., *Toxicology*, **115** (1996), 79–87.

[6] Ablett, R., International Aircraft Fire and Cabin Safety Research Conference, Atlantic City, NJ (2001).

[7] Westbrook, C.K., *Combust. Sci. Technol.*, **34** (1983), 201–225.

[8] Westmoreland, P.R., Burgess, Jr., D.R.F., Zachariah, M.R., and Tsang, W., *25th Symp. (Int.) Combust.*, **25** (1994), 1505–1511.

[9] Saso, Y., *Proc. Combust. Inst.*, **29** (2002), 337–344.

[10] Williams, B.A., and Fleming, J.W., *Proc. Combust. Inst.*, **29** (2002), 345–351.

[11] Duquesne, S., Le Bras, M., Bourbigot, S., Delobel, R., Vezin, H., Camino, G., Eling, B., Lindsay, C., and Roels, T., *Fire Mater.*, **27** (2003), 103–117.

[12] Zhang, J., and Zhang, H.P., *J. Fire Sci.*, **23** (2005), 193–208.

[13] Babrauskas, V., *Heat Release in Fires*, Elsevier, New York (1992).

[14] ASTM D 2863-87, Standard Test Method for Measuring the Minimum Oxygen Concentration to Support Candle-Like Combustion of Plastics (Oxygen Index), Technical report, ASTM International, www.astm.org.

[15] UL94, Standard for tests for flammability of plastic materials for parts in devices and appliances, Technical report, Underwriters Laboratory, Inc., Research Triangle Park, NY (1991).

[16] ASTM E 906, Standard Test Method for Heat and Visible Smoke Release Rates for Materials and Products, Technical report, ASTM International, www.astm.org.

[17] ASTM E 1354, Standard Test Method for Heat and Visible Smoke Release Rates for Materials and Products Using an Oxygen Consumption Calorimeter, Technical report, ASTM International, www.astm.org.

[18] Lyon, R.E., and Walters, R.N., *J. Anal. Appl. Pyrolysis*, **71** (2004), 27–46.

[19] Westmoreland, P.R., Inguilizian, T., and Rotem, K., *Thermo. Acta*, **367-368** (2001), 401–405.

[20] Pawlowski, K.H., and Schartel, B., *93*, (2008).

[21] Onu, P., Vasile, C., Ciocîlteu, S., Iojoiu, E., and Darie, H., *J. Anal. Appl. Pyrolysis*, **49** (1999), 145–153.

[22] McCaffrey, W.C., Kamal, M.R., and Cooper, D.G., *Polymer Degrad. Stabil.*, **47** (1995), 133–139.

[23] Conesa, J.A., Marcilla, A., Font, R., and Caballero, J.A., *J. Anal. Appl. Pyrolysis*, **36** (1996), 1–15.

[24] Tang, L., Huang, H., Zhao, Z., Wu, C.Z., and Chen, Y., *Ind. Eng. Chem. Res.*, **42** (2003), 1145–1150.

[25] Hedrick, S.A., and Chuang, S.S.C., *Thermo. Acta*, **315** (1998), 159–168.

[26] Gao, Z., Amasaki, I., and Nakada, M., *J. Anal. Appl. Pyrolysis*, **67** (2003), 1–9.

[27] Gao, Z., Amasaki, I., Kaneko, T., and Nakada, M., *Polymer Degrad. Stabil.*, **81** (2003), 125–130.

[28] Westerhout, R.W.J., Waanders, J., Kuipers, J.A.M., and van Swaaij, W.P.M., *Ind. Eng. Chem. Res.*, **36** (1997), 1955–1964.

[29] Ranzi, E., Dente, M., Faravelli, T., Bozzano, G., Fabini, S., Nava, R., Cozzani, V., and Tognotti, L., *J. Anal. Appl. Pyrolysis*, **40-41** (1997), 305–319.

[30] Ceamonos, J., Mastral, J.F., Millera, A., and Aldea, M.E., *J. Anal. Appl. Pyrolysis*, **65** (2002), 93–110.

[31] Faravelli, T., Bozzano, G., Columbo, M., Ranzi, E., and Dente, M., *J. Anal. Appl. Pyrolysis*, **70** (2003), 761–777.

[32] Bockhorn, H., Hornung, A., Hornung, U., and Schwaller, D., *J. Anal. Appl. Pyrolysis*, **48** (1999), 93–109.

[33] Mastral, J.F., Berruecco, C., and Caemanos, J., *J. Anal. Appl. Pyrolysis*, **79** (2007), 313–322.

[34] Horvat, N., and Ng, F.T.T., *Fuel*, **78** (1999), 459–470.

[35] Gillespie, D.T., *J. Comput. Phys.*, **22** (1976), 403–434.

[36] Gillespie, D.T., *J. Phys. Chem.*, **81** (1977), 2340–2361.

[37] Battaile, C.C., and Srolovitz, D.J., *Ann. Rev. of Mat. Res.*, **32** (2002), 297–319.

[38] Frenklach, M., Schuetz, C.A., and Ping, J., *Proc. Combust. Inst.*, **30** (2005), 1389–1396.

[39] Barker, J.R., *J. Chem. Phys.*, **72** (1980), 3686–3694.

[40] Mei, D., Ge, Q., Neurock, M., Kieken, L., and Lerou, J., *Mol. Phys.*, **102** (2004), 361–369.

[41] Kieken, L.D., Neurock, M., and Mei, D., *J. Phys. Chem. B*, **109** (2005), 2234–2244.

[42] Golden, D.M., Barker, J.R., and Lohr, L.L., *J. Phys. Chem. A*, **107** (2003), 11057–11071.

[43] Barker, J.R., *Int. J. Chem. Kinet.*, **33** (2001), 233–245.

[44] Barker, J.R., *Int. J. Chem. Kinet.*, **33** (2001), 246–261.

[45] Violi, A., Kubota, A., Truong, T.N., Pitz, W.J., Westbrook, C.K., and Sarofim, A.F., *Proc. Combust. Inst.*, **29** (2002), 2343–2349.

[46] Violi, A., *Combust. Flame*, **139** (2004), 279–287.

[47] Violi, A., Sarofim, A.F., and Voth, G.A., *Combust. Sci. Technol.*, **176** (2004), 991–1005.

[48] Car, R., and Parrinello, M., *Phys. Rev. Lett.*, **55** (1985), 2471–2474.

[49] Tuckerman, M.E., and Parrinello, M., *J. Chem. Phys.*, **101** (1994), 1302–1315.

[50] Iftimie, R., Minary, P., and Tuckerman, M.E., *Proc. Natl. Acad. Sci.*, **102** (2005), 6654–6659.

[51] Blaisten-Barojas, E., and Nyden, M.R., *Chem. Phys. Lett.*, **171** (1990), 499–505.

[52] Nyden, M.R., and Noid, D.W., *J. Phys. Chem.*, **95** (1991), 940–945.

[53] Nyden, M.R., Forney, G.P., and Brown, J.E., *Macromolecules*, **25** (1992), 1658–1666.

[54] Nyden, M.R., Coley, T.R., and Mumby, S., *Polym. Eng. Sci.*, **37** (1997), 1496–1500.

[55] van Duin, A.C.T., Dasgupta, S., Lorant, F., and Goddard III, W.A., *J. Phys. Chem. A*, **105** (2001), 9396–9409.

[56] van Duin, A.C.T., Stachan, A., Stewman, S., Zhang, Q., Xu, X., and Goddard III, W.A., *J. Phys. Chem. A*, **107** (2003), 3803–3811.

[57] Brenner, D.W., *Phys. Rev. B*, **42** (1990), 9458–9471.

[58] Brenner, D.W., *Phys. Rev. B*, **46** (1992), 1948.

[59] Stuart, S.J., Li, Y., Kum, O., Mintmire, J.W., and Voter, A.F., *J. Chem. Phys.*, **112** (2000), 6472–6486.

[60] Brenner, D.W., Shenderova, O.A., Harrison, J.A., Stuart, S.J., Ni, B., and Sinnott, S.B., *J. Phys.-Condens. Mat.*, **14** (2002), 783–802.

[61] Warshel, A., and Weiss, R.M., *J. Am. Chem. Soc.*, **102** (1980), 6218–6226.

[62] Åqvist, J., and Warshel, A., *Chem. Rev.*, **93** (1993), 2523–2544.

[63] Hopfinger, A.J., and Pearlstein, R.A., *J. Comput. Chem.*, **5** (1984), 486–499.

[64] Morley, S.D., Abraham, R.J., Haworth, I.S., Jackson, D.E., Saunders, M.R., and Vinter, J.G., *J. Comput. Aid. Mol. Des.*, **5** (1991), 475–504.

[65] Gundertofte, K., Lilefors, T., Per-Ola, N., and Pettersson, I., *J. Comput. Chem.*, **17** (1996), 429–449.

[66] Feller, S.E., and MacKerell Jr., A.D., *J. Phys. Chem. B*, **104** (2000), 7510–7515.

[67] Gaedt, K., and Holtje, H.D., *J. Comput. Chem.*, **19** (1998), 935–946.

[68] Li, H.C., McCabe, C., Cui, S.T., Cummings, P.T., and Cochran, H.D., *Mol. Phys.*, **100** (2002), 265–272.

[69] Rappé, A.K., Casewit, C.J., Colwell, K.S., Goddard III, W.A., and Skiff, W.M., *J. Am. Chem. Soc.*, **114** (1992), 10024–10035.

[70] Li, H.C., McCabe, C., Cui, S.T., Cummings, P.T., and Cochran, H.D., *Mol. Phys.*, **101** (2003), 2157–2169.

[71] Klauda, J.B., Brooks, B.R., MacKerell Jr, A.D., Venable, R.M., and Pastor, R.W., *J. Phys. Chem. B*, **109** (2005), 5300–5311.

[72] Sancho-García, J.C., and Cornil, J., *J. Chem. Theory Comput.*, **1** (2005), 581–589.

[73] Jensen, F., and Norrby, P., *Theor. Chem. Acc.*, **109** (2003), 1–9.

[74] Hayes, J.M., Greer, J.C., and Morton-Blake, D.A., *J. Comput. Chem.*, **25** (2004), 1953–1966.

[75] Rowley, R.L., Yang, Y., and Pakkanen, T., *J. Chem. Phys.*, **114** (2001), 6058–6067.

[76] Jalkanen, J.P., Mahlanen, R., and Pakkanen, T.A., *J. Chem. Phys.*, **116** (2002), 1303–1312.

[77] Rowley, R.L., and Pakkanen, T., *J. Chem. Phys.*, **110** (1999), 3368–3377.

[78] Abraham, R.J., and Haworth, I.S., *J. Comput. Aid. Mol. Des.*, **2** (1988), 125–135.

[79] Nagy, J., Weaver, D.F., and Smith Jr., V.H., *Mol. Phys.*, **85** (1995), 1179–1192.

[80] Chiu, S.W., Clark, M.M., Jakobsson, E., Subramaniam, S., and Scott, H.L., *J. Phys. Chem. B*, **103** (1999), 6323–6327.

[81] Kaminski, G., Duffy, E.M., Matsui, T., and Jorgensen, W.L., *J. Phys. Chem.*, **98** (1994), 13077–13082.

[82] Bruehl, M., and Schatz, G.C., *J. Phys. Chem.*, **92** (1988), 7223–7229.

[83] Lim, K., *J. Chem. Phys.*, **100** (1994), 7385–7399.

[84] Lim, K., *J. Chem. Phys.*, **101** (1994), 8756–8767.

[85] Linhananta, A., and Lim, K.F., *Phys. Chem. Chem. Phys.*, **2** (2000), 1385–1392.

[86] Jonsdottir, S.O., and Rasmussen, K., *New J. Chem.*, **24** (2000), 243–247.

[87] Casewit, C.J., Colwell, K.S., and Rappé, A.K., *J. Am. Chem. Soc.*, **114** (1992), 10035–10046.

[88] Casewit, C.J., Colwell, K.S., and Rappé, A.K., *J. Am. Chem. Soc.*, **114** (1992), 10046–10053.

[89] Rappé, A.K., Colwell, K.S., and Casewit, C.J., *Inorg. Chem.*, **32** (1993), 3438–3450.

[90] Cleveland, T., and Landis, C.R., *J. Am. Chem. Soc.*, **118** (1996), 6020–6030.

[91] Weiner, S.J., Kollman, P.A., Case, D.A., Singh, U.C., Ghio, C., Alagona, G., Profeta, Jr., S., and Weiner, P., *J. Am. Chem. Soc.*, **106** (1984), 765–784.

[92] Pearlman, D.A., Case, D.A., Caldwell, J.A., Ross, W.S., Cheatham, III, T.E., DeBolt, S., Ferguson, D., Seibel, G., and Kollman, P., *Comput. Phys. Comm.*, **91** (1995), 1–41.

[93] Cornell, W.D., Cieplak, P., Bayly, C.I., Gould, I.R., Merz Jr., K.M., Ferguson, D.M., Spellmeyer, D.C., Fox, T., Caldwell, J.W., and Kollman, P.A., *J. Am. Chem. Soc.*, **117** (1995), 5179–5197.

[94] Hermans, J., Berendsen, H.J.C., van Gunsteren, W.F., and Postma, J.P.M., *Biopolymers*, **23** (1984), 1513–1518.

[95] Ott, K., and Meyer, B., *J. Comput. Chem.*, **17** (1996), 1068–1084.

[96] Scott, W.R.P., Hünenberger, P.H., Tironi, I.G., Mark, A.E., Billeter, S.R., Fennen, J., Torda, A.E., Huber, T., Krüger, P., and van Gunsteren, W.F., *J. Phys. Chem. A*, **103** (1999), 3596–3607.

[97] Niketić, S.R., and Rasmussen, K., *The Consistent Force Field: A Documentation*, volume 3, Springer-Verlag (1977).

[98] Hwang, M.J., Stockfisch, T.P., and Hagler, A.T., *J. Am. Chem. Soc.*, **116** (1994), 2515–2525.

[99] Vinter, J.G., Davis, A., and Saunders, M.R., *J. Comput. Aid. Mol. Des.*, **1** (1987), 31–51.

[100] Dauber-Osguthorpe, P., Roberts, V.A., Osguthorpe, D.J., Wolff, J., Genest, M., and Hagler, A.J., *Proteins*, **4** (1988), 31–47.

[101] Brooks, B.R., Bruccoleri, R.E., Olafson, B.D., States, D.J., Swaminathan, S., and Karplus, M., *J. Comput. Chem.*, **4** (1983), 187–217.

[102] MacKerell Jr., A.D., Bashford, D., Bellott, M., Dunbrack Jr., R.L., Evanseck, J D Field, M.J., Fischer, S., Gao, J., Guo, H., Ha, S., Joseph-McCarthy, D., Kuchnir, L., Kuczera, K., Lau, F.T.K., Mattos, C., Michnick, S., Ngo, T., Nguyen, D.T., Prodhum, B., Reiher III, W.E., Roux, B., Schlenkrich, M., Smith, J.C., Stote, R., Straub, J., Watanabe, M., Wiórkiewics-Kuczera, J., Yin, D., and Karplus, M., *J. Phys. Chem. B*, **102** (1998), 3586–3616.

[103] Allinger, N.L., *J. Am. Chem. Soc.*, **99** (1977), 8127–8134.

[104] Allinger, N.L., Yuh, Y.H., and Lii, J., *J. Am. Chem. Soc.*, **111** (1989), 8552–8566.

[105] Lii, J., and Allinger, N.L., *J. Am. Chem. Soc.*, **111** (1989), 8576–8582.

[106] Lii, J., and Allinger, N.L., *J. Am. Chem. Soc.*, **111** (1989), 8566–8575.

[107] Allinger, N.L., Chen, K., and Lii, J.H., *J. Comput. Chem.*, **17** (1996), 642–668.

[108] Sun, H., *J. Phys. Chem. B*, **102** (1998), 7338–7364.

[109] Hobza, P., Kabeláč, M., Šponer, J., Mejzlík, P., and Vondrášek, J., *J. Comput. Chem.*, **18** (1997), 1136–1150.

[110] Rudnicki, W.R., and Lesyng, B., *Computers and Chemistry*, **19** (1995), 253–258.

[111] Martin, M.G., and Thompson, A.P., *Fluid Phase Equilibr.*, **217** (2004), 105–110.

[112] Nyden, M.R., Stoliarov, S.I., Westmoreland, P.R., Guo, Z.X., and Jee, C., *Mat. Sci. Eng. A-Struct.*, **365** (2004), 114–121.

[113] Knyazev, V.D., *J. Phys. Chem. A*, **111** (2007), 3875–3883.

[114] Nyden, M.R., and Gilman, J.W., *Comput. Theor. Polym. S.*, **7** (1997), 191–198.

[115] Stoliarov, S.I., Lyon, R.E., and Nyden, M.R., *Polymer*, **45** (2004), 8613–8621.

[116] Chenoweth, K., Cheung, S., van Duin, A.C.T., Goddard III, W.A., and Kober, E.M., *J. Am. Chem. Soc.*, **127** (2005), 7129–7202.

[117] Tersoff, J., *Phys. Rev. Lett.*, **56** (1986), 632–635.

[118] Tersoff, J., *Phys. Rev. B*, **37** (1988), 6991–7000.

[119] Tersoff, J., *Phys. Rev. Lett.*, **61** (1988), 2879–2882.

[120] Tersoff, J., *Phys. Rev. B*, **39** (1989), 5566–5568.

[121] Brenner, D.W., Harrison, J.A., White, C.T., and Colton, R.J., *Thin Solid Films*, **206** (1991), 220–223.

[122] Robertson, D.H., Brenner, D.W., and White, C.T., *J. Phys. Chem.*, **99** (1995), 15721–15724.

[123] Che, J., Çağin, T., and Goddard III, W.A., *Nanotechnology*, **10** (1999), 263–268.

[124] Liew, K.M., He, X.Q., and Wong, C.H., *Acta Mater.*, **52** (2004), 2521–2527.

[125] Ni, B., Sinnott, S.B., Mikulski, P.T., and Harrison, J.A., *Phys. Rev. Lett.*, **88** (2002), 205505.

[126] Delcorte, A., and Bertrand, P., *J. Phys. Chem. B*, **105** (2001), 9474–9486.

[127] WenXing, B., ChangChun, Z., and WanZhao, C., *Physica B*, **352** (2004), 156–163.

[128] Ni, B., Lee, K., and Sinnott, S.B., *J. Phys.-Condens. Mat.*, **16** (2004), 7261–7275.

[129] Longhurst, M.J., and Quirke, N., *Mol. Sim.*, **31** (2005), 135–141.

[130] Braga, S.F., and Galvão, D.S., *J. Comput. Chem.*, **28** (2007), 1724–1734.

[131] Ito, A., and Nakamura, H., *J. Plasma Phys.*, **72** (2006), 805–808.

[132] Xiao, S., and Hou, W., *Fullerenes, Nanotubes, and C Nanost*, **14** (2006), 9–16.

[133] Wu, G., and Dong, J., *Phys. Rev. B*, **73** (2006), 245414.

[134] Ma, T., Hu, Y., Wang, H., and Li, X., *Phys. Rev. B*, **75** (2007), 035425.

[135] Roussel, T., Didion, A., Pellenq, J., Gadiou, R., Bichara, C., and Vix-Guterl, C., *J. Phys. Chem. C*, **111** (2007), 15863–15876.

[136] Strachan, A., van Duin, A.C.T., Chakraborty, D., Dasgupta, S., and Goddard III, W.A., *Phys. Rev. Lett.*, **91** (2003), 098301.

[137] Cheung, S., Deng, W., van Duin, A.C.T., and Goddard III, W.A., *J. Phys. Chem. A*, **109** (2005), 851–859.

[138] van Duin, A.C.T., and Damsté, J.S.S., *Org. Geochem.*, **34** (2003), 515–526.

[139] Zhang, Q., Çağin, T., van Duin, A., and Goddard III, W.A., *Phys. Rev. B*, **69** (2004), 045423.

[140] Strachan, A., Kober, E.M., van Duin, A.C.T., Oxgaard, J., and Goddard III, W.A., *Phys. Rev. Lett.*, **122** (2005), 054502.

[141] Buehler, M.J., van Duin, A.C.T., and Goddard, III, W.A., *Phys. Rev. Lett.*, **96** (2006), 095505.

[142] Ludwig, J., Vlachos, D.G., van Duin, A.C.T., and Goddard, III, W.A., *J. Phys. Chem. B*, **110** (2006), 4274–4282.

[143] Pudar, S., Oxgaard, J., Chenoweth, K., van Duin, A.C.T., and Goddard, III, W.A., *J. Phys. Chem. C*, **111** (2007), 16405–16415.

[144] Su, H., Nielson, R.J., van Duin, A.C.T., and Goddard, III, W.A., *Phys. Rev. B*, **75** (2007), 134107.

[145] Chenoweth, K., van Duin, A.C.T., and Goddard, III, W.A., *J. Phys. Chem. A*, **112** (2008), 1040–1053.

[146] Nielson, K.D., van Duin, A.C.T., Oxgaard, J., Deng, W., and Goddard III, W.A., *J. Phys. Chem. A*, **109** (2005), 493–499.

[147] Yina, K., Xiaa, Q., Xub, D., Yec, Y., and Chen, C., *Computers and Chem Eng*, **30** (2006), 1346–1353.

[148] Woodward, R.B., and Hoffmann, R., *J. Am. Chem. Soc.*, **87** (1965), 395–397.

[149] Woodward, R.B., and Hoffmann, R., *J. Am. Chem. Soc.*, **87** (1965), 2046–2048.

[150] Voter, A.F., *Phys. Rev. B*, **57** (1998), R13985–R13988.

[151] Stuart, S.J., Li, Y., Kum, O., Mintmire, J.W., and Voter, A.F., *Struct. Chem.*, **15** (2004), 479–486.

[152] Voter, A.F., *Phys. Rev. Lett.*, **78** (1997), 3908–3911.

[153] Pal, S., and Fichthorn, K.A., *Chem. Eng. J.*, **74** (1999), 77–83.

[154] Miron, R.A., and Fichthorn, K.A., *J. Chem. Phys.*, **119** (2003), 6210–6216.

[155] Wang, J., Pal, S., and Fichthorn, K.A., *Phys. Rev. B*, **63** (2001), 085403.

[156] Tai, K., *Biophys Chem.*, **107** (2004), 213–220.

[157] Sørensen, M.R., and Voter, A.F., *J. Chem. Phys.*, **112** (2000), 9599–9606.

[158] Montalenti, F., Sørensen, M.R., and Voter, A.F., *Phys. Rev. Lett.*, **87** (2001), 126101.

[159] Montalenti, F., and Voter, A.F., *J. Chem. Phys.*, **116** (2002), 4819–4828.

[160] Montalenti, F., Voter, A.F., and Ferrando, R., *Phys. Rev. B*, **66** (2002), 205404.

[161] Shvartsman, S.Y., and G, K.I., *AIChE J.*, **44** (1998), 1579–1595.

[162] Theodoropoulos, C., Qian, Y.H., and Kevrekidis, I.G., *Proc. Natl. Acad. Sci.*, **97** (2000), 9840–9843.

[163] Makeev, A.G., Maroudas, D., and Kevrekidis, I.G., *J. Chem. Phys.*, **116** (2002), 10083–10091.

[164] Hummer, G., and Kevredidis, I.G., *J. Chem. Phys.*, **118** (2003), 10762–10773.

[165] Roothaan, C.C.J., *J. Chem. Phys.*, **19** (1951), 1445.

[166] Hall, G.G., *Proc. Royal Soc. London*, **A205** (1951), 541.

[167] Møller, C., and Plesset, M.S., *Phys. Rev.*, **46** (1934), 618–622.

[168] Hehre, W.J., Stewart, R.F., and Pople, J.A., *J. Chem. Phys.*, **51** (1969), 2657–2664.

[169] Collins J B, Scheleyer, P.v.R., Binkley, J.S., and Pople, J.A., *J. Chem. Phys.*, **64** (1976), 5142–5151.

[170] Ditchfield, R., Hehre, W.J., and Pople, J.A., *J. Chem. Phys.*, **54** (1971), 724–728.

[171] Hohenberg, P., and Kohn, W., *Phys. Rev.*, **136** (1964), B864–B871.

[172] Kohn, W., and Sham, L.J., *Phys. Rev.*, **140** (1965), A1133–A1138.

[173] Frisch, M.J., Trucks, G.W., Schlegel, H.B., Scuseria, G.E., Robb, M.A., Cheeseman, J.R., Zakrzewski, V.G., Montgomery Jr, J.A., Stratmann, R.E., Burant, J.C., Dapprich, S., Millam, J.M., Daniels, A.D., Kudin, K.N., Strain, M.C., Farkas, O., Tomasi, J., Barone, V., Cossi, M., Cammi, R., Mennucci, B., Pomelli, C., Adamo, C., Clifford, S., Ochterski, J., Petersson, G.A., Ayala, P.Y., Cui, Q., Morokuma, K., Malick, D.K., Rabuck, A.D., Raghavachari, K., Foresman, J.B., Cioslowski, J., Ortiz, J.V., Stefanov, B.B., Liu, G., Liashenko, A., Piskorz, P., Komaromi, I., Gomperts, R., Martin, R.L., Fox, D.J., Keith, T., Al-Laham, M.A., Peng, C.Y., Nanayakkara, A., Gonzalez, C., Challacombe, M., Gill, P.M.W., Johnson, B., Chen, W., Wong, M.W., Andres, J.L., Gonzalez, C., Head-Gordon, M., Replogle, E.S., and Pople, J.A., Gaussian 98, A.7 and A.9, Gaussian, Inc., Pittsburgh, PA (1998).

[174] Frisch, M.J., Trucks, G.W., Schlegel, H.B., Scuseria, G.E., Robb, M.A., Cheeseman, J.R., Montgomery, Jr, J.A., Vreven, T., Kudin, K.N., Burant, J.C., Millam, J.M., Iyengar, S.S., Tomasi, J., Barone, V., Mennucci, B., Cossi, M., Scalmani, G., Rega, N., Petersson, G.A., Nakatsuji, H., Hada, M., Ehara, M., Toyota, K., Fukuda, R., Hasegawa, J., Ishida, M., Nakajima, T., Honda, Y., Kitao, O., Nakai, H., Klene, M., Li, X., Knox, J.E., Hratchian, H.P., Cross, J.B., Bakken, V., Adamo, C., Jaramillo, J., Gomperts, R., Stratmann, R.E., Yazyev, O., Austin, A.J., Cammi, R., Pomelli, C., Ochterski, J.W., Ayala, P.Y., Morokuma, K., Voth, G.A., Salvador, P., Dannenberg, J.J., Zakrzewski, V.G., Dapprich, S., Daniels, A.D., Strain, M.C., Farkas, O., Malick, D.K., Rabuck, A.D., Raghavachari, K., Foresman, J.B., Ortiz, J.V., Cui, Q., Baboul, A.G., Clifford, S., Cioslowski, J., Stefanov, B.B., Liu, G., Liashenko, A., Piskorz, P., Komaromi, I., Martin, R.L., Fox, D.J., Keith, T., Al-Laham, M.A., Peng, C.Y., Nanayakkara, A., Challacombe, M., Gill, P.M.W., Johnson, B., Chen, W., Wong, M.W., Gonzalez, C., and Pople, J.A., Gaussian 03, Revision C.02 and Gaussian Development Version, Revision D.02, Gaussian, Inc., Wallingford, CT, 2004.

[175] Nyden, M.R., and Petersson, G.A., *J. Chem. Phys.*, **75** (1981), 1843–1862.

[176] Petersson, G.A., and Al-Laham, M.A., *J. Chem. Phys.*, **94** (1991), 6081–6090.

[177] Petersson, G.A., Tensfeldt, T.G., and Montgomery, Jr., J.A., *J. Chem. Phys.*, **94** (1991), 6091–6101.

[178] Montgomery, Jr., J.A., Ochterski, J., and Petersson, G.A., *J. Chem. Phys.*, **101** (1994), 5900–5909.

[179] Ochterski, J., Petersson, G.A., and Montgomery, Jr., J.A., *J. Chem. Phys.*, **104** (1996), 2598–2619.

[180] Montgomery, Jr., J.A., Frisch, M.J., Ochterski, J.M., and Petersson, G.A., *J. Chem. Phys.*, **110** (1999), 2822–2827.

[181] Curtiss, L.A., Raghavachari, K., Trucks, G.W., and Pople, J.A., *J. Chem. Phys.*, **94** (1991), 7221–7230.

[182] Curtiss, L.A., Raghavachari, K., Redfern, P.C., and Pople, J.A., *J. Chem. Phys.*, **109** (1998), 7764–7776.

[183] Curtiss, L.A., Raghavachari, K., Redfern, P.C., and Pople, J.A., *J. Chem. Phys.*, **108** (1998), 692–697.

[184] Curtiss, L.A., Raghavachari, K., Redfern, P.C., and Pople, J.A., *J. Chem. Phys.*, **106** (1997), 1063–1079.

[185] Curtiss, L.A., Redfern, P.C., Raghavachari, K., and Pople, J.A., *J. Chem. Phys.*, **109** (1998), 42–55.

[186] Curtiss, L.A., Raghavachari, K., Redfern, P.C., and Pople, J.A., *J. Chem. Phys.*, **112** (2000), 7374–7383.

[187] Wiener, J.J.M., and Politzer, P., *J. Mol. Struct. (Theochem)*, **427** (1998), 171–174.

[188] Martin, J.M.L., *Theor. Chem. Acc.*, **97** (1997), 227–231.

[189] Schlegel, H.B., *J. Comput. Chem.*, **3** (1982), 214–218.

[190] Gonzalez, C., and Schlegel, H.B., *J. Chem. Phys.*, **90** (1989), 2154–2161.

[191] Gonzalez, C., and Schlege, H.B., *J. Phys. Chem.*, **94** (1990), 5523–5527.

[192] Baboul, A.G., and Schlegel, H.B., *J. Chem. Phys.*, **107** (1997), 9413–9417.

[193] Smith, K.D., Stoliarov, S.I., Nyden, M.R., and Westmoreland, P.R., *Mol. Sim.*, **33** (2007), 361–368.

[194] Smith, K.D., Stoliarov, S.I., Nyden, M.R., and Westmoreland, P.R., *Mol. Sim.*, **XX** (2008), XX–XX.

[195] Verlet, L., *Phys. Rev.*, **159** (1967), 98–102.

[196] Kim, Y., Corchado, J.C., Villà, J., Xing, J., and Truhlar, D.G., *J. Chem. Phys.*, **112** (2000), 2718–2735.

[197] Truong, T.N., *J. Chem. Phys.*, **113** (2000), 4957–4964.

[198] Kungwan, N., and Truong, T.N., *J. Phys. Chem. A*, **109** (2005), 7742–7750.

[199] Boys, S.F., and Bernardi, F., *Mol. Phys.*, **19** (1970), 553–561.

[200] Stortz, C.A., *J. Comput. Chem.*, **26** (2005), 471–483.

[201] Tsuzuki, S., Uchimaru, T., Tanabe, K., and Kuwajima, S., *J. Phys. Chem.*, **98** (1994), 1830–1833.

[202] Truhlar, D.G., and Garrett, B.C., *Acc. Chem. Res.*, **13** (1980), 440–448.

[203] Miller, W.H., Handy, N.C., and Adams, J.E., *J. Chem. Phys.*, **72** (1980), 99–112.

[204] McMillen, D.F., and Golden, D.M., *Annu. Rev. Phys. Chem.*, **33** (1982), 493–532.

[205] Carneiro, J.W.d.M., Dias, J.F., Tostes, J.G.R., Seidl, P.R., and Taft, Carlton, A., *Int. J. Quantum Chem.*, **95** (2003), 322–328.

[206] Kim, S., Jang, E.S., Shin, D.H., and Lee, K.H., *Polymer Degrad. Stabil.*, **85** (2004), 799–805.

[207] Marcilla, A., Ruiz-Femenia, R., Hernández, J., and García-Quesada, J.C., *J. Anal. Appl. Pyrolysis*, **76** (2006), 254–259.

[208] Doruker, P., Wang, Y., and Mattice, W.L., *Comput. Theor. Polym. S.*, **11** (2001), 155–166.

[209] Poutsma, M.L., *Macromolecules*, **36** (2003), 8931–8957.

[210] Ballice, L., Yüksel, M., Sağlam, M., Reimert, R., and Schulz, H., *Energy and Fuel*, **12** (1998), 925–928.

[211] Bockhorn, H., Hornung, A., and Hornung, U., *J. Anal. Appl. Pyrolysis*, **50** (1999), 77–101.

[212] Murata, K., Sato, K., and Sakata, Y., *J. Anal. Appl. Pyrolysis*, **71** (2004), 569–589.

[213] Bounaceur, R., Warth, V., Marguarire, P.M., Scacchi, G., Domin, F., Dessort, D., Pradier, B., and Brevart, O., **64** (2002), 103–122.

[214] Madorsky, S.L., *J. Poly. Sci.*, **9** (1952), 133–156.

[215] Poutsma, M.L., **54** (2000), 5–35.

[216] Popov, K.V., and Knyazev, V.D., Eastern States Fall Technical Meeting of The Combustion Institute, Charlottesville, VA (2007).

[217] Jellinek, H.H.G., *J. Poly. Sci.*, **4** (1949), 13–36.

[218] Zeppieri, S.P., Klotz, S.D., and Dryer, F.L., *Proc. Combust. Inst.*, **28** (2000), 1587–1595.

[219] Dean, A.M., *J. Phys. Chem.*, **89** (1985), 4600–4608.

[220] Mastral, J.F., Berruecco, C., and Caemanos, J., *J. Anal. Appl. Pyrolysis*, **80** (2007), 427–438.

[221] Ellzey, K.A., Ranganathan, T., Zilberman, J., Coughlin, E.B., Farris, R.J., and Emrick, T., *Macromolecules*, **39** (2006), 3553–3558.

[222] Ranganathan, T., Zilberman, J., Farris, R.J., Coughlin, E.B., and Emrick, T., *Macromolecules*, **39** (2006), 5974–5975.

[223] Schoemann, A., *Flammability and Pyrolysis Chemistry of Standard and Novel Fire-Safe Polymers*, Ph.D. thesis, University of Massachusetts Amherst (February 2006).

[224] van der Waals, A.C.L.M., Klunder, A.J.H., van Buren, F.R., and Zwanenburg, B., *J. Mol. Cat. A*, **134** (1998), 179–189.

[225] Obi, M., Morino, S., and Ichimura, K., *Chem. Mater.*, **11** (1999), 1293–1301.

[226] Emdee, J.L., Brezinsky, K., and Glassman, I., *J. Phys. Chem.*, **96** (1992), 2151–2161.

[227] Schlitter, J., *Chem. Phys. Lett.*, **215** (1993), 617–621.